GENETIC AND FUNCTIONAL DISSECTION OF CILIARY GENES

AOIFE MARY WATERS

A thesis submitted in conformity with the requirements for the degree of

Doctor of Philosophy

Institute of Child Health,

University College London

Supervisor: Professor Philip Beales

2012

DECLARATION

I, Aoife Waters, confirm that the work presented in this thesis is my own. Where information has been derived from other sources, I confirm that this has been indicated in the thesis.

ACKNOWLEDGEMENTS

Over the past three years, I have benefited from the help and expertise of many talented and wonderful people. To begin with, I would like to thank Phil Beales for hosting my fellowship and providing me with the opportunity to work on this project. Peter Scambler is graciously acknowledged for the provision of an inspiring environment in which to work. I also wish to thank the GOSgene team for playing a key role in establishing the exome pipeline, for which this work would not have been possible. Paul Winyard, Paul Riley and Ania Koziell are graciously acknowledged for their support and guidance on projects and career direction. Members of the UCL Genomics team, Molecular Medicine and Nephro-Urology Units are acknowledged for their help over the past 3 years. In particular, I would like to acknowledge Dr Ariane Chapgier, Dr Catherine Roberts and Dr Sonja Christou. I acknowledge the help of all our collaborators within the field of cilia biology. I am grateful to all the staff at ICH for providing a friendly environment in which to work. I would like to thank the Medical Research Council for their support of my research training. Finally, I am forever grateful to my husband, Jonathan and clinical colleagues at Great Ormond Street Hospital for their love and support.

ABSTRACT

Ciliopathy disorders are associated with either abnormal formation or function of cilia. Mutations have been described in over 60 ciliary genes to date. With the identification of over 1,000 ciliary polypeptides, other disorders exhibiting ciliopathy features could result from mutations in other ciliary genes. A new ciliopathy disease gene, *CENPF*, has been identified in a kindred exhibiting midgestation lethality with congenital malformations suggestive of a novel ciliopathy phenotype. Where conventional approaches such as genome-wide linkage analysis and homozygosity mapping had failed, whole exome capture coupled with massive parallel deep sequencing was successful in elucidating the genetic cause in a single affected case. Identification of compound heterozygous mutations in the causative gene was facilitated through analysis of an unfiltered approach for depth of coverage. Utilising a combinatorial approach of comparative genomics and proteomics, a novel ciliogenic role for the causative gene was identified and proposed by modelling *cenpf* loss of function in *D. rerio* and supported by interactions found with Ift88 and Kif3b, key regulators of ciliogenesis. These data support emerging evidence for the existence of a cytoplasmic dynein 1– dependent multiprotein complex which has dual roles in mitosis and ciliogenesis.

TABLE OF CONTENTS

LIST OF FIGURES

LIST OF TABLES

LIST OF ABBREVIATIONS

AHI1	abelson helper integration site 1
AIPL1	aryl-hydrocarbon receptor interacting protein-like 1
APC	adenomatous polyposis coli
ARL13B	ADP-ribosylation factor-like 13b
ARPKD	autosomal recessive polycystic kidney disease
ARPE	adult retinal pigment epithelial cells
ASPM	abnormal spindle associated microcephaly protein
ATP	adenosine triphosphate
BB	basal bodies
BCA	bicinchoninic acid
BBS	Bardet Biedl Syndrome
BBSIP1	BBSsom interacting protein 1
BMP	bone morphogenetic protein
BSA	bovine serum albumin
CBB	centrioles and basal bodies
CC2D2A	coiled-coil and c2 domains-containing protein 2a
CDK5RAP2	CDK5 regulatory subunit associated protein 2
CELSR	cadherin EGF LAG seven-pass G-type receptor 1a
CEP135	centrosomal protein 135kDa
CEP152	centrosomal protein 152kDa

CEP192	centrosomal protein 192kDa
CEP290	centrosomal protein, 290-kDa
CK	cytokeratin 8
COP-1	coat-protein-I
CPAP	centrosomal P4.1-associated protein
CPK	congenital polycystic kidney
CRB1	crumbs homologue 1
DAPT	gamma secretase inhibitor
DbSNP	database synonymous nucleotide polymorphisms
DHC	dynein heavy chain
DMEM	Dulbecco's modified medium
DNA	deoxyribonucleic acid
DNAH	dynein axonemal heavy chain
DVL	dishevelled
EB	elution buffer
ECL	enhanced chemiluminescence
EDTA	ethylenediamine tetra-acetic acid
ENU	N-ethyl-N-nitrosourea
EZ	exome
FAP58	flagellar associated protein 58
FBS	fetal bovine serum
FGF	fibroblast growth factor

FGFR1	fibroblast growth factor receptor 1
FLH	floating head
FOXJ1	forkhead box J1
FZ	frizzled
GSK3β	glycogen synthase kinase 3β
GTP	guanosine triphosphate
GUCY2D	retinal-specific guanylate cyclase gene
HEK	human embryonic kidney
HGG1	hatching gland 1
IFT	intraflagellar transport
IHC	immunohistochemistry
IMCD3	inner medullary collecting duct cells
IMPDH1	inosine-5-prime-monophosphate dehydrogenase, type 1
INV	inversin
ISH	*in situ* hybridisation
JBTS	Joubert Syndrome
KT	Kinetochore
KV	Kupffer's vesicle
LC8	Light chain 8
LCA	Leber's congenital amaurosis

LEF1	lymphoid enhancer factor-1
LRP	low-density lipoprotein receptor
MAB	maleic acid buffer
MAF	minor allele frequency
MAM	mastermind
MB	megabases
MCC	multiciliated cells
MDCK	Madin Darby canine kidney cells
MGC1203	coiled-coil domain-containing protein 28b
MKS	Meckel Gruber Syndrome
MKKS	McKusick-Kaufman Syndrome
MO	morpholino
mRNA	messenger ribonucleic acid
MT	microtubule
MTOC	microtubule organising centre
MW	molecular weight
MYO	myogenin
NBT/BCIP	nitro-blue tetrazolium chloride 5-bromo-4-chloro-3'-indolyphosphate p-toluidine salt
NCBI	National Centre for Biotechnology Information
NDE1	Nudel
NE	nuclear envelope

NEK2 never in mitosis gene a-related kinase 2

NEK8 never in mitosis gene a-related kinase 8

NICD notch intracellular domain

NIH 3T3 mouse embryonic fibroblast cells

NS non-synonymous

NSC Nimblegen sequence capture

NTDE nucleotide

Ntl no tail

NPHP nephronophthisis

OCD oriented cell division

ORC origin recognition complex

ORPK oak ridge polycystic kidney

PAPC paraxial protocadherin

PBS phosphate buffered saline

PCM pericentriolar matrix

PCTN pericentrin

PCP planar cell polarity signalling

PCR polymerase chain reaction

PFA paraformaldehyde

PKA protein kinase A

PKD polycystic kidney disease

PLK4 polo-like kinase 4

PMSF phenylmethanesulfonyl fluoride

PTCH1 patched 1

PVDF polyvinylidene difluoride

RBP-J recombinant binding protein

RDH12 retinal dehydrogenase 12

RFX regulatory transcription factor X

RIPA radio-immunoprecipitation assay

RPE65 retinal pigment epithelium-specific protein, 65-kd

RPGRIP1 retinitis pigmentosa GTPase regulator -interacting protein

RT reverse transcriptase

SAS6 spindle assembly abnormal protein 6

SDCCAG8 serum-derived colonic cancer antigen 8

SDS sodium dodecyl sulfate

SHH sonic hedgehog

shRNA short-hairpin RNA

SLS Senior Loken Syndrome

SMO smoothened

SNP single nucleotide polymorphisms

SPL splice

SS splice site

STD	standard
STIL	SCL-interrupting locus protein
TAE	Tris base/acetic acid/EDTA
TBE	Tris/borate/EDTA
TCF	T cell-specific transcription factor
TMEM67	transmembrane protein 67
TMEM138	transmembrane protein 138
TMEM216	transmembrane protein 216
TRPV4	transient receptor potential cation channel, subfamily v, member 4
UCSC	University of California, Santa Cruz
WBDD	Winter-Baraitser Dysmorphology Database
WDR	WD-repeat
WNT	wingless
WT-1	Wilm's tumour 1

CHAPTER 1. INTRODUCTION

1.1 OVERVIEW OF CILIA BIOLOGY

1.1.1 The structure of the primary cilium

Projecting from the cell surface, cilia are microtubule based hair-like cytoplasmic extensions with motile and sensory functions, which are critical for developmental and physiological functions (Afzelius, 1976; Barrett, 1947; Nonaka et al., 1998). Expressed on almost all eukaryotic cells, cilia show remarkable conservation from protozoa to humans, whereby as many as 1000 different polypeptides have been identified through combined genomics and proteomics studies, thereby highlighting their structural complexity (Blacque et al., 2004; Gherman et al., 2006). Comprising the microtubular backbone, the ciliary axoneme develops from and is anchored to a specialized centriole called the basal body, which acts as a microtubule organising centre for its ciliary counterpart (Figure 1.1). The ciliary axoneme consists of nine doublet microtubules that originate at the triplet microtubules of the basal body centriole and extend the length of the cilium. The ciliary gate lies proximal to the basal body and is composed of two structurally distinct sub-regions known as the transition fibres and the transition zone (TZ) (Omran et al, 2010).

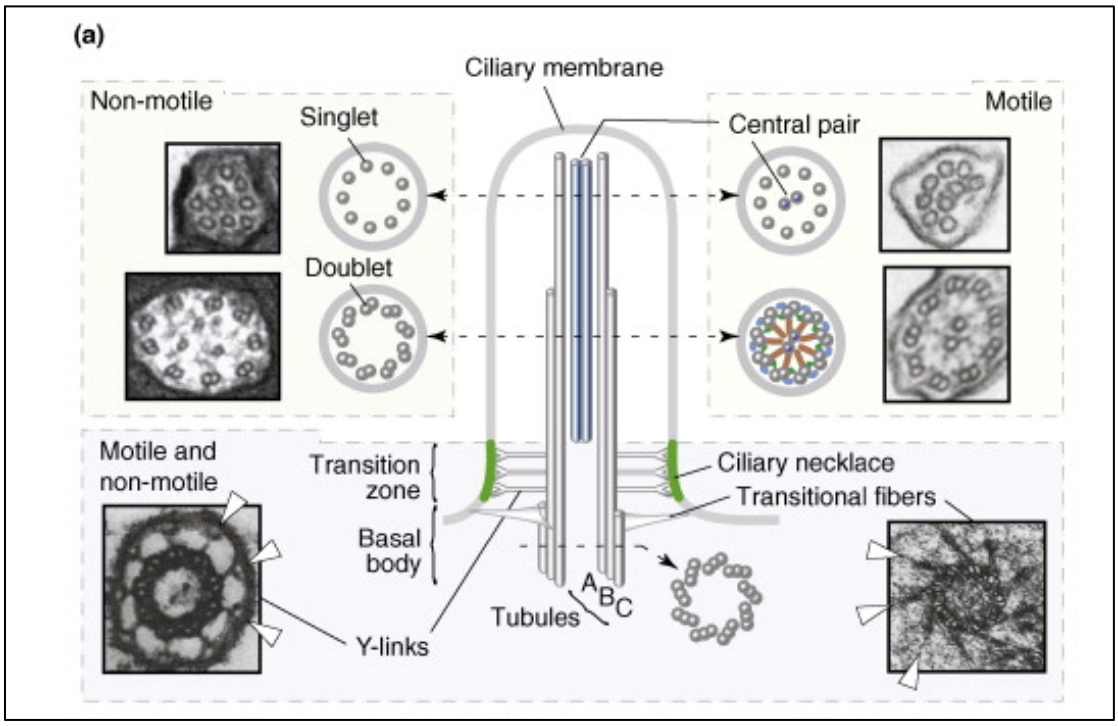

Figure 1.1: Structure of non-motile and motile cilia. Cilia are cytoplasmic extensions projecting from the cell surface and are composed of a microtubular based ciliary axoneme. Representative cross-section transmission electron micrographs (TEM) from non-motile and motile cilia are shown on the left and right respectively. Motile cilia are characterized by the presence of nine peripheral doublet microtubules and a central doublet pair connected to the peripheral microtubule doublets by radial spoke proteins (orange). The outer dynein arms connect the peripheral microtubule doublets to the ciliary membrane (blue) while the inner dynein arms connect the outer doublet microtubules to the radial spoke proteins. Non-motile cilia are characterized by the absence of the central doublet pair. The basal body region is built from triplet microtubules, labelled A, B and C. The transition zone is where the microtubules are reorganized into pairs and anchor the pairs to the membrane. Transitional fibers and Y-links are shown by arrowheads in the TEM micrographs.Transitional fibers, which emanate from the distal end of the basal body and contact the ciliary membrane, are shown schematically and above these are the Y-linkers which link the microtubules to the ciliary membrane necklace. Within this region, these two membrane-contacting structures form a ciliary (flagellar) pore complex that restricts vesicle and perhaps protein entry into the organelle. (Adapted from Silverman et al, 2009).

Ciliary gate formation occurs during early ciliogenesis and precedes intraflagellar transport (IFT). The basal body terminates proximal to to the ciliary gate with the end of the C-tubule and the beginning of the transition fibres. While the basic structural components of the TZ appear to be conserved, the complexity of the TZ varies between species and cell-type (Fisch et al., 2011). The transition fibres arise from the B-tubules of the basal body triplet and form a 'pinwheel-like' structure on TEM cross-sections. The microtubules are anchored to the plasma membrane by the tips of the transition fibres, which are observed on the mature mother centriole. Two proteins which have been implicated in this process include CEP164 and ODF2 (outer dense fibre 2/cenexin) (Graser et al, 2007; Ishikawa et al, 2005). IFT52 has also been observed on transition fibres in Chlamydomonas, suggesting that transition fibres play a role in docking IFT and motor proteins required for ciliogenesis (Deane et al, 2001). While the exact protein composition of the transition fibres is largely unknown, they are thought to form a pore complex similar to the nuclear pore complex and are required for transporting proteins in and out of cilia (Rosenbaum et al, 2002).

Y-shaped linkers constitute another component of the TZ and are located on the distal side of the ciliary gate. They play a role in

connecting the outer doublets of microtubules to the plasma membrane and the ciliary necklace (O'Toole et al, 2007). Encircling the ciliary membrane, the ciliary necklace is formed by strands of fibres which space from the membrane to the basal plate. In photoreceptor cells, CEP290 has been localized to the TZ of the connecting cilia (Craige et al, 2010). Similar to the transition fibres, the TZ has been proposed to regulate intracellular trafficking to and from the cilium.

Depending on the cell type, ciliary morphology can diversify from the characteristic slender rod shape. An example of this diversification is exemplified by the connecting cilium of the rod and cone photoreceptor cells. Vertebrate photoreceptor cells are ciliated sensory cells specialized for single photon detection. The outer segment corresponds to the prototypical cilium. Within this compartment, membranous disks are enveloped by plasma membrane and constitute the highly modified ciliary membrane along which a centrin G-protein coupled receptor transduction pathway regulates the light driven translocation of the visual G-protein transducin through the connecting cilium. This light sensitive outer segment is linked to the inner segment by the connecting cilium which constitutes the TZ of the photoreceptor cell. The function and maintenance of photoreceptor cells is regulated by the import and export

of molecules into and out of the outer segment. Mediating this transport, are proteins implicated in intraflagellar transport as well as multiprotein complexes consisting of retinitis pigmentosa GTPase regulator (RPGR) and nephrocystin proteins. Photoreceptor cell death can occur if any of these proteins are defective as a result of mutations in the encoding genes and give rise to retinal degeneration underlying syndromic and non-syndromic blindness (Roepman et al., 2007).

Cilia fall into two broad functional categories: motile and non-motile cilia. Motile cilia are distinguished from primary cilia by their ability to beat rhythmically, an activity which is powered by adenosine triphosphate (ATP), hydrolysed by dynein proteins which are anchored to the inner and outer aspects of peripheral doublet microtubules (Woolley, 2000). Motile cilia are utilised in both unicellular and multicellular organisms for locomotion. In addition, beating cilia are located on the surfaces of cells of many tissues where they are utilised for creating localised fluid flow. For example, multiple motile cilia extending from cells lining the respiratory tract produce a continuous flow of mucus that is essential for pulmonary clearance (Stannard and O'Callaghan, 2006). Typically, motile cilia consist of a set of nine doublet microtubules, which surround a central pair of singlet microtubules ("9+2"

arrangement) to which they are connected by the radial spoke proteins (Figure 1.1). Non-motile cilia are characterised by the absence of the central pair of singlet microtubules ("9+0" arrangement) (Figure 1.1) (Satir et al., 2007).

In motile cilia, the radial spoke complex consists of 23 proteins (RSPs) that work as a mechanochemical transducer between the central pair apparatus and the peripheral microtubule doublets (Pigino et al, 2012). Characterised by a T-shaped structure, a radial spoke is composed of an elongated stalk that is anchored on the A-microtubule of the peripheral microtubule doublet while the orthogonal head has transient contacts with the inner sheath and central pair. Radial spokes mediate signal transduction between the central pair and the dynein motors (Smith et al., 2004). Sequences found within RSPs 2 and 23 suggest a role for signal transduction via cyclic nucleotides due to the presence of a cyclic GMP-binding domain, an adenylyl cyclase domain and a nucleotide diphosphate kinase domain. Phosphorylation is thought to play an essential role in RSP function whereby the sliding velocity of axonemes has been shown to be dependent on the activity of phosphate kinases such as protein kinase A (PKA) and casein kinase 1 (CK1) (Howard et al., 1994; Yang et al., 2000).

During early embryogenesis, nodal cilia generate a leftward flow of fluid that is critical in initiating asymmetric cues during organogenesis (Nonaka et al., 1998). In addition to locomotion, sensory perception is another key process mediated by cilia (Ginger et al., 2008). For example, immotile cholangiocyte cilia express TRPV4, a calcium channel that is regulated by tonicity of the biliary duct (Gradilone et al., 2007).

1.1.2 Intraflagellar Transport

Cilia are assembled and maintained by a process called intraflagellar transport (IFT) which utilises microtubule-associated motor proteins called kinesins to mobilise ciliary cargo such as structural axonemal components and membrane receptors in an anterograde fashion along the ciliary axoneme (Kozminski et al., 1995; Pazour et al., 1999; Qin et al., 2004). Studies from Chlamydomonas and Caenorhabditis elegans show that two dynein subunit motors transport and recycle proteins in a retrograde direction down along the axoneme toward the basal body (Kozminski et al., 1993; Pazour et al., 1999; Pedersen and Rosenbaum, 2008; Porter et al., 1999; Signor et al., 1999) (Figure 1.2). One encodes LC8, which is a light chain of several dynein isoforms (King et al., 1996) (Pazour et al., 1998) while the other encodes DHC1b, which is a cytoplasmic dynein heavy chain (DHC) isoform (Mikami et

al., 2002; Pazour et al., 1999; Porter et al., 1999; Signor et al., 1999). The mammalian orthologue, DHC2, is associated with mammalian cilia (Mikami et al., 2002) and was also reported to play a role in the organisation and/or function of the Golgi apparatus (Vaisberg et al., 1996). IFT particles contain 16 different polypetides with masses ranging from 20kDa to 172kDa, which are organised into two complexes, A and B (Cole, 2003; Cole et al., 1998; Vaisberg et al., 1996). Disruption of either of the IFT motors or the basal body proteins essential for their function leads to impaired cilia assembly (Brazelton et al., 2001; Pazour et al., 2000).

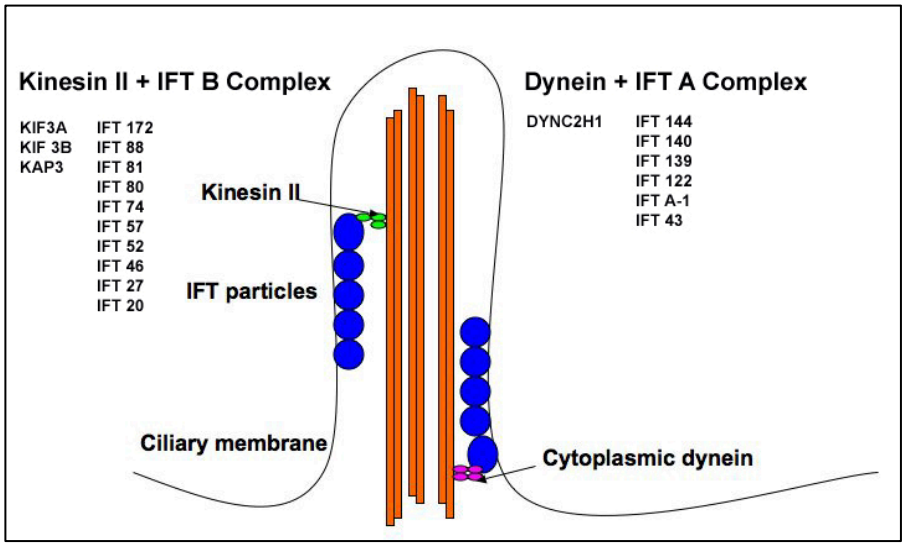

Figure 1.2: Intraflagellar transport. Elongation of the axoneme at the distal tip relies on intraflagellar transport (IFT). Anterograde IFT is mediated by kinesin-II motors along with axonemal precursors while retrograde IFT is mediated by a dynein motor. IFT Type A complexes are linked to retrograde transport and IFT type B complexes are linked to anterograde transport.

Microtubule organisation and polarised membrane trafficking regulates early ciliary assembly and several lines of evidence support a role for vesicular transport. During ciliogenesis, the Golgi apparatus lies in close proximity to the basal body and formation of the new ciliary sheath is associated with flattening of a vesicular sheath near the distal end of the centriole destined to become the new basal body as revealed by sequential electron micrographs (Sorokin, 1968). Vesicle tethering to the plasma membrane is mediated by the exocyst, an octameric protein complex, composed of Sec3, Sec5, Sec6, Sec8, Sec10, Sec15, Exo70 and Exo84 (Amlan et al., 2011). Extracytoplasmic extension of the plasma membrane and intracellular vesicular trafficking is modulated by proteins, which are members of the Arf and Rab family (Nachury et al., 2007). The Rab family of small GTPases are master regulators in exocytosis. In their GTP-bound form, Rab proteins interact with downstream effectors, thereby controlling various steps of exocytosis. Components of the exocyst are localized at the base of the cilia (Park et al, 2008). Disruption of Rabin8, a GTP nucleotide exchange factor specific for Rab8, leads to loss of BBS4 from centriolar satellites and impaired cilia formation. Furthermore, Rabin8 interacts with BBS1, a component of the BBSome, a multi-protein complex (consisting of BBS

1, 2, 4, 5, 7, 8 and 9), involved in cargo transport to primary cilia (Figure 1.3) (Nachury et al., 2007). Rabin8 is a direct downstream effector of Rab11 (Knödler A et al., 2010), which mediates vesicle transport from the trans-Golgi network (TGN) and recycling endosomes (Ullrich et al., 1996) to vesicle docking and fusion at the plasma membrane.

Other players in the exocytic pathway include Arf4, Rab11, FIP3, and the Arf GTPase-activating protein ASAP1 which have been shown to be important for the transport of rhodopsins to the retina outer segments (Mazelova et al.,2009). The Arf4-based protein complex has been postulated to be involved in the selection and packaging of specific cargos, including GPCRs, for their delivery to the cilia. Once incorporated into the plasma membrane, ciliary cargos are collected by the BBSome, which acts as a planar coat that transports proteins to the cilia. How vesicle fusion is connected to subsequent cargo entry to cilia requires further investigation as does the underlying molecular mechanisms governing how the BBSome is coupled to IFT proteins (IFTs) for cargo movement within the cilia. IFT proteins share sequence homology to coat-protein-I (COP-1) and clarithrin-coated vesicle components, thereby suggesting a role for IFT proteins in vesicle transport (Jekely and Arendt, 2006).

1.1.3 Centriole and basal body biogenesis

Centrioles and basal bodies (CBB) are assembled in a variety of cellular contexts that are cell cycle dependent and include cell division, cell motility, cell adhesion and cell polarity (Beisson and Wright, 2003) (Bettencourt-Dias and Glover, 2007; Delattre and Gonczy, 2004).

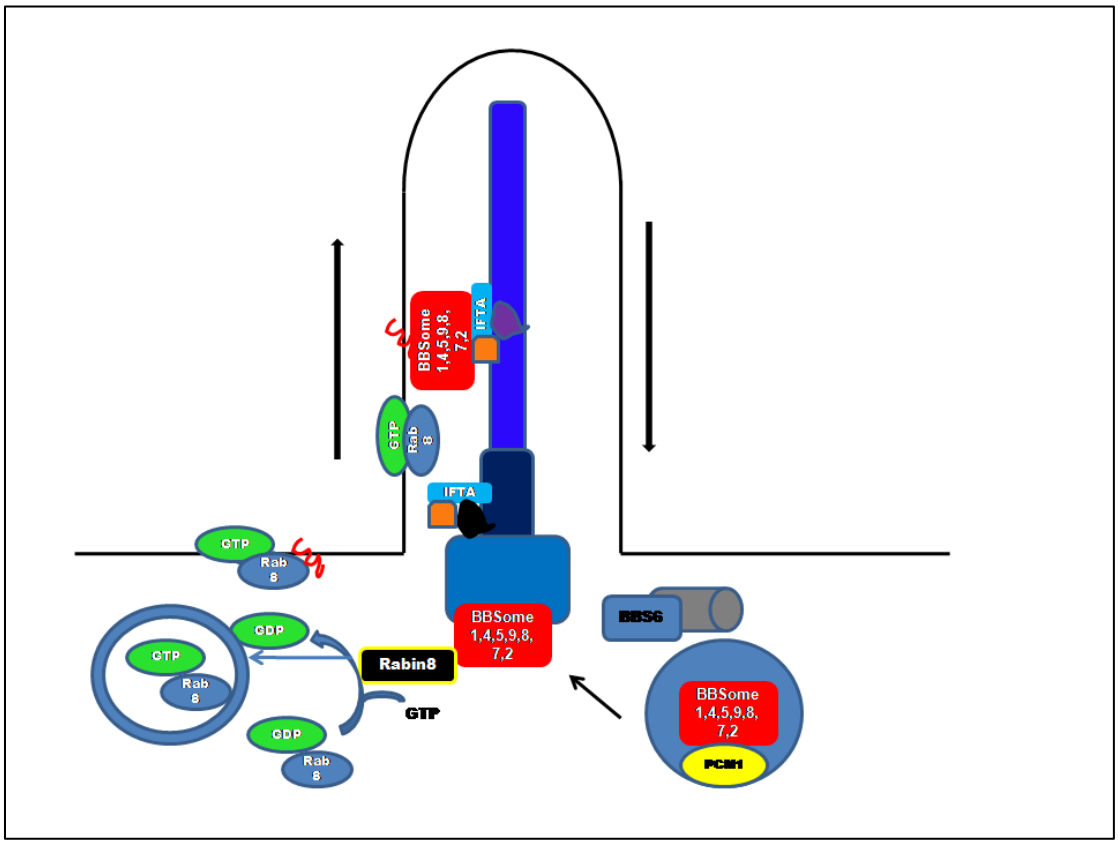

Figure 1.3: The BBSome and vesicular trafficking to the primary cilium. The BBSome is a stable protein complex that functions in primary ciliogenesis. It is composed of seven highly conserved BBS proteins (BBS1, BBS2, BBS4, BBS5, BBS7, BBS8 and BBS9) and BBIP10. The BBSome binds to Rabin8, the GTP/GDP exchange factor for the small GTPase Rab8, which localises to the primary cilium. In the connecting cilium of photoreceptors, Rab8 is required for ciliogenesis and mediates the docking and fusion of rhodopsin carrier vesicles.

Centrosomes also act as signalling platforms in cell cycle transitions and checkpoints (Doxsey et al., 2005; Sluder, 2005). Furthermore, during mitosis, organisation of the spindle poles is a key process regulated by the centrosome. The centrosome is the major microtubule (MT) organising centre (MTOC) of mammalian cells and plays a crucial role in the formation of the mitotic spindle and thereby ensures correct chromosome segregation. Centrosome structure is dynamically regulated throughout the cell cycle and in G1, is characterised by the presence of two MT-based structures called centrioles surrounded by an electron dense pericentriolar matrix (PCM) (Figure 1.4). Centrioles consist of nine MT triplets and measure 0.5μm long and 0.2μm in diameter. The mother centriole has subdistal and distal appendages, which dock the cytoplasmic MTs and nucleate cilia and flagella by tethering the MTs to the cell membrane as basal bodies (BB) which provide the template of the ciliary axoneme which consists of nine MT doublets (Figure 1.4). Centrioles and basal bodies (CBB) have been found in all eukaryotic groups which suggests that there is a highly conserved common molecular assembly pathway (Carvalho-Santos et al., 2010). Through electron micrographic studies, four stages of centriole

biogenesis have been identified: (1) centriole disengagement, (2) nucleation of daughter centrioles, (3) elongation of daughter centrioles and (4) chromosome separation (Bettencourt-Dias and Glover, 2007; Nigg, 2007) (Figure 1.5).

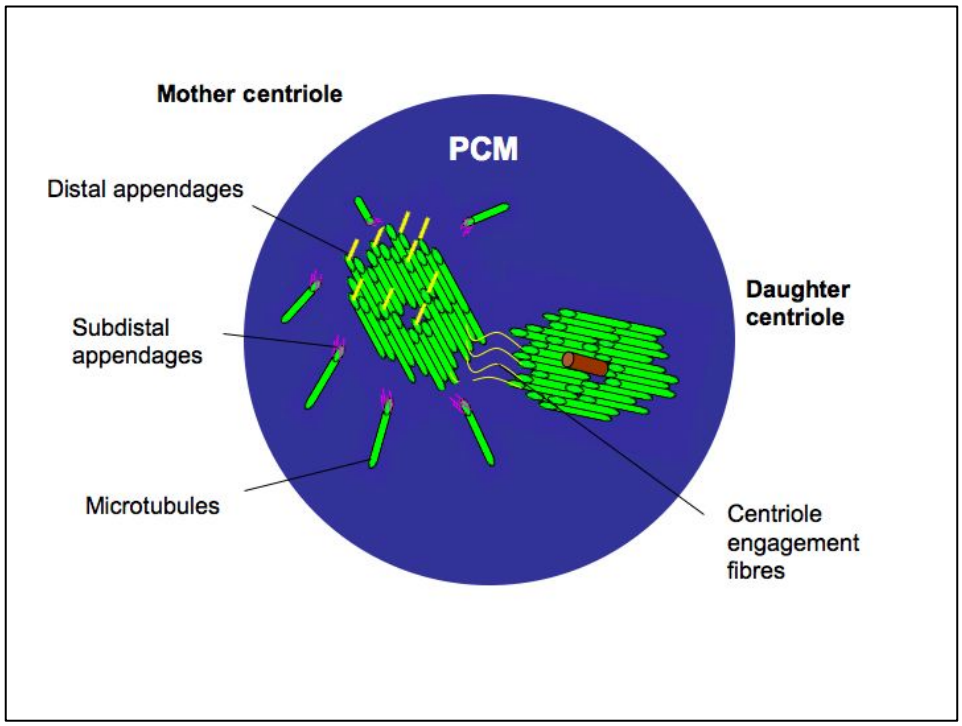

Figure 1.4: The centrosome. The centrosome consists of two microtubule-based structures, the mother and daughter centrioles, arranged in nine microtubule triplets. The mother centriole has distal and subdistal appendages, which dock cytoplasmic microtubules and anchor centrioles to the cell membrane to serve as basal bodies.

During mitotic exit, centriole disengagement is coordinated with chromatid segregation and is required for duplication in the next cell

cycle. In G1, the centrioles are disengaged from one another. As the cells enter S-phase, new centrioles (daughter centrioles) are built orthogonally to existing centrioles (mother centrioles) in a process called procentriole formation, which occurs once per cell cycle and is coordinated with DNA synthesis. In most organisms, procentrioles consist of short MT triplets and a structure called the cartwheel, which is made up of a central cylinder with a core and nine spokes radiating from the hub to the MT triplets (Bettencourt-Dias and Glover, 2007) (Figure 1.6). Cartwheel formation occurs at a very early stage of centriole assembly, followed by formation of the peripheral MTs (Anderson et al., 1971). Thus, the cartwheel might serve as a scaffold that determines centriole diameter and symmetry through the radial arrangement of its nine spokes. Recent work has highlighted a crucial role for SAS-6 in the synthesis of cartwheel hubs and assembly (van Bruegel et al., 2011).

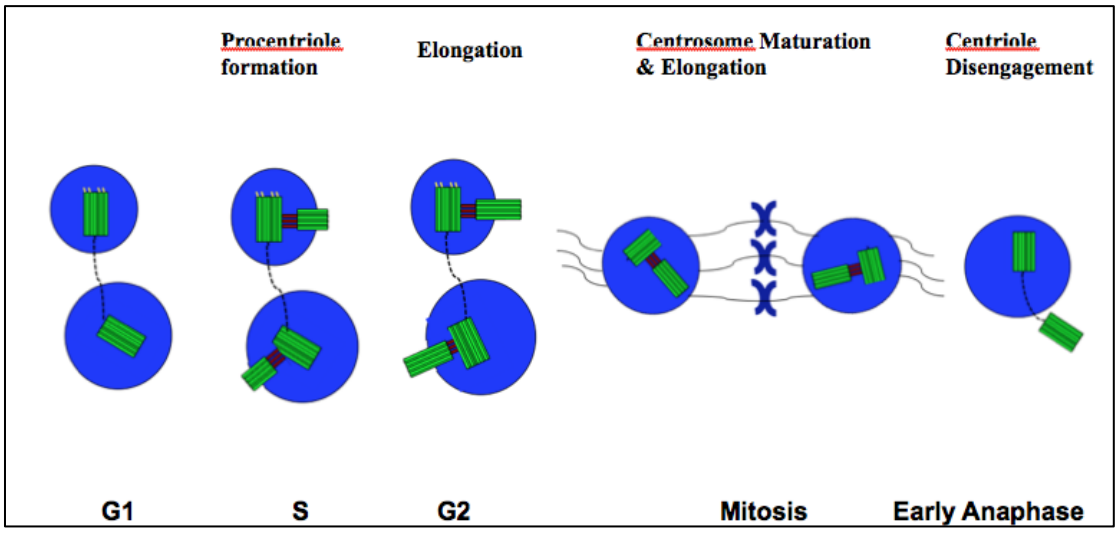

Figure 1.5: Stages of centriole biogenesis. Centrioles are disengaged from each other in G1. On entry into S-phase, new centrioles arise orthogonally from the mother centriole. In G2, daughter centrioles elongate and on entry into mitosis, separation of duplicated centrosomes occurs. Centrosomes are held together by a proteinaceous linker that connects the proximal ends on the two older centrioles during interphase.

Loss of known cartwheel component, CEP135, results in aberrant centrioles with nine shortened cartwheel spokes and a decreased diameter that can accommodate only eight triplet MTs (Hiraki et al, 2007).

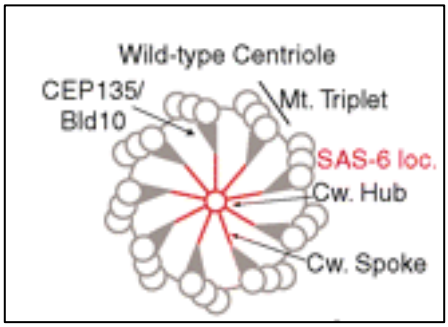

Figure 1.6: Cartwheel structure. Wild-type centriole scheme with peripheral MT triplets and central cartwheel structure (Cw.) with hub and spokes.

Aberrant number of triplet MTs occurs in SAS-6 deficient *Chlamydomonas, Drosophila* and *Paramecium* suggesting that self-assembly of SAS-6 might lead to the formation of the cartwheel hub and thereby dictate centriole symmetry (Strnad et al., 2008). Tubule formation consists of an initiation and a growth phase. Initiation begins with the formation of the A tubule as it lies juxtaposed to a cartwheel spoke within the wall material of the annulus. Following initiation of all nine A tubules, formation of B and C tubules then occurs. Sequential initiation of

all three tubules occurs around the procentriole. Simultaneous with tubule initiation is a nonsequential growth of each tubule. The tubules lengthen and the procentriole is complete when it is about 200μm long. The procentriole increases in length and diameter during its maturation into a basal body. The addition of a basal foot, nine alar sheets, and a rootlet completes the maturation process.

During interphase, the centrosomes are held together by a proteinaceous linker that extends between the proximal ends of the two older centrioles (Fry et al., 1998; Yang et al., 2006). Centriole elongation occurs in G2 phase of the cell cycle and on mitotic entry, the duplicated centrosomes separate and nucleate the microtubules of the mitotic spindle. This process is called centrosome dysjunction whereby dissembly of the proteinaceous linker occurs (Faragher and Fry, 2003).

Molecular components of the centriole assembly pathway

Polo-like kinase 4 (PLK4/SAK) is critical for centriole biogenesis in human cells and Drosophila melanogaster (Bettencourt-Dias et al., 2005), (Habedanck et al., 2005), (Kleylein-Sohn et al., 2007), (Rodrigues-Martins et al., 2007). PLK4 is recruited to the centrosome by centrosomal protein 152kDa (CEP152), which also binds centrosomal P4.1-associated protein (CPAP, also called SAS4 in Caenorhabditis elegans) (Figure 1.7)

(Dzhindzhev et al., 2010). CEP152 acts as a scaffold protein to recruit PLK4, a trigger of centriole biogenesis and CPAP, a regulator of centriole-microtubule recruitment and elongation. Procentriole formation begins in S-phase with recruitment of spindle assembly abnormal protein 6 (SAS6), CEP135 and SCL-interrupting locus protein (STIL also known as SAS5) which are required for the cartwheel structure that defines the ninefold symmetry of the centriole.

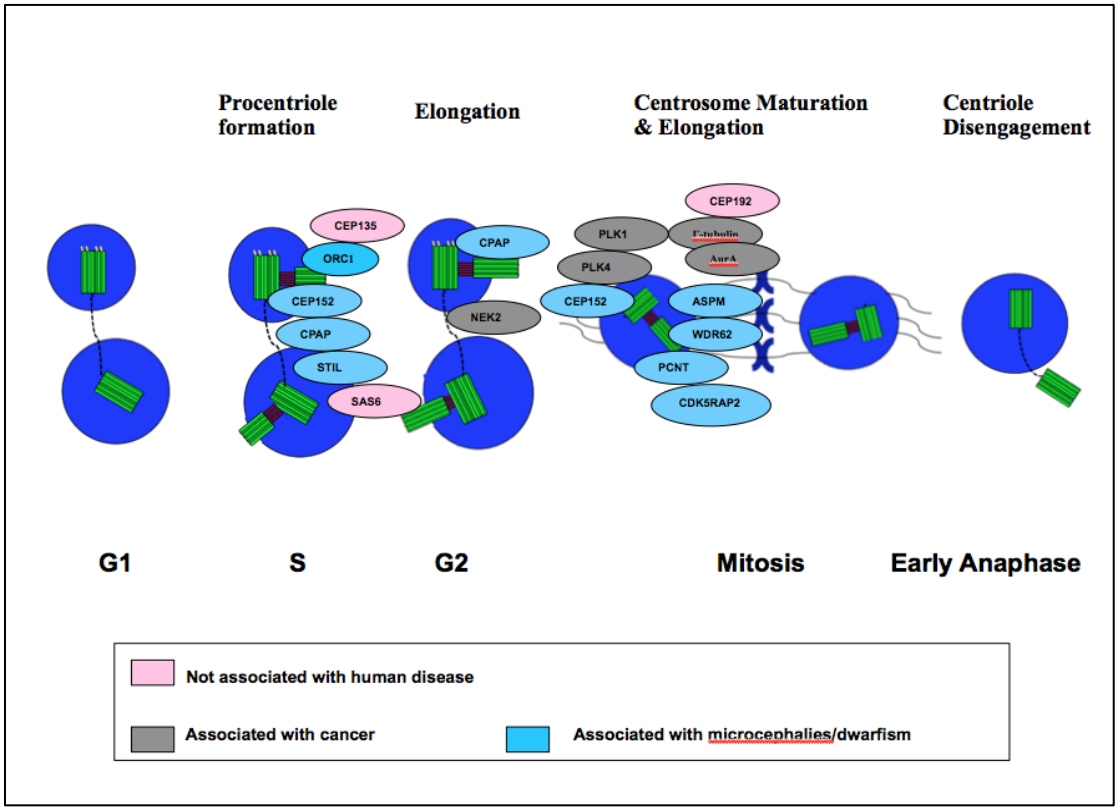

Figure 1.7: Molecular regulation of centriolar biogenesis. Centriolar biogenesis is triggered by polo-like kinase-4 (PLK-4) and is recruited to the centrosome by CEP152 which also binds CPAP. Other proteins implicated in procentriole formation include SAS6, CEP135 and STIL which form the cartwheel and confer the centriole ninefold symmetry. CPAP also plays a role in centriole elongation. In G2, several molecules are needed for entry into microtubule (MT) nucleation, stability and

focusing the pericentriolar material (PCM), including pericentrin (PCTN), CEP192, CDK5RAP2 and ASPM. NEK2 regulates separation of the two centrosomes and on mitotic exit, the centrioles disengage, a process regulated by PLK1 and separase. Adapted from (Bettencourt-Dias et al., 2011).

CPAP and CEP152 also have a role in centrosome maturation where CPAP plays a role in centriole elongation (Bettencourt-Dias and Glover, 2007; Nigg and Raff, 2009). CDK2 accelerates procentriole formation and elongation and is coordinated with DNA replication. In G2, the daughter centriole reaches full elongation and maturation with the recruitment of several molecules that are needed for MT nucleation, stability and focusing of the PCM, which include pericentrin (PCTN), CEP192 (also called SPD2 in C elegans), CDK5 regulatory subunit associated protein 2 (CDK5RAP2, also called CNN in Drosophila) and abnormal spindle associated microcephaly protein (ASPM). CDK5RAP2 plays an important role in tethering the centrosome and spindle pole during mitosis (Barrera et al., 2010) (Barr et al., 2010), (Lee, 2010). Without CDK5RAP2, centrioles detach from the PCM and form the mitotic spindle (Gonzalez et al., 1990). Centrosome separation is mediated by the kinase, never in mitosis gene a-related kinase 2, (Nek2). On mitotic exit, the centrioles within the centrosomes disengage through the action of PLK4 and separase. Centriole reduplication is prevented by

molecules that prevent DNA re-replication such as Origin recognition complex (ORC) 1.

1.1.4 Transcriptional regulation of ciliogenesis

1.1.4.1 RFX and FOXJ-1 transcription factors

Over 1000 proteins have been identified within the ciliary proteome and as a result of the complexity of ciliary biogenesis, coordinated control of a great number of proteins is required (Thomas et al., 2010). A highly conserved role for both the forkhead box J1 (FOXJ1) and the regulatory transcription factor X (RFX) family of transcription factors has been shown in both vertebrates and invertebrates (Dubruille et al., 2002; Liu et al., 2007; Swoboda et al., 2000), (Bonnafe et al., 2004; Brody et al., 2000; Chen et al., 1998), (Chung et al., 2012; Ma and Jiang, 2007), (Bisgrove et al., 2012). Characterised by a winged-type DNA binding domain, RFX proteins are comprised of seven mammalian members (RFX1-7) which have been shown to regulate target gene expression by binding to a cis-acting transcriptional regulatory element called an X-box within the promoter of target genes (Emery et al., 1996). In *Drosophila* and *C elegans*, a single X-box transcription factor (dRFX and daf-19, respectively) regulates ciliogenesis in sensory neurons via transcriptional regulation of intraflagellar transport (IFT) proteins (Blacque et al., 2005;

Dubruille et al., 2002; Efimenko et al., 2005; Swoboda et al., 2000). *Rfx3*$^{-/-}$ mutant mice display left-right asymmetry and stunted nodal cilia (Bonnafe et al., 2004; Brody et al., 2000; Chen et al., 1998). Additional features include hydrocephalus resulting from ciliary defects on the specialised ependymal cells in addition to diabetes from abnormal differentiation of the pancreatic β cells (Ait-Lounis et al., 2007; Ait-Lounis et al.; Baas et al., 2006). Ependymal cells are multiciliated epithelial cells that line the cerebrospinal fluid-filled ventricles in the brain and the central canal of the spinal cord. Ependymal cell cilia have a 9+2 structure and project from the cell's apical surface into the ventricle. Planar-polarised ciliary beating generates directional fluid flow (Tissir et al., 2010) and is believed to be involved in the circulation of CSF from the choroid plexuses, where it is produced, to the subarachnoid spaces, where it is absorbed. Hydrocephalus has been reported in animal models of ependymal ciliary dysfunction as well as human syndromes associated with defective ciliary gene function (Olbrich et al., 2012). Therefore, the directional beating of planar-polarised ependymal cilia is important for maintaining proper brain function.

Regarding other RFX genes, an N-ethyl-N-nitrosourea, (ENU) screen identified a *Rfx4* (L298P) mouse mutant which displayed defects

in cilia formation with distinct dorsoventral patterning defects in the ventral spinal cord and telencephalon due to aberrant Sonic hedgehog (Shh) signaling and Gli3 activity (Ashique et al., 2009). More recently, RFX4 has been shown to mediate the coordinated expressions of *TMEM138* and *TMEM216*, transmembrane proteins that regulate ciliogenesis (Lee et al., 2012). A hierarchial transcriptional network in motile ciliogenesis programmes has recently been highlighted whereby *rfx2* expression in ciliated tissues is regulated by *foxj1* transcription factors (Yu et al., 2008). Mice deficient for *Foxj1*, develop hydrocephalus and heterotaxia and their respiratory epithelia are devoid of cilia (Brody et al., 2000; Chen et al., 1998). As *Foxj1*$^{-/-}$ deficient mice lack motile cilia only, it has been suggested that *Foxj1* specifically regulates motile ciliogenesis. Studies in *Xenopus* and *Danio rerio* have confirmed that *foxj1* morphant embryos fail to form cilia in the zebrafish embryonic node known as Kupffer's vesicle (KV), in addition to cilia of the floor plate and pronephric duct (Yu et al., 2008).

Table 1.1: Molecular components of the centriole-assembly pathway (Bettencourt-Dias and Glover, 2009)

PCM Recruitment and Duplication	Protein	Resultant Phenotype
	SPD2 (Ce, Dm)	No centriole duplication (Ce)
	CEP192 (Hs)	<PCM recruited (Ce, Dm and Hs); no basal body duplication (Dm)
	Asterless (Dm)/ CEP152 (Hs)	Aberrant PCM recruitment (Dm) and centriole elongation
	γ-tubulin (Dm, Hs, Tt, Pt)/TBG (Ce)	Aberrant centriole duplication (Ce, Hs, Tt) centriole structure & separation (Pt, Dm) Overexpression: de novo formation; amplification of basal bodies
Triggers of Biogenesis	SAK/PLK4 (Dm, Hs)	No duplication (Dm, Hs); no reduplication (Hs); no formation of basal bodies (Dm) Overexpression: amplification (Dm; Hs); de novo formation (Dm)
	ZYG1 (Ce)	No duplication
Essential Molecules for Centriole Biogenesis	SAS6 (Ce, Hs)/DSAS6 (Dm)/Bld12 (Cr)	No duplication (Hs, Dm, Ce); no reduplication (Hs) Overexpression: amplification (Dm, Hs)
	SAS4 (Ce/DSAS4 (Dm/CPAP (Hs)	No duplication (Hs, Ce, Dm, Cr); No reduplication (Hs)
	SAS5 (Ce)	No duplication
	CP110 (Hs)/DCP110 (Dm)	No reduplication or amplification (Hs)
	Centrin (Hs)/Cdc31 (Sc, Sp)/VLF2 (Cr)/CEN2/3 (Pt)/CEN1 (Tt)	No duplication (Sp, Sc, Tt); differing duplication results (Hs); aberrant centriole segregation (Cr), aberrant duplication geometry (Pt)
	SFL1 (Sc)	No SPB duplication
	δ-tubulin (Hs); δ-PT1 (Pt); UNI3 (Cr)	Centrioles with fewer tubules (Cr, Pt)
	ε-tubulin (XI, Hs, Pt); Bld2 (Cr)	Centriole stability disrupted, singlets (Cr); no duplication (XI, Pt); aberrant PCM organization (XI)
	Ana1, Ana 2, Ana 3 (Dm)	No duplication
	Centrobin (Hs)	No duplication
	Cep135 (Hs)/BLD10 (Cr)/DBld10 (Dm)	No amplification upon SAK/PLK4 overexpression (Hs); no duplication (Dm); disorganized microtubules (Hs); no basal body duplication (Cr) Overexpression: accumulation of particles (Hs)
Cell Cycle Regulators	CDK2 (Hs, XI, Gg)	No reduplication, normal duplication, needed for duplication in absence of CDK1
	Separase (XI)	No centriole disengagement, impaired duplication
	Spliced Sgo 1 (Mm)	Precocious centriole disengagement
	p53 (Mm, Hs)	Amplification
	CHK1 (Gg, Hs)	No centrosome amplification upon DNA damage
	PLK1, PLK2 (Hs)	No reduplication in S phase-arrested cells
	MPS1 (Hs, Mm, Sc)	No reduplication (Hs, Mm); normal duplication (Dm); no spindle pole body duplication
	BRCA1 (Hs, Mm)	Premature centriole separation and reduplication in S-G2 boundary 9Hs); amplification (Mm)
	Cdc14B (Hs)	Amplification
	PP2 (Dm)	Centrosome amplification Overexpression: prevents reduplication
	Nucleophosmin/B23 (Mm, Hs)	Amplification
	CAMKII (XI)	Blocks early steps in duplication
	CDK1 (Dm, Sc)	Amplification
	Skp1, Skp2, Cul1, Slimb (SCF complex) (Dm, Hs, Mm, XI)	Blocks separation of M-D pairs and reduplication (XI); increased centrosome number (Dm, Mm)

Loss of expression of the ciliary genes, *dnah9* (dynein axonemal heavy chain, 9) and *centrin 2* was noted in *foxj1* morphant fish while ectopic expression of *foxj1* led to ectopic expression of *dnah9* and *centrin 2* thereby further suggesting a hierarchial regulatory role for *foxj1* in ciliogenesis. Furthermore, supernumerary long motile cilia were observed throughout the dorsoventral extent of the neural tube of zebrafish when *foxj1* was misexpressed by hyperactivating the Hh pathway using dominant negative protein kinase A (Yu et al, 2008). Chromatin immunoprecipitation assays (ChIP) confirmed that *foxj1* directly binds to the promoters of the ciliary genes, *dynein* and *wdr78* (Yu et al., 2008). ChIP assays are a type of immunoprecipitation experimental technique used to investigate the interaction between proteins and DNA in the cell. The objective is to determine whether specific proteins are associated with specific genomic regions, such as transcription factors on promoters or other DNA binding sites. When undertaking a ChIP assay, protein and associated chromatin in a cell lysate are temporarily bonded, the DNA-protein complexes (chromatin-protein) are then sheared and DNA fragments associated with the protein(s) of interest are selectively immunoprecipitated, and the associated DNA fragments are purified and their sequence is determined. These DNA sequences are supposed to be associated with the protein of interest *in vivo*.

During early embryogenesis, the homeodomain transcription factor, *Noto* has been shown to be important for nodal ciliogenesis and therefore establishment of left-right asymmetry in the developing embryo (Beckers et al., 2007). Nodal cilia in *Noto*$^{-/-}$ deficient mice are present but in less numbers and are stunted with incomplete microtubular structures evident on electron microscopy (Beckers et al., 2007). *In situ* hybridisation analysis for the transcription factors, *Foxj1* and *Rfx3* revealed reduced expression in the embryonic node in *Noto*$^{-/-}$ mice (Beckers et al., 2007), suggesting that both *Foxj1* and *Rfx3* gene expression are regulated by *Noto*.

1.1.4.2. FGF signalling and ciliogenesis

Very little is known about the signalling pathways which regulate the activation of ciliogenic programmes. Fibroblast growth factor signalling through fibroblast growth factor receptor 1, FGFR1, has recently been shown to regulate ciliogenesis in the zebrafish KV (Neugebauer et al., 2009). Both *fgfr1* morphant fish and embryos treated with a pharmacological inhibitor of FGF, display abnormal ciliogenesis in the pronephric ducts and otic vesicle. Expression of both *rfx2* and *foxj1* were downregulated in *fgfr1* morphant fish as was their ciliary target

gene, polaris (Neugebauer et al., 2009), thereby supporting a role for FGF signalling in the regulation of ciliogenesis.

1.1.4.3 Notch signalling and ciliogenesis

Genetic and pharmacological studies in zebrafish and *Xenopus* have implicated Notch signalling in the specification of multiciliated cell (MCC) fate in the zebrafish pronephros, *Xenopus* epidermis and in murine respiratory epithelia (Deblandre et al., 1999; Liu et al., 2007) (Ma and Jiang, 2007), (Morimoto et al., 2010). Binding of the Notch ligand (*jagged 2a*) on prospective MCCs to its receptor (*notch3*) on adjacent cells results in cell autonomous repression of *rfx2* following nuclear translocation of the cleaved intracellular domain of *notch3* (NICD) (Figure 1.8). Zebrafish mutant for *jagged 2a*, *notch3*, *mindbomb* (required for Notch ligand signalling) and *her9*, results in MCC hyperplasia with expansion of *rfx2* expression. *Jagged2a* knockdown and pharmacological inhibition of Notch is sufficient to rescue the pronephric cystic phenotype of the ciliopathy mutant, double bubble (Liu et al., 2007). Recent mammalian studies have shown that an expansion of ciliated respiratory epithelial cells occurs at the expense of Clara cell fate in murine embryos deficient for the canonical Notch effector, RBP-J kappa (Morimoto et al.;

Tsao et al., 2009). The downstream targets of RBP-J kappa in the inhibition of ciliogenic programmes requires further investigation.

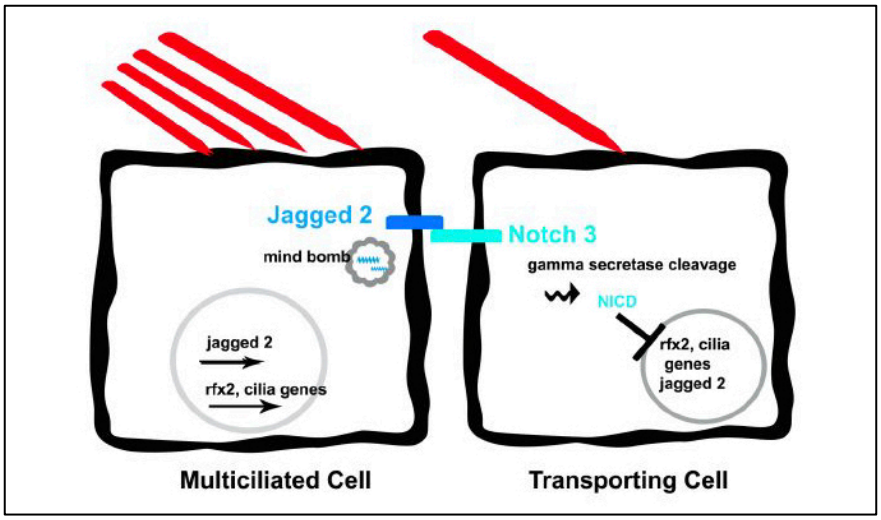

Figure 1.8: A model of Notch regulation of multiciliated cell fate versus monociliated cell fate in the developing zebrafish pronephros. Activation of notch 3 on ligand binding by jagged 2 represses ciliation programmes in the transporting cell (Adapted from Liu et al, 2007).

1.1.4.4 PCP signalling and ciliogenesis

Cells orient themselves relative to an axis along the plane of a tissue in a process called planar cell polarity (PCP) and is mediated by noncanonical Wnt signalling (Wallingford and Mitchell, 2011). Planar polarity is determined by the accumulation of core PCP components to distinct regions of the cell. Core PCP components include the transmembrane proteins, Frizzled, Vangl and Celsr, respectively in addition to the

cytoplasmic proteins, Prickle and Dishevelled (McNeill, 2010). A highly conserved role for the core PCP effector proteins, *Inturned* and *Fuzzy* in cilia assembly has been suggested by studies in Xenopus and mice (Dai et al., 2011; Gray et al., 2009; Heydeck et al., 2009; Park et al., 2006; Zeng et al., 2010). Mice mutant for core PCP effectors, *Fuzzy* and *Inturned* have neural tube defects, skeletal dysmorphologies and Hedgehog signalling defects stemming from disrupted ciliogenesis (Gray et al., 2009). Knockdown of *Inturned* in *Xenopus* revealed a role for *Inturned* in actin assembly, Rho localisation and docking of basal bodies at the apical surface in multiciliated cells (Park et al., 2008). *Fuzzy* appears to be important for axoneme elongation whereby it acts together with a Rab-similar GTPase to regulate from the cytoplasm to the basal bodies and from the basal bodies to the tips of cilia (Gray et al., 2009). In addition to a role for core PCP 'effector' proteins in ciliogenesis, a role for core PCP components in cilia formation has also been suggested. As for Inturned, Dvl was also shown to mediate apical actin assembly, Rho activity and basal body docking (Park et al., 2008). Basal body docking requires the association of membrane-bound vesicles and the vesicle tethering exocyst complex (Sorokin, 1968; Zuo et al., 2009). In Dvl morphants, basal bodies failed to associate with either vesicles or the exocyst (Park et al., 2008). Defective ciliogenesis has also been described in Celsr mutant

mice whereby a failure of basal body docking at the apical membrane of ependymal cells has been described (Tissir and Goffinet, 2010). Therefore, both core PCP effector proteins in addition to core components of PCP play a role in ciliogenesis.

1. 2. THE PRIMARY CILIUM IN SIGNAL TRANSDUCTION

1.2.1 Regulation of Hedgehog signalling

Previous studies have implicated IFT machinery in vertebrate-specific Hedgehog signal transduction (Huangfu et al., 2003) (Figure 1.9). Mutations in genes encoding *Ift172* and *Ift88* were identified in two mouse mutants which showed characteristic defects in Sonic hedgehog signalling (Shh) following an ENU mutagenesis screen undertaken for embryonic patterning mutations. Genetic studies showed that IFT proteins act at the heart of the Shh pathway, downstream of the transmembrane *Shh receptor*, *Patched 1* (*Ptch1*) and its downstream effector, *Smoothened* (*Smo*) and upstream of the *Gli* transcription factors that implement the pathway (Huangfu and Anderson, 2005; Huangfu et al., 2003). Furthermore, *Ptch1* and *Smo* are dynamically expressed in cilia during *Shh* signalling (Corbit et al., 2005; Rohatgi et al., 2007) and activated *Smo* increases the accumulation of *Gli2*, the major transcriptional activator of Hedgehog signalling, at the ciliary tip. In the

absence of ligand, *Patched 1* (*Ptch1*) localizes to cilia and prevents translocation of *Smoothened* (*Smo*) into cilia (Rohatgi et al., 2007). *Kif7* localizes to the ciliary base, where it forms a complex with *Gli* proteins, the serine-threonine kinase, *Fused (FU), Suppressor of Fused (SU(FU))* and in other kinases including *Protein kinase A (PKA), Casein kinase I (CKI)* and *Glycogen synthase kinase 3β (GSK3β)*, that promote the processing of *Gli* protein into its repressor form (*GliR*) which repress Hh target genes in the absence of *Shh*. (Lefers et al., 2001). After activation of the pathway, *Smo* moves to the ciliary membrane and *Kif7* translocates into the cilium, thereby promoting *Gli2* accumulation at the cilium tip. The regulatory subunits of vertebrate PKA have recently been localized to the ciliary base proximal to the basal body. *Gli2* accumulates at the tips of primary cilia in *Pka-null* cells and supports a model whereby the accessibility of *Gli* proteins to *PKA* at the ciliary base controls the fate of *Shh* signalling (Tuson et al., 2011). Studies in murine embryonic epidermis have recently shown that *Sufu* restricts the activity of *Gli2* through cytoplasmic sequestration (Li et al., 2012). Furthermore, *Kif7* can promote *Hh* pathway activity through the dissociation of *Sufu-Gli2* complex and it can also contribute to the repression of *Hh* target genes in the absence of *Sufu* (Li et al., 2012).

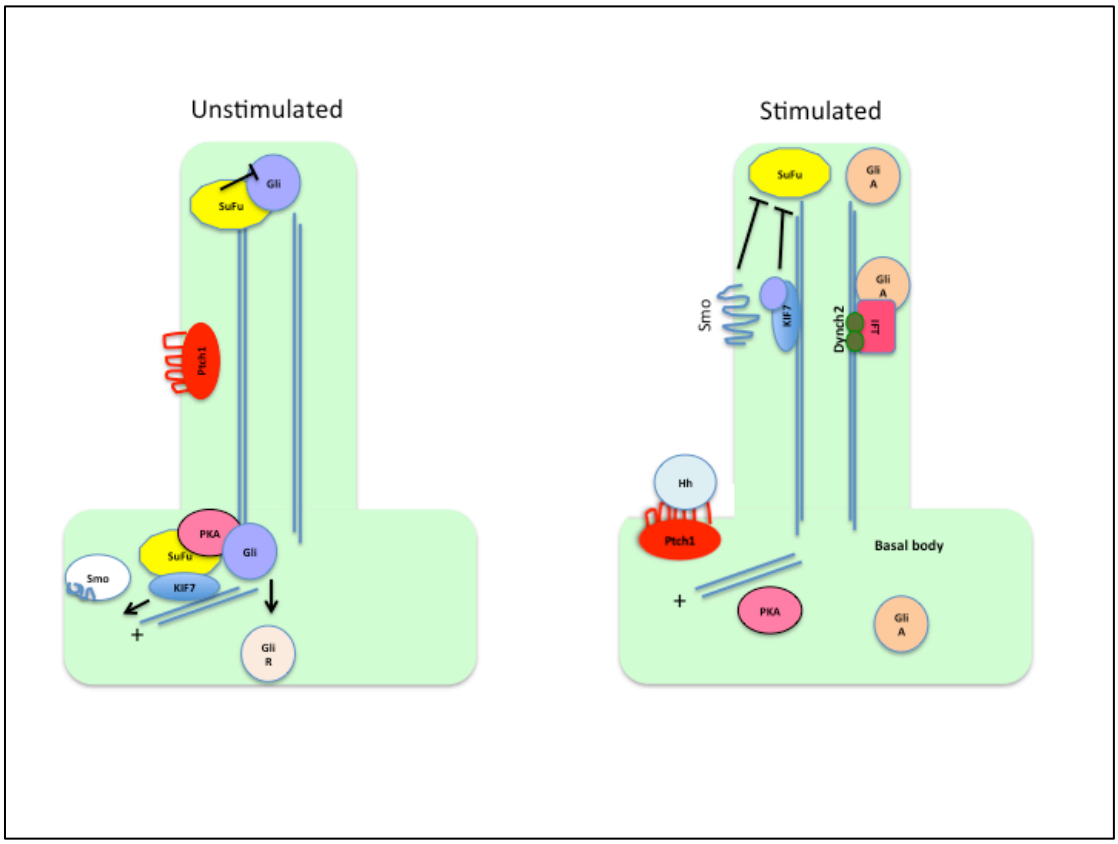

Figure 1.9: The primary cilium in Hedgehog signal transduction. In vertebrates, Shh signal transduction is dependent on cilia. Shh ligand binding to Ptch results in Smo moving to the ciliary membrane and Kif7 translocates into the cilium thereby promoting Gli2 accummulation at the cilium tip. Activated Gli is transported out of the cilium by dynein and IFT particles. (Adapted from Goetz et al, 2011).

1.2.2 Regulation of Wnt signalling

Several studies have implicated ciliary and basal body proteins in the regulation of Wnt signalling (Corbit et al., 2008; Gerdes et al., 2007; Ross et al., 2005). Wnt proteins are a family of 19 secreted glycoproteins that regulate a variety of biological processes implicated in development and disease. In canonical Wnt signalling, a Wnt ligand binds to a complex of

the Frizzled (Fz) receptor and low-density lipoprotein receptors (LRP5/6) coreceptor, which then binds to Axin and Dishevelled (Dvl), leading to stabilisation of β-catenin in the cytoplasm. β-catenin migrates into the nucleus, replaces TLE, and activates transcription of β-catenin/TCF/LEF1-responsive genes. In noncanonical signalling, activated Dvl is targeted to the membrane and activates downstream targets. Disruption of ciliary or basal body components leads to loss of noncanonical Wnt signalling and stabilisation of both Dvl and β-catenin in the cytoplasm and nucleus, resulting in activation of canonical Wnt signalling. Spatial mechanisms involving compartmentalisation of signalling components mediated by primary cilia dampen canonical Wnt signalling (Lancaster et al., 2011). Jouberin (Jbn), a ciliopathy protein and context-specific Wnt pathway regulator, which is regulated by IFT, is diverted away from the nucleus and limits β-catenin nuclear entry. This repressive regulation maintains a discrete range of Wnt responsiveness; cells without cilia have potentiated Wnt responses, whereas cells with multiple cilia have inhibited responses.

Inversin, the gene mutated in nephronophthisis, has been shown to interact with Dvl and localizes to cilia (Otto et al., 2003; Simons et al., 2005; Watanabe et al., 2003). Supporting a role for the cilium in the

regulation of Wnt signalling has been the finding of a hyperactive Wnt response in cultured cells in which BBS1, BBS4 and MKKS have been knocked down (Gerdes et al., 2007). Further in vivo support comes from murine studies of *Kif3a*, *Ift88* and *Ofd1*-deleted mice which reveal a marked increase in cellular responses to canonical Wnt pathway activation (Corbit et al., 2008). Finally, chibby, a basal body associated protein is able to bind β-catenin, prevent its nuclear entry and thereby negatively regulate Wnt (Voronina et al., 2009). Therefore, cilia-related proteins appear to play a role in the regulation of canonical Wnt signalling, the molecular details of which appear to involve spatial compartmentalisation of context-specific Wnt pathway regulators.

1.2.3 Regulation of Notch signalling

Notch signal transduction has also been proposed to be regulated by the primary cilium (Ezratty et al., 2011). Conditional ablation of *Ift88* and *Kif3a* in mice in addition to knockdown of several IFT genes have shown epidermal differentiation defects reminiscent of defective Notch signalling whereby enhanced proliferation and expansion of basal cells were observed (Ezratty et al., 2011). Keratinocytes transduced with Ift shRNA lentiviral vectors containing a Notch reporter construct showed reduced Notch reporter activity. Secondly, basal to spinous cell defects

could be partially rescued by transgenic expression of NICD. Ciliary localisation of the Notch 3 receptor and Presenilin-2, the catalytic subunit of γ-secretase, which mediates cleavage of the Notch receptor transmembrane domain during signal transduction has been demonstrated both *in vitro* and *in vivo* on mammalian epidermal cells (Figure 1.10) (Mumm et al., 2000).

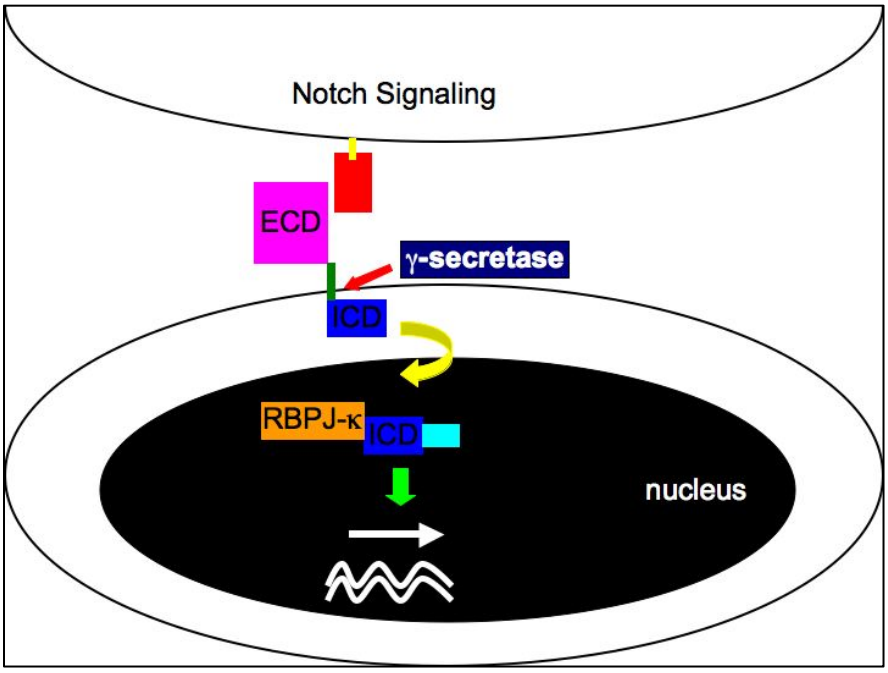

Figure 1.10: The Notch signalling pathway. Notch ligand (red) binding to the extracellular domain (purple) of the Notch receptor on reciprocal cells results in γ-secretase (blue) mediated cleavage of the Notch receptor transmembrane domain. Following release of the Notch intracellular domain (ICD) (turquoise), nuclear entry occurs followed by interaction with DNA-binding RBPJ-κ complex and co-repressors are released.

1.3. DISEASES ASSOCIATED WITH CILIA DYSFUNCTION

1.3.1 Overview of clinical features of ciliopathies

Systemic involvement characterised by the constellation of overlapping phenotypes that include retinal degeneration, polydactyly, situs inversus, mental retardation, encephalocele and cysts in the kidney, liver, and pancreas are caused by mutations in proteins localised to cilia and ciliary basal bodies. As a result, these phenotypically similar and rare recessive disorders have been classified as "ciliopathies" (Table 1.2 & 1.3). It has been predicted that over 100 known conditions fall into this category with only a handful studied to date.

1.3.2 Renal disease in ciliopathy disorders

A spectrum of renal diseases has been described as a feature of several ciliopathy syndromes and includes renal dysplasia, polycystic kidney disease (PKD) and nephronophthisis (NPHP) (Table 1.4). Renal dysplasia occurs as a result of defective differentiation of the renal parenchyma during renal morphogenesis (Woolf et al., 2004). PKD is a group of monogenic disorders that result in renal cyst development (Harris, 2009). Polycystic kidneys are more commonly inherited in an autosomal dominant or recessive fashion but may also be a feature of a

rare group of recessively inherited pleiotropic cystic disorders including cystic dysplasia. Over the past decade more than 20 genes have been identified as causing these disorders (1994) (Hughes et al., 1995) (1995; Mochizuki et al., 1996) (Onuchic et al., 2002) (Ward et al., 2002) (Consugar et al., 2008). PKD proteins have been shown to localise to the cilium and/or its basal body (Pazour et al., 2002; Yoder et al., 2002). Evidence that cilia are important in cystic kidney disease comes from the initial observation of renal cysts in the Oak Ridge polycystic kidney (*orpk*) mouse that mimics autosomal recessive polycystic kidney disease (ARPKD). *Orpk* mice are hypomorphic for *Tg737*, which encodes the mouse orthologue of *Chlamydomonas ift88*. Cilia in renal epithelia of hypomorphic *Tg737orpk* mice are structurally shorter than their wild-type littermate controls while complete *Tg737 null*-mice lack cilia and exhibit neural tube defects, left-right asymmetry and growth arrest during embryogenesis (Moyer et al., 1994) (Yoder et al., 1995) (Murcia et al., 2000) (Pazour et al., 2000). Several other mouse models linking cilia to cystic kidney disease exist (Hou et al., 2002). Genetic inactivation of *Kif3a* in mice leads to renal cyst formation and renal epithelia are deficient for cilia (Lin et al., 2003). Almost all of the proteins mutated in nephronophthisis (NPHP), have also been localised to the primary cilium

Table 1.2. Phenotypic overlap in the ciliopathies

	Ciliopathy	LCA	SLS	NPHP	MKS	BBS	JBS
Phenotype	**Cerebellar hypoplasia**			√		√	√
	Encephalocele				√		
	Hepatic disease		√	√	√	√	√
	Renal disease		√	√	√	√	√
	Intellectual disability	√		√		√	√
	Obesity					√	√
	Polydactyly				√	√	√
	Retinopathy	√	√	√		√	√
	Situs Inversus		√		√	√	√

LCA, Leber congenital amaurosis; SLS, Senior Loken Syndrome; NPHP, nephronophthisis; MKS, Meckel Gruber Syndrome; BBS, Bardet Biedl Syndrome; JBS, Joubert Syndrome

Table 1.3. Genotypic overlap in the ciliopathies

Gene	SLS	NPHP	MKS	BBS	JBTS
CEP290	√	√	√	√	√
NPHP1	√	√			√
INVS	√	√			
NPHP3	√	√	√		
NPHP4	√	√			
NPHP5	√	√			
GLIS2		√			
NEK8		√			
AHI1					√
TMEM67			√	√	√
TMEM138					√
TMEM216			√		√
CEP41					√
RPGRIPL1		√	√		√
INPP5E					√
CXORF5					√
TTC21B					√
TCTN1					√
TMEM237					√
TCTN2			√		
TCTN3					√
SDCCAG8	√	√		√	
ARL13B					
Bd91			√		
BBS1				√	
BBS2				√	
BBS3				√	
BBS4				√	
BBS5				√	
BBS6				√	
BBS7				√	
BBS8				√	
BBS9				√	
BBS10				√	
BBS11				√	
BBS12				√	
MGC1203				√	
MKS1			√	√	
CC2D2A		√	√	√	√
FRITZ					
LZTFL1				√	

LCA, Leber congenital amaurosis; SLS, Senior Loken Syndrome; NPHP, nephronophthisis; MKS, Meckel Gruber Syndrome; BBS, Bardet Biedl Syndrome; JBS, Joubert Syndrome

(Hildebrandt et al., 1997; Saunier et al., 1997) (Otto et al., 2002) (Mollet et al., 2002) (Yoder et al., 2002) (Pazour et al., 2002) (Lin et al., 2003) (Hildebrandt and Otto, 2005) (Sayer et al., 2006) (Ferland et al., 2004) (Dixon-Salazar et al., 2004) (Attanasio et al., 2007; Delous et al., 2007) (Watnick and Germino, 2003) (Germino, 2005) (Arts et al., 2007) (Valente et al., 2006) (Wolf et al., 2007) (Otto et al., 2008) (Hoefele et al., 2007) (Otto et al., 2009) (O'Toole et al.) and therefore suggest a role for cilia proteins in renal cystogenesis. Several molecular mechanisms underly the development of renal cystogenesis. Initiating events described in the pathogenesis of cystogenesis include hyperproliferation of incompletely differentiated epithelial cells (Nadasky et al., 1995) followed by cyst growth and expansion which are caused by abnormalities in the extracellular matrix and transepithelial fluid secretion. Cellular proliferation and fluid secretion can be accelerated by growth factors such as epidermal growth factor (EGF) (Du et al., 1995). EGF has been shown to hyperstimulate proliferation in autosomal dominant polycystic kidney disease (ADPKD) and ARPKD cystic

epithelia. EGF and EGF-reactive peptide species are secreted into the apical medium of cultured ADPKD epithelia, and high, potentially mitogenic concentrations have been measured in cyst fluids collected from ADPKD patients. Ligand-induced activation of EGFR receptors can stimulate a variety of intracellular pathways including PKC/AKT, PLCγ, MEK/Erk or c-Src. c-Src binds to and phosphorylates EGFR at Y845 and is required for EGFR family-mediated signalling and proliferation in normal cells as well as in cystic renal epithelia (Richards et al, 1998; Biscardi et al, 1999). Overexpression, constitutive activation, and abnormal location of EGFR and ErbB2 receptors on the apical (luminal) surface of cyst lining epithelia, together with secretion of soluble ligands by PKD cyst lining epithelia, creates a sustained cycle of autocrine–paracrine stimulation of proliferation in cysts (Zheleznova et al., 2011).

cAMP stimulated fluid secretion occurs early in embryonic renal tubule development in wild-type and PKD kidneys at the time when renal cysts first appear in ADPKD, suggesting that a cAMP-driven mechanism may be involved in the initial stages of cyst formation in ADPKD (Magenheimer et al., 2006). The cystic fibrosis transmembrane conductance regulator Cl-channel (CFTR) exists in apical membranes of human ADPKD cells and cAMP has been shown to stimulate solute and

fluid secretion through activation of CFTR (Hanaoka et al, 1996). cAMP stimulates the proliferation of PKD cystic epithelial cells, but not normal renal cells, through activation of the ERK mitogen-activated protein kinase pathway. Aberrant intracellular calcium signaling and/or reduced steady-state calcium levels in PKD cells determine the mitogenic response to cAMP. Several approaches to reduce renal cAMP and inhibit cAMP-dependent cell proliferation and fluid secretion are being considered for the treatment of PKD. CFTR inhibitors partially inhibited cyst growth and preserved renal function in a mouse model of ADPKD (Yang et al, 2008). Apicobasal polarity of some transporters and receptors is abnormal in ADPKD. EGF and its related growth factors have a biphasic effect on ENaC-mediated sodium absorption. ENaC-mediated sodium absorption might be involved in the development of PKD. Composition and regulation of adherens, focal adhesion and polarity complexes determine polarity. Cystic proteins form multi-molecular complexes with adhesive polarity complexes. Mutations in adhesive polarity complexes and trafficking proteins have also been shown to cause renal cystogenesis.

Primary cilia dysfunction alters renal tubular cell proliferation and differentiation and associates with accelerated cyst formation in PKD.

Conditional knockout of the *Ift88* gene leads to delayed, adult-onset renal cystic disease. Recent studies have demonstrated a significant two-fold increase in the number of proliferating BrdU-positive cells in contralateral kidneys of *Ift88* conditional knockout mice following unilateral nephrectomy (Bell et al., 2011). Enhanced mammalian target of rapamycin complex (mTORC) signalling was also observed in association with increased cell proliferation in the contralateral kidneys of *Ift88* conditional knockout mice following unilateral nephrectomy (Bell et al., 2011). Tuberous sclerosis complex (TSC) is a multiorgan hamartomatous disease caused by loss of function mutations of either the TSC1 or TSC2 genes (Kwiatkowski et al, 2003). Conditional inactivation of *Tsc1* in murine distal convoluted tubules (DCT) leads to renal cystogenesis and is also associated with increased mTORC1 but decreased mTORC2 signalling (Armour et al, 2012). mTOR inhibition ameliorates cyst formation in murine cystic kidney disease (Novalic et al, 2012). Interestingly, von Hippel-Lindau (VHL) disease also results in renal cystogenesis with similar features to ADPKD. Recent work has shown polycystin-1 (PC1) and pVHL proteins may participate in the same key signalling pathways (Foy et al, 2012). pVHL has been shown to stabilize Jade-1, a pro-apoptotic and growth suppressive ubiquitin ligase for beta-catenin and transcriptional coactivator associated with histone

acetyltransferase activity. Elegant studies have highlighted a role for PC-1 in the regulation of Jade-1 activity whereby PC-1 can bind and inhibit Jade-1 ubiquitination. ADPKD-associated PC1 mutants fail to regulate Jade-1, indicating a potential disease link between VHL disease and ADPKD (Foy et al., 2012). Defects in the establishment and maintenance of nephron diameter have been shown by several investigators to be implicated in the pathogenesis of cyst formation. Aberrant activation of signal transduction pathways have also been implicated. For example, constitutive expression of β-catenin in transgenic mice leads to renal cysts supporting a role for canonical Wnt activation in renal cystogenesis (Saadi-Kheddouci et al., 2001). Furthermore, mutations in *NPHP7* (*GLIS2*), a component of the SHH pathway, also point towards a role for defective SHH signalling in renal cystogenesis (Attanasio et al., 2007). As these key pathways are implicated in cell proliferation and differentiation, several other pathways regulating these processes in renal epithelia have been implicated in renal cystogenesis (Torres and Harris, 2009). Studies in mice suggest that severity of cyst formation is temporally related to renal tubule morphogenesis. Murine conditional inactivation of *Pkd1*, the gene mutated in 85% of cases of PKD before postnatal (PN) day 13 results in rapid progressive cystic enlargement whereas later inactivation results in a much milder course.

Table 1.4. The renal ciliopathies

Renal Phenotype	Histopathology	Gene (protein)	Subcellular localisation	Extrarenal Signs
Polycystic kidneys				
1. ADPKD	1. Focal cysts at all levels of the nephron	1. *PKD1 (PC-1)* 2. *PKD2 (PC-2)*	Cilia/basal bodies Cell-cell junctions Cell-matrix Interactions	Hepatic & pancreatic cysts, intracranial aneurysms
2. ARPKD	2. Radial pattern of fusiform cysts in the dilated collecting ducts	1. *PKHD1* (Fibrocystin)	Cilia/basal bodies Interacts with polycystins	Liver cysts/fibrosis
3. Syndromic	1. Focal cysts at all levels of the nephron	*1. BBS1-15*	Cilia/basal bodies	Obesity, diabetes, RP, Polydactyly
		2. MKS1-4	Cilia/basal bodies	Encephalocele, polydactyly, dysplasia of multiple organs
Nephronophthisis	Cortico-medullary cysts, tubular basement membrane disruption and tubulointerstitial nephropathy	*NPHP1-11* *NPHP1L* *SDCCAG8* *ZNF423* *CEP164*	Primary cilia, basal bodies & centrosomes	RP Liver cysts/fibrosis JS MKS Skeletal dysplasia
Renal Dysplasia	Incompletely branched collecting duct precursors surrounded by undifferentiated mesenchymal stroma.	*BBS* *NPHP3* *MKS1-4*		

1.3.2.1 Defective oriented cell division and renal cystogenesis

During renal morphogenesis, tubule diameter is established during early morphogenetic stages by convergent extension processes and maintained by polarized cell divisions whereby > 95% of renal epithelial cells divide at an angle < 34^0 relative to the longitudinal axis of the developing tubule (Karner et al., 2009). Defective oriented cell division (OCD) has been described in at least five distinct models of PKD (Fischer et al., 2006; Jonassen et al., 2008; Patel et al., 2008), (Saburi et al, 2008) (Figure 1.11). Hypomorphic *Wnt9b* mutant mice exhibit defects in polarised cell orientation during kidney tubule morphogenesis and by day 30 of postnatal life, exhibit severely dilated and cystic tubules (Karner et al, 2009). Further evidence that defective PCP signalling plays a role in renal cystogenesis comes from murine studies demonstrating renal cyst formation at embryonic day 16.5 in mice deficient for the core PCP effector, *Fat4* (Saburi et al., 2008). Inversin, the gene mutated in nephronophthisis (*NPHP2*) is localized to the primary cilium and is involved with the activation of PCP signalling (Simons et al, 2005). During urine flow, increased levels of inversin target Dvl for ubiquitinylation, which allows reassembly, and activation of the β-catenin

destruction complex and thereby mediating a switch from canonical to noncanonical Wnt signalling (Simons et al., 2005).

Defective OCD has also been observed in Notch-deficient proximal tubular epithelia prior to the development of renal cysts (Surendran et al., 2010). Furthermore, in MDCK cells treated with DAPT, a γ-secretase inhibitor, the fraction of cells dividing parallel to the basement membrane was less than 58% and the mitotic angle between the plane of the spindle poles and the plate surface was > 25^{o} compared to controls where the mitotic angle was <10^{o} in >94% of cells.

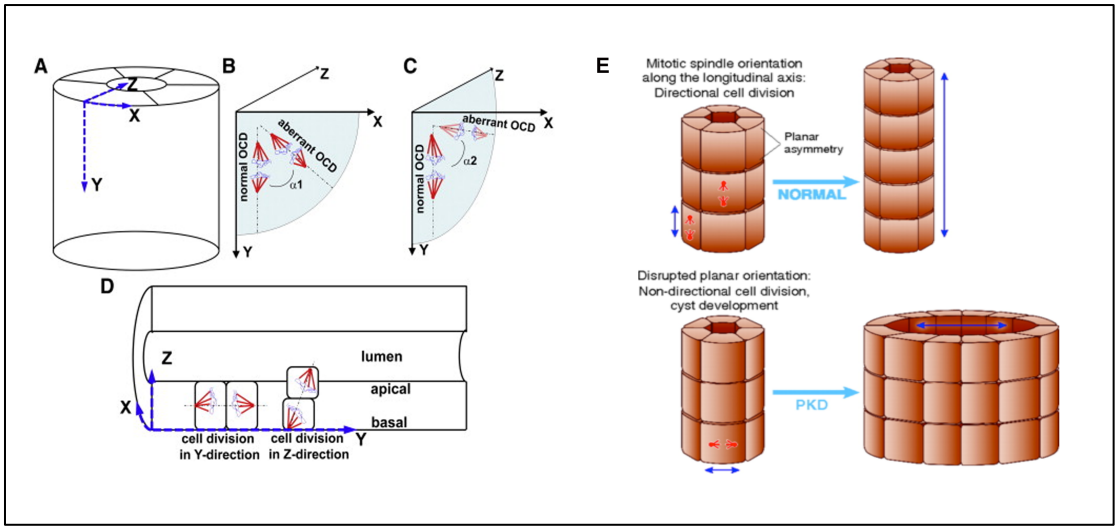

Figure 1.11: Malfunction of cystoprotein leads to disruption of planar cell polarity and renal cystogenesis. Alignment of mitotic spindle perpendicular to the tubular lumen in polycystic kidney disease leads to tubular dilation and cyst formation (Adapted from (Happe et al., 2011), (Hildebrandt et al., 2009).

The occurrence of mitotic spindle planes perpendicular to the basement membrane before cyst formation in *Notch*-deficient proximal tubular epithelia indicates that Notch 1 and Notch 2 are components of a molecular programme that restrict mitotic spindles to a plane parallel to the basement membrane (Surendran et al.). Future investigation will be necessary to determine the molecular components of this programme.

1.3.2.2 Role of cilia proteins in mitotic spindle orientation

During mitosis, centrosomes (spindle poles) participate in the organisation and orientation of the mitotic spindle (Luders and Stearns, 2007; O'Connell and Wang, 2000). Mitotic spindle orientation is facilitated by the interaction of astral microtubules with the cell cortex (O'Connell and Wang, 2000). Several proteins involved in cilia function have been localised to the spindle poles including IFT88, polycystins, Nde1 and CEP290. Intriguingly, IFT88 protein depletion has been reported to cause mitotic delay associated with spindle pole disruption, chromosome misalignment and spindle misorientation where IFT88-depleted cells result in a spindle angle greater than 10^{o} relative to the cell-substrate adhesion plane (Delaval et al., 2011) (Figure 1.11). Cystogenesis has been previously associated with structural cilia abnormalities and misoriented cell division (Fischer et al, 2006). While

cilia appear to regulate planar cell polarity, which has been implicated mechanistically in cystogenesis, the mechanism leading to misoriented cell division remains unclear (Saburi et al, 2008). Therefore the mechanisms underlying cystogenesis in diseases associated with mutations in cilia genes, could actually be the result of cilia proteins playing a role in spindle orientation rather than cilia formation.

1.3.3 Predicting new ciliopathy disorders

Mutations in over 60 genes to date, have been implicated in human ciliopathy disorders. Depending on the cell type, the ciliary proteome has been found to contain between 500 and 1800 ciliary proteins. Therefore, it has been estimated that potentially many more cilia-related diseases exist (Baker and Beales, 2009). Recent work has shown that Mainzer Saldino and Sensenbrenner syndromes, disorders characterised by skeletal dysplasia, renal disease and retinal degeneration are also ciliopathy disorders. Mutations in *IFT122*, *WDR35*, *WDR19*, *IFT43* and *IFT140* have been found in to be mutated in Sensenbrenner and Mainzer Saldino syndromes respectively (Arts et al., 2011; Bredrup et al., 2011; Gilissen et al., 2010; Walczak-Sztulpa et al., 2010)(Isabelle et al, 2012). Through accurate phenotyping approaches together with a greater awareness of the range of ciliopathy morphological features, coupled with

next generation sequencing technologies, it is highly anticipated that the genetic aetiology of several new ciliopathy disorders will be uncovered.

Summary

Ciliopathies are disorders associated with genetic mutations resulting in dysfunctioning cilia. As cilia are a component of almost all vertebrate cells, cilia dysfunction can manifest as a constellation of features that include characteristically, situs inversus, retinal degeneration, cystic renal disease, obesity, diabetes, cerebral malformations and skeletal disorders. With over 1,000 polypeptides currently identified within the ciliary proteome, several other disorders associated with this constellation of clinical features will likely be ascribed to mutations in other ciliary genes. The mechanisms underlying many of the disease phenotypes associated with ciliary dysfunction have yet to be fully elucidated. Recent work has shown that cilia proteins such as IFT components can play a role in mitotic spindle orientation, a mechanism, which when defective, could help explain certain ciliopathy phenotypes such as cystic kidney disease. The focus of the current work was to identify a new ciliopathy disease gene and elucidate a novel ciliogenic function for its encoded protein, whose function had been previously well characterised in mitosis.

CHAPTER 2. MATERIALS AND METHODS

2.1 MATERIALS

2.1.1 General laboratory reagents and materials

All the reagents that were used were obtained from Sigma Aldrich or BDH laboratory supplies, except where indicated. Glassware was obtained from Fisher Scientific (UK), Pyrex ® (USA) and schott Duran (Germany). Plastic ware was from Becton Dickson Labware or Bibby Sterilin Ltd. 0.2ml PCR tube strips were obtained from ThermoScientific Ltd. Glassware, solutions and media were autoclaved at 15pst, 121 ºC for 20 minutes as required. Water was purified using MiliRo Water Purification System (Milipore SA) and further purified where necessary using a Mili-Q reagent Grade Water Ultrafiltration System (Milipore SA) and sterilized by autoclaving.

2.1.2 Other reagents and materials

Electrophoresis molecular biology grade agarose was obtained from Invitrogen Life Technologies. Bacto-agar, bactotryptone, bactopeptone, agar and yeast extract were from Fisher. Absolute alcohol, methanol and isopropanolol were obtained from Fisher VWR International. NBT/BCIP were purchased from Roche. Sterile loops were obtained from Greiner

BioOne. Super Premium microscope slides were purchased from VWR International. Vectashield mounting medium kit for fluorescence with DAPI was purchased from Vector Laboratories Inc.

2.1.3 General laboratory stock solutions and buffers

A buffer is an aqueous solution consisting of a mixture of a weak acid and its conjugate base or a weak base and its conjugate acid. Buffer solutions are used as a means of keeping pH at a nearly constant value.

1x PBS	137mM NaCl, 3mM KCl, 10mM Na_2HPO_4, 1.8mM KH_2PO_4, pH 7.2
1x PBT	1x PBS + 0.1% Tween-20
1x TE buffer	10mM Tris-HCl, 1mM EDTA, pH 8.0
1x TAE	40mM Tris-acetate, 1mM EDTA, pH 8.0
RIPA lysis buffer	50 mM Tris–HCl [pH 7.5], 150 mM NaCl, 0.5% Triton X-100, 0.5% sodium deoxycholate, 0.1% sodium dodecyl sulphate
10x Running Buffer	30 g Tris base, 144g glycine, 10 g SDS, 1L H_2O, [pH 8.3]
5x Transfer Buffer	14.5 g Tris, 72g glycine, 1L H_2O
5% Milk	2.5g Skimmed milk powder, 50mls 1xPBS

2.2 METHODS

2.2.1 Exome capture

2.2.1.1 Research subjects

In addition to the index family, we obtained blood samples following informed consent from families with Bardet Biedl syndrome. Approval for human subjects research was obtained from the Institute of Child Health Research Ethics Board, University College London and the other institutions involved.

2.2.1.2 Linkage analysis

Genetic studies were approved by the Institute of Child Health–Great Ormond Street Hospital Research Ethics Committee, and the parents provided written informed consent. For genome-wide single-nucleotide polymorphism (SNP) mapping the GeneChip® Human Mapping 500k Array from Affymetrix was used. Genotypes were examined with the use of a multipoint parametric linkage analysis and haplotype reconstruction performed with GENEHUNTER 2.1 (Kruglyak et al, 1996, Strauch et al, 2000) through stepwise use of a sliding window with sets of 110 SNPs and the program ALLEGRO (Gudbjartsson et al, 2000) for an autosomal

recessive model with complete penetrance and a disease allele frequency of 0.0001 and Caucasian marker allele frequencies.

2.2.1.3 Target selection and sequencing

Targeted capture was performed on genomic DNA from 1 affected and 1 unaffected sibling.

2.2.1.4 Oligonucleotides and adaptors

All oligonucleotides were synthesised by Roche Nimblegen. SeqCap EZ Human Exome Library v1.0 design utilized genomic content from RefSeq, CCDS and miRBase databases which encompassed 25, 000 coding genes and 180, 000 exons. Oligonucleotides were resuspended in nuclease-free water to a stock concentration of 100 μM. Double-stranded library adaptors SP1 and SP2 were prepared to a final concentration of 50 μM by incubating equimolar amounts of SP1_HI and SP1_LO together and SP2_HI and SP2_LO together at 95°C for 3 mins and then leaving the adaptors to cool to room temperature in the heat block.

2.2.1.5 Sample library construction

Sample libraries were generated from 3μγ of genomic DNA (gDNA) using the Illumina Paired-End Genomic DNA Sample Prep Kit protocol. For each sample, gDNA in 100μl 1× Tris-EDTA was first sonicated for

30 min using a Covaris Sonolab set at high, then end-repaired for 55 mins in a 100µl reaction volume using 1× End-It Buffer, 10µl dNTP mix and 10µl ATP as supplied in the Paired-End Genomic DNA Sample Prep Kit (Illumina). The End-It™ DNA End-Repair Kit converts DNA containing damaged or incompatible 5′- and/or 3′-protruding ends to 5′-phosphorylated, blunt-ended DNA. The fragments were then A-tailed for 55 mins at 70°C in a 100µl reaction volume with 1× PCR buffer (Applied Biosystems), 1.5mM $MgCl_2$, 1mM dATP and 5U AmpliTaq DNA polymerase (Applied Biosystems). Next, library adaptors SP1 and SP2 were ligated to the A-tailed sample in a 90µl reaction volume with 1× Quick Ligation Buffer (New England Biolabs) with 5µl Quick T4 DNA Ligase (New England Biolabs) and each adaptor in 10× molar excess of sample. Samples were purified on MinElute columns (Qiagen) after each of these four steps and DNA concentration determined on an Agilent DNA 1000 chip when necessary. MinElute Kits contain a silica membrane assembly for binding of DNA in high-salt buffer and elution with low-salt buffer or water. The purification procedure removes primers, nucleotides, enzymes, mineral oil, salts, agarose, ethidium bromide, and other impurities from DNA samples. Silica-membrane technology eliminates the problems and inconvenience associated with loose resins and slurries. Specialized binding buffers are optimized for

specific applications and promote selective adsorption of DNA molecules within particular size ranges.

Each sample was subsequently size selected for fragments of size 200–400bp using gel electrophoresis on a 6% TBE-polyacrylamide gel (Invitrogen). A gel slice containing the fragments of interest was then excised and transferred to a siliconized 0.5ml microfuge tube (Ambion) with a 20G needle-punched hole in the bottom. This tube was placed in a 1.5ml siliconised microfuge tube (Ambion), and centrifuged at 13.2 xg for 5mins to create a gel slurry that was then resuspended in 200 µl 1× Tris-EDTA and incubated at 65°C for 2hrs, with periodic vortexing. This allowed for passive elution of DNA, and the aqueous phase was then separated from gel fragments by centrifugation through 0.2 µm NanoSep columns (Pall Life Sciences) and the DNA recovered using a standard ethanol precipitation.

Recovered DNA was resuspended in EB buffer (10mM Tris-Cl, pH8.5, Qiagen) and 4µl was used in a 200 µl bulk PCR reaction volume and thereafter divided into 4 reaction volumes with 2 x Phusion High-Fidelity PCR Master Mix and 2 uM each of primers PE-PRE 1 and PE-PRE 2 in the following conditions – 98°C for 30s; 98°C for 10s; 65°C for 30s and 72°C for 30s; 11 cycles of 98°C for 10s; 65°C for 30s and 72°C for 30s; and finally 72°C for 5 min. Combined 4 PCR products were

purified across 1 QIAquick columns (Qiagen) and eluted with PCR grade water. DNA concentration determined on a Nanodrop spectrophotometer and then run on an Agilent DNA 1000 chip when necessary with fragments between 200-400bp.

2.2.1.6 Hybridization to exome libraries

100 µl of 1mg/ml Cot DNA and 1µg of amplified sample library was added to a 1.5 ml microfuge tube. 1 µl of each 1000 µM PE-HE1 and PE-HE2 oligos to the amplified sample library plus Cot DNA. A hole was then made in the closed lid of the tube with a 20G needle. The amplified sample library/Cot-1 DNA/PE-HE Oligos were then dried in a SpeedVac at 60°C for at least 30 minutes. Cot-1 DNA is genomic DNA that is highly enriched for repetitive elements, such as SINES (short interspersed repetitive elements, or Alu repeats) and LINES (long interspersed repetitive elements, or L1 elements). Cot-1 DNA is used as an unlabelled blocking agent in hybridization experiments to prevent non-specific hybridization by hybridizing to repetitive elements in the genome. Following drying, 7.5 µl of 2x SC Hybridization buffer was added with 3 µl of SC Hybridization component A. The hole in the lid of the microfuge was then covered with a sticker and the amplified library/Cot DNA/PE-HE Oligos plus Hybridization Cocktail was vortexed for 10 seconds and

centrifuged at maximum speed for 10 seconds. The amplified sample library/Cot DNA/PE-HE/Hybridization Cocktail was centrifuged at maximum speed for 10 seconds at 25ºC. The amplified sample library/Cot/DNA/PE-HE Oligos/Hybridization Cocktail was transferred to the 4.5 µl aliquot of EZ Exome Library (Roche Nimblegen) which was vortexed for 3 seconds and then centrifuged at maximum speed for 10 seconds. The amplified sample library/Cot/DNA/PE-HE Oligos/Hybridization Cocktail with the EZ Exome Library was then incubated in a thermocycler at 47°C for 64-72 hours.

2.2.1.7 Recovery of captured DNA

10X SC Wash Buffers (I, II and III) and 2X Stringent Wash Buffer was diluted to 1X working concentrations. 1X Stringent Wash Buffer and 1X SC Wash Buffers I was heated to 47°C in a water bath. The streptavidin dynabeads were warmed to room temperature for 30 minutes prior to use. The beads were then mixed thoroughly by vortexing for 1 minute. For each capture, 100 µl of beads were aliquoted into a single 1.5 ml tube, which was then placed in a Dyna-Mag2 device. The liquid was then removed and the beads left behind were washed with 200 µl of wash buffer. After removal of the tube from the Dyna-Mag2 device, the tube was vortexed for a further 10 seconds and the tube was replaced again in the Dyna-Mag2 device and washed with wash buffer for another 2

washes. Following the second wash, the beads were resuspended by vortexing in 1x the original volume using the Streptavidin bead binding and wash buffer. 100 µl of beads were aliquoted into 2 new tubes and the beads were again bound using the Dyna-Mag2 device. The hybridization samples were then transferred to the streptavidin dynabeads and mixed by pipetting. The solution with the hydridization samples and streptavidin dynabeads were then incubated in a thermocycler at 47°C for 45 minutes. The sample was vortexed every minute for 3 seconds to maintain the beads in suspension. The dynabeads with bound DNA was then placed in the Dyna-Mag2 device, the liquid was first removed and thereafter the tube, from the Dyna-Mag2 device. The beads and bound DNA was then washed with 200µl of Stringent wash buffer heated to 47°C for a total of 2 washes. Subsequently the beads and bound DNA were then washed in SC Wash Buffer I, II and III following placement in the Dyna-Mag2 device with removal of liquid after each wash. 50 µl of PCR grade water was then added to the bead-bound captured DNA sample.

2.2.1.8 Amplification of captured DNA

The bead-bound captured DNA sample was vortexed to achieve a homogenous mixture of beads. 4µl of bead-bound captured DNA was aliquoted into 10 reaction tubes each containing 46µl of LM-PCR Post

Capture Master Mix (2X Phusion High Fidelity PCR Master Mix, 2μM PE-POST Oligo 1, 2μM PE-POST Oligo 2 and PCR grade water) , in the following conditions – 98°C for 30s; 98°C for 10s; 60°C for 30s and 72°C for 30s; 19 cycles of 98°C for 10s; 65°C for 30s and 72°C for 30s; and finally 72°C for 5 min. Combined 10 PCR products were purified across 2 QIAquick columns (Qiagen) and eluted into EB buffer. DNA concentration from the combined eluates was then determined on a Nanodrop spectrophotometer and then run on an Agilent DNA 1000 chip when necessary with fragments between 200-400bp. The LM-PCR yield > 1 μg.

2.2.1.9 Measurement of enrichment using qPCR

A standardised set of qPCR SYBR Green assays were employed as internal quality controls to estimate the relative abundance of control targets in amplified sample library and amplified captured DNA. For each PCR reaction, 1μl of 5ng/ μl template (amplified sample library, amplified captured library DNA, positive control genomic DNA or negative control PCR grade water) was added to 5.9μl PCR grade water, 0.3μl NSC assay forward primer (2μM) and reverse primer (2μM) and 7.5 μl SYBR Green Master Mix (2X). Primers used were NSC-0237, NSC-0247, NSC-0268, NSC-0272 (Nimblegen). The PCR conditions

were as follows: 95°C for 10 minutes, 40 cycles of 95°C for 10 seconds with 60°C for 1 minute, 95°C for 10 seconds, 65°C for 1 minute, 95°C for 5 acquisitions per degree, 40°C for 10 seconds. The relative mRNA abundance of target enrichment of amplified captured DNA from amplified sample library was calculated using the second derivative maximum method. The cut-off values for successful fold enrichment were as follows: NSC-237, 250; NSC-247, 50; NSC-268, 300 and NSC-272, 300.

2.2.1.10 Massive parallel deep sequencing

Following amplification of captured DNA, single-stranded DNA fragments were annealed to a flow cell surface in a cluster station, automated flow cell processor, (Illumina) and 46 cycles of bridge amplification were applied on a single lane of a Solexa/Illumina Genome Analyzer II platform. "Bridged" amplification occurs on the surface of the flow cell which is a water-tight microscope slide. The flow cell surface is coated with single stranded oligonucleotides that correspond to the sequences of the adapters ligated during the sample preparation stage. Single-stranded, adapter-ligated fragments are bound to the surface of the flow cell exposed to reagents for polyermase-based extension. Priming occurs as the free/distal end of a ligated fragment "bridges" to a complementary oligo on the surface. Repeated denaturation and extension

results in localized amplification of single molecules in millions of unique locations across the flow cell surface. 'Sequencing by synthesis' is a process whereby automated cycles of extension and imaging are undertaken in a flow cell containing millions of unique clusters following loading into the 1G sequencer. The first cycle of sequencing consists the incorporation of a single fluorescent nucleotide, followed by high resolution imaging of the entire flow cell. These images represent the data collected for the first base. Any signal above background identifies the physical location of a cluster (or polony), and the fluorescent emission identifies which of the four bases was incorporated at that position. This cycle is repeated, one base at a time, generating a series of images each representing a single base extension at a specific cluster. Base calls are derived with an algorithm that identifies the emission color over time. Image analysis and base calling was generated by the Genome Analyzer Pipeline 1.5 with default parameters. Illumina specific FASTQ file containing sequence information and quality scores for each base call were exported for further analysis.

2.2.1.11 Quality control

After the sequencing reactions were complete, the Illumina analysis pipeline was used to process the raw sequencing data (Bustard and Gerald) and produce FASTQ format files (Justyna Porwisz, UCL

Genomics Facility). The quality of the sequencing runs were assessed by evaluating the percentage of clusters passing the filter, and by running the FastQC software and evaluating read length and base quality profiles, GC content, average GC content per base, average base content per read position, and checking for any indication of over-represented sequences.

Sample	**Clusters (raw)**	**Clusters (PF)**	**% PF**	**PCR Duplicates removed (mln)**
Affected	252567 +/- 5886	180734 +/- 7104	71.55 +/- 2.32	6.85
Unaffected	234697 +/- 4834	180749 +/- 3459	77.02 +/- 1.15	11.69

2.2.1.11 Alignment (undertaken by Francesco Lescai)

Once the raw sequence data was assessed for quality, the reads were aligned to a human reference genome (GRC37 release, downloaded from the ENSEMBL database). Three different software programmes were used: Maq, BWA and Novoalign. Maq performed an ungapped

alignment, with limited gapped alignment on non-paired reads. BWA and Novoalign perform gapped alignments. Maq and BWA were used with their default parameters. Novoalign was launched with the additional hard clipping option based on read base quality (-H) and the default adaptor removal option (-a). The alignment summary was reported by using in-house perl scripts that count the bitwise flags for the sam files produced during the alignments steps. The coverage along the genome was calculated using BEDtools (GenomeCoverageBed function), without omitting zero values. Alignments were visualized in UCSC Genome Browser using the BED files and in Integrated Genome Browser using the BAM files.

2.2.1.13 SNP and InDel calling (undertaken by Francesco Lescai)

2.2.1.13.1 SNP calling with Maq and Samtools

On Maq alignments, its internal function was used in order to remove PCR duplicates (maq rmdup). Although Maq performs mostly an ungapped alignment, two internal functions exist to call consistent indels from paired end reads (maq indelpe) and to call potential homozygous indels and break points by detecting the abnormal alignment pattern around indels and break points (maq indelsoa). These two functions were used to generate potential indels locations and to mask these loci during

the SNP calling. SNP calling with Samtools version 0.1.7-6 was also employed. The internal function (rmdup) was used in order to remove potential PCR duplicates. The new bam was then used as an input to extract a pileup with a Maq-like consensus sequence (paramenters "-vc"). A preliminary pileup output was used to filter the variant calls (function samtools.pl varFilter) with parameters (set by Francesco Lescai). The final output was then converted to variant call format (VCF) format.

2.2.2 Tissue Culture

Human Embryonic Kidney (HEK) 293T, National Institute of Health 3T3 fibroblasts and retinal pigment epithelial (RPE) cells were grown and serially passaged in order to produce Cenp-F proteins. For passaging, cells were incubated in 2ml 0.05% trypsin solution (Gibco) at 37ºC until all cells had detached from the flask (between 3 to 5 minutes): after addition of an equal volume of growth medium, the number of cells was determined using a haemocytometer; the cells were then pelleted, resuspended in growth medium and replated according to the determined total number of cells. Cells were grown in a humidified incubator at 37ºC with 5% CO_2 on tissue culture grade plastic dishes purchased from Invitrogen (Corning MA).

2.2.2.1 Transfection

Human embryonic kidney cells (HEKT293), mouse embryonic fibroblast cells (NIH 3T3) and RPE cells were cultured in DMEM media (Gibco containing 10% foetal bovine serum (Gibco) and 1% penicillin/streptomycin (Gibco). Cells were transfected using the Effectene ® transfection reagent (Qiagen). Following condensation of DNA, the Effectene® reagent coats the condensed DNA molecules with cationic lipids to the plasmid DNA resulting in micelle formation. The complexes are mixed with growth medium and are added directly to the cells which are then incubated and harvested at optimal time-points to analyze gene expression.

Preparation of the transfection solution in 24-well plates:

Cells were plated on the day before transfection at 2-8 x 10^5 cells per 60mm dish in 5mls of DMEM with 10% FBS and 1% penicillin/streptomicin. Cells were incubated at 37ºC and 5% CO_2 and were between 40-80% confluent on the day of transfection. On the day of transfection, 1μg of plasmid DNA was diluted in 150 µl of the DNA-condensation buffer, Buffer EC. 8 µl of Enhancer was added to the solution, which was then vortexed for 1 second. The solution was then incubated for 2 to 5 minutes at room temperature and then spun down for

a few minutes to remove drops from the top of the tube. Next 25 µl of Effectene transfection reagent (Qiagen) was then added to the DNA-Enhancer mixture and gently mixed by vortexing for 10 seconds. Samples were then incubated for 5-10 minutes at room temperature to allow transfection-complex formation. While complex formation was taking place, growth medium was gently aspirated from the plate and cells were washed once with 4mls of 1xPBS. 4 mls of fresh DMEM with 10% FBS and 1% penicillin/streptomycin was added to the cells. After incubation, 1 ml of DMEM containing 10% FBS and penicillin with streptomycin was added to the tube containing the transfection complexes. The solution was gently mixed by pipetting up and down twice and the transfection complexes were then added drop-wise onto the cells in the 60mm dishes. The dish was gently swirled to ensure uniform distribution of the transfection complexes.

2.2.2 Bacterial culture

2.2.3.1 Bacterial strains

The bacterial strain used was *Escherichia coli* JM109 (Promega) for plasmid DNA propagation.

2.2.3.2 Bacterial growth media

L-Broth	10g/l Bacto-tryptone, 5g/l yeast extract, 5g/l NaCl
LB agar	L-Broth + 15g/l agar added prior to autoclaving
NZY+ Broth	5g/l NaCl, 10g/l casein hydrolysate,
	5g/l yeast extract, 12.5mls 1M $MgSO_4$,
	12.5mls 1M $MgCl_2$, 10mls 2M glucose

2.2.3.3 Selection antibiotics for bacteria

Ampicillin (stock 50mg/ml in sterile water, stored at -20ºC) was added to L-Broth, LB agar to a final concentration of 100 μg/ml.

2.2.3.4 Bacterial transformation

Preparation of transformation-competent bacteria:

A single colony of JM109 bacteria was cultured overnight without shaking in 10 ml L-broth medium at 37ºC. 100 ml of L-broth medium were inoculated with the entire overnight culture and grown in a 37ºC bacterial shaker until the $O.D_{600}$ reached 0.4 (approximately 4 hours). The bacteria were pelleted by centrifugation at 6000 rpm for 10 minutes at 4ºC, washed once in ice cold 10mM NaCl, resuspended in 100ml ice

cold 50 mM $CaCl_2$ and incubated on ice for 15 minutes. Bacteria were pelleted again by centrifugation at 6000 rpm for 10 minutes at 4ºC, resuspended in 10 ml ice cold 50 mM $CaCl_2$ containing 16% glycerol (w/v) and aliquoted into 1.5 ml tubes which were pre-cooled in a dry ice/ethanol bath. Aliquots were stored at -70ºC. Competence was tested by transformation with the plasmid pBluescript II KS (+/-). Typically, 100 μl of competent bacteria were able to produce approximately 10^6 colonies per μg DNA.

Transformation of bacteria:

50 μl of competent bacteria were thawed on ice and then gently mixed with 25ng of plasmid DNA. The cells were then chilled on ice for 10 minutes and then transferred to a water bath at 42ºC and electroporated by heating for 50 seconds. The cells were then transferred back to ice for another 2 minutes before adding 450 μl of cold L-broth and the cell suspension was gently mixed and incubated with shaking for 1 hour at 37ºC. 225 μl culture was spread onto LB agar containing a suitable antibiotic and incubated overnight at 37ºC. Next, single colonies were picked with a sterile loop to inoculate 2.5 mls LB medium containing the appropriate antibiotic and incubated overnight in an orbital shaker at 37ºC. 1ml was then inoculated into 50 mls of LB containing the

appropriate antibiotic in a sterile conical flask and incubated at 37ºC in an orbital shaker overnight. For glycerol stocks, 140 µl of the overnight culture was added to 40 µl of 80% glycerol and stored at -80ºC. Colonies were tested to determine if bacterial transformation was effective by restriction enzyme digestion of mini- and midi- prepared DNA.

2.2.4 DNA techniques

2.2.4.1 Purification of plasmid DNA from bacteria

For purification of plasmid DNA from bacteria, QIAquick mini and midiprep kits (Qiagen Ltd.) were used. The procedure for plasmid DNA purification from bacteria is a modified version of alkaline lysis method of Birnboim and Doly (Birnboim and Doly, 1979). Briefly, bacteria are lysed under alkaline conditions, leading to release of the cell contents and subsequent denaturation of proteins, chromosomal and plasmid DNA. The lysate is subsequently neutralized and adjusted to high-salt binding conditions, causing denatured proteins, chromosomal DNA and cellular debris to precipitate, while the smaller plasmid DNA renatures and stays in solution ready to be purified. Depending on the size of the plasmid DNA scale preparation, DNA can be purified by isopropranolol precipitation (small scale) or through a Qiagen anion-exchange resin under appropriate high-salt and pH conditions (medium scale).

For small scale preparation of plasmid DNA (”miniprep”), eg to screen colonies after transformation, 3mls LB-media containing a suitable antibiotic was inoculated with a single bacterial colony and grown overnight in a 37ºC orbital shaker. Plasmid DNA was isolated from the pelleted bacteria by resuspension in 500 µl ice cold solution P1 (containing RNase A), followed by addition of 500 µl solution P2 (NaOH/SDS-containing lysis solution) and mixing, then 500 µl ice cold solution P3 (high-salt neutralizing solution) and mixing, centrifugation at 14000 rpm in a microfuge for 5 minutes, and finally precipitation with 0.7 volumes of isopropranolol. DNA was dissolved in 1x TE containing 100 µg/ml RNAse A.

For medium scale preparations (“midiprep”), 3 mls LB-media containing a suitable antibiotic was inoculated with a single bacterial colony and grown overnight in a 37ºC orbital shaker. Next day, 50 ml LB-media containing a suitable antibiotic was inoculated with 1.5 ml of the overnight culture and grown overnight in a 37ºC orbital shaker. On the following day, the 50ml culture was harvested by centrifugation at 6000 rpm for 15 minutes at 4ºC. The pellet was resuspended in 6 ml of Buffer P1. 6ml of Buffer P2 was added, mixed thoroughly by vigorously inverting the tube 4-6 times and then incubated at room temperature (15-25ºC) for 5 minutes. Then, 6ml of chilled Buffer P3 was added, mixed

vigorously by inverting the solution 4-6 times. The lysate was then poured into the barrel of the QIAFilter cartridge and incubated at room temperature for 10 minutes. A HiSpeed MIDI was equilibrated by applying 4 mls of QBT and the column was allowed to empty by gravity flow. The nozzle was removed from the QIAFilter cartridge and the plunger was inserted into the QIAFilter midi cartridge and the cell lysate was filtered into the previously equilibrated HiSpeed tip. The cleared lysate was allowed to enter the resin by gravity flow. The HiSpeed Midi was washed with 20mls of Buffer QC. The DNA was eluted by adding 3.5mls of room temperature isopropanolol to the eluted DNA. The sample was then mixed and incubated at room temperature for 5 minutes. During the incubation procedure, the plunger was removed from the 20ml syringe and attached to the QIAprecipitator Midi Module onto the outlet nozzle. The eluate/isopropanolol mixture was transferred into the 20mls syringe and the plunger was inserted under constant pressure. The QIAprecipitator was re-attached and 2mls of 70% ethanol was added to the syringe. The DNA was washed by inserting the plunger and pressing the ethanol through the QIAprecipitator. The QIAprecipitator was removed from the 20ml syringe and pulled out and inserted again while the membrane was dried by pressing air through the QIApercipitator forcefully and quickly. A 5 ml syringe was then attached to the QIAprecipitator and 1ml of water was added to the syringe and the

plunger was inserted to elute into a 1.5ml Eppendorf. This step was repeated. Next, the DNA concentration was determined and the plasmid was validated by diagnostic restriction enzyme digestion.

2.2.4.2 Quantification of DNA

A 2 µl aliquot of DNA was diluted in 198 µl of sterile distilled water and its absorbance measured at 260 nm using a NanoDrop ND1000 Spectrophotometer. The concentration of the DNA was then calculated from the A260 value (1 A_{260} unit = 50 µg of double stranded DNA).

2.2.4.3 Restriction enzyme digestion of DNA fragments

Restriction enzymes (New England Biolabs) were used with the appropriate buffers, as recommended and supplied by the manufacturers. For most digestions, 1 µg of DNA was digested with 1.5 units of the required restriction enzyme(s) with the appropriate buffer in 50 µl reactions. Bovine serum albumin (BSA) was added if required. The reaction was incubated at 37ºC for 2 hours. Following digestion, the products were then electrophoresed on a 1% agarose gel containing ethidium bromide (see below).

2.2.4.4 Amplification of DNA by Polymerase Chain Reaction (PCR)

Genotyping was performed by polymerase chain reaction (PCR). Amplification was performed on an MJ Research PTC-200 Peltier Thermal Cycler (check this). Briefly, PCR was performed with 1 μl of genomic DNA solution, 12.5 μl of PWO reaction mix (Roche), containing Taq polymerase, dNTPs, buffer, blue agarose loading dye and stabiliser and 0.2 μl of each oligonucleotide primer (1μg/μl solution) specific for the gene-targeted genomic loci (Table 2.1), using the PCR cycling parameters described in Table 2.2. Oligonucleotides were synthesised to order by Invitrogen. A negative control was prepared for each reaction, using 2 μl of sterile water instead of DNA as well as a positive control, using 2 μl of control DNA known to give a product of correct size. PCR products were electrophoresed through 2% agarose gels containing ethidium bromide.

2.2.4.5 Agarose gel electrophoresis

The concentration of the agarose gel used was dependent on the size of the fragments that were being electrophoresed. In general, 1% agarose gels were used to electrophorese diagnostic plasmid digestion products, while 2% agarose gels were used to separate PCR products. The agarose was weighed and added to the appropriate volume of 1 xTAE buffer. This was then heated in the microwave to dissolve the agarose and then cooled

to approximately 50ºC. Next, 10 mg/ml ethidium bromide was added to a final concentration of 0.2 mg/ml. The gel was then poured into a gel tray of a suitable size containing a comb. The gel was left to set for approximately 30 minutes. The gel was then placed into a tank and covered with 1 x TAE. The comb was then removed and the samples were added by pipetting. The appropriate DNA ladder (100 bp and 1Kb DNA ladders from Invitrogen) were also loaded. Electrophoresis carried out at 140V until the fragments had separated sufficiently. The DNA fragments in the gel were then visualized by exposure to UV light, which allowed ethidium bromide fluorescence detection at 300 nm on a GENEgenius Bio Imaging System dark room from Syngene. Gels were photographed using the GENESnap software from Syngene and printed on a Syngene digital graphic printer UP-D895 using Sony UPP-110HA thermal print media.

2.2.4.6 Site-directed mutagenesis

Mutant human CENPF plasmids were synthesised using the QuikChange Site-Directed Mutagenesis kit ® (Stratagene, Catalogue #200518). Full length human CENPF cDNA plasmid was kindly provided by X Zhu, Shanghai Institutes for Biological Sciences and N-myc-tagged CENPF was kindly provided by David Bader, Vanderbilt University. Control and sample reactions were prepared as indicated in Table 2.3. Next, 1 μl of

Pfu Turbo DNA polymerase (2.5U/ μl) was added to each control and sample reaction. Each reaction was then overlaid with 30 μl of mineral oil. Each reaction was then cycled following the cycling parameters outlined in Table 2.4. Next, 1 μl of Dpn I restriction enzyme (10 U/ μl) was added below the mineral oil overlay. Each reaction was gently and thoroughly mixed and spun down in a microfuge for 1 minute and then immediately incubated at 37^{o}C for 1 hour to digest the parental supercoiled DNA. 1 μl of the Dpn I-treated DNA from each control and sample reaction was transformed into separate 50 μl aliquots of XL1-Blue supercompetent cells in pre-chilled 14ml Falcon polypropylene round bottom tubes. As a control, the transformation efficiency of the XL1-Blue supercompetent cells was verified by adding 1 μl of pUC18 control plasmid (0.1ng/ μl) to a 50 μl aliquots of XL1-Blue supercompetent cells. The transformation reactions were swirled gently to mix and incubated on ice for 30 minutes. Next, the transformation reactions were heat pulsed at 42ºC for 45 seconds and then placed on ice for a further 2 minutes. Next, 0.5ml of NZY+ broth was pre-heated to 42ºC and the transformation reactions were incubated at 37ºC for 1 hour while shaking at 220-250 rpm. Following incubation, 250 μl of each transformation reaction was plated onto agar plates containing ampicillin. For the mutagenesis and transformation controls, cells were spread onto

Table 2.1 Oligonucleotide primers used for *CENPF* sequencing.

Gene	Primer sequences (5' to 3')	Product size
CENPF Exon 2 F	GAAACTTGATTTTTAGGGGTGGT	324bp
CENPF Exon 2 R	AAATACCAGCACTTCTCTGTCAA	324bp
CENPF Exon 3 F	TGGCTTATTGCAGCTGTATCTC	417bp
CENPF Exon 3 R	ACGGTACAGAGACCGAATCA	417bp
CENPF Exon 4 F	CTCTGGGAATGTAAGGCATTG	387bp
CENPF Exon 4 R	GAATTTCTTTGAAAATATGCCACA	387bp
CENPF Exon 5 F	TGTGTTTTGATATTTGAGTAATTTGA	358bp
CENPF Exon 5 R	TGAGCCCAAAACCTTTTCTC	358bp
CENPF Exon 6 F	AACTTCTTGGGATTATGGCTTT	457bp
CENPF Exon 6 R	CGATGTGCCTAACAAAACACA	457bp
CENPF Exon 7 F	GAAAATCTGTTTCTCCTGCTTTC	546bp
CENPF Exon 7 R	CGGATCTGCCCAACTTAAAA	546bp
CENPF Exon 8 F	TTTTTCATGGCACAAATTAGGA	439bp
CENPF Exon 8 R	GCGCAAAAGTGAAGATGTGA	439bp
CENPF Exon 9 F	ACCTGGATTTGATGCCTGAG	448bp

CENPF Exon 9 R	GGAAACCTAGAGCCAGAATGG	448bp
CENPF Exon 10 F	GACGTCGCAAGGTCACATTA	443bp
CENPF Exon 10 R	GCAATCATATTCTGTCATGGGTTA	443bp
CENPF Exon 11 F	TTAATAGGCGTATGAACAATGAGAA	477bp
CENPF Exon 11 R	TTTCTCTAATATGTTAATGCCATCC	477bp
CENPF Exon 12A F	CCAAGTGATCCACTTTCTAGGAG	600bp
CENPF Exon 12A R	AACACGTTGTGAAGGTTTCTGA	600bp
CENPF Exon 12B F	AACTTGTCTGAAGACACAGCAAA	549bp
CENPF Exon 12B R	TTCATCTGTTTTTGAGACTCTAATGA	549bp
CENPF Exon 12C F	CTGCCATGCATCATTCCTTT	737bp
CENPF Exon 12C R	TCTTTTCCTGTGCTGCTTTG	737bp
CENPF Exon 12D F	CAGAGTTATCTGATCAGTACAAGCAA	672bp
CENPF Exon 12D R	TGCAAATTGCTGGTTTCAAG	672bp
CENPF Exon 12E F	CGCAGTTGGTGCAATTAGAA	413bp
CENPF Exon 12E R	CACCATGGAGAAGACCACTG	413bp
CENPF Exon 12F F	AAGAGGTAGGGAAACTACTAAATGAA	600bp
CENPF Exon 12F R	TCAGATTCTCCTCCTGCAGAC	600bp

CENPF Exon 12G F	TCTTGTGTGCCTGACAGC TC	662bp
CENPF Exon 12G R	TTGGTGTATTTTATTTCCT TGAACC	662bp
CENPF Exon 13A F	CCTGAATATTCTTAGCAA GGGAAA	592bp
CENPF Exon 13A R	CCCGCAGTTGAAGATTAT GG	592bp
CENPF Exon 13B F	GAAACCCACAGGAGAGT GCT	456bp
CENPF Exon 13B R	TTCACGTGATGATTTATC TGCAT	456bp
CENPF Exon 13C F	CAGGAGGTACAACTAATG ACCAAA	422bp
CENPF Exon 13C R	ATCCAGTGCCGTGGTTTT T	422bp
CENPF Exon 13D F	TGAGCATGAAGCCCTCTA CC	453bp
CENPF Exon 13D R	TGCAGGCTTTCAGATTCC TT	453bp
CENPF Exon 13E F	GGCAGAGGTGAAGGAAA AGA	389bp
CENPF Exon 13E R	GCTCCTGGTTTTCTTCTG ACA	389bp
CENPF Exon 13F F	ACACAGGAGGAAGTGCA TCA	446bp
CENPF Exon 13F R	GGGCTCTCAGCTTTTCAA TG	446bp
CENPF Exon 13G F	AAAACTGCAGTGGAGAT GCTT	393bp
CENPF Exon 13G R	TTCGCTCTTGCTCTTTTT GTAA	393bp

CENPF Exon 13I F	AGCCCTGCATAATGACCAAG	478bp
CENPF Exon 13I R	TGGTTTCCTGCCTCATGACT	478bp
CENPF Exon 14 F	TGTTGTATCAGAGTGGTCGATCT	262bp
CENPF Exon 14 R	GGAACCAATAAGGAGAGTGTGC	262bp
CENPF Exon 15 F	TGTACAGATTTTATCTTGCCCATAA	413bp
CENPF Exon 15 R	CTGGGGAAAAGATCGTGAAG	413bp
CENPF Exon 16 F	ACTGCGCCCAGCTGTTTT	352bp
CENPF Exon 16 R	TGATGAATGACATCATTTTTGACT	352bp
CENPF Exon 17 F	CGTGAATGGTTTTGTGCATC	432bp
CENPF Exon 17 R	GCACAAAATTCAGAAATTGGAA	432bp
CENPF Exon 18 F	CCCGAACAAGAGTTGTTTGAA	773bp
CENPF Exon 18 R	GGAAAACATATGCCTCATCCA	773bp
CENPF Exon 19 F	TGACCACAGTGGCTAGGACA	352bp
CENPF Exon 19 R	GTCCAATCCTCACCCAGGTA	352bp
CENPF Exon 20 F	GGGACGTCTGATGACTGGTT	454bp
CENPF Exon 20 R	TCCTGTAGGCACAGCCTTATC	454bp

LB-ampicillin agar plates containing 80 μg/ml of X-gal and 20mM IPTG. The transformation plates were incubated at 37ºC for 16 hours.

2.2.5 Immunolabelling techniques

2.2.5.1 Antibodies

The following antibodies and their dilutions were used. Mouse monoclonal anti-CENPF [1: 200; Abcam (catalogue number, ab 90)], rabbit polyclonal anti-IFT88 (1:800; Proteintech, catalogue number, 13967-1-AP), mouse monoclonal anti-NuMA (1:200; BD Transduction Laboratories, 610562), rabbit polyclonal anti-KIF3B (1:50; Abcam, ab42494), mouse monoclonal anti-acetylated-tubulin (1:800; Sigma-Aldrich, T6793 - clone 6-11B-1), mouse monoclonal anti-gamma-tubulin (1:500; Sigma-Aldrich, T6557), mouse monoclonal anti-GT335 (1:800; Novus Biologicals), anti-myc antibody (1:100, Sigma M4439), anti-Pericentrin (1:200; Abcam, ab4448), rabbit polyclonal anti-Ninein (1:200; Abcam, ab 4447), mouse monoclonal p150 ^{Glued} Dynactin (1:100; BD Transduction laboratories, catalogue number 612709), anti-Phospho-histone serine 10 (1:250, BD Transduction Laboratories) and anti-Cytokeratin 8 (1:100; Sigma). Alexa-488, Alexa-594 and Alexa-647 conjugated secondary antibodies were obtained from Invitrogen.

2.2.5.2 Preparation of cells for immunolabelling

For immuno-staining of NIH 3T3 fibroblasts, cells were seeded onto 18mm round glass coverslips (VWR International, catalogue number 631-053) and grown in DMEM +10% Foetal Bovine Serum + Penicillin/Streptomycin until they reached 70% confluency after which medium was replaced with DMEM without serum overnight. For immuno-staining of cilia, basal bodies and centrosomes, coverslips were fixed in 4% formaldehyde for 5 minutes. Following washing with 1x PBS, coverslips were incubated in 1% foetal bovine serum/PBS and washed again in 1xPBS. Coverslips were then incubated in ice cold acetone for 1 minute and were then rehydrated in PBS prior to blocking in 1% foetal bovine serum/PBS. Primary antibody incubations were performed at room temperature for one hour in 1% foetal bovine serum/PBS. Secondary antibody and DAPI incubations were performed for 1 hour at room temperature in 1% foetal bovine serum/PBS. Coverslips were mounted in Vectashield antifade reagent (Invitrogen).

2.2.5.3 Preparation of tissue sections for immunolabelling

For immunostaining of mouse and human kidney tissue, kidneys were dissected from wild-type mice and were fixed in 4% paraformaldehyde at

4ºC overnight. Murine kidneys were then dehydrated, embedded in wax and sectioned at 12 μm.

2.2.5.4 Tissue immunolabelling

Microwave antigen retrieval was carried out in citrate buffer in four 5-minute cycles at medium-hi setting (Panasonic NN-S758WC, 950W max. output) followed by a 20 minute cooling period at room temperature. Tissue sections were blocked in Universal Blocking Reagent (DAKO). For monoclonal incubations, sections were blocked in 5% goat serum for one hour. Primary antibody incubations were carried out at 4°C overnight. Biotin-conjugated secondary antibodies were diluted 1:1000 in blocking reagent, and incubated at room temperature. Primary antibody incubations were carried out simultaneously. AlexaFluor 488-, AlexaFluor 594-, or Cy5- conjugated secondary antibodies (1:1000; Invitrogen) were used for multi-immunofluorescence labelling. Sections were counterstained with DAPI, and imaged by fluorescence microscopy using a Zeiss Axioskop microscope with an EXFO X-Cite120 120W mercury vapour lamp (Photonics Solutions). Digital photographs were obtained as above, and merged images were obtained using Photoshop v6.0.

Table 2.2: Reaction mixtures for control and sample reactions for site-directed mutagenesis.

Reagents	Control Reaction	Sample Reaction
10x Reaction buffer	5µl	5µl
pWhitescript 4.5Kb control template (5ng/µl)	2 µl (10ng)	
dsDNA template		5-50ng
Oligonucleotide control primer #1 (100ng/ µl)	1.25 µl (125ng)	
Oligonucleotide control primer #2 (100ng/ µl)	1.25 µl (125ng)	
Oligonucleotide sample primer #1 (100ng/ µl)		1.25 µl (125ng)
Oligonucleotide sample primer #1 (100ng/ µl)		1.25 µl (125ng)
dNTP mix	1 µl	1 µl
ddH_2O	50 µl	50 µl

Table 2.3: Cycling parameters for site-directed mutagenesis reaction.

Segment	Cycles	Temperature	Time
1	1	95°C	30 seconds
2	12-18	95°C 55°C 68°C	30 seconds 1 minute 1 minute/kb length

2.2.6. Microscopy

2.2.6.1 Confocal microscopy

Confocal imaging was performed using a Zeiss LSM-710 system with an upright DM6000 compound microscope. Confocal imaging uses a pinhole to restrict further the volume of light detected to create an optical slice. The thickness of the optical slice may be changed by modifying the pinhole aperture diameter. Fluorescent immunolabelling of tissue was imaged with a 63 x objective using 488, 568 and DAPI filters. Images were processed with the Zen software suite. Z stacks were acquired at 0.5-μm intervals and converted to single planes by maximum projection with FiJi software.

2.2.6.2 ApoTome microscopy

ApoTome imaging was performed using a Zeiss HBO-100 system with a Zeiss Imager Z.1 and images were processed with the Axiovision software suite (version 4.8). ApoTome imaging uses a grid and an algorithim to create an optical slice. Optical slice thickness is fixed and depends on the wavelength and the numerical aperture of the objective. Images were taken with 20x, 40x and 63x objective. Fluorescent immunolabelling of tissue was imaged using 488, 568 and DAPI filters.

2.2.6.3 Electron microscopy

For immunogold labelling of RPE cells, cells were serum starved at 70% confluency for 3 days and then fixed in 0.25% glutaraldehyde + 4% formaldehyde in 0.1 M cacodylate buffer, pH 7.4, and processed for embedment in LR White. Ultrathin sections (70 nm) were labelled with primary antibody, followed by secondary antibody conjugated to 12 nm gold particles.

2.2.7 Protein techniques

2.2.7.1 Cell synchronisation studies

HEKT293, NIH 3T3 fibroblasts and RPE cells were grown under standard media conditions. Cells were serum-starved at 40-70% confluency for 72 hours. For mitosis block, cells were treated with 2mM

Thymidine at 40% confluency for 24 hours, released into standard media for 3 hours and then treated with Nocodazole 100ng/μl for a further 12 hours.

2.2.7.2 Protein lysis

On the day before protein lysis, HEKT293, NIH 3T3 fibroblasts or RPE cells were plated onto tissue culture 100mm (Corning Incorporated, catalogue number 430166) dishes with 10 mls of DMEM medium containing 10% FBS and 1% Penicillin/streptomycin. The following day, the medium was removed from the adhered cells, which were then washed with 1xPBS. Following removal of 1xPBS, 1ml of RIPA lysis buffer supplemented with protease inhibitors as follows: 50μl sodium orthovanadate, 200μl protease inhibitor cocktail (Sigma, P8340 AEBSF, 104mM Aprotinin, 80 μM Bestatin, 4mM E-64, 1.4mM Leupeptin, 2mM Pepstatin A, 1.5mM), 100 μl phenylmethanesulfonyl fluoride (PMSF) were added to the cells while the tissue culture dishes were placed on ice. Using sterile cell scrapers (Greiner BioOne), cells were scraped from the bottom of the tissue culture dish, while placed on ice, in the cold lysis buffer. 1ml of protein lysate per tissue culture dish was pipetted into a fresh 1.5ml Eppendorf tube on ice. Using an 18-guage needle and a 1 ml syringe, cells were further lysed in the Eppendorf tube by syringing the lysate 10 times. The Eppendorf tubes containing the lysates were then left

on ice and gently rocked for 15 minutes. Next, the Eppendorf tubes containing the lysates were placed in a microfuge at 4ºC and centrifuged at 14,000rpm for 15 minutes. The supernatant was then removed and placed in a fresh 1.5ml Eppendorf tube.

2.2.7.3 Quantification of protein

Protein content of cell lysates was quantified using a Pierec bicinchoninic acid (BCA protein assay kit (ThermoScientific, catalogue number 23225). Diluted albumin standards were prepared with 2mg/ml albumin standard ampoules (Table 2.5). Next the BCA working reagent was prepared by mixing 50 parts of BCA Reagent A with 1 part of BCA Reagent B (50:1, Reagent A:B). 10µl of each standard and unknown sample replicate was pipetted into each well of a 96-well plate. Then 200 µl of the BCA working reagent was added to each tube and mixed well. The plate was then covered and incubated at 37ºC for 30 minutes. The protein samples were added to the plate in triplicate. Protein quantification was then determined by its absorbance at 562 nm on a plate reader (MultiSKAN FC, ThermoScientific). The concentration of the protein was then calculated from the A562 value ($1A_{562}$ Unit= 500 µg/ml protein).

Table 2.4: Diluted albumin standards

	Volume of Diluent	**Volume and Source of BSA**	**Final BSA Concentration (µg/ml)**
Vial	µl	µl	µl
A	0	300 of stock	2000
B	125	375 of stock	1500
C	325	325 of stock	1000
D	175	175 of vial B dilution	750
E	325	325 of vial C dilution	500
F	325	325 of vial E dilution	250
G	325	325 of vial F dilution	125
H	400	100 of vial F dilution	25
I	400	0	0

2.2.7.4 Co-Immunoprecipitation studies

2.2.7.4.1 Antibody coupling with cell lysates

On the first day, 1 ml (1000mg/ml) of protein lysate was incubated with primary antibody (dilution 1:100) in a 1.5ml Eppendorf tube while rotating gently on a roller overnight at 4ºC.

2.2.7.4.2 Dynabeads

Prior to use, host-specific Dynabeads ® (Invitrogen, catalogue numbers 110.41, 112.03D) were completely resuspended by rotating on a roller for 5 minutes. Next, the Dynabeads were washed by pipetting 50 µl into a 1.5ml Eppendorf tube with 1ml of 1xPBS and gently rotating for 5 mins. Following each wash, the Eppendorf tubes containing the Dynabeads were placed in a magnet (Invitrogen, Dyna-Mag2™ device, catalogue number 123-21D) and the supernatant was removed. Following removal from the magnet, the Dynabeads were resuspended in 1ml of fresh PBS and the wash was repeated as before. Following the third wash, the lysates containing the Ag-Ab complexes were removed from their Eppendorf tubes and subsequently incubated with 50 µl of the washed host-specific Dynabeads, while rotating gently on a roller, overnight at 4ºC. The following day, the Eppendorf tubes containing the Dynabeads-Ab-Ag complexes were then placed in the magnet the supernatant was

removed with a pipette with care to avoid touching the bound Dynabeads and placed into a clean 1.5 ml Eppendorf tube on ice.

2.2.7.4.3 Protein denaturation

Prior to use, 50 µl of β-mercaptoethanol was added to 950µl of Laemmli Sample Buffer (BioRad). Fifty microlitres of protein lysate from both the supernatant and immunoprecipitates were placed in an equal volume of sample buffer and samples were mixed by gentle pipetting up and down. Next, proteins were then denatured by heating the samples containing the sample buffer for 5 min at 90ºC.

2.2.7.4.4 SDS-Page gel electrophoresis

Proteins of the desired molecular weights were separated by electrophorectic separation by SDS-polyacrylamide gel electrophoresis (SDS-Page). For proteins with a molecular weight within the range of 25-250kDa, 10% SDS-page gels were prepared as follows: (4mls H_2O, 3.3mls 30% Acrylamide, 2.5mls 1.5M Tris-HCl pH8.8, 100µl 10% SDS, 50µl 10% APS, 5µl TEMED). Cast gels were allowed to set between a short plate and a spacer plate (BioRad, Mini-PROTEAN Tetra Electrophoresis system, catalogue number, 165-8004). Once set, 4% stacking gel was prepared as follows: 3mls H_2O, 0.65mls 30% Acrylamide, 1.25mls 0.5M Tris-HCl pH 6.8, 50µl 10% APS, 5µl

TEMED) and poured on top of the set SDS-page gel. A ten prong comb (BioRad) was inserted into the stacking gel solution, which was then allowed to set. After solidifying, the set gels were then placed in a Mini-PROTEAN Tetra Electrophoresis system container with 1x Running Buffer. The first lane of the stacking gel was loaded with 20 µl of protein pre-stained standard (Precision Plus Protein Kaleidoscope Standard, BioRad, catalogue number 161-0375; MW 10-250kDa) with 1:1 Laemmli Buffer. Thirty microliters of denatured protein lysate were then loaded into each well of the stacking gel. The lid of the gel apparatus was then placed on top and was connected to the PowerPac TM HC power supply (BioRad) under constant voltage at 120V for 90 minutes until proteins were electrophoresed to the desired molecular weight as determined by the position of the protein ladder relative to the end of the SDS-page gel

2.2.7.4.5 Membranes

Immuno-Blot ® Polyvinylidene difluoride (PVDF) membranes (BioRad, catalogue # 162-0177) were used for protein electroblotting. Prior to electrophorectic transfer, PVDF membranes cut to the dimensions of the SDS-page gel (measuring 8cm x 6cm), were thoroughly soaked in 100% methanol for one minute and then washed in distilled water for a further minute before being thoroughly soaked and equilibrated in transfer buffer for 15 minutes.

2.2.7.4.6 Transfer

Proteins from the SDS-page gel were transferred to PVDF membranes by semi-dry electrophorectic transfer. Firstly, 6 sheets of Whatman filter paper per PVDF membrane, cut to the dimensions of the SDS-page gel (measuring 8cm x 6cm), were equilibrated with the SDS-page gel for 15 minutes in transfer buffer prior to electrophorectic transfer. On completion of protein electrophoresis to the desired molecular weight, the stacking gel was excised using a sharp scalpel from the SDS-page gel. In preparation for a semi-dry transfer, the transfer buffer was spread lightly over the surface of the platinum anode plate of the Trans-Blot SD Semi-Dry cell (BioRad). Next, three pieces of buffer-soaked Whatman filter paper were placed onto top of each other, and a plastic 19ml pipette was rolled over the surface of the filter paper to push out all air bubbles. Next, the pre-soaked membrane was placed on top with the protein standard on the left-hand side and air bubbles were further rolled out with the pipette. Next, the pre-soaked gel was then placed on top of the membrane so that it aligned with the centre of the membrane. Three further pieces of buffer-soaked Whatman filter paper were placed, one after the other, on top of the PVDF membrane. Any trapped air bubbles were further rolled out. Care was taken not to move the membrane or gel after it was positioned to avoid ghost prints or artifacts. The cathode plate was then carefully

placed on top of the stack. Next, the safety cover was placed back onto the unit. The cables of the Trans-Blot SD Semi-Dry cell were then connected to the PowerPac™ HC power supply (BioRad) under constant voltage at 12 V for 45 minutes. Upon completion of the run, the cathode assembly was removed and the gel and membrane sandwich was removed. The membrane was rinsed briefly in distilled water to ensure that no residual gel pieces or sample adhere to the membrane.

2.2.7.4.7 Blocking of transferred proteins

Protein transfer was determined by the presence of the clarity of the transferred protein ladder. The membrane was immersed in Ponceau stain for up to one hour with gentle agitation, after which the membrane was washed in distilled water to remove background. PVDF membranes with the transferred proteins were then placed in clean containers of proportionate size containing 5% nonfat dry milk to block unbound membrane sites while gently rocking for 1 hour at room temperature.

2.2.7.4.8 Primary antibody incubation

Protein interactions were assessed by immunoblotting onto PVDF membranes (Millipore), detected using primary antibodies (dilution 1:100) incubated overnight at 4ºC while gently shaking on a roller.

2.2.7.4.9 Secondary antibody incubation

Following overnight incubation with primary antibody at 4ºC, excess antibody was removed by washing the PVDF membranes in 1xPBS for 4 washes with each wash lasting 10 minutes. Next, the membranes were incubated with secondary rabbit and mouse- conjugated horseradish peroxidase (HRP) antibodies (dilution 1:2000) by gently shaking on a roller at room temperature for one hour.

2.2.7.4.10 Enhanced chemiluminescence detection

Following secondary antibody incubation, PVDF membranes were then washed in 1xPBS for 4 washes with each wash taking 10 minutes. Next, identification of specific proteins immunoblotted onto the PVDF membranes was detected by enhanced chemiluminescence (ECL System, Amersham Pharmacia Biotech; substrate, luminol). Reagent A was mixed with Reagent B in a 1:1 ratio and 2 mls were pipetted onto the PVDF membrane placed in a fresh clean container of proportionate size. The container was gently rocked by hand to ensure the entire PVDF membrane contained within was immersed in the developing solution for at least 1 minute. Using a forceps the edge of the PVDF membrane was gently lifted out of the container pouring off excess solution and was placed on a layer of clean dry Saran wrap so that the membrane was

positioned with the protein standard on the left hand side and the highest MW was superior whilst the lower MW was inferior. Another layer of clean dry Saran wrap was then placed on top of the PVDF membrane with care to avoid trapping of any bubbles underneath. The PVDF membrane covered in Saran wrap was then secured in a developing cassette so that the membrane was positioned with the protein ladder on the left hand side and the highest MW was superior whilst the lower MW was inferior.

2.2.7.4.10 Developing reagents & developer

Detection of the activated light signal was captured on X-ray film, which was placed on top of the PVDF membrane wrapped in Saran and exposure time varied between 30 seconds and 5 minutes depending on the antibody. Radiographs were processed using the Compact X4 processor (Xograph).

2.2.8 shRNA experiments

For CENPF gene knockdown, the ThermoScientific Open Biosystems pGIPZ Cenp-F (V3LMM_104294) and non-silencing control vectors (RHS4346) were used. RPE cells were cultured in DMEM:F12 1:1 in 10% FBS. 5 x 10^4 cells were seeded per well in 24-well dishes (plastic bottom) in triplicate, 24 hours prior to being transduced with 1 μg of

Cenp-F shRNA and 1 μg non-silencing control vector. One plate was harvested to determine knockdown efficiency by quantitative real-time PCR four days following transduction, another was harvested to determine knockdown efficiency by western blotting for Cenp-F protein at 6, 12, 24, 30 and 48 hours following knockdown.

2.2.9 Rescue experiments

Following determination of earliest point of Cenp-F depletion, RPE cells were transfected with either FLAG-CENPF-WT (kind gift from Xueliang Zhu, Shanghai Institutes for Biological Sciences), FLAG-CENPF-p.E582X or Nm-myc-CENPF $_{aa\ 1\text{-}474}$ (kind gift from David Bader, Vanderbilt University) plasmids by using Effectene ® transfection reagent (Qiagen). After 48 hours, cells were processed for quantitative real-time PCR and western blotting to confirm restoration of CENPF mRNA and protein. Cells were also fixed in 4% paraformaldehyde and immunolabelled with anti-acetylated tubulin and % cilia-positive nuclei were counted (n=700).

2.2.10 Analysis of ciliation

Ciliation was induced in NIH 3T3 fibroblasts and RPE cells following serum starvation (1% FBS) at 70% confluency for 72 hours. Immunolabelling of ciliary axonemes with anti-acetylated tubulin

antibody allowed for detection of ciliation. Percentage of ciliated cells compared to total cell number as determined by number of DAPI-positive nuclei were quantified. Measurement of cilia length was determined using the Simple Neurite tracer software programme following Z-stack projection of imaged micrographs.

2.2.11 Zebrafish studies

2.2.11.1 Zebrafish husbandry and embryogenesis

Wild type zebrafish, from AB x Tup LF were staged and housed as previously described (Westerfield et al., 1986). Groups of 25-50 stage-matched embryos were collected at 8 and 18-somite stages, 24 hours post fertilisation (hpf), 36hpf, 48hpf, 72hpf and 96hpf.

2.2.11.2 Morpholino injection

For *cenpf* knockdown, antisense morpholino oligonucleotides (MO) (GeneTools, LLC) were designed against the 25 base pairs upstream of transcript start codon of *cenpf* (Table 2.5).

Table 2.5: Morpholino sequences for zebrafish studies

Oligos	5'-3' sequence
ATG *cenpf* MO	TCCACTCTTCTACAGCCCAACTCAT
Splice *cenpf* MO	TGGAGTCTGAAAATGCAATATTTGA

Embryos were injected with MO (2ng/embryo) at the 1- to 2-cell stage and allowed to develop at 28.5°C to desired stages.

2.2.11.3 Whole-mount in situ hybridization

Groups of 25-50 stage-matched embryos were collected at 18-somite stages were fixed in 4% PFA/PBS overnight at 4ºC.

2.2.11.3.1 Probe linearisation

The vector containing the probe of interest was linearised using a restriction enzyme located at the 3' end of the cDNA insert. Electrophoresis of an aliquot of the digest on an agarose gel subsequently determined linearisation of the vector. The linearised plasmid was then excised from the agarose gel with a scalpel and thereafter was extracted using QIAGEN PCR purification kit. The gel slice was weighed and 3 volumes of Buffer QG to 1 volume of gel was added. During the 10 minute incubation of the gel at 50ºC, the gel was vortexed every 2-3 until the gel slice had completely dissolved. One volume of isopropranolol was

then added to the sample and mixed. The QIAquick spin column was placed in a 2ml collection tube and the sample was added to the QIAquick spin column and centrifuged for 1 minute. The flow-through was then discarded and the QIAquick column was placed back in the same collection tube. Next, 0.5ml of Buffer QG was added to the QIAquick column and centrifuged for 1 minute. Then, 0.75mls of Buffer PE was added to the QIAquick column and the sample was centrifuged for 1 minute. The flow-through was discarded and the QIAquick column was centrifuged for an additional 1 minute at 13,000 rpm. Next, the QIAquick column was placed into a clean 1.5ml microcentrifuge tube. DNA was eluted by adding 50µl of Buffer EB to the centre of the QIAquick membrane and the column was centrifuged for 1 minute. The concentration of DNA was then measured using the Nanodrop spectrophotometer as previously described.

2.2.11.3.2 Transcription

The linearised plasmid was transcribed with the appropriate enzyme (T3, T7 or SP6 polymerase). For a 20 µl reaction, 1 µg of DNA template was used as well as 20mM nucleotide mix, including digoxygenin (DIG) labeled-UTP, 40 units/ml of RNAse inhibitor, 10mM transcription buffer-containing dithiothreitol (DTT) and 20 units/ml of the appropriate

enzyme. This was incubated at 37ºC for 2 hours, upon which the probe was precipitated by addition of 100 µl ddH_2O, 8 µl of 5M LiCl, 1µl of glycogen and 300 µl of absolute alcohol and then incubating at -20ºC for 30 minutes to overnight. The probe was centrifuged at 4ºC for 15 minutes and washed firstly with 70% ethanol and then absolute alcohol. The pellet was dissolved in 15-45 µl of water for a final concentration of approximately 1mg/ml. The probe was denatured by heating to 95ºC for 3 minutes and diluted to a final concentration of 500-1000 ng/ml in hybridization buffer and stored at -20ºC until required.

2.2.11.3.3 Embryo pre-treatments

Following removal of 4% PFA/PBS by pipetting, fixed embryos were washed 4 times in PBTween 0.5% each wash lasting 5 minutes. After the last wash, embryos were then washed into 100% MeOH and incubated at -20ºC overnight. The following day, the embryos were then washed back into PBTween 0.5% for 5 washes, each wash lasting 10 minutes. Following the last wash, the embryos were then washed into Hybe:PBTween 0.5% at a ratio of 1:1.

2.2.11.3.4 Hybridization

The embryos were then incubated for 1 hour at 65ºC in 100% Hybe containing yeast tRNA and heparin (see below) in an Eppendorf tube with gentle rocking in a Hybe oven. Next, the Hybe was removed by

pipetting and replaced with the riboprobe of choice at a dilution of 1:200 to 1:600 and the embryos were incubated with the riboprobe at 65ºC overnight. The following day, the embryos were washed in Hybe buffer, 2xSSC followed by 0.2xSSC in the 65ºC Hybe oven and then at room temperature.

2.2.11.3.5 Post-hybridization washes

Following the last wash, the embryos were washed in 1xMAB and incubated in blocking solution (Boehringer block 2% w/v) for 1 hour at room temperature with gentle shaking. After blocking, the embryos were incubated with anti-digoxigenin labelled antibody (Roche Applied Science, catalogue number, 11093274910) diluted in blocking buffer (dilution 1:2000) in 4ºC overnight on a rolling platform.

2.2.11.3.6 Developing

The following day, the embryos were washed in 1xMAB for 8 washes, each wash lasting 15 minutes. Next, to develop the staining, the embryos were incubated in nitro-blue tetrazolium chloride/5-bromo-4-chloro-3'-indolyphosphate p-toluidine salt (NBT/BCIP) solution in the dark until an insoluble black-purple precipitate forms, as a result of NBT/BCIP reaction with AP. After the colour had developed, the reaction was stopped by washing twice for 10 minutes in 1xTBST. The embryos were post-fixed in 4% PFA/PBS for 30 minutes at room temperature.

2.2.11.3.7 Solutions for in situ hybridization

1x PBS	137mM NaCl, 3mM KCl, 10mM Na_2HPO_4, 1.8mM KH_2PO_4, pH 7.2
1x PBT	1x PBS + 0.1% Tween-20
Hybridization buffer	50% Formamide, 5x SSC pH 4.5, 50µg/ml tRNA,1% SDS,50µg/ml heparin
Washing solution 1	50% Formamide, 5x SSC pH 4.5
Washing solution 2	50% Formamide, 2x SSC pH 4.5
10x TBST	1.4M NaCl, 27.0mM KCl,250.0mM Tris-HCl
Blocking buffer	Boehringer block 2% w/v
NTMT	100mM NaCl, 100mM Tris-HCl pH 9.5,50mM $MgCl_2$, 1% Tween-20
NBT	75mg/ml in 70% DMF
BCIP	50mg/ml in 100% DMF
Staining solution	NTMT+ 4.5µl/ml NBT+3.5µl/ml BCIP

2.2.12 Statistical analysis

Statistical analyses were performed in GraphPad Prism version 5 (GraphPad Prism Software Inc, USA). Numbers were reported as median values and comparison was made using the two sample Wilcoxon rank sum test where the data was not normally distributed. The empirical distribution of normally distributed data (the histogram) should be bell-shaped. Numbers were reported as mean values and comparison was made using the Student's t-test where the data was normally distributed. $p < 0.05$ was considered statistically significant.

CHAPTER 3. MUTATIONS IN HUMAN *CENPF* CAUSE A NEW CILIOPATHY SYNDROME

3.I INTRODUCTION

Historically, the genetic basis of human disease has been classified as either monogenic and rare or polygenic and common. Monogenic diseases are a group of rare diseases accounted for by a mutation in a single gene (of about 25,000 genes). Currently, allelic variants have been identified in only about 3,000 of nearly 5,400 known Mendelian disorders, thereby leaving the remaining 2,400 unaccounted for (Bamshad et al., 2011). Several factors have historically limited more traditional gene-discovery strategies (Antonarakis and Beckmann, 2006) which include a small number of affected individuals or kindreds, low penetrance, locus heterogeneity and an inability to reliably reproduce results. Therefore, the recent discovery of novel genomic technologies that involve deep sequencing of all human genes for discovery of pathogenic variants could potentially assist the discovery of new genes underlying any rare monogenic disorder. Owing to the fact that about 85% of all disease-causing mutations in Mendelian disorders are within coding exons, the recent application of massive parallel deep-sequencing with exon capture has shown the efficacy of this technique for the rapid identification of mutations in single-gene disorders (Choi et al., 2009; Ng et al., 2008). Exome sequencing involves the targeted resequencing of all protein-coding sequences, which requires 5% as much sequencing as a whole human genome (Ng et al., 2009). As the majority of Mendelian disorders are due to mutations that disrupt protein-coding sequences, the use of exome capture to identify allelic variants in

rare monogenic disorders is well justified. Furthermore, highly functional variation can also be accounted for by changes in splice acceptor and donor sites, sequences of which, will also be targeted by exome capture. Exome sequencing has led to the genetic identification of over 180 Mendelian disorders over the past 3 years (Bamshad et al., 2011; Gilissen et al., 2011). Also beginning to emerge as a consequence of next generation sequencing strategies is the molecular basis of novel and rare developmental phenotypes (Glazov et al., 2011).

According to population-based registries of congenital anomaly in Europe, birth defects affect 1 in every 40 pregnancies with 360,000 new cases arising every year (Dolk et al., 2010). Foetal malformation syndromes account for 20% and investigation thereof, represent a unique opportunity to explore the molecular mechanisms of critical processes involved in human embryogenesis. Consequences of a greater understanding of how the human embryo develops, should provide mechanistic insight into foetal re-programming strategies in certain disease contexts. Therefore, in the era of regenerative medicine, it seems particularly timely that personalised genomics can greatly facilitate the elucidation of novel molecular mechanisms underlying lethal developmental phenotypes.

In the current study, we employed whole exome capture coupled with massive parallel, deep sequencing to identify mutations in human *CENPF* as the genetic defect underlying a novel developmental phenotype.

3.2 RESULTS

3.2.1 Exome capture of a single affected case is sufficient to identify the genetic aetiology of a novel phenotype

A nonconsanguineous kindred consisting of six offspring of which four foetuses exhibited intrauterine death during the second trimester of pregnancy (Figure 3.1). All affected foetuses were dysmorphic with craniofacial features that included a high nasal bridge, short columella, micrognathia, wide mouth and low-set ears (Figure 3.2). Of note, neither parent nor two unaffected siblings exhibited dysmorphic features. Autopsy findings revealed underlying systemic malformations that included cerebellar vermis hypoplasia, corpus callosum agenesis, cleft palate, duodenal atresia and bilateral renal hypoplasia (Table 3.1). A search of several validated dysmorphology databases including the Winter-Baraitser Dysmorphology Database (WBDD) failed to show phenotypic identity with any known syndrome. While there was some overlap with syndromes such as Fryns Syndrome, Miller-Dieker lissencephaly and Feingold syndrome (Table 3.2), the craniofacial features were not typical of that described with Fryns and neither did the foetuses exhibit any terminal phalangeal hypoplasia, congenital diaphragmatic hernia nor pulmonary hypoplasia. Cytogenetic studies of the placenta, muscle and cartilage did not reveal any abnormalities.

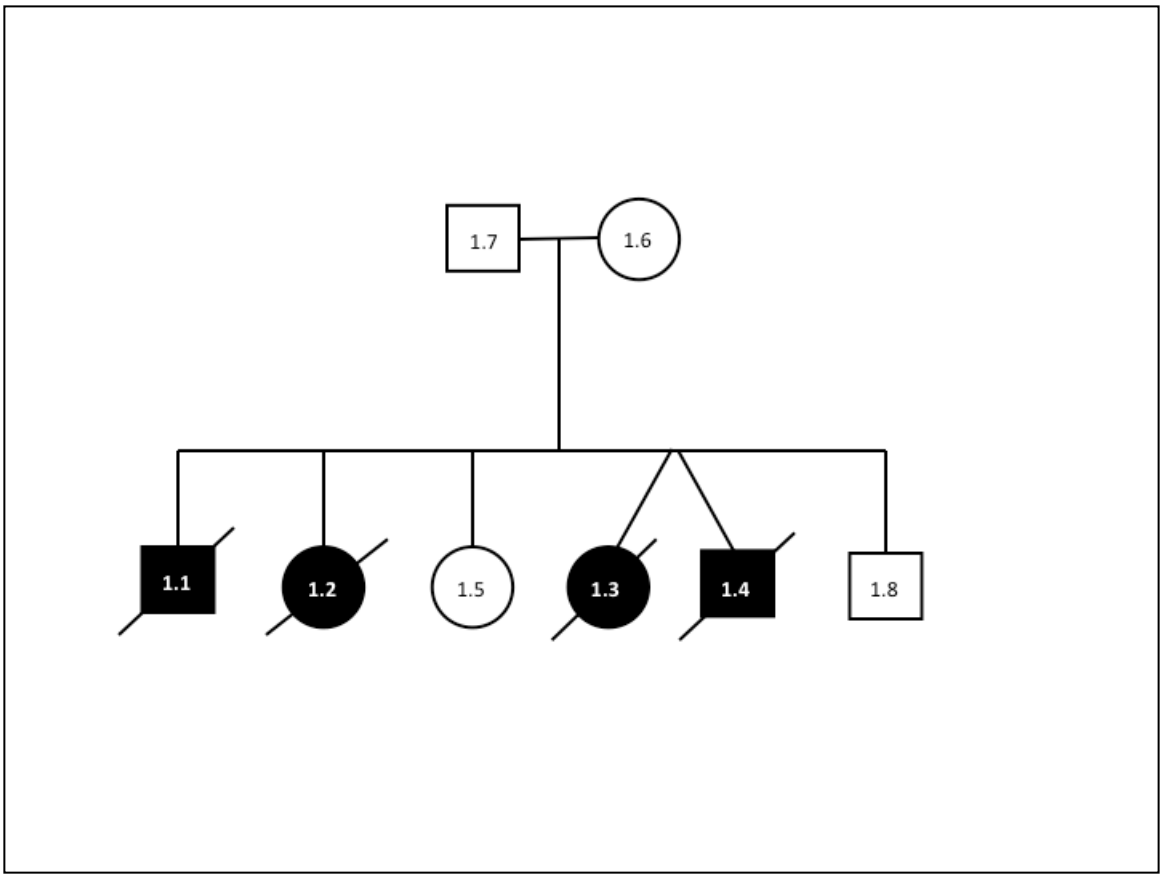

Figure 3.1: *Pedigree of novel ciliopathy phenotype.* A single kindred consisting of nonconsanguineous parents with six offspring, of which, four were affected and died *in utero* and two were unaffected and are healthy.

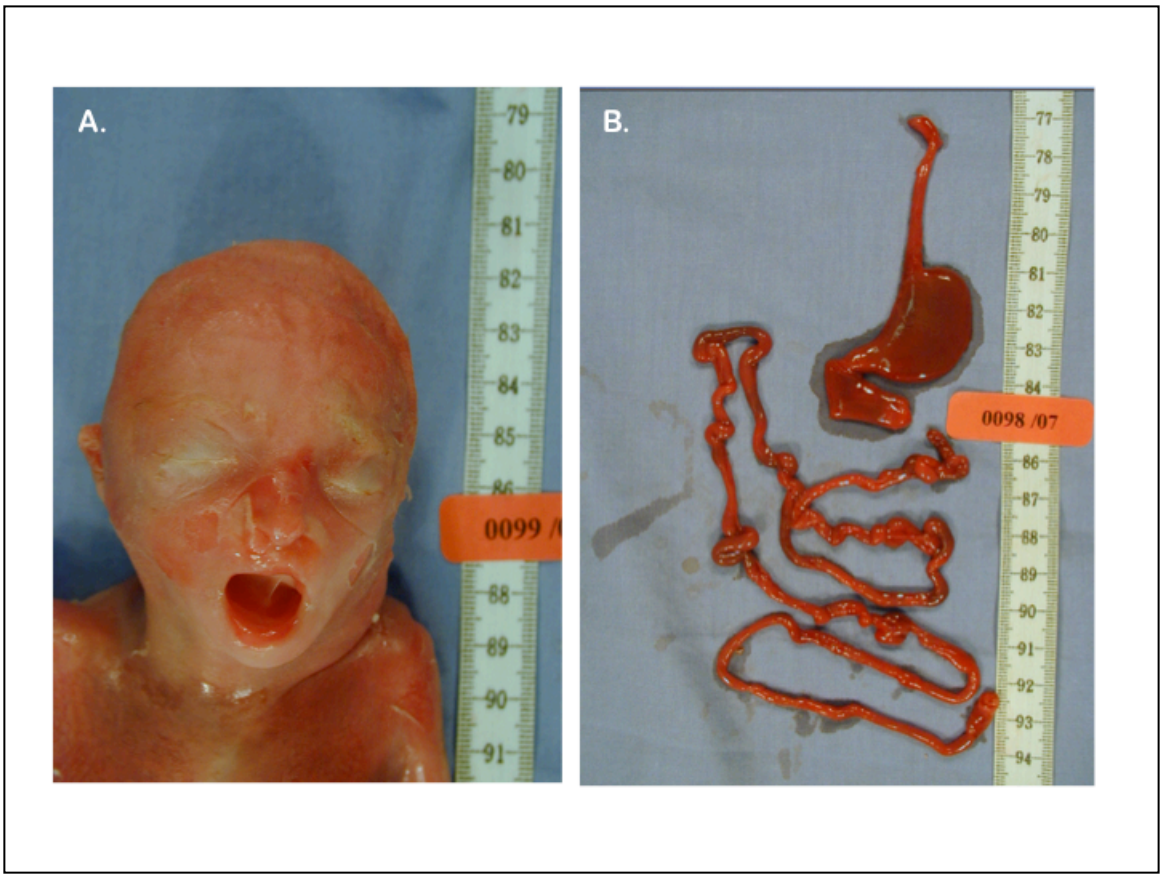

Figure 3.2: *Gross morphological features of an affected foetus.* (A) Dysmorphic craniofacial features included a high nasal bridge, short columella, micrognathia, wide mouth and low-set ears (B) Gross morphological examination of dissected gastrointestinal tract from the same affected foetus revealed complete duodenal atresia (Photos courtesy of Dr Charu Deshpande).

Table 3.1: Clinical characteristics of genotyped subjects

Status*	Cerebral	Cranio-facial	Gastrointestinal	Genitourinary
1.5 XX	Normal	Normal	Normal	Normal
1.8 XY	Normal	Normal	Normal	Normal
1.1 XY TOP 21wk	Hydrocephalus Cerebellar hypoplasia Agenesis of corpus callosum	Cleft palate Micrognathia Rounded head Low set ears	Duodenal atresia	Bilateral renal hypoplasia
1.2 XX IUD 17wk	Hydrocephalus	Prominent nose High nasal bridge Short columella Wide mouth	Duodenal atresia	Bilateral renal hypoplasia
1.3 XX Twin1 IUD 22wk	Hydrocephalus Agenesis of corpus callosum	Cleft palate	Duodenal atresia Malrotation Accessory spleens	Bilateral renal hypoplasia
1.4 XY Twin 2 IUD 22wk	Hydrocephalus Agenesis of corpus callosum	Microcrania Hypertelorism Broad nasal root Low set ears	Duodenal atresia Multiple SI** atresia Malrotation	Bilateral renal hypoplasia

Affected or unaffected; ** SI= small intestine

Table 3.2: Differential diagnoses for novel phenotype

Characteristics	Subject Syndrome	Fryns Syndrome OMIM 229850	Miller-Dieker Lissencephaly OMIM 247200	Feingold Syndrome OMIM 164280
Genetic Findings	*CENPF* mutations	1q41q42 microdeletion	*LIS1* mutations	1. *MYCN* Mutations 2.*MIR17HG*
Microcephaly	√	√	√	√
Brain Abnormalities	√	√	√	
Growth Retardation	√	√	√	√
Downslanting palpebral fissures	√			
Microretrognathia	√	√	√	√
Ear anomalies	√	√	√	√
Anteverted nostrils		√		√
Depressed Nasal Bridge	√	√		√
Broad nasal tip		√		
Hypertelorism	√	√	√	
Prominent philtrum			√	
Cleft palate	√	√		
CDH*		√		
CHD**		√	√	√
Limb shortening		√		
Clubfoot				
Short fingers	√	√		√
Nail/terminal phalanges hypoplasia		√		
Gastrointestinal malrotations & multiple atresias	√	√	√	√
Renal Malformations	√	√		√
Hydrocephalus	√	√		
Cerebellar Malformations	√	√		
Coarse facies		√		
Hypoplastic thorax		√		
Urogenital anomalies		√	√	

* CDH= congenital diaphragmatic hernia; ** CHD=congenital heart disease

Genome-wide single nucleotide polymorphism (SNP) analysis using high density SNP arrays (Affymetrix 500k Marshfield version 2) was undertaken on all except one member (CIL 1.1). Linkage analysis using GENEHUNTER version 2.1 lr5 (Multipoint) revealed ten regions with a maximum positive HLOD of 1.32. Linked intervals were identified on Chromosome 1 (2 intervals), 2, 6, 7, 8, 13, 19, and 20. One of the intervals on Chromosome 1 and the interval on Chromosome 19 were the largest and contained the most homozygous markers covering a total 839 genes. Using IBD Finder, significant regions of homozygosity were not present, consistent with declared non-consanguinity. We prioritised candidate genes based on their presence in the ciliome (www.ciliaproteome.org Version 3) and excluded mutations in eight transcripts including *TUBB4, WDR63, DNAJB4, CENPJ, MCPH6* and *RFX2*.

Given that the linked regions were large, spanning up to 33Mb on chromosome 1 and the recent success of whole exome capture and consecutive massive parallel deep sequencing for gene identification (Figure 3.3), I undertook exome capture of one affected and one unaffected offspring as a strategy to identify the underlying genetic aetiology of this novel phenotype (Methods).

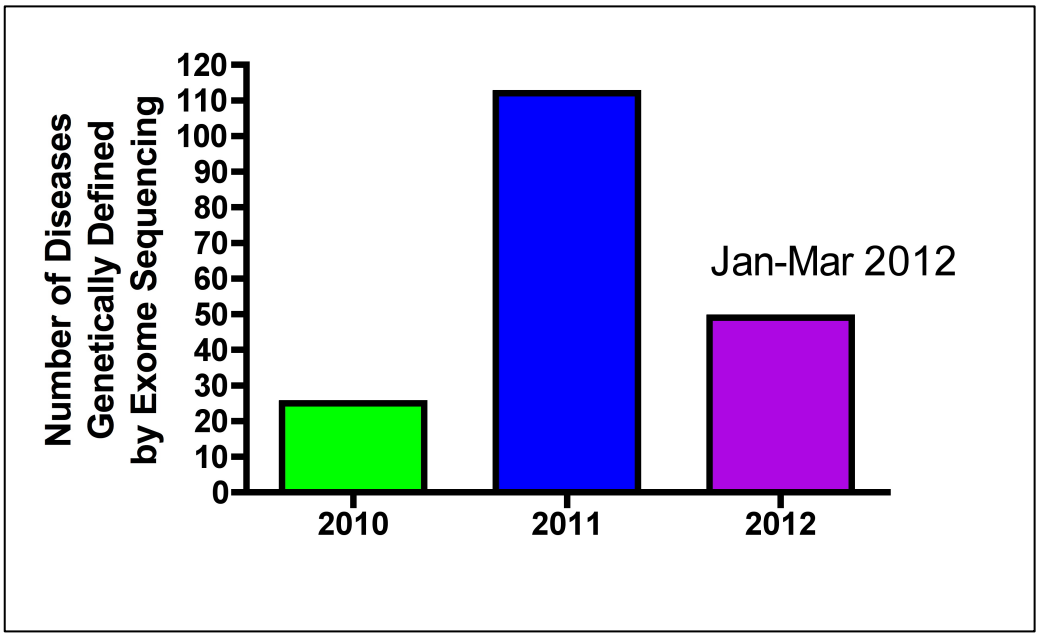

Figure 3.3: *Increasing number of genetically defined Mendelian disorders diagnosed by exome sequencing strategies.* Twenty five disorders were defined genetically in 2010. In 2011, another 112 disorders were identified by exome analysis. For the first 3 months of 2012, the genetic aetiology of 48 diseases has been uncovered.

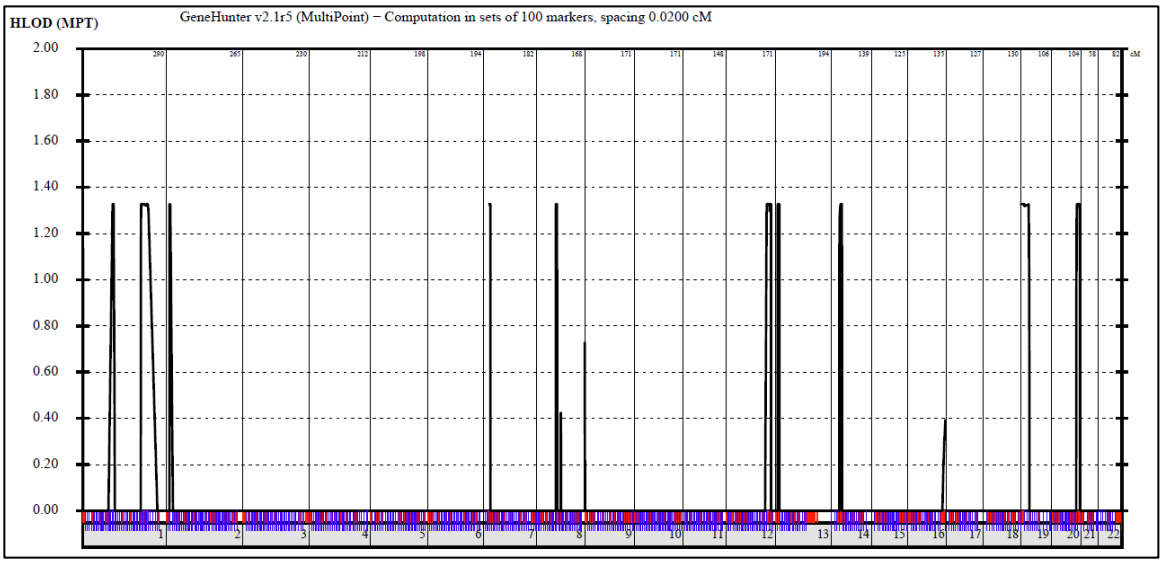

Figure 3.4: *Manhattan plot of multipoint linkage analysis in a kindred with novel ciliopathy phenotype.* Ten chromosomal regions were identified with a positive LOD score. Linked intervals were identified on Chromosome 1 (2 intervals), 2, 7, 8, 12, 13, 14, 16, 19, and 20. One of the intervals on Chromosome 1 and the interval on Chromosome 19 were the largest and contained the most homozygous markers covering a total 839 genes. Plot derived from GENEHUNTER version 2.1 (Kruglyak et al., 1996).

Variants were prioritised for analysis on the basis of novel coding loss of function variants (predicted to severely disrupt protein coding genes): nonsense variants, splice-site disrupting variants, frameshift insertions or deletions, missense variants (Table 3.3). A further variant filtering strategy based on an autosomal recessive mode of inheritance, as suggested by the pedigree, identified 2 novel homozygous and 40 novel compound heterozygous mutations in 20 genes that were unique to the affected offspring (Table 3.3). Only 1 of the 22 candidate genes, were present in a linked interval which was located on chromosome 1.

3.2.2 Compound heterozygous mutations of human *CENPF* cause a novel syndrome

Two novel pathogenic variants were found in the *CENPF* gene (NM_016343.3), involving a heterozygous splice-site mutation in intron 5 (IVS5-2A>C) that was predicted to abolish the consensus splice-acceptor site from exon 6 (Figure 3.5.1, Figure 3.5.2) and a second heterozygous nonsense substitution (c.1744G>T; encoding p.E582X; NP_057427.3) (Figure 3.5.3). The truncating mutation in exon 12 was predicted to be “probably damaging” by PolyPhen (Figure 3.4.4).

Table 3.3: Prioritisation of variant analysis

	Foetus 1.2 (Affected)	Foetus 1.5 (Unaffected)
Total Reads	43, 376, 158	43, 379, 788
Mappable Reads	39, 220, 720	40, 429, 960
Mean Coverage (x)	29.95	24.27
Total variants called	42, 606	48, 254
Novel variants	10, 432	10, 970
Exonic + Disruptive Splice Site (Phred>50)	4, 112	4, 306
Nonsense, Disruptive Splice Site, Frameshift InDels & Missense	648	656
Homozygous	3	4
Compound Heterozygous	24 (48 variants)	17 (34 variants)
Unique to sample Homozygous	2	3
Unique to sample Compound Heterozygous	20 (40 variants)	12 (24 variants)
Linked regions	1	
Segregation analysis	1	

Figure 3.4.5 describes the locations of the mutated base pairs in the genomic DNA, cDNA and amino acid sequence. Sanger sequencing of both variants confirmed segregation with affected offspring and revealed that each parent carried a single variant (Figure 3.6). Neither variant was detected in 200 ethnically matched control alleles, further supporting the concept of pathogenicity. Furthermore, neither variant was identified in 200 control in-house exomes. With RT-PCR, I confirmed altered splicing of *CENPF* RNA in the heterozygous parent compared to an unrelated control individual (Figure 3.7). Sequencing revealed that the affected allele introduced a frameshift resulting in a premature stop codon at amino acid position 202. (p.K191fs202). The mutated amino acid sequence is highly conserved amongst vertebrates (Figure 3.8). Human *CENPF* consists of 20 coding exons that generate at least two protein-coding transcripts (as determined in Ensembl, Table 3.4).

Table 3.4: Protein coding transcripts for *CENPF*

Name	Transcript ID	Length (bp)	Protein ID	Length (aa)
CENPF-001	ENST00000366955	10307	ENSP00000355922	3114
CENPF-201	ENST00000391896	525	ENSP00000375766	175

The small transcript (ENST00000391896) is protein coding, as is the long transcript (ENST00000366955). The small transcript comes from an alternative transcription start within the intron of the long transcript (between exon 13 and 14). The small transcript is sharing 3 exons with the long transcript (exons 14/15/16 are similar to exons 3/4/5 in the short transcript). *CENPF* encodes a 350kDa protein consisting of 3114 amino acid residues (Figure 3.9). Cenp-F is required for kinetochore-microtubule interactions and spindle checkpoint function (Yang et al., 2003) (Figure 3.10). Cenp-F was first characterised as a kinetochore (KT)-interacting protein, which has since been shown to have a dynamic localisation pattern throughout the cell cycle (Liao et al, 1995), (Figure 3.11). In G2, Cenp-F is predominantly nuclear and binds to the nuclear envelope at the transition between G2 and M. In early prophase until anaphase onset, it is found at the KT, the attachment point for the microtubule (MT) network at the centromere. In early anaphase, it is found at the spindle midzone while in late anaphase, it migrates with dynein to the spindle poles. In early G0, it undergoes proteasome degradation (Varis et al., 2006). Previous studies have revealed many different domains, binding partners and functions of Cenp-F, which include microtubule-binding domains, kinetochore-binding domains and Nde1-binding domains. In Chapter 4, I will discuss novel functions for Cenp-F that helps explain the phenotype observed in the affected foetuses carrying *CENPF* mutations.

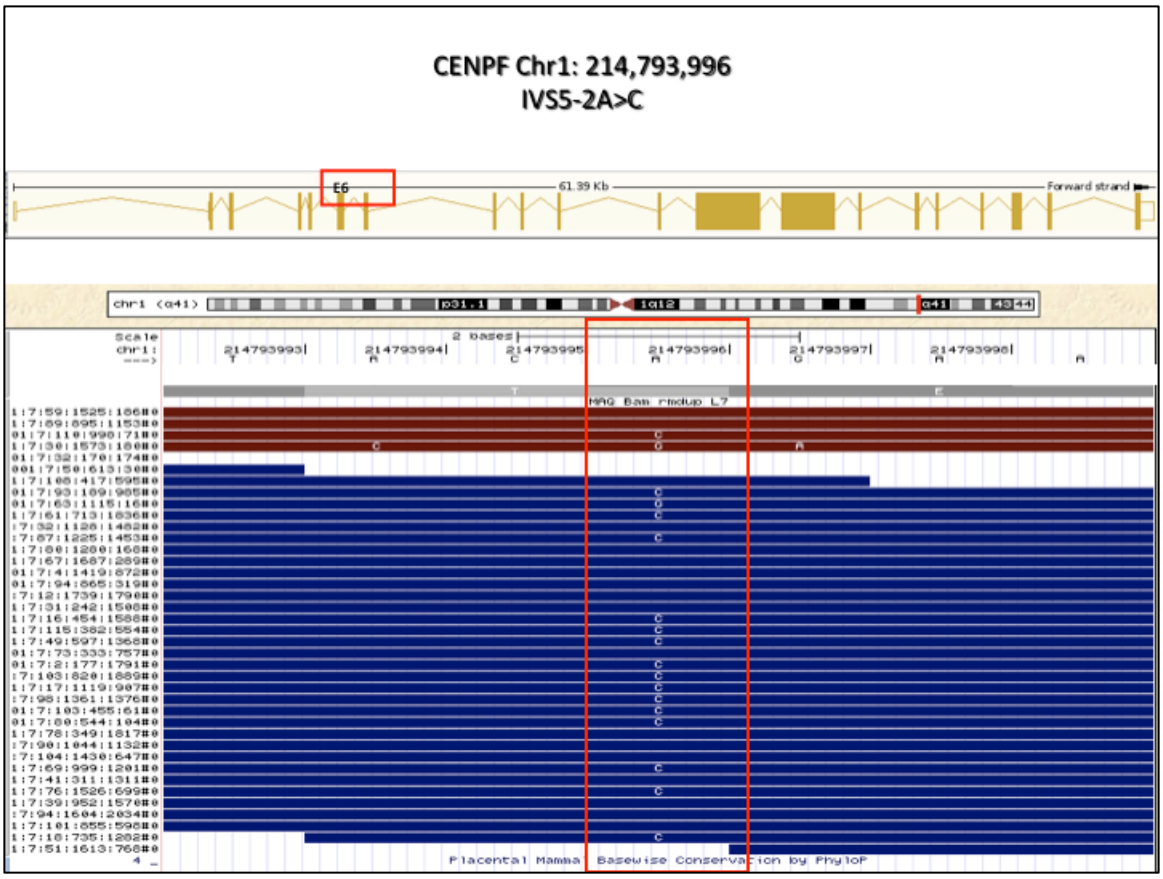

Figure 3.5.1: Representation of a BAM file demonstrating a heterozygous essential splice site nonsynonymous mutation, IVS5-2A>C at the splice acceptor site of human *CENPF* at a depth of 36x coverage. Blue lines represent forward reactions while maroon lines represent reverse reactions.

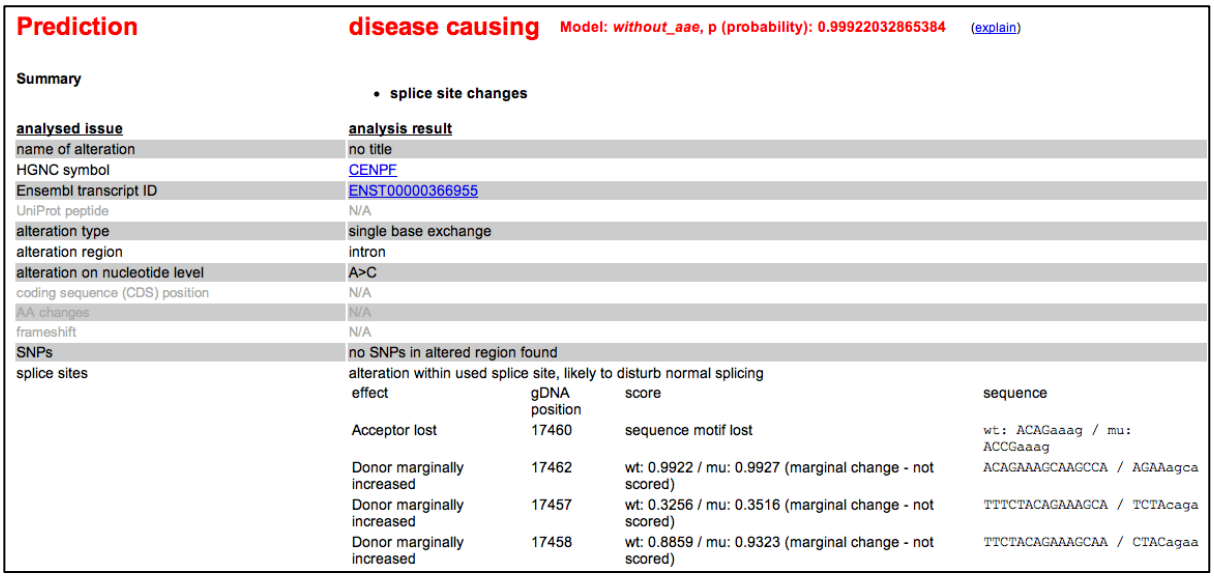

Prediction **disease causing** Model: *without_aae*, p (probability): 0.99922032865384 (explain)

Summary

- **splice site changes**

analysed issue	**analysis result**
name of alteration	no title
HGNC symbol	CENPF
Ensembl transcript ID	ENST00000366955
UniProt peptide	N/A
alteration type	single base exchange
alteration region	intron
alteration on nucleotide level	A>C
coding sequence (CDS) position	N/A
AA changes	N/A
frameshift	N/A
SNPs	no SNPs in altered region found
splice sites	alteration within used splice site, likely to disturb normal splicing

effect	gDNA position	score	sequence
Acceptor lost	17460	sequence motif lost	wt: ACAGaaag / mu: ACCGaaag
Donor marginally increased	17462	wt: 0.9922 / mu: 0.9927 (marginal change - not scored)	ACAGAAAGCAAGCCA / AGAAagca
Donor marginally increased	17457	wt: 0.3256 / mu: 0.3516 (marginal change - not scored)	TTTCTACAGAAAGCA / TCTAcaga
Donor marginally increased	17458	wt: 0.8859 / mu: 0.9323 (marginal change - not scored)	TTCTACAGAAAGCAA / CTACagaa

Figure 3.5.2: *Pathogenicity prediction of IVS5-2A>C CENPF mutation.*

CENPF mutation IVS5-2A>C is likely to disturb normal splicing with loss of *CENPF* acceptor site.

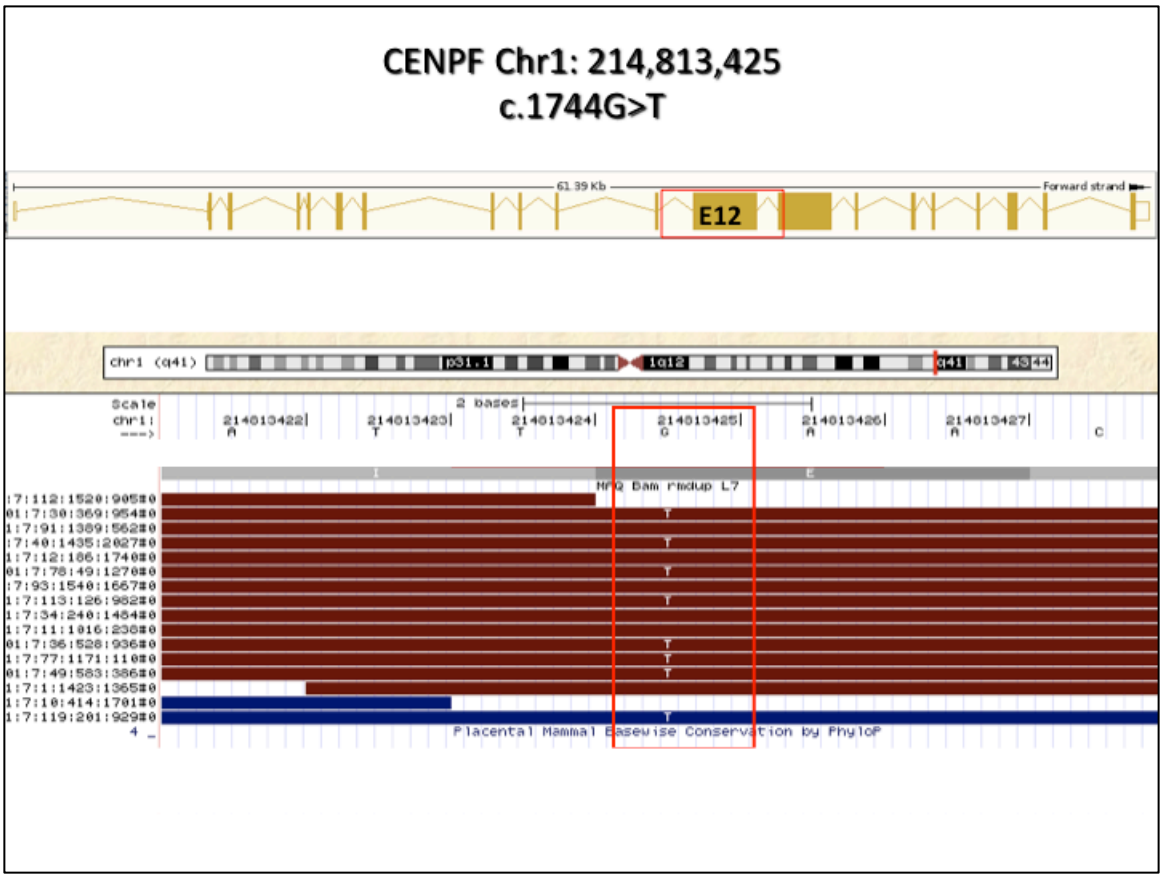

Figure 3.5.3: Representation of a BAM file demonstrating a heterozygous nonsynonymous mutation, c.1744G>T in exon 12 of human *CENPF* at a depth of 13x coverage.

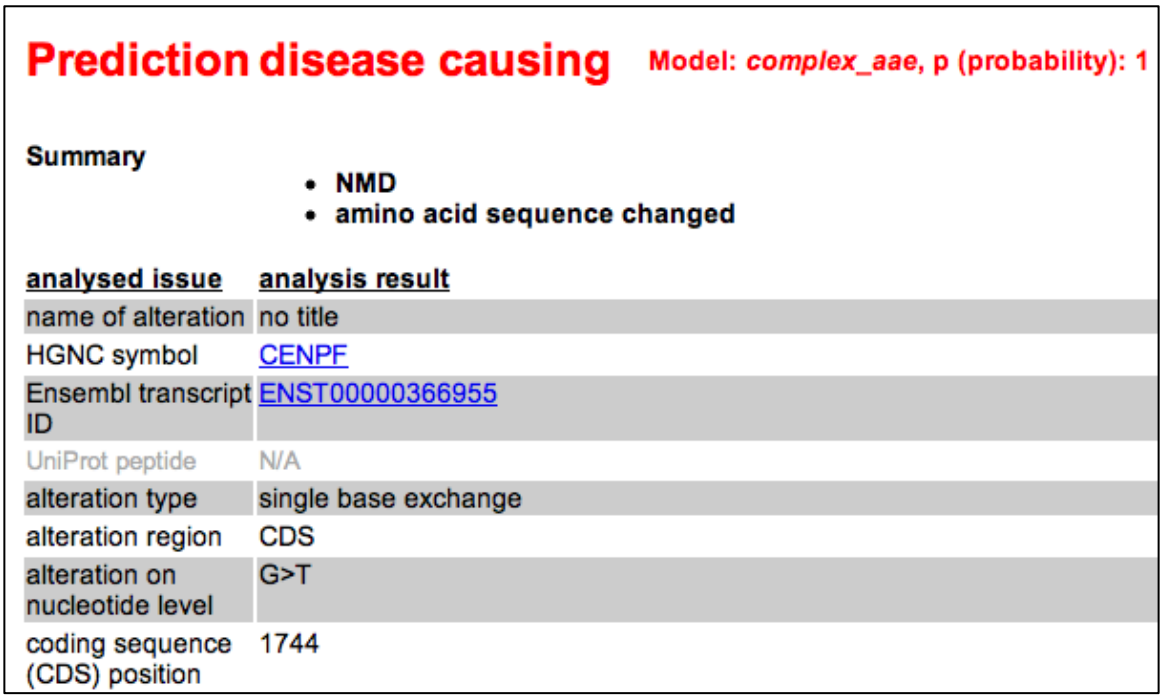

Prediction disease causing Model: *complex_aae*, p (probability): 1

Summary

- **NMD**
- **amino acid sequence changed**

analysed issue	analysis result
name of alteration	no title
HGNC symbol	CENPF
Ensembl transcript ID	ENST00000366955
UniProt peptide	N/A
alteration type	single base exchange
alteration region	CDS
alteration on nucleotide level	G>T
coding sequence (CDS) position	1744

Figure 3.5.4: *Pathogenicity prediction of c.1744G>T CENPF mutation.*

CENPF mutation c.1744G>T is predicted to have deleterious consequences and results in a premature stop codon at p.E582X.

Figure 3.5.5: *Mutated amino acids resulting from mutations in CENPF*. (a) The heterozygous mutation, IVS5-2A>C affects the essential splice acceptor site of human *CENPF* at lysine (K) residue. (b) The heterozygous truncating mutation, c.1744G>T results in a premature stop codon at glutamic acid (E) residue, 582 of human *CENPF*. Top rows represent position on genomic DNA, middle row represents position in cDNA and last row represents position in protein sequence.

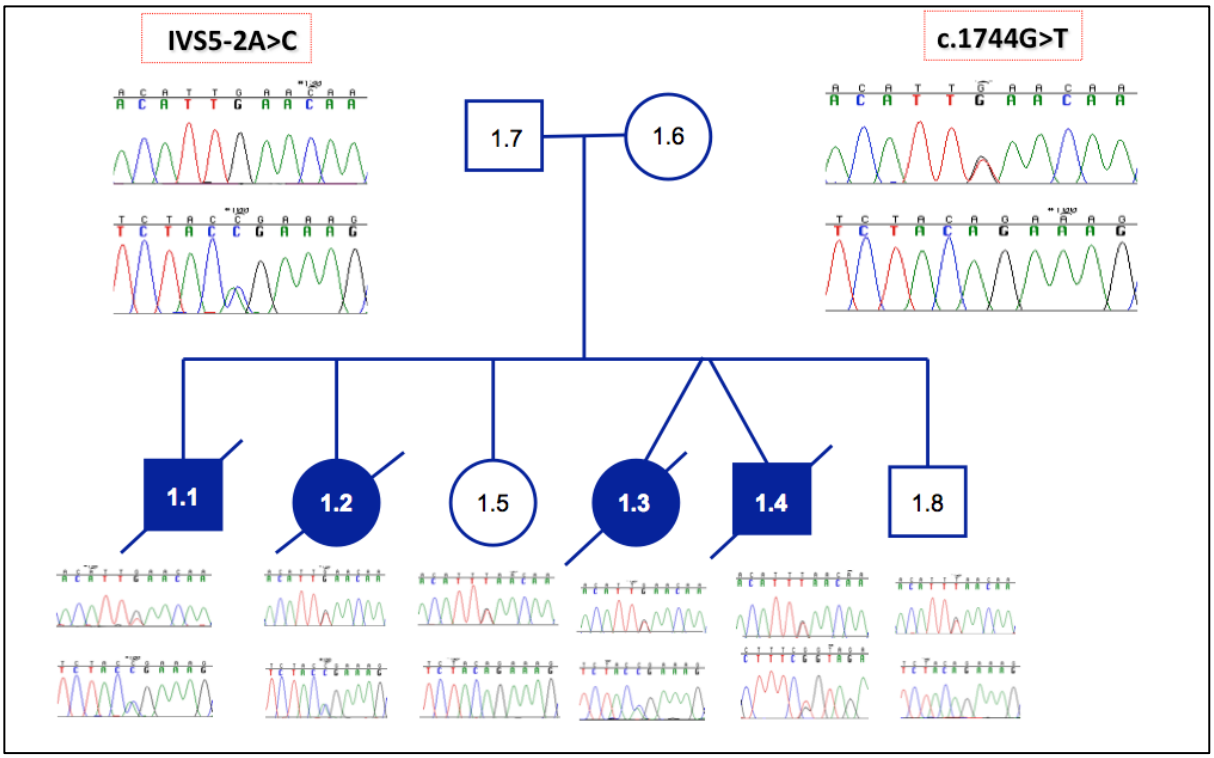

Figure 3.6: *Segregation of compound heterozygous mutations in CENPF.*

The heterozygous essential splice site nonsynonymous mutation, IVS5-2A>C segregates to the unaffected father while a heterozygous nonsynonymous nonsense mutation, c.1744G>T segregates to the unaffected mother and two unaffected siblings. Both mutations are present in all four affected foetuses.

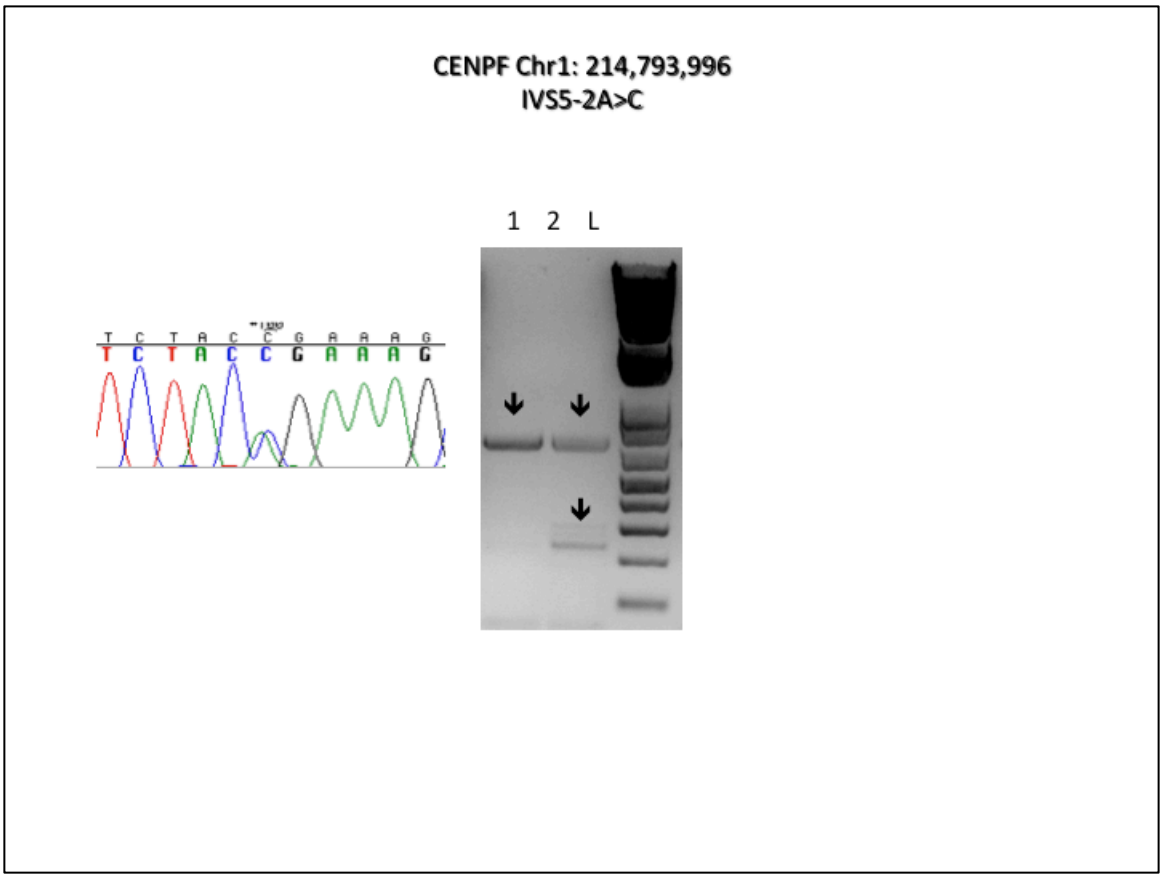

Figure 3.7: *Altered splicing in CENPF variant IVS5-2A>C.*

Effect of the splice-site mutation on the RNA of the heterozygous father shows two different products of equal intensity in lane 2 (650 bp and 230 bp for the upper and lower band, respectively). Lane 1 shows the product of an unrelated control (650 bp).

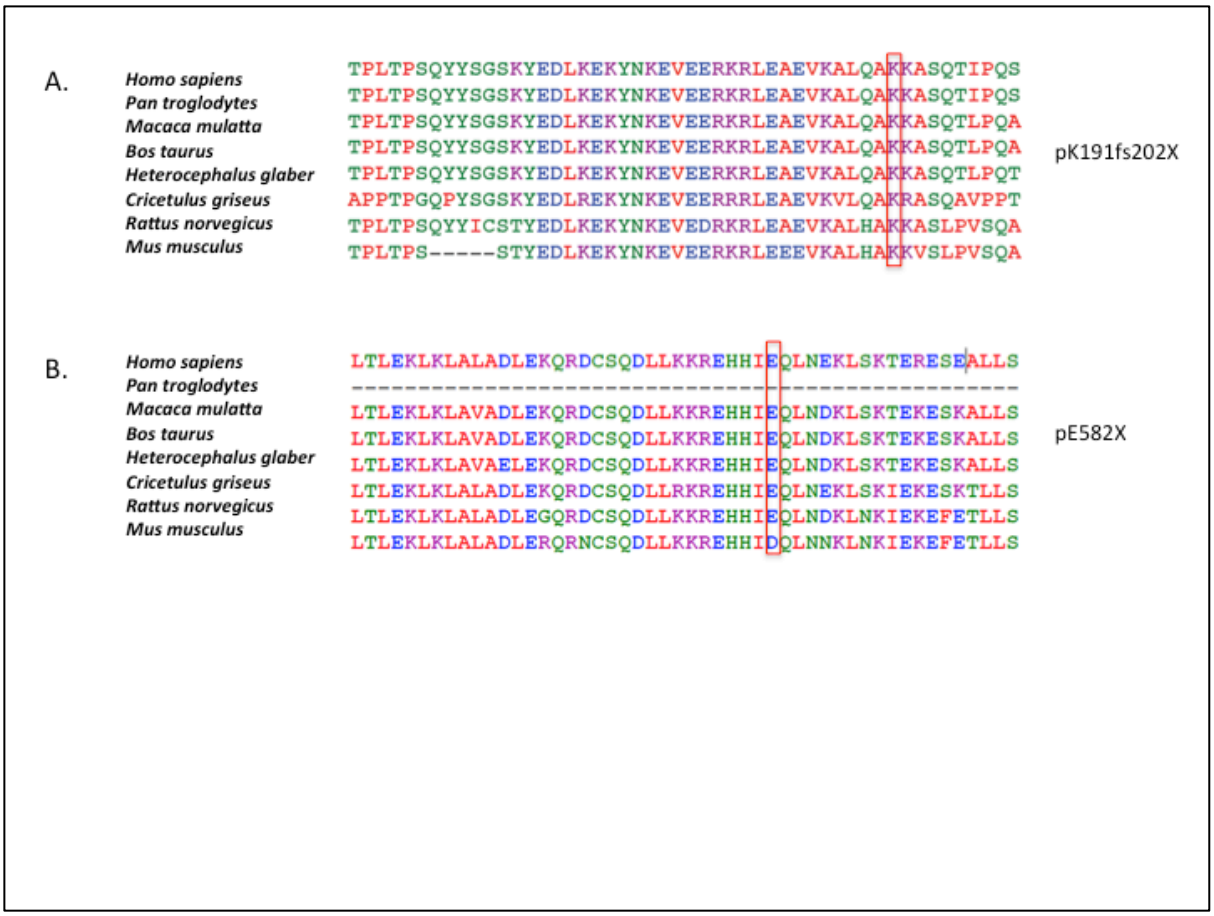

Figure 3.8: *Conservation of mutated CENPF amino acid sequence.*

(A) Conservation of lysine residue across species from *H. sapiens* to *M. musculus*. (B) Conservation of glutamic acid residue across species from *H. sapiens* to *R norvegicus*.

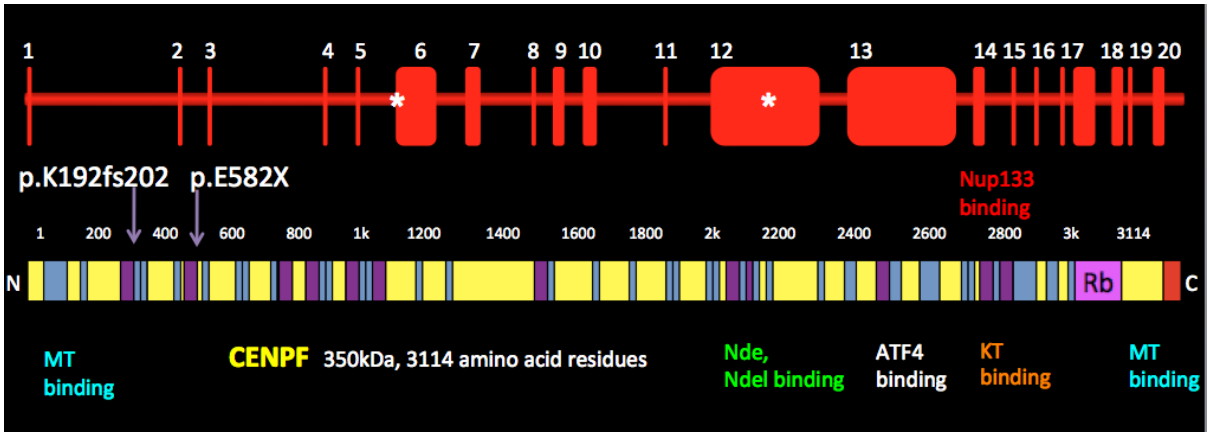

Figure 3.9: *Schematic of CENPF gene and protein.* The *CENPF* gene contains 20 exons. Astersisks (white) denote location of mutations identified. *CENPF* encodes a protein of 350kDa, consisting of 3114 amino acid residues. CENPF protein consists of mainly colied coil domains (blue), several leucine heptad repeats (purple), microtubule (MT) binding domains at both the N- and C-termini in addition to Nudel (Nde) binding, Kinetochore (KT) and Nup133-binding domains. The kinetochore localization domain and a bipartite nuclear localization sequence reside in the C-terminal region. Purple arrows show location of two *CENPF* mutations near N-terminus, p.K191fs202 and p.E582X.

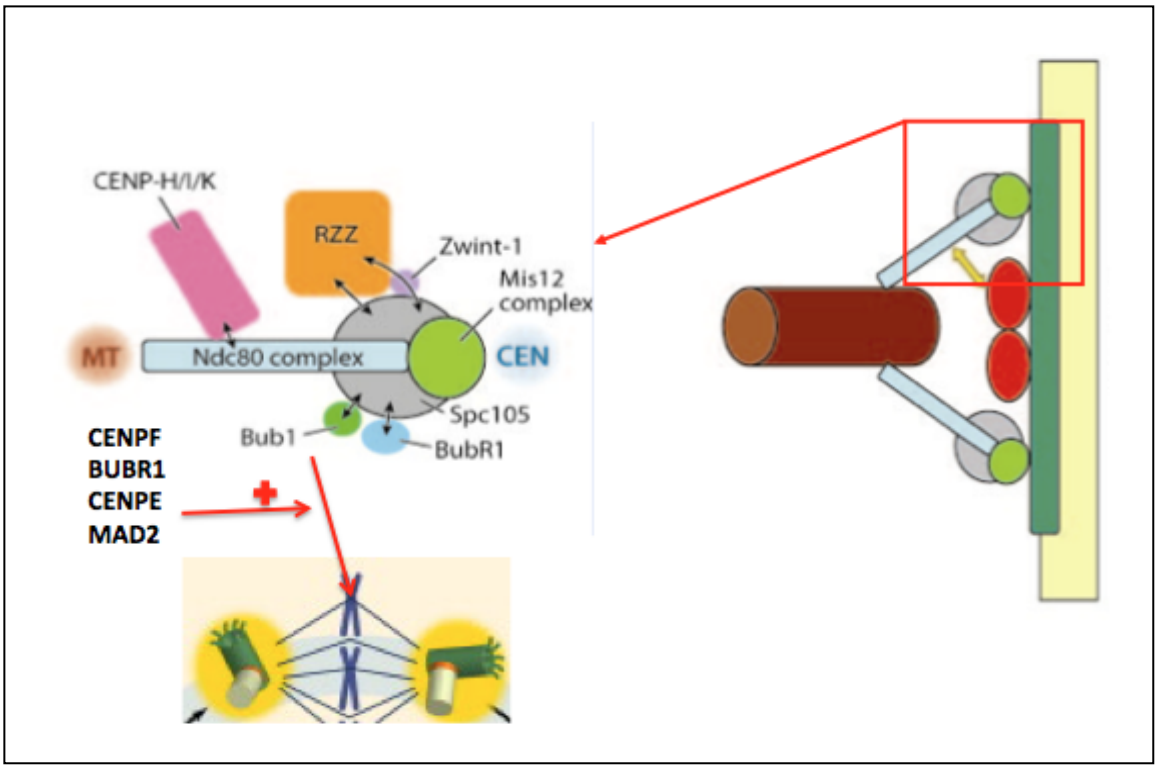

Figure 3.10: *Kinetochore-microtubule interaction network.* The kinetochore-microtubule network consists of a multiprotein complex assembled on centromeres in mitosis and meiosis and connects with spindle microtubules. The C-terminal domain of Cenp-F interacts with itself, the kinesin-related motor protein Cenp-E and the spindle checkpoint component, Bub1 which is consistent with roles in chromosome segregation and/or spindle checkpoint control. [Adapted from (Przewloka and Glover, 2009)].

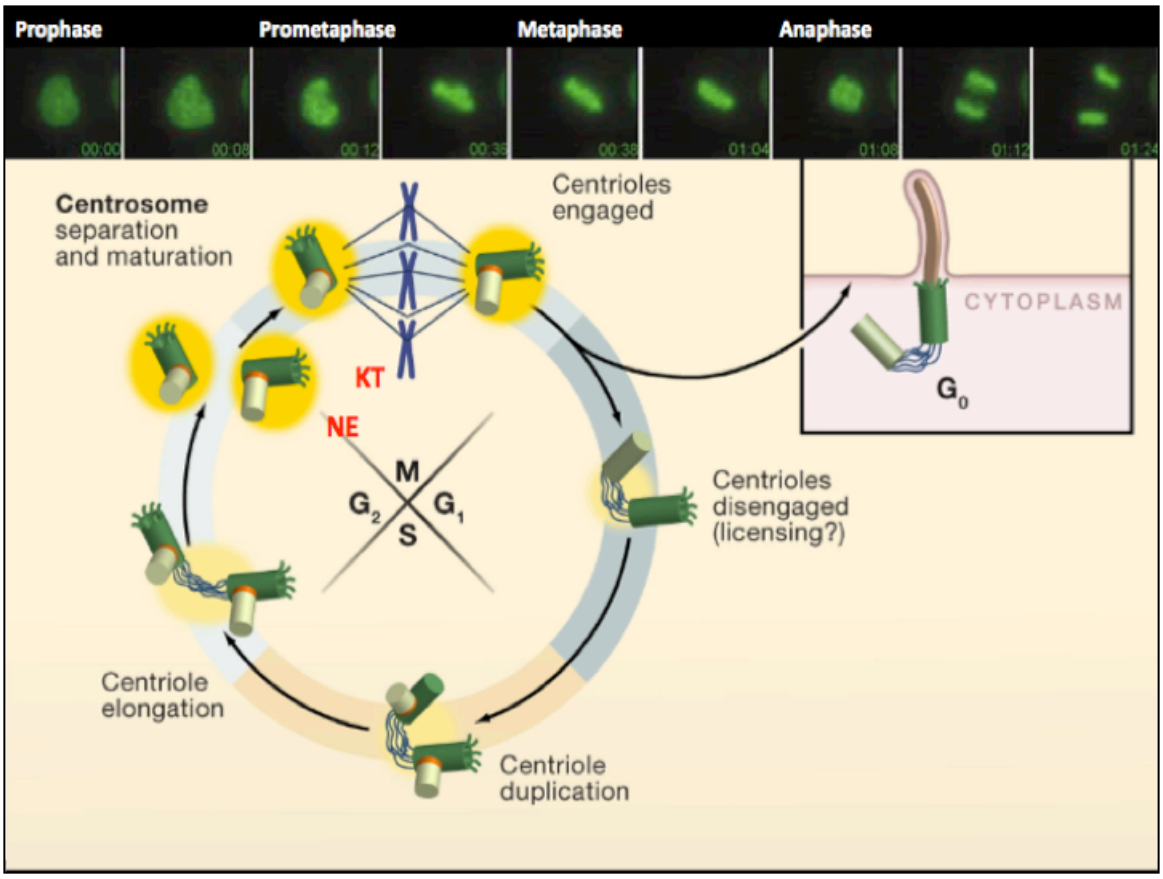

Figure 3.11: *Cenp-F has a dynamic localisation throughout the cell cycle.*

In G2, Cenp-F is predominantly nuclear and binds to the nuclear envelope (NE) at the transition between G2 and M phases. In early prophase until anaphase onset, it is found at the kinetochore (KT), the attachment point for the microtubule network at the centromere. In early anaphase, it is found at the spindle midzone while in late anaphase, it migrates with dynein to the spindle poles. In early G0, it undergoes proteasomal degradation. [Adapted from (Holt et al., 2005; Nigg and Raff, 2009), Liao et al, 1995]

3.3 DISCUSSION

3.3.1 Whole exome sequencing identifies the genetic cause of a novel phenotype where conventional approaches had failed

Whole exome capture coupled with massively parallel DNA sequencing has become a powerful new tool for determining nearly all the coding variation present in an individual human genome in a cost-effective manner. In the current report, I show the success of exome sequencing in circumstances where conventional approaches such as linkage analysis had failed. Significant locus heterogeneity was observed following linkage analysis with the identification of ten linked regions on Chromosome 1 (2 intervals), 2, 6, 7, 8, 13, 19, and 20. One of the intervals on Chromosome 1 and the interval on Chromosome 19 were the largest and contained the most homozygous markers covering a total 839 genes. Using IBD Finder, significant regions of homozygosity were not present, consistent with declared non-consanguinity. *CENPF*, the causative gene identified herein, lies amongst 311 other genes in a large region spanning 33Mb on chromosome 1. With traditional candidate gene sequencing approaches, the cost of time to undertake DNA sequencing would have been estimated to be four-fold higher than exome sequencing (Metzker, 2010). Furthermore, given the fact that both parents were nonconsanguineous and the compound heterozygous nature of the mutations identified in *CENPF*, it is not surprising that homozygosity mapping had failed.

3.3.2 Identification of the causal alleles through analysis of an unfiltered approach for depth of coverage

A key challenge of using exome sequencing in this study was how to identify two different disease-related alleles in the same gene. In the current study, I utilised a commercial kit (Nimblegen version 1), which targeted 180,000 exons of 25,000 genes. Newer kits now target over 50 Mb encompassing coding exons annotated by the GENCODE project as well as CCDS and RefSeq databases and incorporates exonic regions and non-coding RNAs (Clark et al., 2011). Limitations remain despite existing targets. First of all, data pertaining to the true nature of all protein-coding exons in the genome is still incomplete so that current capture probes only target exons that have been correctly annotated. Secondly, the efficiency of the capture probes varies such that some sequences fail to be targeted by capture probe design altogether. Thirdly, not all templates are sequenced with equal efficiency and alignment to the reference genome to facilitate base calling cannot be achieved with all sequences. Effective coverage (eg 50x) of exons using currently available commercial kits varies substantially. Indeed, in the current study, a key step in the identification of the second disease-related allele was achieved by not filtering the variants for depth of coverage, as the second allele was found at a depth of 13x coverage.

3.3.3 A single affected case was sufficient following application of a successful filtering strategy for finding the disease-causing variants

Gene identification in over 180 Mendelian disorders has been achieved in less than 3 years (Bamshad et al., 2011) (Figure 3.1). The majority of these studies have compared exome sequences and variants in a small number of unrelated or closely related affected individuals. In the current study, I have shown that it is possible to identify the genetic cause in a single affected case through the use of a successful filtering strategy that is summarised in Table 3.2. From a template of over 40,000 polymorphisms, variants could be further filtered on the basis of novelty, assuming that disease-causing alleles are likely to be novel and not previously described in public databases such as dbSNP and 1000 Genomes Project in addition to those found in a set of unaffected individuals (> 200 in house control exomes). Therefore, all previously described single nucleotide polymorphisms (SNPs) are removed by the filter. In the current study, this reduced the number of candidate genes to just over 10,000 variants. This strategy may be disadvantageous as potentially pathogenic variants may be filtered on the assumption that dbSNP does not contain any pathogenic alleles which is untrue. Secondly, filtering independent of the minor allele frequency (MAF) runs the risk of eliminating truly pathogenic alleles that segregate in the general population at low frequencies.

Further stratification of candidate alleles was determined on the basis of their predicted impact with greater emphasis being given to frameshift, stop codons and disruptions of canonical splice sites than to missense variants (MacArthur et al., 2012). The disadvantage to using this strategy is that certain causal alleles may not directly alter protein-coding sequences or canonical splice sites. Based on this strategy, further stratification to 650 alleles was achieved in the current study.

An important next step was to consider the autosomal recessive mode of inheritance. A search for homozygous mutations led to the stratification of only 3 candidate genes, none of which were in the linked region. As a result of this finding, a search for compound heterozygous mutations in the same gene led to the stratification of a further 24 candidate genes, only 1 of which lay within a linked interval. Therefore, the mode of inheritance clearly influenced the stratification design in the penultimate stages of gene identification of this monogenic novel disorder. The strategy of combining discrete filtering of exome datasets with mapping data is supported by several other successful reports (Bamshad et al., 2011). Depending on the production pipeline, the success of exome sequencing in gene identification currently lies at 50% (Gilissen et al., 2011). Failure to identify the candidate gene by this strategy may occur as a result of the causative gene not being in the target definition (either the gene is unknown or is not targeted by the capture probe); there is

inadequate coverage that contains the causal variant (attributable to poor capture or poor sequencing); the causal variant is covered but not accurately called (eg in the context of a small complex indel); true novel variants are called in the same gene but only because of the size of the gene; false variants are called because of mismapped reads or errors in alignment.

In addition to these technical failures, failure to identify the candidate gene by the aforementioned strategy, may also be accounted for by analytical failures. A major limitation of the current study was a failure to identify further cases of *CENPF* mutations in families with phenotypic overlap in the context of other known ciliopathy disorders. However, the likelihood that the mutations identified were neutral mutations was greatly reduced by the nature of the two mutations with one mutation affecting a canonical splice site and the second mutation resulting in a premature stop codon (Chen et al., 2010). Furthermore, an analysis of the quantitative estimate of the functional impact of both mutations based on analysis of high sequence conservation of affected nucleotides and amino acid residues for the mutated bases and amino acids was also applied to predict the pathogenicity. Both *CENPF* mutations identified were predicted to result in (i) loss of a splice acceptor site and (ii) truncation of the mutated protein.

3.4 SUMMARY

In this chapter, I have identified the causative gene for a novel disorder through the application of next generation sequencing technologies where linkage analysis and homozygosity mapping had previously failed. Following exome capture with an early version of Nimblegen's exome capture kit and establishment of a production pipeline at University College London, I subsequently optimised a filtering strategy for gene identification. A key step was to consider to omit stratification for depth of coverage. Further filtering thereafter for novelty and functional impact, facilitated the reduction in the number of possible disease-causing variants. Importantly, I have shown that, with this filtering strategy, it is possible to utilise the exome of just one affected case to identify the causative gene, provided the gene is in the target definition and a productive pipeline exists. Following analysis of pathogenicity predictions for the mutated alleles, I have shown that indeed, the mutated alleles segregate with the other affected foetuses in the kindred and with each parent carrying a single mutated allele. Importantly, it will now be possible to screen for further affected foetuses in future pregnancies in this kindred.

CHAPTER 4. DETERMINING THE ROLE OF CENPF IN CILIA FORMATION AND FUNCTION

4.1 INTRODUCTION

Mutations in human *CENPF* have been identified for the first time in a novel phenotype, features of which are inconsistent with any known syndrome. Considering the embryonic lethality in mid-gestation in all affected foetuses, together with the constellation of defects affecting craniofacial development, cerebellar morphogenesis, palatogenesis, foregut and renal development, malfunction of a critical cellular process seemed most likely to underlie the phenotypic features observed in affected foetuses with *CENPF* mutations. Interestingly, Shh plays an important role in early craniofacial development (Hu and Helms, 1999), in cerebellar morphogenesis (Kim et al., 2011), in foregut development (Mao et al., 2010), and in renal development (Cain et al., 2009). Furthermore, the constellation of clinical features such as hydrocephalus, cerebellar malformations, cleft palate and renal malformations have been described in disorders associated with either abnormal formation and/or function of primary cilia (Table 1.2). As discussed in Chapter 1, genetic studies have shown that IFT proteins act at the heart of the *Shh* pathway, downstream of the transmembrane *Shh* receptor, *Patched 1 (Ptch1)* and its downstream effector, *Smoothened (Smo)* and upstream of the *Gli* transcription factors that implement the pathway (Huangfu et al., 2003). As a result, I hypothesised that some of the phenotypic features observed in foetuses carrying *CENPF* mutations could be attributed to defects in cilia function.

Several studies supported this hypothesis. Firstly, a centrosomal localisation has recently been shown for murine Cenp-F, where it acts as a major regulator of microtubule (MT) nucleation (Moynihan et al., 2009). Secondly, Cenp-F has previously been shown to interact with Nde1 (Vergnolle and Taylor, 2007), a centrosomal phosphoprotein, recently shown to negatively regulate cilia length. Nde1-mediated control of ciliogenesis relies on its interaction with the dynein light chain, LC8, which is tethered by Nde1 to the basal body (Kim et al, 2011). LC8 is a component of retrograde IFT in *C. reinhardtii* (Pazour et al., 1998) where it is required for the formation of flagella, and has been localised to the human ciliary axoneme (Ostrowski et al., 2002). Intriguingly, IFT88 has been shown to rescue the Nde-1 effect on ciliary length, (Kim et al, 2011). Furthermore, recent studies have shown that cytoplasmic dynein is required for the transport of IFT88 to the spindle poles (Delaval et al, 2011). In late anaphase, the poleward migration of cytoplasmic dynein depends on Nde1 (Yan et al., 2003; Zylkiewicz et al., 2011). Cenp-F also migrates poleward with cytoplasmic dynein in late anaphase (Yang et al, 2003) but whether Cenp-F functions in the Nde1-LC8-IFT88 ciliogenic pathway is currently unknown. In this chapter, I will explore the hypothesis that Cenp-F regulates cilia formation.

4.2 RESULTS

4.2.1. Human CENP-F shares 40% identity with a *C. reinhardtii* FAP58

Given the elucidation of the Nde1-LC8-IFT88 pathway in ciliogenesis and the role of *Chlamydomonas reinhardtii* LC8 in retrograde IFT, a comparative genomics approach was employed as a strategy to identify potential novel functions of CENP-F that could be extrapolated to the loss of function phenotype. A BLAST analysis of the *C. reinhardtii* proteome revealed that human CENP-F protein (NP_057427.3) has 33% identity (E-value, 0.010) with a flagellar associated protein (FAP58, Accession: XP_001693603.1), previously discovered in the flagellar proteome of *C. reinhardtii* (Pazour et al., 2005) (Figure 4.1.1). BLAST analysis of the *Schmidtea mediterranea* proteome for sequence similarity to *C. reinhardtii* FAP58 protein revealed sequence similarity to KIF3A-like and KIF3B-like protein sequences in the *S. mediterranea* proteome (28% identity, E-value, $2e^{-08}$; 20% identity, E-value, $7e^{-05}$). CLUSTALW alignment with human CENP-F showed sequence similarity with human KIF3A (Figure 4.1.2).


gi|55770834|ref|NP_057427.3| KQCEELVQIKGEIEENLMKAEQMHQSFVAETSQRISKLQEDTSAHQNVVA 900
gi|159470917|ref|XP_001693603. ----------MASDFSTGLHGGHHETLEQYNKVL 24
gi|55770834|ref|NP_057427.3| ETLSALENKEKELQLLNDKVETEQAEIQELKKSNHLLEDSLKELQLLSET 950
gi|159470917|ref|XP_001693603. EELAAD----------AVMDPFRVEYEKLHRALRKTYESQAR 56
gi|55770834|ref|NP_057427.3| LSLEKKEMSSIISLNKREIEELTQENGTLKEINASLNQEKMNLIQKSESF 1000
gi|159470917|ref|XP_001693603. LAKKCQELNSDISLNASKVQSALKLNEEDRETAVALKREIN----KAWKM 102
gi|55770834|ref|NP_057427.3| ANYIDERKKSISELSDQIKQEKLILLQRCEETGNAYEDLSQKYKAAQEKN 1050
gi|159470917|ref|XP_001693603. VDDSTVKETKAKETAQQLKVEIANLSRLVEEG----------AGLAIGEE 142
gi|55770834|ref|NP_057427.3| SKLECLLNECTSLCENRKNELEQLKEAFAKEHQEFLTKLAFAEERNQNLM 1100
gi|159470917|ref|XP_001693603. TALNELLKQKEELARERDAQVEQLMKYRS---------- 171
gi|55770834|ref|NP_057427.3| LELETVQQALRSEMTDNQNNSKSEAGGLKQEIMTLKEEQNKMQKEVNDLL 1150
gi|159470917|ref|XP_001693603. -DLMETQEKLR---------AADAEKLQLDADIQHLRGTINDKKAEAEREI 212
gi|55770834|ref|NP_057427.3| QENEQLMKVMKTKHECQNLESEPIRNSVKERESERNQCNFKPQMDLEVKE 1200
gi|159470917|ref|XP_001693603. RKKERMEKEMKELRQQLEIRSSEIKS----------KQ 240
gi|55770834|ref|NP_057427.3| ISLDSYNAQLVQLEAMLRNKELKLQESEKEKECLQHELQTIRGDLETSNL 1250
gi|159470917|ref|XP_001693603. LQVTSTEEQVARLEQMLRDAKFATEKVQKEYNMLNERMQKLHHDLEEQIH 290
gi|55770834|ref|NP_057427.3| QDMQSQEISGLKDCEIDAEEKYISGPHELSTSQNDNAHLQCSLQTTMNKL 1300
gi|159470917|ref|XP_001693603. TNTQLLTENSAKQVELRVKEEEISGIKQEASRVN---------- 324
gi|55770834|ref|NP_057427.3| NELEKICEILQAEKYELVTELNDSRSECITATRKMAEEVGKLLNEVKILN 1350
gi|159470917|ref|XP_001693603. ----------
gi|55770834|ref|NP_057427.3| DDSGLLHGELVEDIPGGEFGEQPNEQHPVSLAPLDESNSYEHLTLSDKEV 1400
gi|159470917|ref|XP_001693603. ----------
gi|55770834|ref|NP_057427.3| QMHFAELQEKFLSLQSEHKILHDQHCQMSSKMSELQTYVDSLKAENLVLS 1450
gi|159470917|ref|XP_001693603. ----------
gi|55770834|ref|NP_057427.3| TNLRNFQGDLVKEMQLGLEEGLVPSLSSSCVPDSSSLSSLGDSSFYRALL 1500
gi|159470917|ref|XP_001693603. ----------
gi|55770834|ref|NP_057427.3| EQTGDMSLLSNLEGAVSANQCSVDEVFCSSLQEENLTRKETPSAPAKGVE 1550
gi|159470917|ref|XP_001693603. ----------
gi|55770834|ref|NP_057427.3| ELESLCEVYRQSLEKLEEKMESQGIMKNKEIQELEQLLSSERQELDCLRK 1600
gi|159470917|ref|XP_001693603. ----------KLREQTVKKTKQLEEQRVEVEKER-------- 348


gi|55770834|ref|NP_057427.3| QYLSENEQWQQKLTSVTLEMESKLAAEKKQTEQLSLELEVARLQLQGLDL 1650
gi|159470917|ref|XP_001693603. ----------
gi|55770834|ref|NP_057427.3| SSRSLLGIDTEDAIQGRNESCDISKEHTSETTERTPKHDVHQICDKDAQQ 1700
gi|159470917|ref|XP_001693603. ----------
gi|55770834|ref|NP_057427.3| DLNLDIEKITETGAVKPTGECSGEQSPDTNYEPPGEDKTQGSSECISELS 1750
gi|159470917|ref|XP_001693603. ----------
gi|55770834|ref|NP_057427.3| FSGPNALVPMDFLGNQEDIHNLQLRVKETSNENLRLLHVIEDRDRKVESL 1800
gi|159470917|ref|XP_001693603. ----------
gi|55770834|ref|NP_057427.3| LNEMKELDSKLHLQEVQLMTKIEACIELEKIVGELKKENSDLSEKLEYFS 1850
gi|159470917|ref|XP_001693603. ----------
gi|55770834|ref|NP_057427.3| CDHQELLQRVETSEGLNSDLEMHADKSSREDIGDNVAKVNDSWKERFLDV 1900
gi|159470917|ref|XP_001693603. ----------
gi|55770834|ref|NP_057427.3| ENELSRIRSEKASIEHEALYLEADLEVVQTEKLCLEKDNENKQKVIVCLE 1950
gi|159470917|ref|XP_001693603. ----------DVLRAELAALERELEAKQKEVDVEK 373
gi|55770834|ref|NP_057427.3| EELSVVTSERNQLRGELDTMSKKTTALDQLSEKMKEKTQELESHQSECLH 2000
gi|159470917|ref|XP_001693603. KKLEELTRER------DAENATQKQIDLVKINENAKRN---------- 405
gi|55770834|ref|NP_057427.3| CIQVAEAEVKEKTELLQTLSSDVSELLKDKTHLQEKLQSLEKDSQALSLT 2050
gi|159470917|ref|XP_001693603. ----------LEQEIQGYKMEAQKQSKLIYQLEKEREKYDLE 437
gi|55770834|ref|NP_057427.3| KCELENQIAQLNKEKELLVKESESLQARLSESDYEKLNVSKALEAALVEK 2100
gi|159470917|ref|XP_001693603. AAEAANKYQQAQSEVKLRVDAIMDLQRRIAECESKLKQQQNLYEAVRADR 487
gi|55770834|ref|NP_057427.3| GEFALRLSSTQEEVHQLRRGIEKLRVRIEADEKKQLHIAEKLKERERENE 2150
gi|159470917|ref|XP_001693603. NLYSKNLIEAQDEIQEMKR----------KFKIMQHQIE 516
gi|55770834|ref|NP_057427.3| SLKDKVENLERELQMSEENQELVILDAENSKAEVETLKTQIEEMARSLKV 2200
gi|159470917|ref|XP_001693603. QLKEEITGKDLYLLKEHFEHQKVINEKEQLRNELDRSKSNIKEADSAINA 566
gi|55770834|ref|NP_057427.3| FELDLVTLRSEKENLTKQIQEKQGQLSELDKLLSSFKSLLEEKEQAEIQI 2250
gi|159470917|ref|XP_001693603. QKVEIDKLN---HIINEADQERRRQKKEYDIVVN---------- 597
gi|55770834|ref|NP_057427.3| KEESKTAVEMLQNQLKELNEAVAALCGDQEIMKATEQSLDPPIEEEHQLR 2300
gi|159470917|ref|XP_001693603. ------ERDILGTQLVRRNDELAALYERIKIQQATLQMGQS---QYRDRL 638
gi|55770834|ref|NP_057427.3| NSIEKLRARLEADEKKQLCVLQQLKESEHHADLLKGRVENLERELEIART 2350
gi|159470917|ref|XP_001693603. AEIRQLKVRLADLKR----QLHLLKSSVSNIDVLKREVHQLGRELLQERT 684
gi|55770834|ref|NP_057427.3| NQEHAALEAENSKGEVETLKAKIEGMTQSLRGLELDVVTIRSEKENLTNE 2400
gi|159470917|ref|XP_001693603. KVKALSEELENP---------- 696

Figure 4.1.1: Human CENP-F (NP_057427.3) shares 33% identity with a flagellar associated protein in the *Chlamydomonas reinhardtii* proteome (XP_001693603).


gi|46852174|ref|NP_008985.3|
gi|55770834|ref|NP_057427.3|
MSWALEEWKEGLPTRALQKIQELEGQLDKLKKEKQQRQFQLDSLEAALQK 50
-MPINKSEKPE----SCDNVKVVVRCRPLNEREKSMCYKQAVS------- 38
QKQKVENEKTEGTNLKRENQRLMEICESLEKTKQKISHELQVKESQVNFQ 100
----------VDEMRGTITVHKTDSSNEPPKTFTFDTVFGPESKQLDVYN 78
EGQLNSGKKQIEKLEQELKRCKSELERSQQAAQSADVSLNPCNTPQKIFT 150
LTARP-------IIDSVLEGYN---------- 93
TPLTPSQYYSGSKYEDLKEKYNKEVEERKRLEAEVKALQAKKASQTLPQA 200
------------GTIFAYGQTGTGKTFTMEGVR-------AIPELRGII 123
TMNHRDIARHQASSSVFSWQQEKTPSHLSSNSQRTPIRRDFSASYFSGEQ 250
PNSFAHIFGHIAKAEGDTRFLVR------VSYLEIYNEEVR---------D 159
EVTPSRSTLQIGKRDANSSFFDNSSSPHLLDQLKAQNQELRNKINELELR 300
LLGKDQTQRLEVKERPDVGVYIKDLSAYVVNN---------- 191
LQGHEKEMKGQVNKFQELQLQLEKAKVELIEKEKVLNKCRDELVRTTAQY 350
----------ADDMDRIMTLGHKNRSVGATNMNEH 216
DQASTKYTALEQKLKKLTEDLSCQRQNAESARCSLEQKIKEKEKEFQEEL 400
SSRSHAIFTITIECS----------EKGID 236
SRQQRSFQTLDQECIQMKARLTQELQQAKNMHNVLQAELDKLTSVKQQLE 450
GNMHVRMGKLHLVDLAGSERQAKTGATGQRLKEATKIN---------- 274
NNLEEFKQKLCRAEQAFQASQIKENELRRSMEEMKKENNLLKSHSEQKAR 500
EVCHLEAELKNIKQCLNQSQNFAEEMKAKNTSQETMLRDLQEKINQQENS 550
----------LSLSTLGNVISALVDGKSTHVPYRNSKLTR---------- 304
LTLEKLKLAVADLEKQRDCSQDLLKKREHHIEQLNDKLSKTEKESKALLS 600
----------LLQDSLGGNSKT 316
ALELKKKEYEELKEEKTLFSCWKSENEKLLTQMESEKENLQSKINHLETC 650
MMCANIGPADYNYDETISTLRYANRAKNIKNKARINEDP---------- 355
LKTQQIKSHEYNERVRTLEMDRENLSVEIRNLHNVLDSKSVEVETQKLAY 700
----------KD 357
MELQQKAEFSDQKHQKEIENMCLKTSQLTGQVEDLEHKLQLLSNEIMDKD 750
ALLRQFQKEIEELKKKLEEGEE--ISGSDISGSEEDDDEE---------- 395
RCYQDLHAEYESLRDLLKSKDASLVTNEDHQRSLLAFDQQPAMHHSFANI 800
-GEVGEDGEKRKKRRGKKKVSPDKMIEMQAKIDEERKALETKLDMEEEER 444
IGEQGSMPSERSECRLEADQSPKNSAILQNRVDSLEFSLESQKQMNSDLQ 850

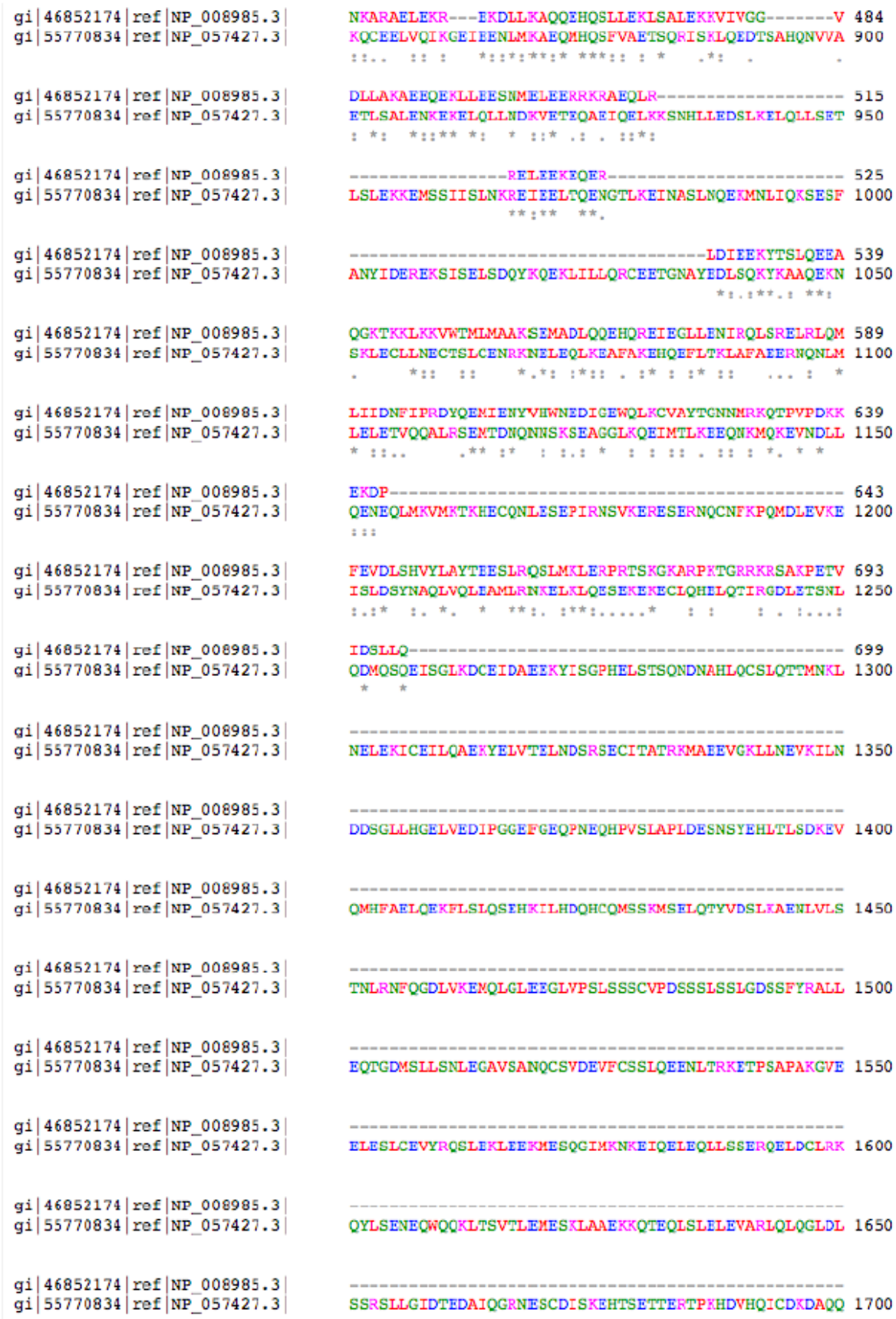

Figure 4.1.2: CLUSTALW alignment with human CENP-F (NP_057427.3)

showed 36% sequence similarity with human KIF3A (NP_008985.3).

4.2.2. CENP-F is localised to the basal bodies and subdistal appendages of the mother centriole of ciliated 3T3, IMCD3 and RPE cells

Based on the sequence similarity of CENP-F to *C. reinhardtii* FAP58 and the phenotypic overlap of the developmental malformations observed in *CENPF*-mutated foetuses with diseases affecting cilia function or formation, I hypothesised that CENP-F may be localised to primary cilia. Dual immunofluorescence microscopy of ciliated NIH 3T3 fibroblasts, with a mouse monoclonal CENPF antibody and acetylated tubulin antibody further confirmed a basal body localisation for CENP-F (Figure 4.2). CENP-F was not detected along the ciliary axonemes but colocalised with Ninein, which marks the subdistal appendages of the mother centriole in IMCD3 cells (Figure 4.3). To gain further insight into the subcellular localisation of CENP-F at the ultrastructural level, immunogold labelling of CENP-F in serum starved RPE cells were imaged by transmission electron microscopy which confirmed a centriolar localisation for CENP-F, where localisation was observed at the subdistal appendages and the distal end of the centriole (Figure 4.4).

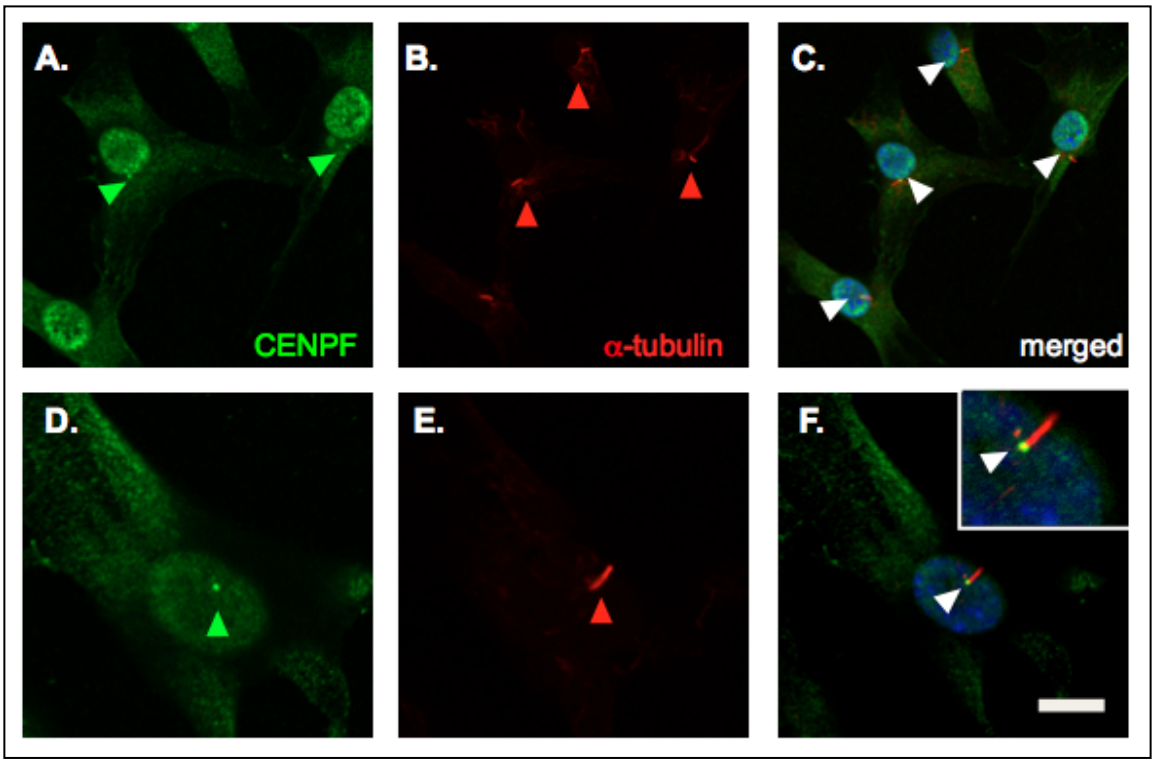

Figure 4.2: *CENP-F is localised at basal bodies of ciliated NIH 3T3 cells* (A-F). Shown are representative micrographs of cilia following dual immunofluorescence labelling of ciliated NIH 3T3 cells with anti-CENPF and anti-acetylated tubulin antibodies (A, D) Green channel images showing anti-CENPF immunodetection with Alexa488-conjugated secondary antibody. (B, E) Red channel images showing anti-acetylated tubulin immunodetection with Alexa594-conjugated secondary antibody. (C, F) Merged images of corresponding micrographs obtained through green and red channel images. Sections are counterstained with 4′, 6-diamidino-2-phenylindole DAPI. (C, F) White arrows, CENP-F localisation at basal bodies of primary cilia. Scale bar, 10 μm.

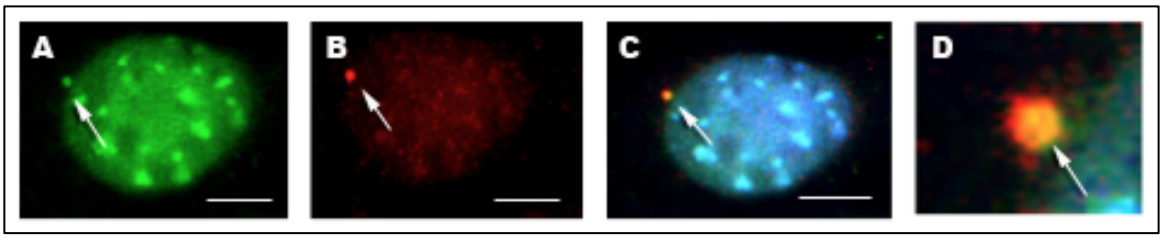

Figure 4.3: *CENP-F is localised at the subdistal appendages of the mother centriole of ciliated IMCD3 cells*

(A-D). Shown are representative micrographs of cilia following dual immunofluorescence labelling of IMCD3 cells with anti-CENPF and anti-Ninein antibodies. (A) Green channel images showing anti-CENPF immunodetection with Alexa488-conjugated secondary antibody. Scale bar 5µm (B) Red channel images showing anti-Ninein immunodetection with Alexa594-conjugated secondary antibody. (C, D) Merged images of corresponding micrographs obtained through green and red channel images. Sections are counterstained with DAPI. (A-C) White arrows, CENP-F localisation at the subdistal appendages of the mother centriole.

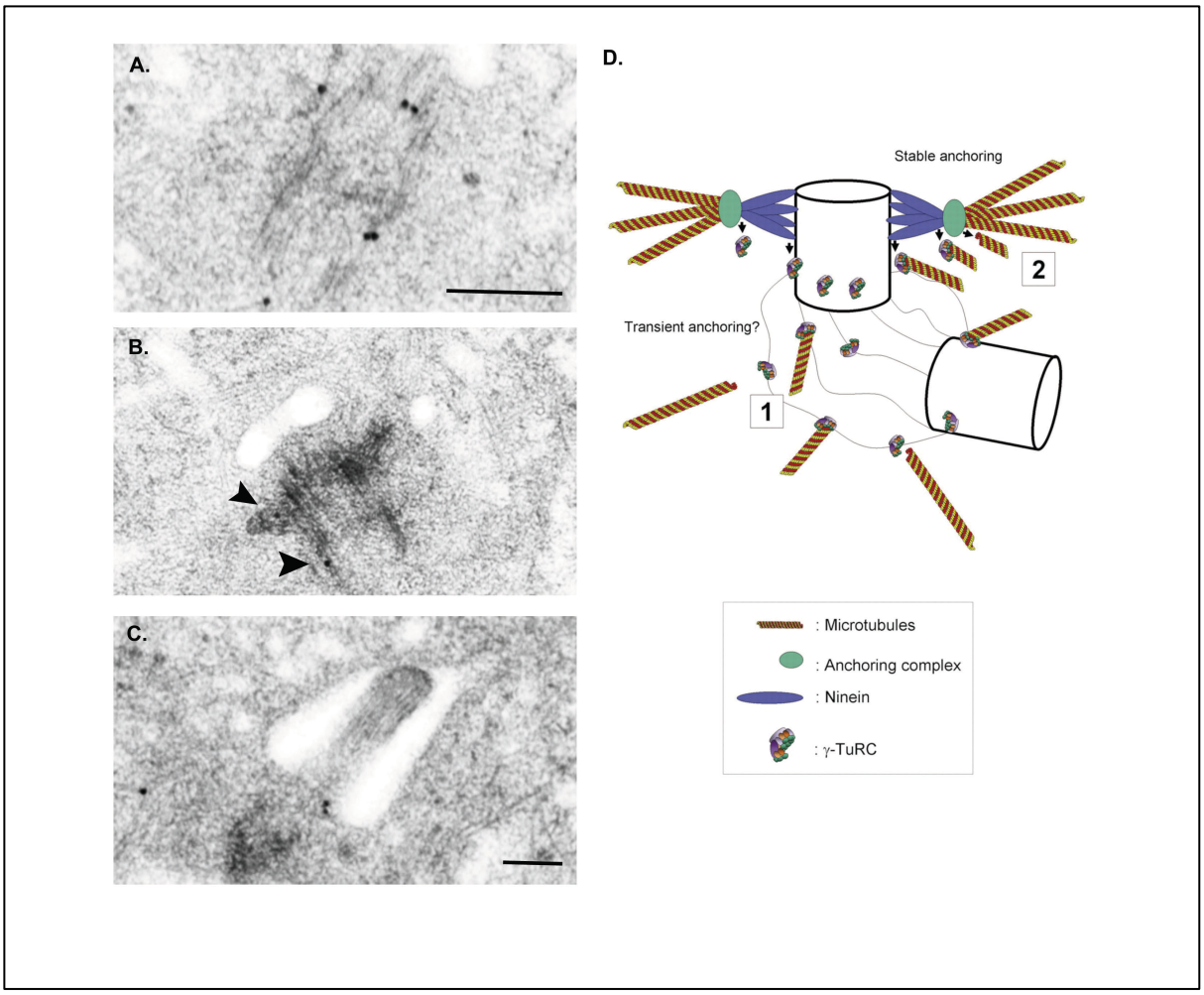

Figure 4.4: *Ultrastructural localisation of CENP-F* (A-C). Immunogold localisation of CENP-F at the subdistal appendages of the mother centriole in serum starved RPE cells. Scale bar 100nm. (A) Black arrows point to immunogold particles along the microtubules of the mother centriole. (B) Black arrows point to immunogold particles at the subdistal appendages of the mother centriole. (C) Black arrows point to the subdistal appendages of the mother centriole of serum starved RPE cells. Scale bar 250nm. (D) Schematic showing molecular components of subdistal appendages.

4.2.3 Zebrafish *cenpf* morphants exhibit a high mortality at 24hpf.

To understand the functional relevance of CENP-F in relation to its localisation at the basal body of primary cilia, I designed both translation-blocking and splice-blocking morpholinos against the intron 3-exon 4 boundary of zebrafish *cenpf*, which shares 60% homology with its human orthologue. Aberrant splicing of zebrafish *cenpf* mRNA in cenpf splice morphants indicating mis-splicing of the *cenpf* transcript (Figure 4.5). Given the embryonic lethality observed in the affected foetuses with CENPF mutations, I next analysed the percentage of surviving zebrafish embryos injected with standard and *cenpf* morpholino at 24 hours post fertilisation to confirm a role for zebrafish *cenpf* in early embryogenesis. Compared to controls (n=118), a significantly reduced number of *cenpf* morphants (1ng, n=136), [Std-MO mean % survival vs. *cenpf*-MO (1ng) mean % survival 85±0.8 vs 46±1.2, $p<0.008$] survived. There was no significant difference in mortality between 1ng and 2ngs of *cenpf* MO [cenpf-MO (1ng) mean % survival vs. *cenpf*-MO (2ng) mean % survival 46±1.2 vs 35±2.8, $p<0.09$, ns] survived (Figure 4.6).

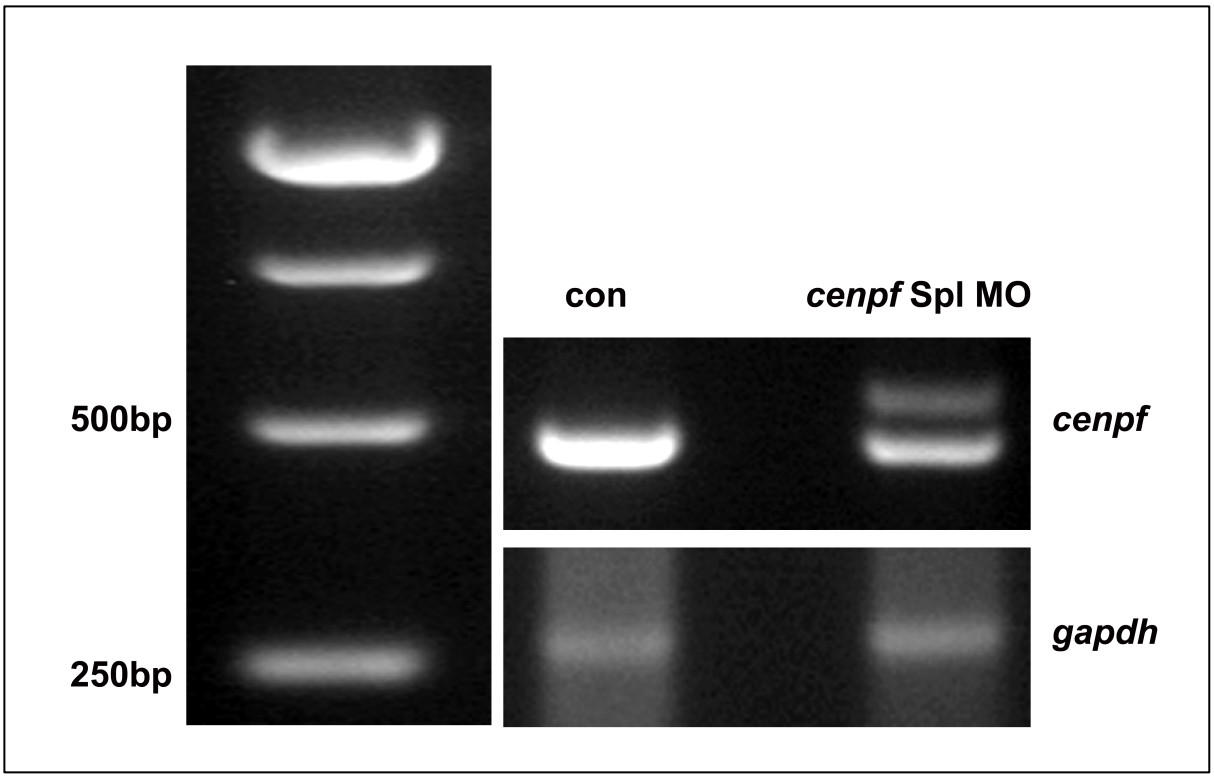

Figure 4.5: RT-PCR of RNA from *cenpf* splice zebrafish morphants demonstrating specificity of splice morpholinos. Aberrant splicing of *cenpf* mRNA in *cenpf* splice morphants compared to control embryos at 24 hpf.

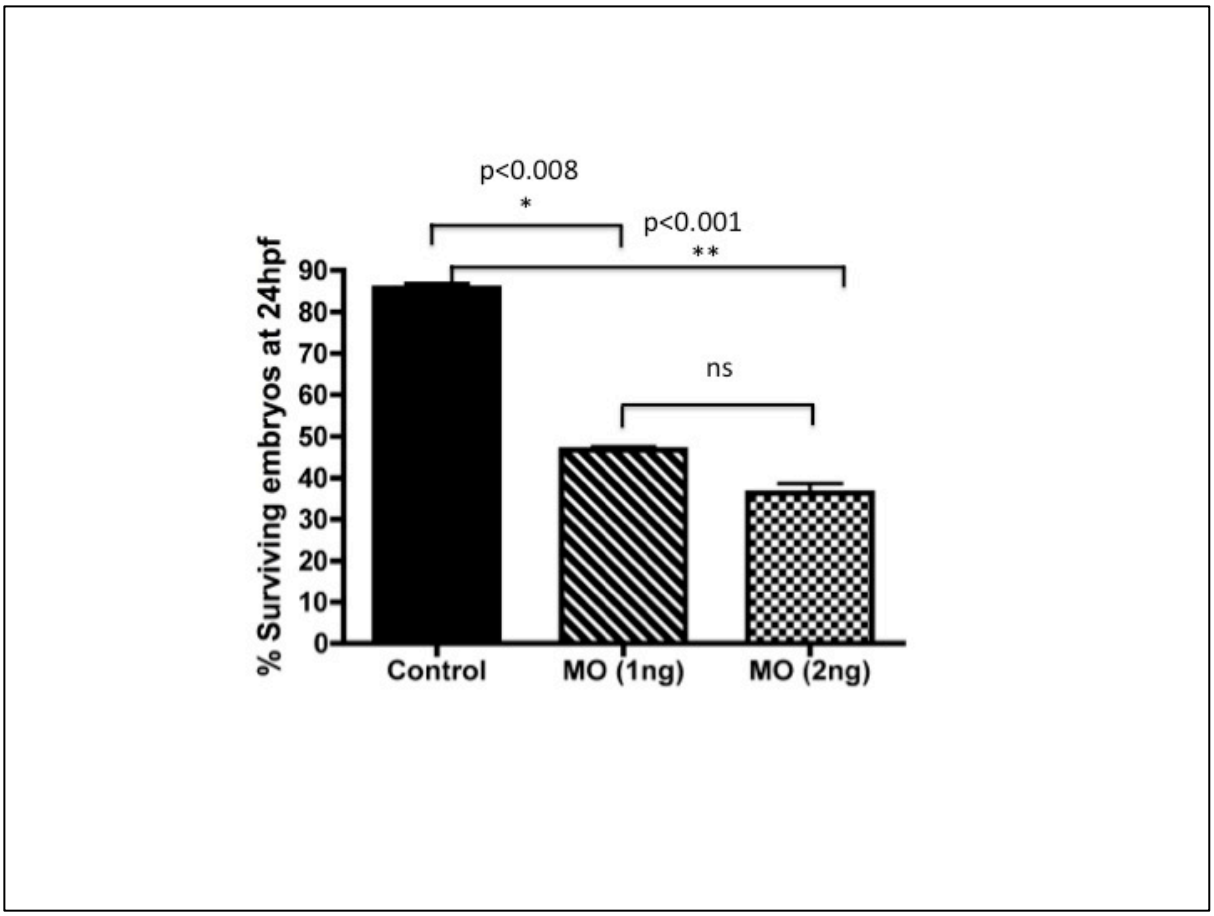

Figure 4.6: *Zebrafish cenpf morphants exhibit high mortality in first 24 hours*. Quantification (%) of surviving zebrafish embryos injected with MO at 24 hours post fertilisation. Graphic representation of results showing the mean percentage of survival at 24hpf of standard-MO, 1ng *cenpf* MO and 2ngs *cenpf* MO. Bars represent an average of three experiments. Error bars denote standard error of the mean (S.E.M). *p< 0.008, ** p< 0.001, ns, p< 0.09. The number of surviving standard-MO injected zebrafish embryos was significantly greater compared to the number of *cenpf*-MO injected embryos at 24hpf.

4.2.3 Zebrafish *cenpf* morphants exhibit a ciliopathy phenotype

Morphological analysis of surviving zebrafish embryos revealed defects in body axis curvature, block-shaped somites and otolith number anomalies at 30hpf (Figure 4.7). As these features have all been previously described in zebrafish injected with morpholinos targeting genes involved in cilia function, I next examined the morphological features of *cenpf*-MO that survived during the later stages of embryogenesis (Figure 4.8). At 48 hpf, *cenpf* morphants carrying the cardiac myosin light chain (*cmcl2*)-*gfp* transgene exhibited abnormal heart looping compared to standard-MO injected embryos. At 72hpf, hydrocephalus was also observed in *cenpf* morphants and at 5dpf, 100% of surviving *cenpf* morphants exhibited pronephric cysts (Figure 4.8).

4.2.4 Zebrafish *cenpf* morphants exhibit left-right patterning defects at 18 somites with defective ciliogenesis at Kupffer's vesicle.

Owing to the significant early embryonic lethality observed in zebrafish embryos within the first 24 hours coupled with the abnormal heart looping observed in embryos who survived to 48hpf, I hypothesised that left-right patterning (LR) defects would also be evident earlier in *cenpf* morphant zebrafish. Cilia-driven fluid flow within zebrafish Kupffer's vesicle or across the mouse ventral node, has been shown to underlie a conserved symmetry breaking event that establishes LR pattern (Hirokawa et al., 2006; Kramer-Zucker et al., 2005).

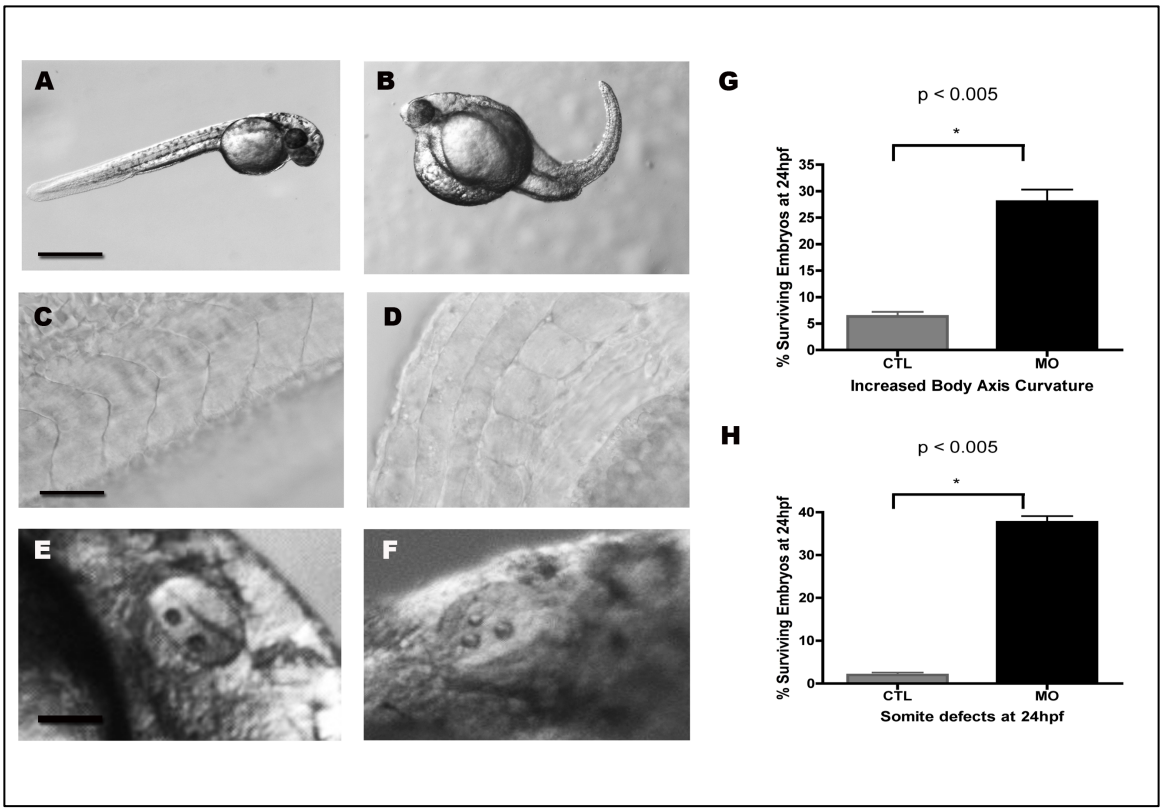

Figure 4.7: *Zebrafish cenpf morphants exhibit ciliopathy features at 30hpf.* (A-F) Representative images of zebrafish embryos at 30hpf from control (A, C, E) and *cenpf*-MO (B, D, F) injected embryos. (A) Normal body axis in wild-type embryos. Scale bar 200 μm (B) Increased body axis curvature in *cenpf*-MO injected embryos. (C) Chevron-shaped somites in control embryos compared to block-shaped somites in *cenpf*-MO injected embryos. Scale bar 100 μm (E) Two otoliths present in control embryos. (F) Excess otoliths in *cenpf*-MO injected embryos. Scale bar 100 μm (G) Significantly increased number of MO-injected embryos with increased body axis curvature. (H) Significantly increased number of MO-injected embryos with somite defects.

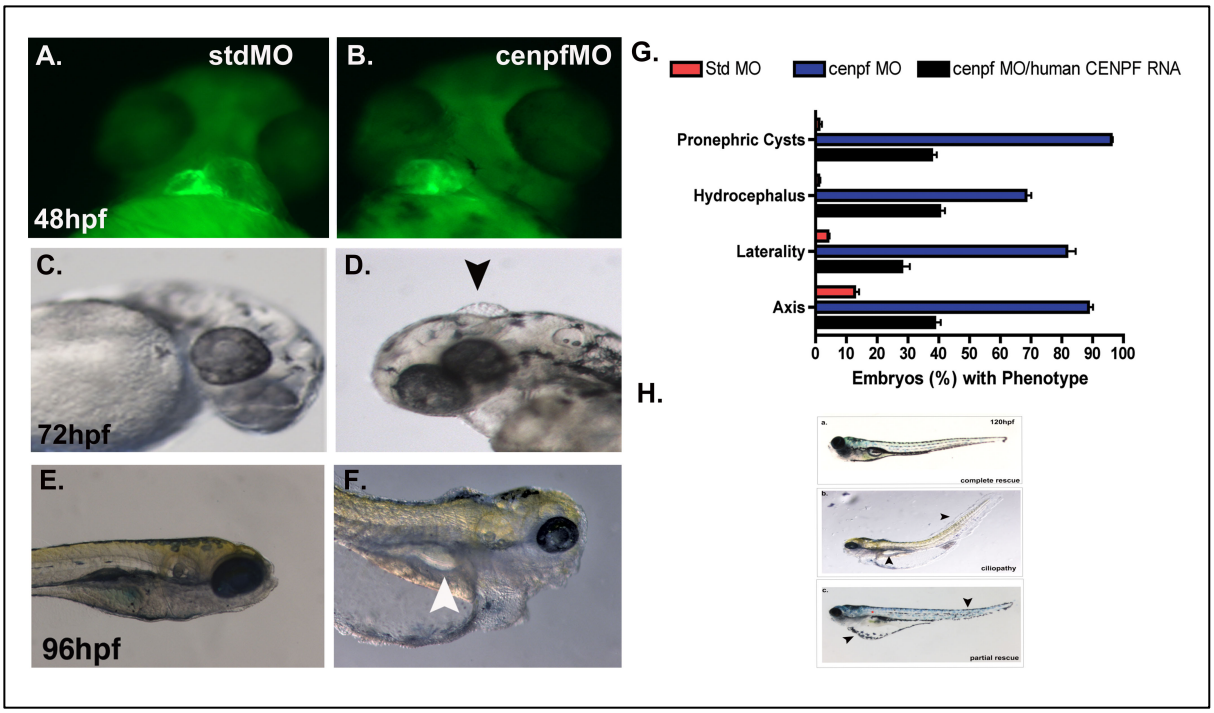

Figure 4.8: *Surviving cenpf morphants have ciliopathy features during the later stages of embryogenesis.* (A, B) Representative images of Tg *cmlc2-gfp* zebrafish embryos at 48hpf from control (A) and *cenpf*-MO (B) injected embryos, showing abnormal heart looping in *cenpf*-MO injected embryos. (C, D) Representative images of zebrafish embryos at 72hpf from control (C) and *cenpf*-MO (D) injected embryos, showing hydrocephalus in *cenpf*-MO injected embryos (red arrow). (E, F) Representative images of zebrafish embryos at 5dpf from control (E) and *cenpf*-MO (F) injected embryos, showing pronephric cysts in *cenpf*-MO injected embryos (red arrow). Scale bar 150µm. (G) Quantitative graph showing increased occurrence of axis curvature defects, laterality malformations, hydrocephalus and pronephric cysts in *cenpf* morphants (blue bars) compared to control embryos (red bars) and compared to *cenpf* morphants injected with human *CENPF* RNA (black bars). Bars represent an average of

three experiments. Error bars denote standard error of the mean (S.E.M). [Std-MO (n=266) % ventral axis curvature at 24hpf vs. *cenpf*-MO (n=173) 12.7±1.5 vs. 88.7±1.4, * p<0.001; *cenpf*-MO (n=173) vs. *cenpf*-MO with human *CENPF* RNA (n=256) 88.7±1.4 vs. 38.7±2.0, * p<0.001; WT (n=223) % laterality defects at 48hpf vs. *cenpf*-MO (n=152) 4.0±0.6 vs. 81.7±2.8, *p<0.001; *cenpf*-MO (n=152) vs. *cenpf*-MO with human *CENPF* RNA (n=229) 81.7±2.8 vs. 28±2.6, ***p <0.01; Std-MO (n=204) % hydrocephalus at 72hpf vs. *cenpf*-MO (n=93) 1±0.6 vs. 68.3±1.7, *p<0.001; *cenpf*-MO (n=93) vs. *cenpf*-MO with human *CENPF* RNA (n=197) 68.3±1.7 vs. 40.3±1.7, *p <0.001; Std-MO (n=158) % pronephric cysts at 120hpf vs. *cenpf*-MO (n=76) 1.2±0.9 vs. 96±0.6, ****p<0.0001; *cenpf*-MO (n=76) vs. *cenpf*-MO with human *CENPF* RNA (n=122) 96±0.6 vs. 37.3±1.9, *p <0.001].

Therefore, I next analysed expression of *southpaw*, the zebrafish paralogue of Nodal, a member of the TGF beta superfamily, which is essential for organisation of left-right axial structures during early embryogenesis (Figure 4.9). At mid-somite stages, normal LR patterning can be defined by *southpaw* expression in the left lateral plate mesoderm (Kramer-Zucker et al, 2005) (Figure 4.9). In *cenpf* morphant embryos, bilateral, right-sided and absent expression of *southpaw* was significantly increased (Figure 4.9).

To determine whether *cenpf* morphant laterality defects are caused by defects in KV cilia, I next analysed cilia formation in the KV of 8-somite-stage control and *cenpf*-MO injected zebrafish embryos. To do this, ciliary axonemes were labelled with an anti-acetylated tubulin antibody following fixation of stage-matched embryos at 8-somites. Z-stack projection of ApoTome micrographs through the KV floor of control (n=5 embryos) and *cenpf*-MO injected embryos (n=5 embryos) revealed that, the length of *cenpf* morphant cilia were shorter compared to controls [Control mean cilia length (μm ±SD) vs. *cenpf*-MO mean cilia length; 4.8 ±0.8 vs. 2.7±0.6, $p<0.0001$) (Figure 4.10).

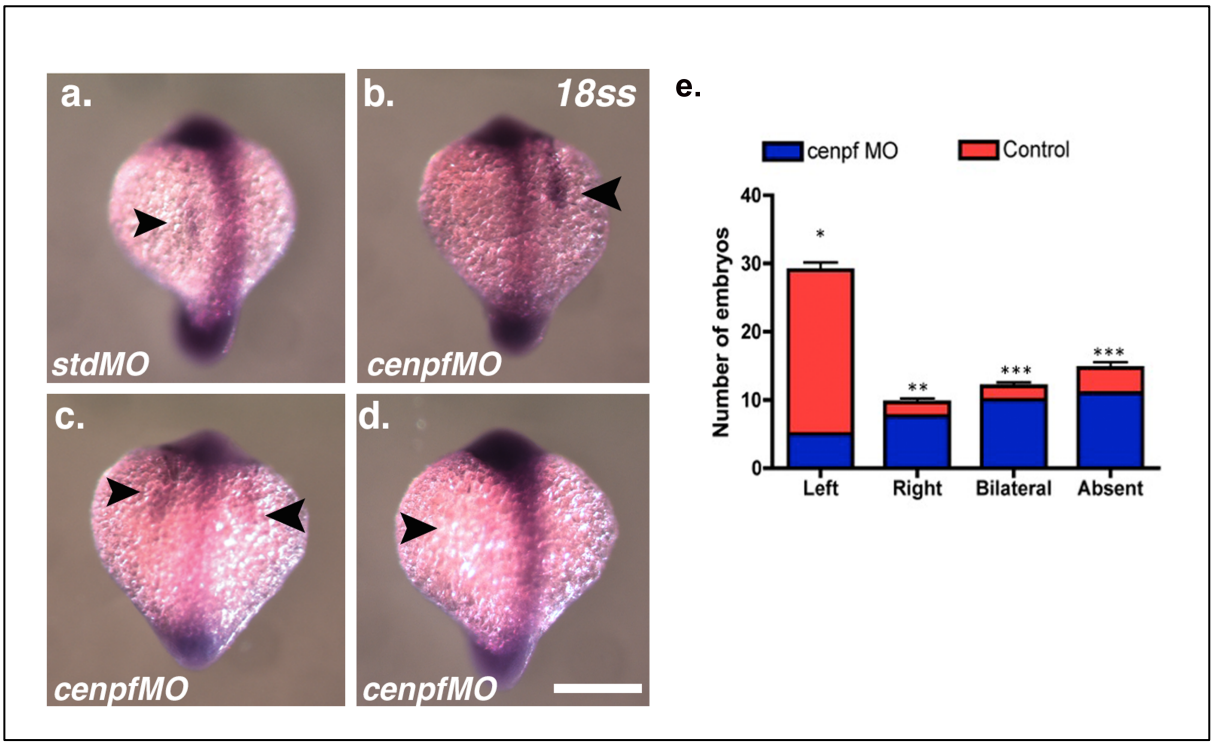

Figure 4.9: *Zebrafish morphants exhibit left-right patterning defects at 18 somites.* (a-d) Representative images of dorsal views of 18-somite stage embryos showing lateral plate mesoderm expression of *southpaw* mRNA by *in situ* hybridisation. Zebrafish *cenpf* knockdown results in left-right patterning defects in 18-somite stage (ss) embryos such as (b) right (arrow), (c) bilateral (arrows), (d) absent (arrow), *southpaw* mRNA expression in the lateral plate mesoderm compared to (a) normal left-sided expression in stage-matched control embryos (arrow, top left panel). Scale bar 100 μm. (e) Quantitative graph demonstrating number of *cenpf* morphants exhibiting right-sided, left-sided, bilateral and absent *southpaw* expression compared to control embryos. Bars represent an average of three experiments.

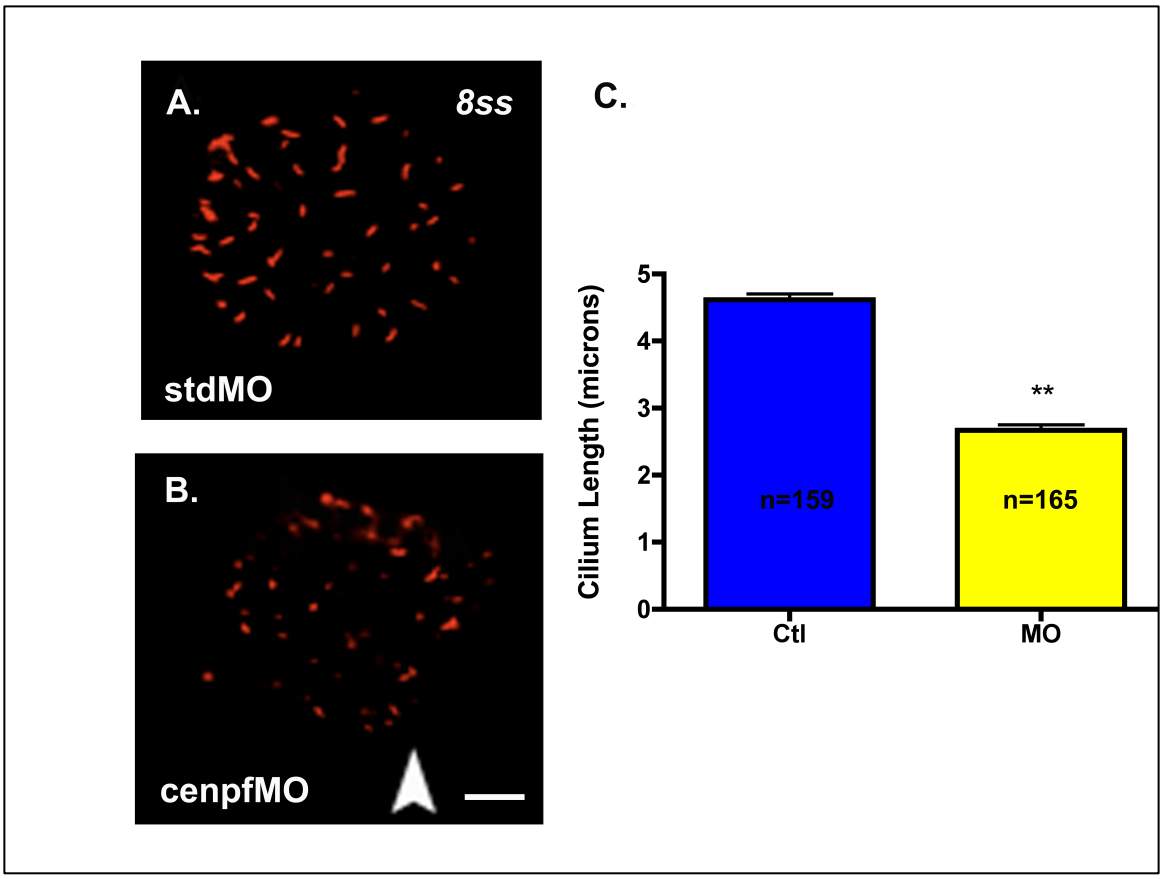

Figure 4.10: *Cenpf morphants exhibit defective Kupffer's vesicle ciliogenesis.* (A, B) Representative images of Kupffer's vesicle of 8-somite stage embryos with immunofluorescence labelling of ciliary axonemes with anti-acetylated tubulin antibodies. (A) Red channel images showing anti- acetylated tubulin immunodetection with Alexa594-conjugated secondary antibody in control embryos. (B) Red channel images showing anti- acetylated tubulin immunodetection with Alexa594-conjugated secondary antibody in *cenpf*-MO injected embryos, white arrow. (C) Mean ciliary length (μm ±SD) is significantly reduced in *cenpf*-MO injected embryos compared to controls, ** $p < 0.0001$. Scale bar 15μm

4.2.5 CENP-F depletion *in vitro* inhibits primary cilia formation.

To test the role of CENP-F in cilia organisation, I next, depleted CENP-F protein levels by shRNA in retinal pigment epithelial cells (RPE). I observed a 3-fold reduction in CENPF mRNA levels and a dramatic reduction in CENP-F protein expression in most cells when compared with control nonsilencing shRNAs (Figure 4.11). Following primary cilia induction by serum starvation for 72 hours, I next determined ciliation by immunolabelling with anti-acetylated tubulin in RPE cells treated with CENP-F shRNA or nonsilencing control shRNA. In the majority of cells treated with shRNA targeting CENP-F (n=227), primary cilia failed to assemble (78%), whereas control cells treated with nonsilencing shRNAs, (n=207) assembled normal full-length primary cilia (22%). Furthermore, transfection of CENP-F depleted cells with full length CENPF rescued defective ciliogenesis while transfection of RPE cells with FLAG CENPF-p.E582X only partially rescued ciliogenesis (Figure 4.12).

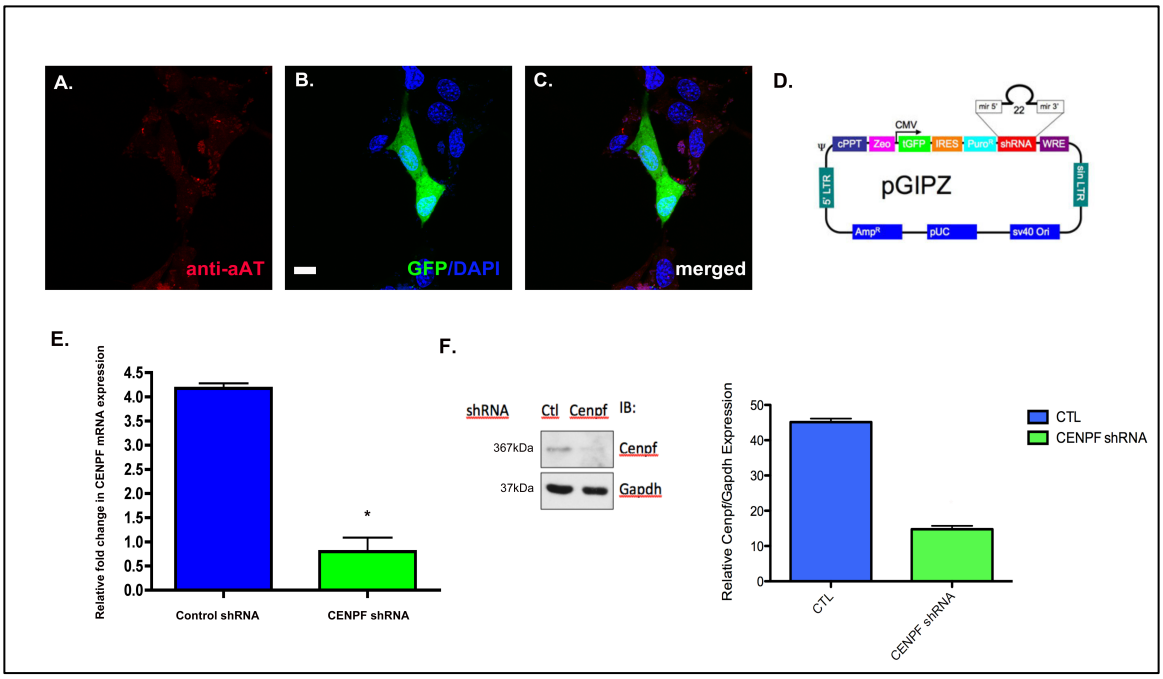

Figure 4.11: *CENP-F depletion inhibits primary cilia formation.* (A-C) Representative image of serum-starved RPE cells treated with GFP-tagged CENP-F shRNA and immunofluorescence labelling of ciliary axonemes with anti-acetylated tubulin antibodies. (D) Schematic of pGIPZ vector with turbo-GFP to track shRNA expression and Puromycin selectable marker. (E) Significant reduction in mean relative fold change in CENPF mRNA expression in CENP-F shRNA-treated RPE cells compared to control nonsilencing shRNA-treated RPE cells. * $p < 0.0001$, standard test. Bars represent mean of three experiments. (F) Western blot showing CENP-F expression in control-shRNA and CENP-F shRNA transduced cells. CENP-F protein expression is significantly reduced at 48 hours post-transfection.

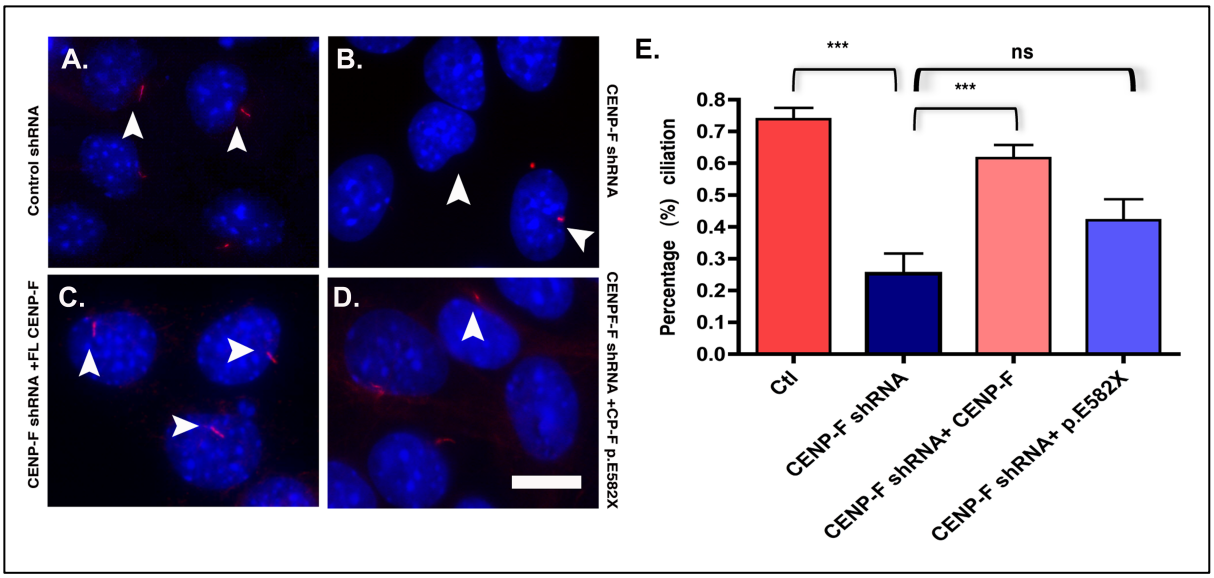

Figure 4.12: *Ciliation in RPE cells treated with control and CENP-F shRNA.* (A-D) Representative images showing ciliation in RPE cells after 72 hours of serum starvation as determined by anti-acetylated tubulin immunolabelling (secondary antibody conjugated with Alexa-568). (A) Normal ciliation in RPE cells transduced with control shRNA. (B) Reduced or absent ciliation in RPE cells transduced with CENP-F shRNA. (C) Rescue of ciliation in RPE cells transduced with CENP-F shRNA and full length CENPF. Scale bar 10µm (D) Transfection of RPE cells with FLAG CENPF-p.E582X only partially rescued ciliogenesis in serum-starved RPE cells. (E) Quantitative graph showing percentage ciliation of RPE cells transduced as follows: control shRNA, CENP-F shRNA, CENP-F shRNA with full length CENPF, CENP-F shRNA with p.E582X CENPF. Control shRNA (n=207 cells) vs. CENP-F shRNA (n=227 cells); 74 ±3.5 vs. 25±6.3, *** p-value<0.0001; CENP-F shRNA (n=227 cells) vs. CENP-F shRNA with full length CENP-F (n=180 cells); 25±6.3 vs. 62±4.1, *** p-value<0.0001; CENP-F shRNA with (n=227 cells) vs. CENP-F shRNA with FLAG CENPF-p.E582X (n=213 cells); 25±6.3 vs. 42.1±6.6, non-significant (ns), p-value<0.09.

4.2.8. CENP-F colocalises with Ift88 and Kif3b *in vitro* and are mislocalised in renal epithelial cells of mutant foetal kidneys

Owing to the fact that vertebrate primary cilia formation and function requires IFT and KIF proteins (Lin et al., 2003; Murcia et al., 2000; Pazour et al., 2000), I hypothesised that CENP-F might function with these proteins during primary ciliogenesis. To test this, I first determined whether CENP-F colocalises with Ift88 and Kif3b in ciliated interphase cells. For Ift88 immunolabelling, I used a rabbit polyclonal anti-IFT88 antibody (Proteintech, 13967-1-AP). Consistent with previous reports, Ift88 localised primarily to the distal portion of the mother centriole near the base of the primary cilium and to the tips and in spots along the length of primary cilia of IMCD3 cells *in vitro* and in renal epithelial cells of wild-type foetal (22 weeks gestation) kidneys *in vivo*. By dual immunofluorescence labelling, I next, showed that Ift88 colocalised with CENP-F at centrosomes in RPE cells transfected with FLAG-tagged full length CENPF (Figure 4.13). In addition, Kif3b also colocalised with CENP-F at centrosomes of NIH 3T3 fibroblasts (Figure 4.14). Next, I sought to determine whether loss of CENP-F function would affect ciliary localisation of Ift88. Compared to ciliary and basal body co-localisation in renal epithelial cells of wild-type foetal kidneys, Ift88 was mislocalised within the cytoplasm of renal epithelial cells of *CENPF*-mutant foetal kidneys (Figure 4.15).

4.2.9. CENP-F interacts with IFT and KIF proteins involved in mitosis and cilia assembly

Following the recent observation that cytoplasmic dynein 1 is required for the microtubule-dependent spindle pole localisation of IFT88 (Delaval et al, 2011), and previous reports that cytoplasmic dynein 1 is required for poleward movement of CENP-F (Yang et al, 2003), I hypothesised that Cenp-F might also be part of a complex with cytoplasmic dynein 1 and IFT88. This hypothesis was further supported by previous and recent observations that Nde-1, which interacts with the C-terminus of CENP-F is crucial in recruiting cytoplasmic dynein 1 to the spindle poles with Lis1 (Yan et al, Mol Cell Biol 2003; Vergnolle et al, 2007; Żyłkiewicz et al, 2011). Furthermore, given the previous localisation of kinesin II with components of the mitotic apparatus such as spindle microtubules and centrosomes (Haraguchi et al., 2006), I hypothesised that CENP-F lies in a mitotic multiprotein complex with key regulators of ciliogenesis that not only included IFT proteins but also kinesin II motor proteins. A combination of gel filtration and co-immunoprecipitation assays of unsynchronised, mitotic and serum-starved HeLa, HEKT293, RPE cells and NIH 3T3 fibroblasts, were used to test this hypothesis. Asynchronous HeLa cell lysates were fractionated over a Superose-6 gel filtration column (Alison Bright, Doxsey Lab, University of Massachusetts). Eluted fractions were probed with antibodies against CENP-F, IFT complex B members: IFT88, IFT52, and IFT20, and motors: cytoplasmic dynein 1 intermediate chain (Dyn IC 74.1) and

Kif3a. CENP-F co-eluted with the IFT proteins and motors, suggesting that it exists as a complex with these proteins (Figure 4.16). Pairwise co-immunoprecipitation assays of unsynchronized, mitotic and serum-starved HEKT293, RPE and 3T3 fibroblasts confirmed that IFT88 precipitates with endogenous CENP-F (Figure 4.17). I did not observe coimmunoprecipitation of IFT88 nor Kif3b when a nonimmune isotype specific IgG control antibody was used (Figure 4.17). As colocalisation of IFT88 was evident with FLAG-tagged full length CENPF and not with an antibody against C-terminus CENP-F, I hypothesised that the N-terminus of CENP-F is important for its interaction with IFT88. Therefore, I next, transfected RPE cells with a vector containing NT-myc CENPF$^{1\text{-}474aa}$ and sought to determine whether endogenous IFT88 pulled down with NT-myc CENPF$^{1\text{-}474aa}$. Following immunoblotting of precipitates of endogenous IFT88 with a MYC antibody, I confirmed that a protein of MW 54kDa immunoblotted with endogenous IFT88 in RPE cells (Figure 4.18), thereby confirming that the N-terminus of CENP-F is important for its interaction with IFT88.

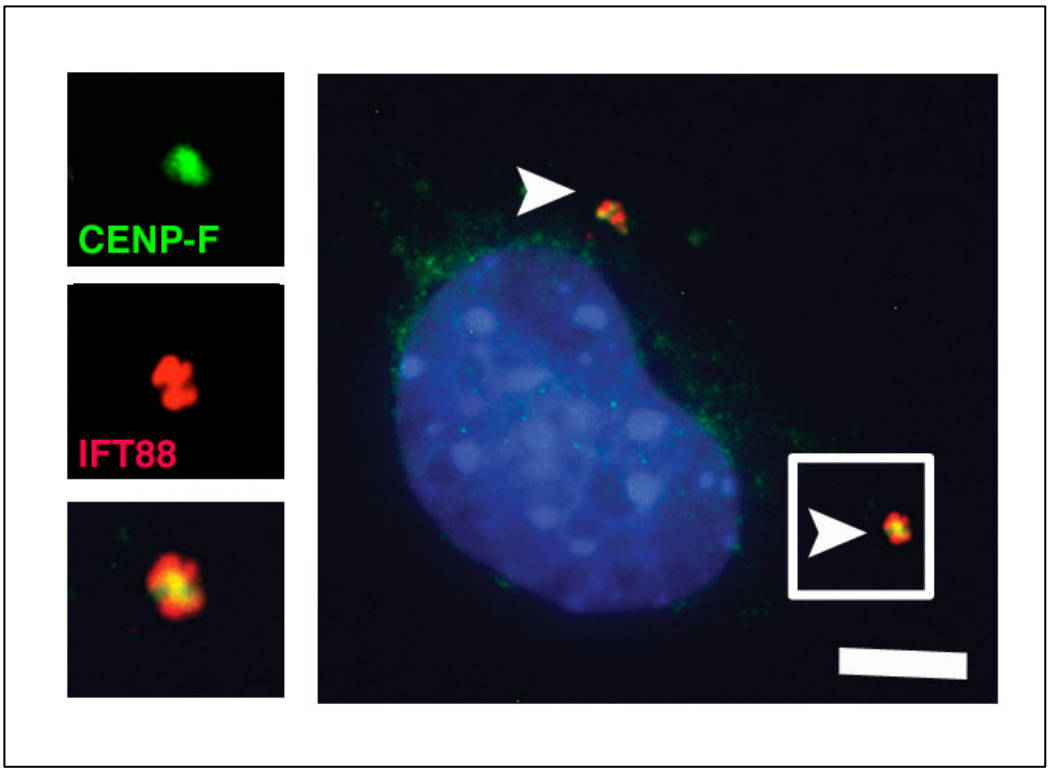

Figure 4.13: *Perinuclear colocalisation of Ift88 with CENP-F.* Representative micrographs of asynchronous RPE cells following dual immunofluorescent labeling of RPE cells with IFT88 and FLAG antibodies following transfection with FLAG-tagged full length CENP-F. Merged red and green channel images showing anti-IFT88 immunodetection with Alexa594-conjugated secondary antibody and anti-FLAG immunodetection with Alexa488-conjugated secondary antibody. CENP-F localizes to the centrosomes with IFT88 (arrows). Scale bar 5 μm. Inset, high power view of CENP-F localization between two IFT88 foci.

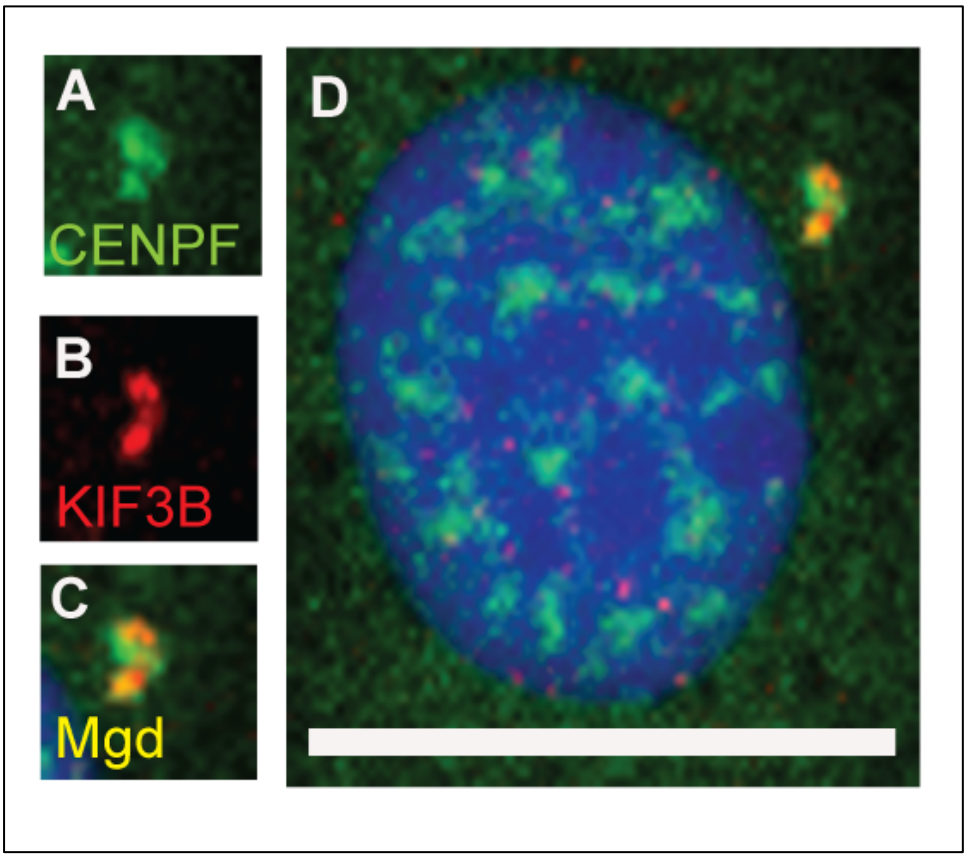

Figure 4.14: *Colocalisation of CENP-F with Kif3b in interphase NIH 3T3 fibroblasts.* (A-D) Representative image of NIH 3T3 fibroblast with immunofluorescence labelling of centrosomes with anti-CENPF and anti-Kif3b antibodies. (A) Green channel images showing anti-CENPF immunodetection with Alexa488-conjugated secondary antibody. (B) Red channel images showing anti-Kif3b immunodetection with Alexa594-conjugated secondary antibody. (C, D) Merged images of corresponding micrographs obtained through green and red channel images. Sections are counterstained with DAPI. Scale bar 10μm

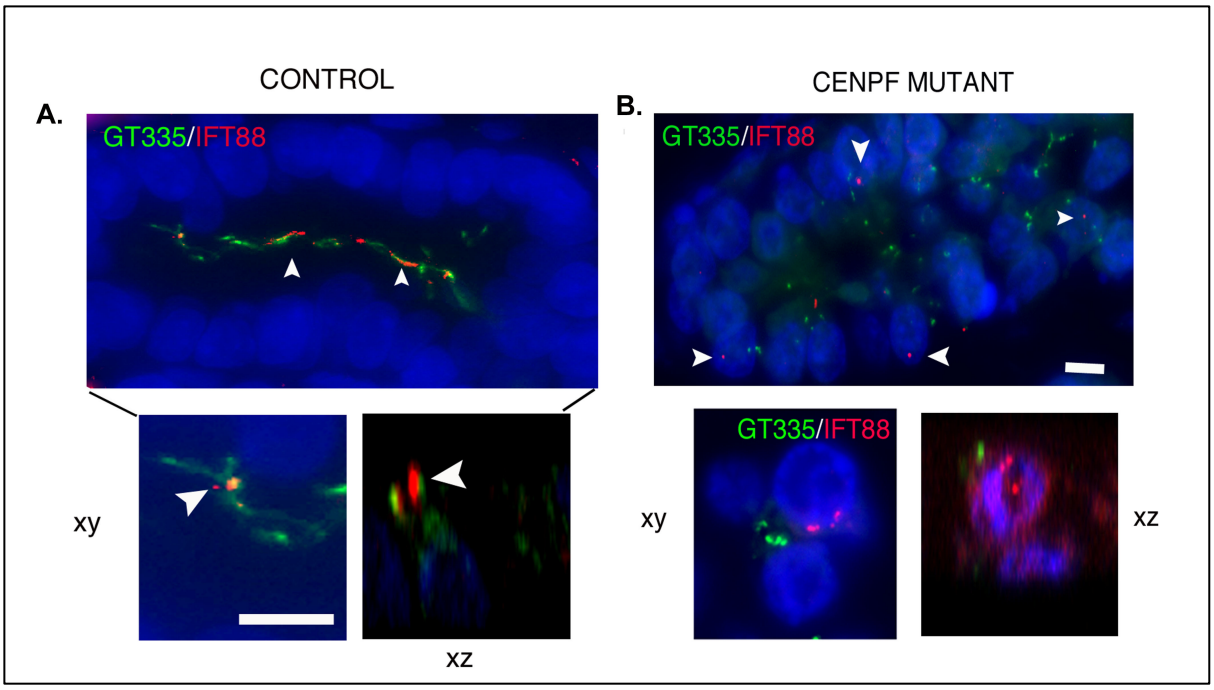

Figure 4.15: *Mislocalisation of Ift88 in renal epithelial cells of mutant CENPF foetal kidneys.* (A, B) Representative micrographs of human fetal renal tubules following dual immunofluorescent labeling with anti-GT335 and anti-IFT88 antibodies. (A) IFT88 localizes to long cilia within the lumina of renal collecting ducts of 22 week old wild-type human fetuses (arrows, left panel). (B) IFT88 does not localize to cilia of *CENPF* mutant fetal kidneys (arrows, right panel). Scale bar 10 µm. Inset shows absent ciliation in cell with intranuclear IFT88. Scale bar 10 µm.

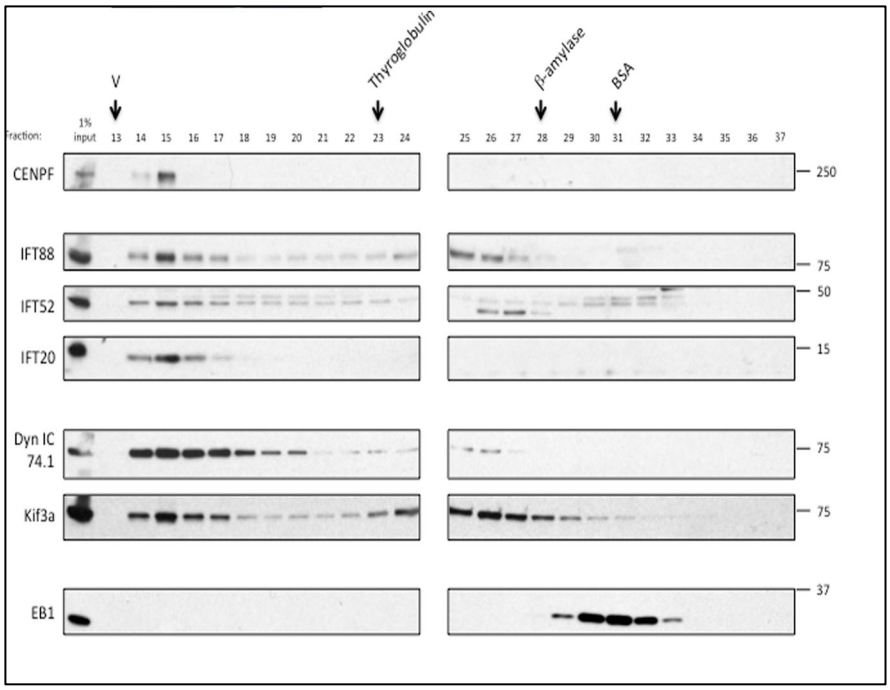

Figure 4.16: Gel filtration assay demonstrating co-elution of CENP-F, IFT complex B members IFT88, IFT52, and IFT20, and motors: cytoplasmic dynein 1 intermediate chain (Dyn IC 74.1) and Kif3a. Arrows indicate peak elution fractions for calibration proteins: Thyroglobulin (669 KDa; fraction 23), β-amylase (200 KDa, fraction 28) and BSA (67 KDa, fraction 31). V, void volume. (Courtesy of Alison Bright, Doxsey Lab, University of Massachusetts).

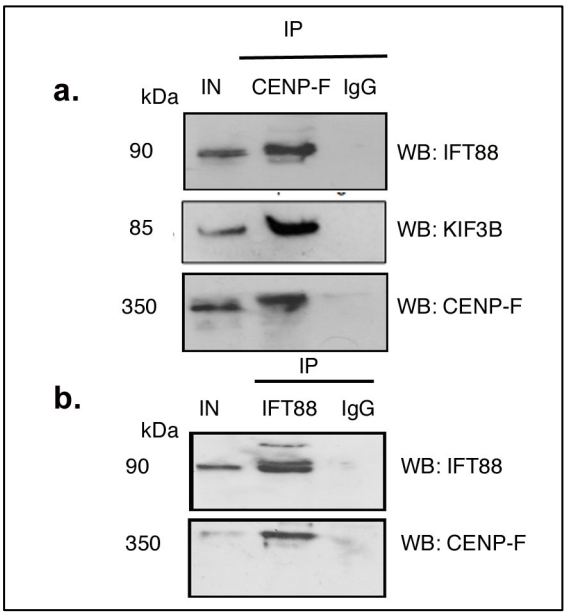

Figure 4.17: *Endogenous IFT88 and KIF3B precipitate with endogenous CENP-F in HEKT293 cells.* (a) Representative images of co-immunoprecipitation experiments carried out on protein lysates from mitotic HEKT293 cells containing endogenous CENP-F (size 367kDa). Immunoblots show that IFT88 and KIF3B co-immunoprecipitates with endogenous CENP-F while an IgG isotype control does not co-immunoprecipitate with IFT88. IN= input; ten per cent of total input is indicated. (b) Representative images of co-immunoprecipitation experiments carried out on protein lysates from serum-starved HEKT293 cells containing endogenous IFT88. Immunoblots show that IFT88 co-immunoprecipitates with endogenous CENP-F while an IgG isotype control does not co-immunoprecipitate with IFT88. IN= input; ten per cent of total input is indicated

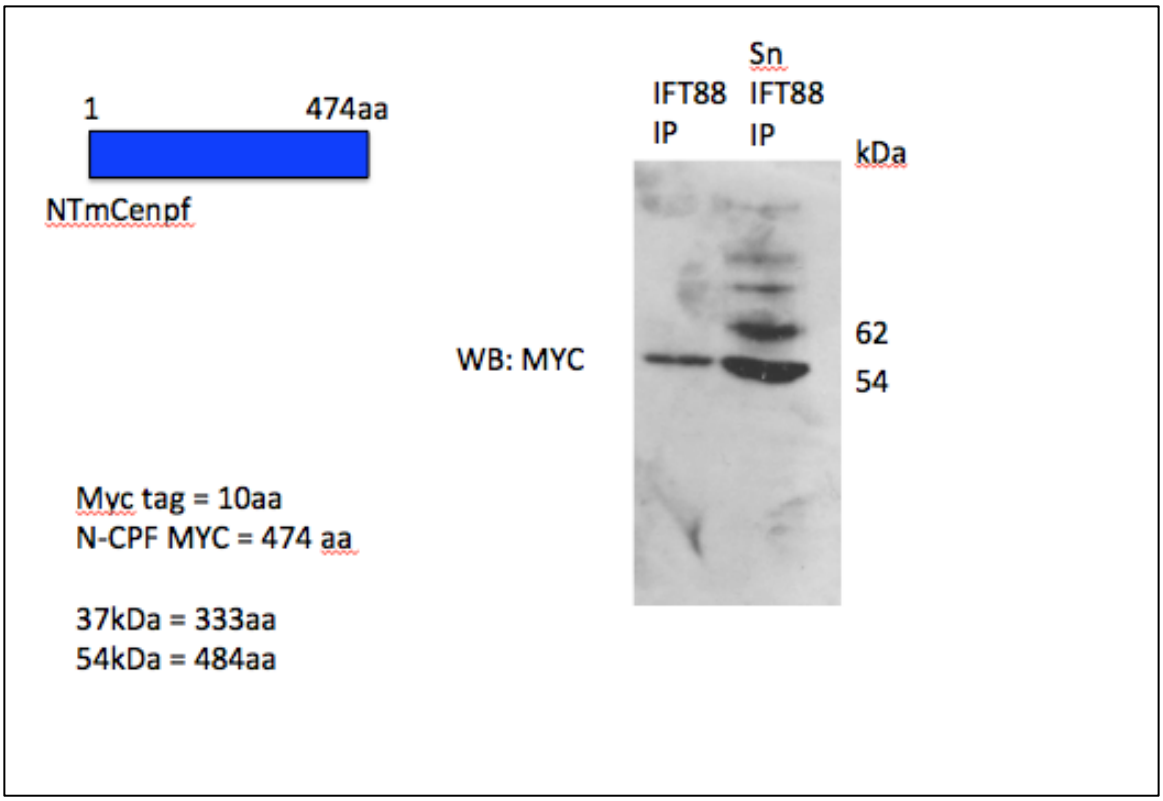

Figure 4.18: *Endogenous IFT88 interacts with the N-terminus of CENP-F.* Representative images of co-immunoprecipitation experiments carried out on protein lysates from confluent unsynchronised RPE cells containing endogenous IFT88 and transfected with NT-myc CENPF1-474aa. Immunoblots show that NT-myc CENPF1-474aa co-immunoprecipitates with endogenous IFT88. IN= input; ten per cent of total input is indicated.

Immunoprecipitation experiments with endogenous CENP-F, failed to identify an interaction with the intermediate chain of cytoplasmic dynein 1, I next determined whether CENP-F interacted with other proteins implicated in dynein function. As the dynein intermediate chains interact directly with the p150 ^{Glued} doublet of dynactin (Vaughan and Vallee, 1995), I sought to determine whether CENP-F interacts with the p150 ^{Glued} doublet of dynactin. As a result, I used co-immunoprecipitation assays of unsynchronised RPE cells to confirm that endogenous CENP-F interacts with the p150 ^{Glued} doublet of dynactin (Figure 4.19). I did not observe coimmunoprecipitation of CENP-F when a non-immune isotype specific IgG control antibody was used (Figure 4.19). Together these biochemical data suggest that CENP-F, IFT88, Kif3b and p150 ^{Glued} doublet of dynactin form a multiprotein complex in mitotic and interphase vertebrate cells, which is also likely to involve cytoplasmic dynein 1 during early ciliogenesis.

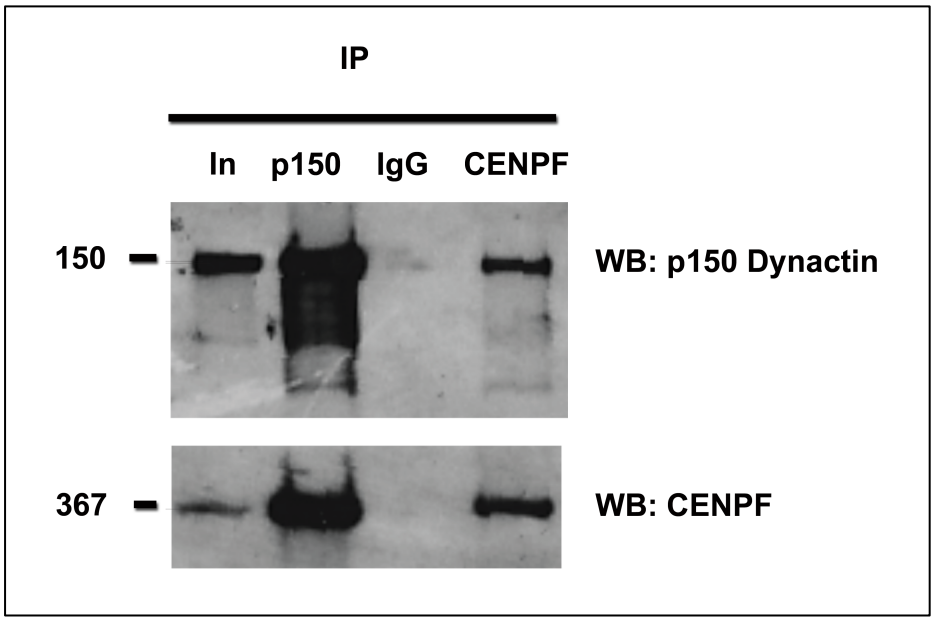

Figure 4.19: *CENP-F interacts with the p150 ^{Glued} dynactin subunit.*

Representative images of co-immunoprecipitation experiments carried out on protein lysates from unsynchronised confluent RPE cells containing endogenous p150 ^{Glued} dynactin. Immunoblots show that CENP-F co-immunoprecipitates with p150 ^{Glued} dynactin and vice versa. IN= input; ten per cent of total input is indicated.

4.2.10 Mutant *CENPF* human foetal kidneys have short stumpy cilia reminiscent of phenotypes of IFT-dynein mutant cilia.

Following my observations that *cenpf* morphant zebrafish show defective KV ciliogenesis together with a lack of ciliation in CENP-F depleted cells and immunoprecipitation experiments suggesting CENP-F interactions with key regulators of ciliogenesis, I next sought to determine what were the consequences of mutant CENP-F on mammalian ciliogenesis *in vivo*. This analysis was facilitated by immunofluorescence labelling of ciliary axonemes with anti-acetylated tubulin antibodies in kidney sections of autopsy tissue from a foetus carrying the *CENPF* mutations identified in Chapter 3 (Figure 4.15, 4.20). While renal epithelial cilia were noted to be present, morphologically, cilia were noted to have a shortened and bulbous distal end appearance, which were reminiscent of phenotypes of IFT-dynein mutant cilia (Merrill et al., 2009; Ocbina et al., 2011)(Pazour et al, 1999; Porter et al, 1999) (Figure 4.15, 4.20). In *Chlamydomonas* dynein-2 mutant flagella, these morphological appearances have been shown to result from accumulation of IFT particles at the flagellar tips (Pazour et al, 1999; Porter et al, 1999).

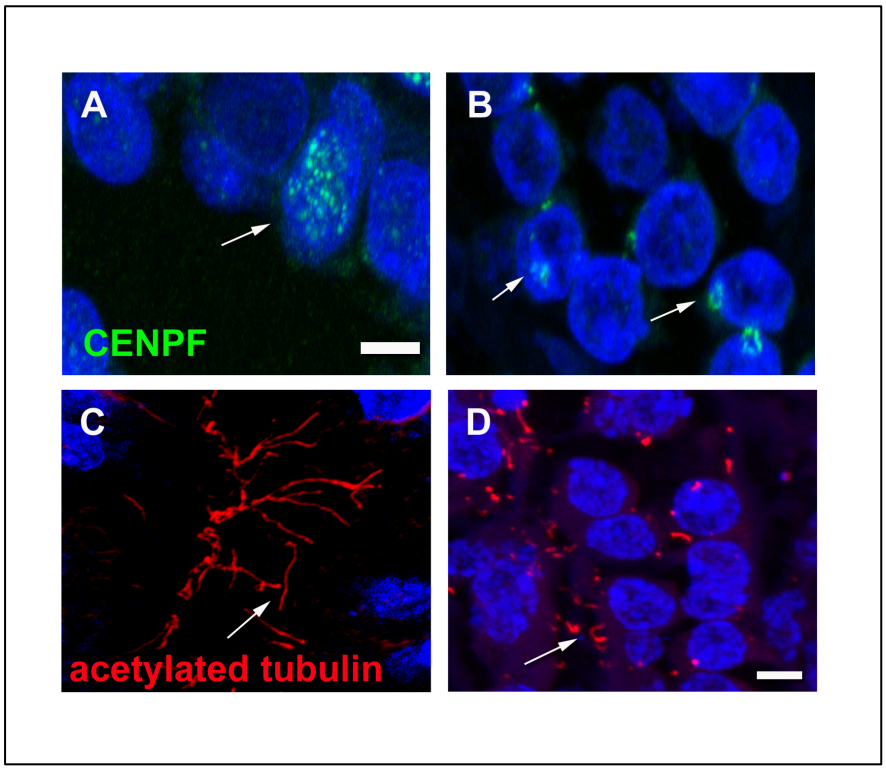

Figure 4.20: *Mutant CENPF human foetal kidneys have short stumpy cilia reminiscent of defective dynein transport.* (A-D) Representative images of renal epithelial cilia of 22 week old wild-type (WT) foetuses (A, C) and foetuses with compound heterozygous CENPF mutations (B, D). (A, B) CENPF immunodetection with Alexa488-conjugated secondary antibody. (A) Nuclear localisation of Cenp-F in renal epithelial cells of wild-type foetuses (white arrow). Scale bar 10 µm (B) Cytoplasmic localisation of Cenp-F in affected foetuses (white arrows). (C, D) Red channel images showing anti-acetylated tubulin immunodetection with Alexa594-conjugated secondary antibody in WT and mutant foetuses. (C) Long cilia are observed in lumina of collecting ducts of WT foetuses (white arrow). (D) Short cilia are evident on renal epithelial cells of *CENPF* mutant foetal kidneys (white arrow). Sections are counterstained with DAPI. Scale bar 10 µm

4.3 DISCUSSION

4.3.1 Identification of a novel role for CENP-F in ciliogenesis

Several studies have investigated the role of CENP-F during mitosis (Serio et al., 2011), (Vergnolle et al, 2007), (Evans et al., 2007; Feng et al., 2006), (Ma et al., 2006), (Bomont et al., 2005), (Holt et al, 2005), (Yang et al., 2005), (Chan et al., 1998), (Zhu et al., 1995). CENP-F depletion leads to a spindle checkpoint-dependent mitotic delay that has been ascribed to its role in recruiting dynein and CENP-E to the kinetochore (Chan et al, 1998, Yang et al, 2005; Feng et al, 2006). CENP-F has also been found in the cytoplasm and has been shown to play a role in vesicular transport and complexes with SNARE proteins including syntaxin 4 in the regulation of vesicular transport (Pooley et al., 2008). More recently, a centrosomal localisation has been shown for murine CENP-F, where it acts as a major regulator of microtubule nucleation (Moynihan et al, 2009). Here, I have identified a novel role for CENP-F in the regulation of ciliogenesis, initially suggested by a comparative genomics approach whereby the *Chlamydomonas* flagellar assembly protein, FAP58, shares 40% sequence similarity with human *CENPF*. Following this preliminary bioinformatics analysis, I subsequently demonstrated that CENP-F is localised to the basal bodies of serum starved 3T3 fibroblasts, which further supported a role for CENP-F in cilia formation and/or function.

In order to explore the temporal role of CENPF in embryogenesis and in the absence of a readily available mammalian model of CENPF loss of function, I chose to explore the phenotypic consequences of *cenpf* gene knockdown in the zebrafish, given the 60% sequence similarity of *D. rerio cenpf* to human *CENPF*. Consequently, I observed phenotypic features that were noted in human foetuses carrying *CENPF* mutations at autopsy such as embryonic lethality, craniofacial defects, hydrocephalus and pronephric cysts. Additional features observed in *cenpf* morphant zebrafish included abnormal heart looping, increased body axis curvature and block-shaped somites, features of which have been described with other zebrafish ciliopathy mutants (Kramer-Zucker et al, 2005; Delaval et al 2011). Owing to the high rate of early embryonic lethality and abnormal heart looping, I hypothesised that *cenpf* may play a role in KV function. Analysis for left-right patterning defects in mid-somite staged embryos revealed a combination of right-sided, bilateral and absent expression of *southpaw* in the lateral plate mesoderm in contrast to its normal left-sided expression in control embryos. Consistent with previous reports (May-Simera et al., 2010) randomisation of *southpaw* expression was also shown here to be a consequence of shortened KV cilia. Further corroborating evidence for a role of CENP-F in vertebrate ciliogenesis came from the observation that CENP-F protein depletion *in vitro* resulted in a significant reduction in ciliation in cells treated with CENPF shRNA compared to control non-silencing shRNA, an

effect which has been described with other centrosomal proteins such as pericentrin (Jurczyk et al., 2004).

4.3.2 CENP-F exists in a multiprotein complex with key regulators of ciliogenesis that also function in mitosis

In order to understand the mechanisms underlying the ciliogenesis defects with CENP-F depletion observed *in vitro* and *in vivo*, several clues existed in recent literature implicating ciliogenic functions for other mitotic spindle pole proteins such as Nde1 and BubR1 (Kim et al, 2011), (Miyamoto et al., 2011). Recent elucidation of a previously uncharacterised Nde1-LC8-IFT88 pathway in ciliogenesis and an elegant study reporting the cytoplasmic dynein 1-dependent spindle pole localisation of IFT88 (Delaval et al, 2011; Kim et al 2011) suggested that other spindle pole proteins might be implicated in ciliogenesis. Supporting this hypothesis were previous observations of poleward movement of CENP-F with cytoplasmic dynein 1 in late anaphase (Yang et al, 2003), a process that is dependent on Nde1, (Vergnolle et al, 2007). Given that CENP-F interacts with Nde1, I hypothesised that CENP-F likely interacts with IFT88. Co-immunoprecipitation assays in protein lysates from mitotic, unsynchronised and serum-starved cells confirmed that Ift88 and Kif3b pulled down with endogenous CENP-F. The converse was also proven to be true, which was highly suggestive that CENP-F exists in a multiprotein complex that perhaps has dual roles in mitosis and ciliogenesis.

Interestingly, in the context of human disease, impaired cilia formation has been recently reported in patients with Mosaic Variegated Aneuploidy (MVA) syndrome, a disorder caused by mutations in *BUBR1* and *CEP57*, a mitotic spindle checkpoint regulator (Miyamoto et al, 2011), (Snape et al., 2011). BUBR1, with other proteins (Mad2, CENP-E, 3F3/2) implicated in spindle checkpoint inactivation are recruited to spindle poles from kinetochores by CENP-F, a process that relies on cytoplasmic dynein-mediated transport. Therefore, it is highly likely that other proteins within the spindle checkpoint regulatory complex will be implicated in cilia function.

4.3.3. Ciliary morphology in *CENPF* mutant human kidneys is reminiscent of an IFT-Dynein defect

Interestingly, in *CENPF* mutant human renal epithelial cells, ciliogenesis defects were observed in some but not all cells based on immunolabelling with an anti-acetylated tubulin and anti-GT335 antibodies. Where cilia were observed, abnormal cilia morphology was noted and was reminiscent of IFT-dynein phenotypes such as that described in individuals with *DYNC2H1* mutations (Merrill et al, 2009) and more recently, in *Dync2h1* mutant mice (Ocbina et al, 2011). Previous studies in *Chlamydomonas dynein-2* mutant flagella showed that these shortened and bulbous cilia were consequences of accumulation of IFT particles at the flagellar tips (Pazour et al, 1999; Porter et al, 1999). Supporting this has been the recent report that double the amount of

IFT88, accumulated in *Dync2h1*$^{lln/lln}$ ciliary axonemes (Ocbina et al, 2011). Given the localization of CENP-F to the subdistal appendages and its putative interactions with p150 ^{Glued} dynactin, it possible that CENP-F might act as a microtubule anchor at the subdistal appendages where ciliary cargo including IFT proteins are loaded during ciliogenesis.

In the absence of the IFT-dynein retrograde motor, Smo, Gli2 and Ptch1 traffic into cilia and accumulate which disrupts downstream Sonic hedgehog signal transduction. Future analysis of *CENPF* deficient tissue should yield important insights into whether certain phenotypic features of this novel syndrome are consequences of aberrant SHH signal transduction.

4.3.4 SUMMARY

In this chapter, I have elucidated a potential explanation for the phenotypic features observed in the affected foetuses carrying mutations in *CENPF*. A novel function for CENP-F in cilia formation and function is proposed through modelling *cenpf* loss of function in *D. rerio* and is supported by the interactions found with IFT88 and Kif3b, key regulators of ciliogenesis together with its ultrastructural localization to the subdistal appendages. Furthermore, my data supports emerging evidence for the existence of a cytoplasmic dynein 1– dependent multiprotein complex that has dual roles in mitosis and ciliogenesis. Enticingly, the morphological appearances of *CENPF* mutant cilia are reminiscent of IFT-dynein phenotypes and further elucidation of the molecular nature and function of this complex in both mitosis and ciliogenesis should yield mechanistic insight into the phenotypic features observed in ciliopathy disorders.

CHAPTER 5. CENPF INTERACTS WITH PROTEINS INVOLVED IN MITOTIC SPINDLE ORIENTATION AND CENPF DEFICIENCY CAUSES DEFECTIVE KIDNEY DIFFERENTIATION.

5.1 INTRODUCTION

In preceding chapters, I have shown a novel role for CENP-F, a component of the spindle checkpoint inactivation complex, in ciliogenesis. Interestingly, impaired cilia formation has been reported in patients with Mosaic Variegated Aneuploidy (MVA) syndrome, a disorder caused by mutations in *BUBR1,* a mitotic spindle checkpoint regulator (Miyamoto et al, 2011; Snape et al, 2011) and which has previously been shown to interact with the C-terminus of CENP-F. BUBR1, with other proteins (Mad2, CENP-E, 3F3/2) implicated in spindle checkpoint inactivation are recruited to spindle poles from kinetochores by CENP-F, a process that relies on cytoplasmic dynein 1 transport. Recent work proposes that spindle-pole and chromosome-derived signals that regulate cytoplasmic dynein localisation generate an intrinsic code for spindle position and orientation (Kiyomitsu and Cheeseman, 2012). Intriguingly, cytoplasmic dynein 1 is required for the microtubule-dependent spindle pole localisation of IFT88 during mitotic spindle orientation, a mechanism, which may help, explain the pathogenesis of ciliopathy-related phenotypes such renal cystogenesis (Delaval et al, 2011).

Given the identification of CENP-F as a novel interacting partner of IFT88 in mitotic and interphase cells, I hypothesised that CENP-F may also be implicated in mitotic spindle orientation. This hypothesis was supported by previous observations of multi-astral and aberrant bipolar spindles in CENPF-

depleted cells (Holt et al, 2005). Spindle bipolarity is achieved by the action of multivalent minus-end directed microtubule motor complexes, including NuMA, cytoplasmic dynein and dynactin in frogs (Heald et al., 1996) and the kinesin-like motor *Ncd* in *Drosophila* (Matthies et al., 1996). These motor complexes tether parallel microtubule bundles and stabilize converging microtubules into spindle poles on either side of the centrally located chromatin. In this chapter, I will explore the role of CENP-F in mitotic spindle orientation and determine potential mechanisms of how CENP-F could regulate differentiation of the renal parenchyma.

5.2 RESULTS

5.2.1 Histological analysis of human mutant *CENPF* kidneys suggests defective differentiation of the renal parenchyma

Given the autopsy reports of renal hypoplasia in *CENPF* mutant foetuses, a systematic analysis of metanephric mesenchymal differentiation was next undertaken to further delineate the nature of the renal phenotype observed. Histological analysis of haematoxylin and eosin (H&E) stained kidney sections from 22-week-old foetuses carrying the *CENPF* compound heterozygous mutations described in Chapter 3 were compared with kidney sections from 22-week-old control human foetuses. Morphological analysis suggested that mutant kidneys exhibited features of abnormal nephrogenesis exhibiting fewer S-shaped bodies (glomerular precursors), glomeruli and tubules (Figure 5.1).

Compared to age-matched wild-type foetal kidney sections, a reduction in nephron number was suggested. To investigate this observation further, I next quantified the number of mature glomeruli. Kidney volume and glomerular number was measured according to published protocols (Bertram et al. 1995). Kidneys sectioned at 5 μm thickness were collected at 100 μm intervals and stained with Haematoxylin and Eosin. The area of the tissue section was measured with a compound microscope (see Materials) and multiplied by the section thickness. Total kidney volume is the sum of volumes for each section. Glomeruli were identified by the presence of both a podocyte layer and Bowman's capsule. A quantitative difference was observed (Figure 5.1) which suggested that CENP-F deficiency results in defective nephrogenesis.

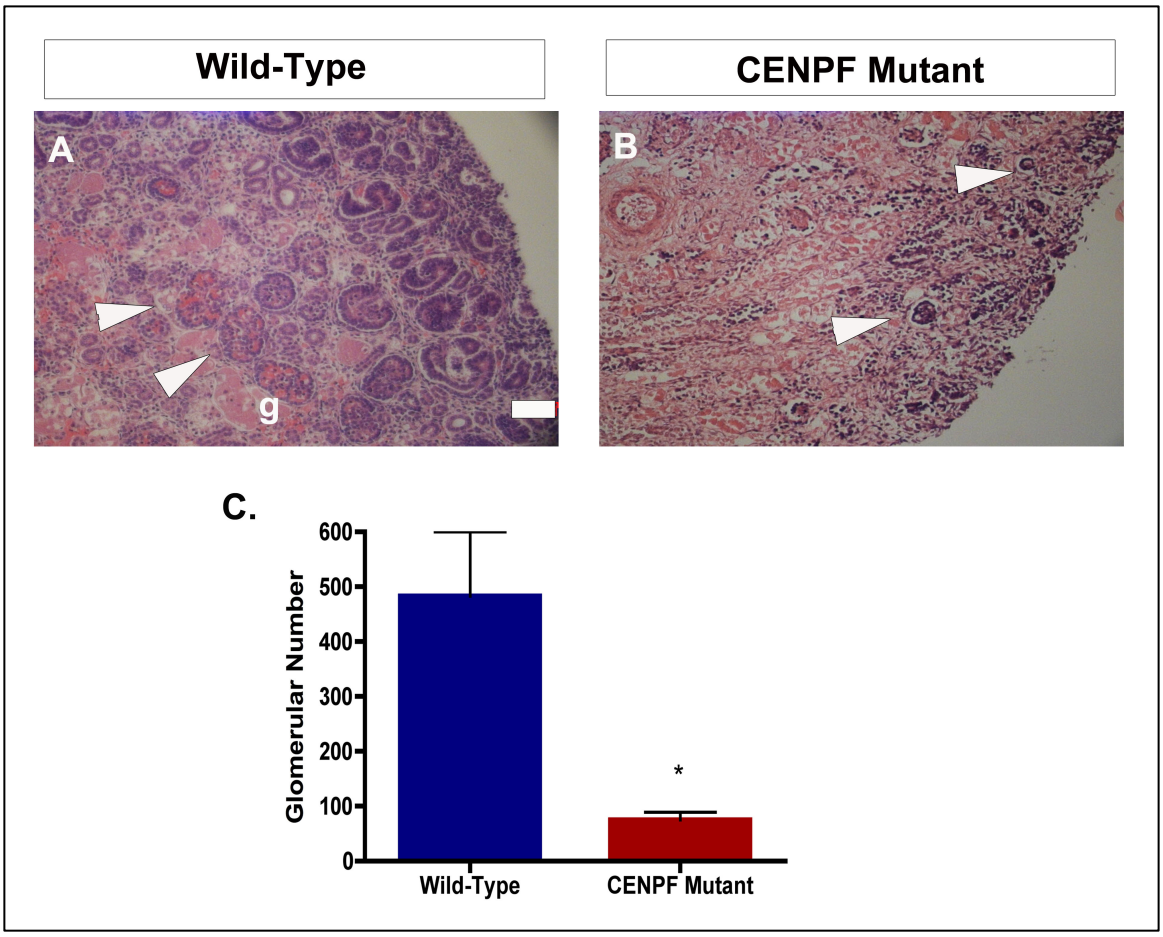

Figure 5.1: *Histological analysis of human mutant CENPF kidneys suggest defective differentiation of the renal parenchyma* (A, B) Representative images of haematoxylin and eosin stained kidney sections from 22 week old wild-type kidneys (A) and kidneys from affected foetuses carrying compound heterozygous mutations in *CENPF*. Scale bar, 100μm. (A) Normal cortical nephrogenesis is evident with S-shaped bodies (s) and glomeruli (g) evident. (B) Abnormal cortical nephrogenesis in *CENPF*-mutant kidneys demonstrating a disorganised cortical area and immature glomeruli. (C). Quantitative graph showing a reduction in glomerular number. Wild-type glomerular number vs. *CENPF* mutant glomerular number 483.3± 116.7 vs. 75±14.4, * $p < 0.02$.

5.2.2. Mutant *CENPF* nephrogenic structures display aberrant NuMA expression within differentiating nephrogenic structures

A key step during metanephric kidney development, is the induction of the metanephric mesenchyme by the outgrowing ureteric bud. Reciprocal signalling between the metanephric mesenchyme and the ureteric bud triggers the ureteric bud to initiate its first T-branch and induces the metanephric mesenchyme to condense and proliferate. If these tissues fail to interact properly, renal agenesis or severe renal hypoplasia will occur. As renal hypoplasia has been described in SALL1-deficient individuals (Towne-Brock Syndrome) and Sall1-deficient metanephric mesenchyme (Kiefer et al., 2003), I next determined, the expression of Sall1 in wild-type and *CENPF*-deficient kidneys. Sall1 is a multi-zinc finger transcriptional regulator that is expressed in the mesenchyme fated to become nephrogenic blastema and is essential for ureteric bud invasion of the metanephric mesenchyme (Nishinakamura et al., 2001). In control foetuses, Sall1 expression was comparable to that of *CENPF* mutant foetuses, thereby suggesting CENP-F does not play a role in the early specification of the metanephric mesenchyme (Figure 5.2).

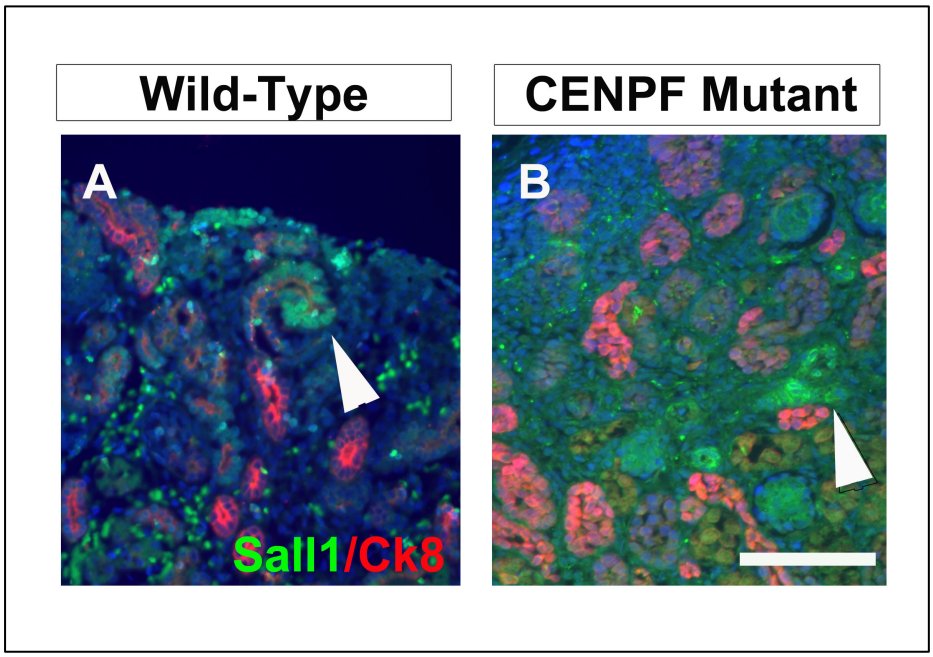

Figure 5.2: *Sall1 expression is similar in wild-type and CENPF-mutant kidneys at 22 weeks gestation.* (A, B) Representative images of kidney sections from 22 week old wild-type kidneys (A) and kidneys from affected foetuses carrying compound heterozygous mutations in *CENPF*. Merged images of micrographs obtained through green channel (Sall1, undifferentiated metanephric mesenchyme, white arrows) and red channel (cytokeratin-8, ureteric buds) images. Sections are counterstained with DAPI. Scale bar 300 μm.

Owing to a reduction in the number of mature glomeruli, I next sought to determine whether the processes governing glomerular specification were present. During mammalian kidney development, the developing nephrogenic structures undergo a series of three primitive transformations from the renal vesicle (RV), to the comma and S-shaped bodies (Figure 5.3). During the S-shaped body stage of glomerulogenesis, the proximo-distal fates of the nephron are specified by asymmetric expression of segment-specific markers (Cheng et al, 2007). Given recent reports that the Gαi-LGN/AG3-NuMA-p150 ^{Glued} dynactin complex is implicated in asymmetric cell division which govern cell fate determination (Williams et al, 2011) and the interactions identified between Cenp-F and p150 ^{Glued} dynactin in Chapter 4, I next sought to determine the expression of NuMA, a component of this pathway, in S-shaped bodies of *CENPF*-mutant kidneys. In control kidneys, NuMA expression was predominantly located within the distal limb of S-shaped bodies while in *CENPF*-mutant kidneys, NuMA was appeared to be expanded along the middle limb of S-shaped bodies. These data suggest that Cenp-F may regulate the localisation of components of the NuMA-p150 ^{Glued} dynactin complex during differentiation of nephrogenic structures.

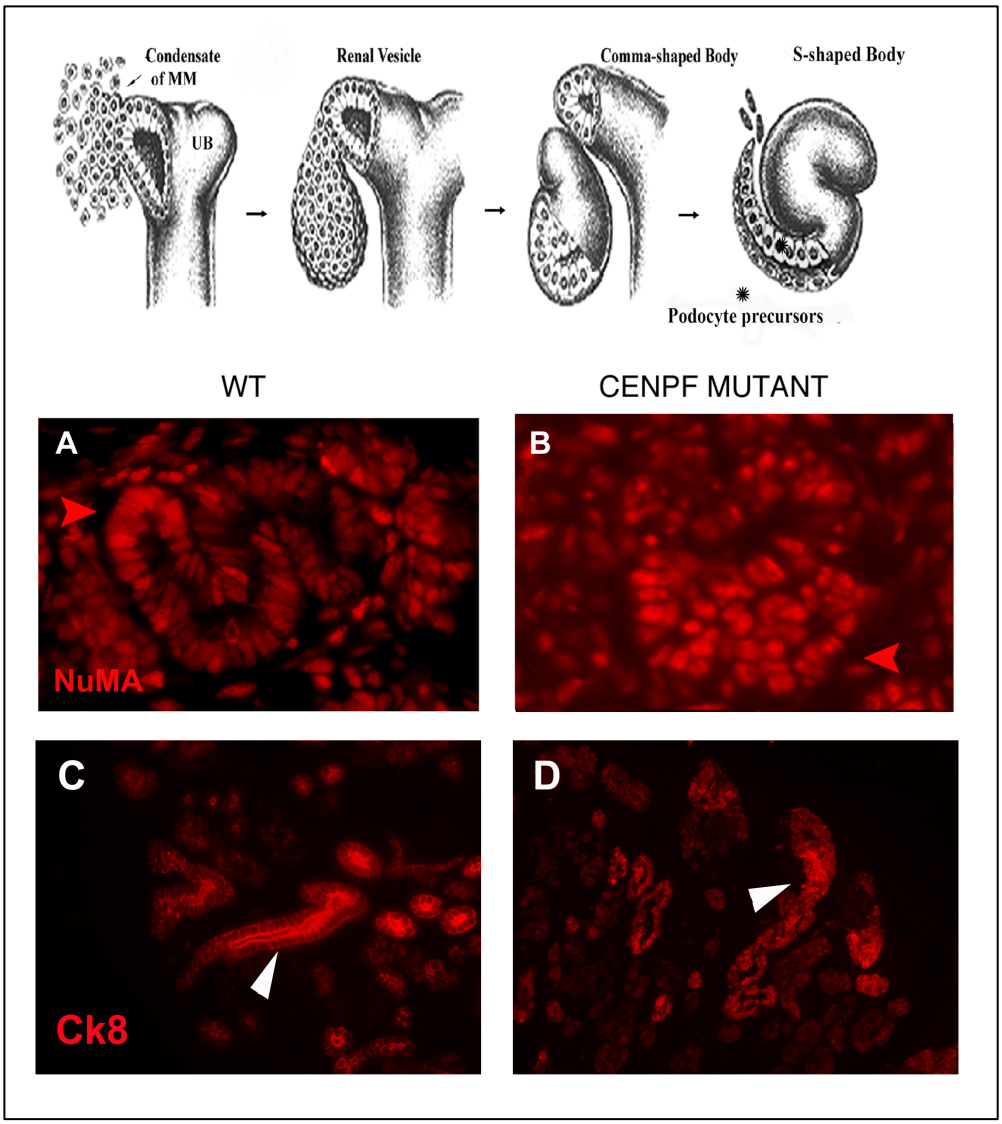

Figure 5.3: *Expansion of NuMA expression in S-shaped bodies of CENPF mutant kidneys*. (A, B) Representative images of merged micrographs of S-shaped bodies of wild-type (A) and *CENPF* mutant (B) kidneys stained with anti-NuMA (red channel, red arrows), anti-CENPF (green channel) and counterstained with DAPI. (C, D). Representative images of ureteric bud derivatives of wild-type (C) and *CENPF* mutant (D) kidneys stained with anti-cytokeratin 8 (red channel, white arrows) showing defective planar polarization of epithelium lining collecting ducts of *CENPF* mutant kidneys.

5.2.3. CENPF interacts with NuMA and Par3, proteins involved in asymmetric cell division

In order to understand the mechanisms underlying defective renal differentiation in *CENPF* mutant kidneys, I next explored the hypothesis that CENP-F is a component of the Gαi-LGN/AGS3-NuMA-p150^{glued} dynactin complex recently implicated in asymmetric cell division and mitotic spindle orientation processes which govern cell fate determination (Williams et al., 2011), (Kiyomitsu et al, 2012). This hypothesis was supported by co-immunoprecipitation experiments in Chapter 4 showing CENP-F and p150 ^{Glued} dynactin interactions in addition to previous reports of multiastral and bipolar spindles in CENP-F depleted cells (Holt et al, 2005). Expression of the cortical targeting protein, NuMA, revealed misoriented and multipolar spindles were evident in renal tubular epithelia of affected foetuses (Figure 5.4). This observation supported the findings of my pairwise co-immunoprecipitation assays of unsynchronized HEKT293 cells which confirmed interactions with CENP-F, NuMA and Par3 (Figure 5.4).

5.2.4. Renal tubular epithelia of *CENPF* mutant kidneys exhibit abnormal mitotic spindle orientation

Given the role of the Gαi-LGN/AGS3-NuMA-p150^{glued} complex in mitotic spindle orientation and my findings that CENP-F interacts with components of this complex in addition to IFT88 which has also recent

implicated in mitotic spindle orientation, I next sought to determine the orientation of the mitotic spindle in renal epithelia of the collecting ducts of CENPF mutant foetuses compared to age-matched wild-type controls. The orientation of mitotic angles to the longitudinal axis of the tubule was determined by dual immunofluorescent labeling of mitotic DNA with an anti-phosphohistone H3 rabbit polyclonal antibody (Karner et al., 2009), (Karner et al, 2009), and of collecting ducts with an anti-cytokeratin 8 mouse monoclonal antibody (Karner et al, 2009). The majority of cell divisions within the collecting duct of wild-type foetal kidneys were well oriented with 83% being oriented within 30 degrees of the longitudinal axis of the tubule compared to 65% of *CENPF* mutant kidneys (Figure 5.5).

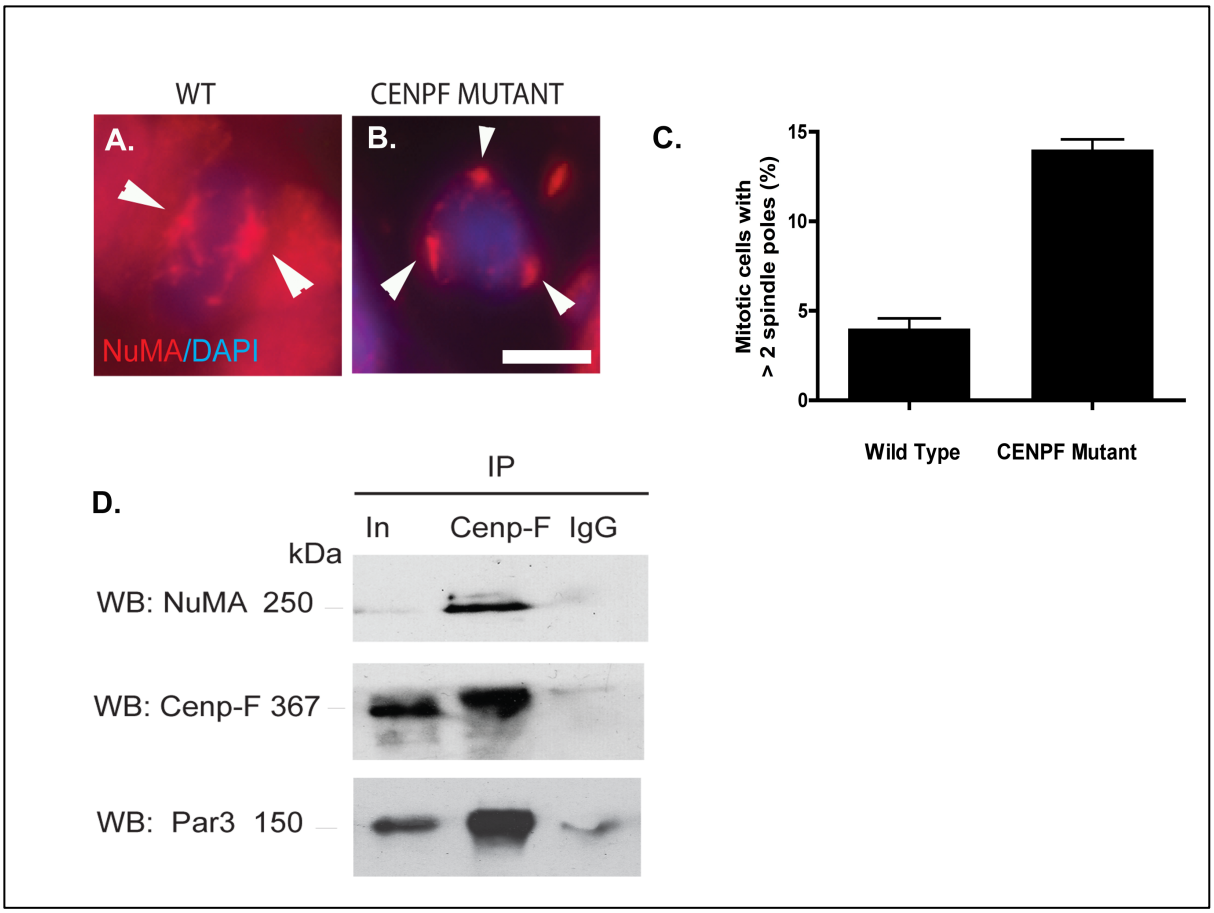

Figure 5.4 *CENP-F interacts with NuMA and Par3, proteins involved in spindle assembly*. (A, B) Representative images of mitotic renal epithelial cells with dual immunofluorescence labelling of spindle poles with anti- NuMA antibodies and DAPI. (A) Normal bipolar spindle poles in wild-type human kidney cells (white arrows). (B) Tripolar and disrupted spindle poles in *CENPF* mutant kidney cells (white arrows). (C) Quantitation of mitotic cells with more than two spindle poles; mean±sem of three independent experiments in which 30 mitotic cells were counted. (D) Immunoblots show that NuMA and Par 3 co-immunoprecipitate with CENP-F in unsynchronised RPE cells. IN= input; ten per cent of total input is indicated.

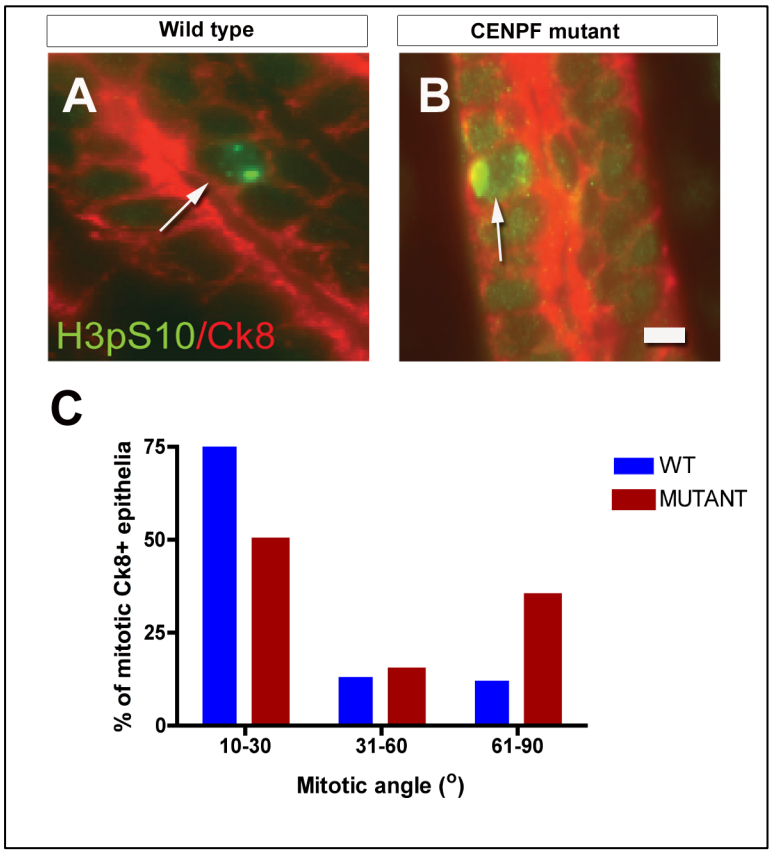

Figure 5.5: *Mitotic spindle misorientation in CENPF mutant renal epithelial cells.* (A, B) Representative merged images of mitotic renal collecting duct epithelial cells with dual immunofluorescence labelling of mitotic DNA with anti- phosphohistone H3 (immunodetection with Alexa488-conjugated secondary antibody) and cytokeratin 8 (immunodetection with Alexa594-conjugated secondary antibody). (A) White arrow points to mitotic orientation parallel to longitudinal axis of collecting duct in wild-type kidneys (B) White arrow points to mitotic orientation perpendicular to longitudinal axis of collecting duct in *CENPF* mutant kidneys. Scale bar 5µm (C) Graph showing distribution of percentage of mitotic collecting duct renal epithelial cells for mitotic angle orientation in wild type (blue) and *CENPF* mutant (red) kidneys.

5.3. DISCUSSION

5.3.1. Characterisation of the renal phenotype of *CENPF* mutant foetuses suggests a role for CENP-F in metanephric kidney development

All four affected foetuses who carried compound heterozygous mutations in *CENPF* were reported to have a renal phenotype suggestive of renal hypoplasia. Renal hypoplasia, defined as abnormally small kidneys with normal morphology and reduced nephron number can be difficult to differentiate form renal dysplasia as hypoplastic kidneys will often exhibit evidence of tissue maldifferentiation (Cain et al., 2010). In the absence of control tissue for comparison at the time of autopsy, I sought to investigate the histopathological features of *CENPF*-mutant foetal kidneys in greater detail by comparing kidney sections with those of age-matched control foetuses. This allowed for a definitive characterisation of the renal phenotype, which showed that the number of mature glomeruli was reduced, thereby suggestive of renal hypoplasia.

As discussed in Chapter 1, a spectrum of renal disease including renal dysplasia, cystic dysplasia and renal cystogenesis have been associated with several ciliopathy disorders. However, detailed characterisation of the histopathological features in the clinical setting is often precluded by the absence of renal biopsy tissue for analysis in affected patients. As a consequence, disease mechanisms are then further investigated in mammalian

systems such as knockout mouse models and may not necessarily take into consideration the effects of hypomorphic mutations on phenotype manifestation. The availability of autopsy tissue facilitated a careful histopathological characterization of the renal phenotype in the current report, which allowed further investigation of the mechanisms underlying the renal phenotype.

5.3.2. Mutant *CENPF* nephrogenic structures display aberrant NuMA expression within differentiating nephrogenic structures

During kidney development, reciprocal interactions between the outgrowing ureteric bud and the surrounding metanephric mesenchyme are critical for induction of nephrogenesis (Saxen and Sariola, 1987). If these tissues fail to interact properly, then renal agenesis and hypoplasia will occur. While early specification of the metanephric mesenchyme was normal as suggested by normal expression of Sall1, a transcription factor implicated in metanephric mesencyhmal cell fate induction (Kiefer et al, 2003), I next examined later differentiation of intermediate nephrogenic structures such as S-shaped bodies, in which the proximo-distal axis is specified through the asymmetric expression of segment-specific markers (Cheng et al, 2003). Here, I observed aberrant NuMA expression within the middle domain of the S-shaped body compared to the distal domain of wild-type S-shaped bodies. NuMA is a component of the Gαi-LGN/AGS3-NuMA-p150^{glued} complex,

which has recently been implicated in asymmetric cell division and cell fate induction (Williams et al, 2011). These findings together with co-immunoprecipitation data from Chapter 4 which suggested that Cenp-F interacts with the p150 ^{Glued} dynactin subunit, proposed a role for Cenp-F in differentiation of nephrogenic structures into proximal fates which include glomeruli.

5.3.3. CENP-F exists in a multiprotein complex implicated in mitotic spindle positioning

Stem and progenitor cells use asymmetric cell divisions to regulate the balance between proliferation and differentiation. Studies in *Drosophila* and *C elegans*, show that this process is regulated by proteins asymmetrically distributed at the cell cortex during mitosis (Knoblich, 2008). Par3-Par6-aPKC, which confer polarity and Gα(i)-LGN/AGS3-NuMA-dynein/dynactin, which govern spindle positioning (Siller and Doe, 2009). In Chapter 4, I show that CENP-F co-immunoprecipitates with the p150 ^{Glued} subunit of dynactin and in the current report, I show that endogenous CENP-F also precipitates with NuMA and Par3, thereby implicating a role for CENP-F in mitotic spindle positioning. These data were further supported by previous reports of multiastral and multipolar spindles in CENPF-depleted cells (Holt et al, 2005). My findings of multipolar spindles, spindle pole disruption and mitotic spindle

orientation in renal epithelial cells of the affected foetuses provide further *in vivo* evidence for a role for CENP-F in spindle assembly and function.

SUMMARY

In the current chapter, I have characterised the renal phenotype of the affected foetuses carrying *CENPF* mutations. A novel role for CENP-F in metanephric kidney development is suggested by findings of renal hypoplasia in the affected foetuses. Furthermore, my data supports emerging evidence for a dual role for proteins implicated in spindle checkpoint inactivation, mitotic spindle orientation and ciliogenesis in the pathogenesis of severe ciliopathy-related phenotypes such as renal dysplasia, hypoplasia and cystogenesis.

CHAPTER 6. OVERALL DISCUSSION

Almost a decade has passed since multisystemic disorders characterised primarily by a combination of retinal degeneration, renal disease and cerebral anomalies were first associated with mutations in ciliary genes. The notion of a "ciliopathic" disorder was initially attributed to Bardet–Biedl syndrome (BBS), when Ansley and colleagues identified genetic mutations in *BBS8* whereby the encoded protein was noted to have a *pilF* domain, suggesting a conserved role for BBS8 in prokaryotic pilus formation (Ansley et al., 2003). Intriguingly, the phenotypic consequences in one family with a homozygous null mutation in *BBS8* included situs inversus, a known defect of the embryonic nodal cilium (Ansley et al, 2003). Subsequent immunohistochemical analysis confirmed the localisation of Bbs8 to centrosomes and basal bodies within human embryonic kidney cells (HEK293) in addition to spermatids, the connecting cilium of the retina and the ciliated columnar epithelial cells of the lung (Ansley et al, 2003). Further supporting evidence for a role in cilia function came from the elegant demonstration that other BBS orthologues in *Caenorhabditis elegans*, *bbs1*, *bbs2* and *bbs7*, all localised to the nematode ciliated sensory neurons where *osm-5*, the orthologue of the mouse polycystic kidney disease gene, *polaris*, was also previously localized (Pazour et al, 2002). Thereafter, the innovative utilisation of comparative genomic studies whereby the proteome of the non-flagellated organism, *Arabidopsis*, was subtracted from the shared proteome of the ciliated/flagellated organisms, *Chlamydomonas* and human, led to the

discovery of mutations in another gene, *BBS5*, in patients with BBS (Li et al., 2004). Following development of the original ciliary proteome database, subsequent integration of ciliary proteomes from a range of different organisms have contributed to the current ciliary proteome database (http://www.ciliaproteome.org) (Gherman et al., 2006). The ciliary proteome database was employed by Beales and colleagues to identify mutations in *IFT80*, which encodes an intraflagellar transport protein in a subset of patients with Jeune asphyxiating thoracic dystrophy (JATD), following the observation that patients with JATD exhibited typical ciliopathy features of retinal degeneration, renal disease and skeletal dysplasia (Beales et al., 2007). Since those early seminal papers, mutations in over 60 genes have been described in 17 ciliopathy disorders (Logan et al., 2011). Depending on the cell type, it has been shown that the ciliary proteome can consist of between 500 and 1800 polypeptides and consequently, it has been estimated that several more ciliopathy disorders exist (Baker et al, 2010).

6.1. SUMMARY OF ACHIEVEMENTS

Novel genomic technologies that involve deep sequencing of all human genes by exon capture has led to the identification of the genetic aetiology of over 180 Mendelian disorders over the past 3 years. In Chapter 3, I show the success of exome sequencing in circumstances where conventional approaches

such as linkage analysis and homozygosity mapping had failed. Furthermore, the genetic aetiology of a novel ciliopathy disorder was identified by analysis of the exome of just one affected foetus following the application of a filtering strategy based on novelty, quality of read and mutation pathogenicity prediction. Owing to the compound heterozygous nature of the mutations and the fact that one of the mutations was discovered at a depth of coverage of only 13x, the final success in gene identification was achieved by not prioritising variants based on depth of coverage. Furthermore, while significant locus heterogeneity was observed following linkage analysis with the identification of ten linked regions on Chromosome 1 (2 intervals), 2, 6, 7, 8, 13, 19, and 20, linkage analysis proved useful during the final steps of candidate gene selection, with only one candidate being present in the linked region following prioritisation based on novelty, quality of read and mutation pathogenicity prediction.

Following a search in several validated dysmorphology databases, the phenotype described in the affected foetuses with *CENPF* mutations, was inconsistent with any known disorder. Considering the embryonic lethality in mid-gestation in all affected foetuses, together with the constellation of defects affecting craniofacial development, cerebellar morphogenesis, palatogenesis, foregut and renal development, malfunction of a critical cellular process seemed most likely to underlie the phenotypic features observed in affected foetuses with *CENPF* mutations. Interestingly, one of the disorders that overlapped with

the phenotype in the context of familial duodenal atresia was Feingold syndrome, in which mutations in the SHH target gene, *MYCN* have been described (Van Bokhoven et al, 2005). Shh plays an important role in early craniofacial development (Hu and Helms et al 1999), in cerebellar morphogenesis (Kim et al, 2011), in foregut development (Mao et al, 2010), and in renal development (Cain et al, 2009). Furthermore, the constellation of clinical features such as hydrocephalus, cerebellar malformations, cleft palate and renal malformations have been described in disorders associated with either abnormal formation and/or function of primary cilia (Table 1.2). Previous genetic studies have shown that IFT proteins act at the heart of the *Shh* pathway, downstream of the transmembrane *Shh* receptor, *Patched 1 (Ptch1)* and its downstream effector, *Smoothened (Smo)* and upstream of the *Gli* transcription factors that implement the pathway (Huangfu et al, 2003). As a result, I considered that some of the phenotypic features observed in foetuses carrying *CENPF* mutations could be attributed to defects in cilia function. In Chapter 4, I then tested the hypothesis that CENP-F could play a role in cilia formation and function. Following the identification of a basal body localisation for CENP-F and its subsequent colocalisation with ninein, a marker of the subdistal appendages, I then confirmed its ultrastructural localisation at the mother centriole in serum-starved RPE cells. In the absence of patient cell availability in which to study the consequences of *CENPF* loss of function, I next determined the *in vivo* consequences of *cenpf* knockdown in the zebrafish. Even

at low doses of morpholino, *cenpf* morphants exhibited a high mortality at 24hpf, suggesting a role for *cenpf* in early embryogenesis. Given the presence of hydrocephalus, pronephric cysts and abnormal heart looping, features which have been described in other zebrafish ciliopathy mutants (Adams et al., 2012), in addition to left-right randomisation during the segmentation stages, I next explored the possibility and thereafter confirmed that *cenpf* function is required for KV ciliogenesis. These data were supported by *in vitro* studies in which CENPF shRNA knockdown resulted in a significant reduction in ciliation of RPE cells even following serum starvation. Next, I confirmed that the *CENPF* mutation, p.E582X, could not fully rescue the lack of ciliation in transduced cells compared with full-length CENPF transduced cells following CENPF knockdown. Thereafter, I identified the cilia-related proteins, IFT88 and KIF3B, as novel protein interactors of CENP-F following reports that spindle pole localisation of IFT88 was dependent on cytoplasmic dynein (Delaval et al, 2011) in addition to previous reports that spindle pole localisation of Nde1, a known interactor of CENP-F is also mediated by dynein. These data were supported by recent studies showing a role for Nde1 in the negative regulation of cilia length, a phenotype that can be rescued by IFT88 knockdown (Kim et al, 2011). Analysis of *CENPF*-mutant kidneys revealed IFT88 mislocalisation compared to wild-type kidneys. Therefore, I hypothesised that CENP-F exists in a multiprotein complex at the spindle pole, with proteins that are implicated in ciliogenesis as well as mitosis. Even though I failed to show that endogenous

CENP-F precipitates with cytoplasmic dynein, I was able to show that the p150 ^{Glued} subunit of dynactin which interacts directly with the dynein intermediate chains (Vaughan et al, 1995) interacted with CENP-F which supported my hypothesis for a role for a spindle pole complex in early ciliogenesis.

Following identification of a novel function for CENP-F in a molecular pathway implicated in ciliogenesis, in Chapter 5, I next focussed on the phenotypic consequences of *CENPF* loss of function *in vivo*. Histological analysis of 22-week-old foetal kidney sections from foetuses carrying the *CENPF* compound heterozygous mutations suggested a renal hypoplastic phenotype when compared to age-matched wild-type human foetal kidneys. Following a quantitative analysis of number of mature glomeruli, which confirmed the renal hypoplasia, I next determined that *CENPF*-mutant kidneys exhibited aberrant NuMA expression within S-shaped bodies, which give rise to glomerular structures. Given the role of the NuMA/p150 ^{Glued} dynactin pathway in asymmetric cell division and my previous findings of p150 ^{Glued} dynactin interactions with CENP-F in Chapter 4, I next tested the hypothesis that CENP-F plays a role in mitotic spindle orientation. Multipolar spindles were observed following immunolabelling with NuMA in *CENPF* mutant kidneys supporting a role for CENP-F in mitotic spindle assembly. Further analysis following dual immunofluorescent labelling of mitotic DNA revealed mitotic spindle orientation defects in collecting ducts of *CENPF*-mutant kidneys. These data supported the notion that CENP-F, like IFT88, plays a role in mitotic spindle

orientation and the renal hypoplastic phenotype could be a consequence of failure of mesenchymal differentiation.

6.2. OVERALL DISCUSSION

6.2.1. Utility of next generation sequencing strategies to identify the genetic aetiology of novel Mendelian diseases

Almost five years has passed since targeted enrichment of an exome by hybridisation of shotgun libraries was first described (Hodges et al, 2007). Two years later, the targeted capture and massive parallel sequencing of the exomes of twelve humans was published (Ng et al, 2009). The following year, the first reports emerged on the use of whole exome sequencing in gene identification (Choi et al, 2009; Ng et al, 2010). Since then, the genetic aetiology of just under 200 Mendelian diseases has been discovered in no less than two and a half years. The major advantage of whole exome sequencing is that virtually all variants within an individual's genome are uncovered simultaneously which allows for direct examination of the list of variants and candidate gene selection in the presence or absence of mapping studies. Variant listing is dependent on several factors that are dependent on the technology used. For example, the type of capture kit, the sequencing platform and sequencing depth can influence the variant listing. Additionally, the lists produced will depend on the alignment algorithms and the stringency settings of the bioinformatics tools employed for

identifying variants. For example, some disease-causing variants can be found at a depth of coverage of less than 10 and if the bioinformatic pipeline has a stringency cut-off greater than 10, it is possible that the disease-causing variant will be missed. Capture kits are continuously improving, initially having covered 27Mb and 180,000 coding exons to now up to 62Mb of the human genome and over 201,121 coding exons. Each platform uses biotinylated oligonucleotide baits complementary to the exome targets to hybridise sequencing libraries prepared from fragmented genomic DNA. These bound libraries are enriched for targeted regions by pull-down with magnetic streptavidin beads and then sequenced. Platforms vary, with some covering fewer genomic regions than the other platforms, while others are able to detect a greater total number of variants with additional sequencing and others capture untranslated regions, which are not targeted by other platforms.

While whole exome sequencing has facilitated the genetic diagnosis of several known Mendelian disorders, the genetic aetiology of rare novel phenotypes such as that outlined in Chapter 1 are beginning to unfold. Investigation of the genetic aetiology of embryonic lethal phenotypes such as that described in the current report, will greatly facilitate the identification of molecular mechanisms underlying critical developmental processes. For example, my finding that mutations in *CENPF*, a gene whose role in mitosis was previously well characterised, can be associated with a phenotype reminiscent of a ciliopathy, provides insight into how mitotic multiprotein

complexes have dual roles to play in mitotic spindle orientation and early ciliogenesis.

6.2.2. Linking absent cilia to mitotic and planar polarity defects

As centriole-ciliation is associated with mitotic exit and previous reports of absent cilia in several *Ift*-knockout mice together with the recent finding that Ift proteins may play a role in mitotic spindle orientation, I was keen to re-examine the original literature describing the role of both Ift and kinesin-II proteins in ciliogenesis. The observation that *Chlamydomonas ift88* insertional mutants exhibit absent flagella led to the conclusion that *Chlamydomonas ift88* plays a critical role in flagellar assembly (Pazour et al, 2000). Scanning electron microscopy of the collecting ducts of the hypomorphic *Tg737*-mutant mice revealed much shorter cilia in homozygous mutants compared to their wild-type littermates when examined at postnatal days 4 and 7 (Pazour et al, 2000). Hypomorphic mutations in *Tg737* cause kidney disease and death within a few weeks of birth (Moyer et al 1994) and closely resemble the cystic kidney phenotype observed in ARPKD. Null alleles of *Tg737* have a more severe phenotype and cause the mice to die during midgestation and exhibit absent nodal cilia (Murcia et al. 2000). While characterisation of cell division has been not been undertaken in *Tg737* mutants *in vivo*, *Chlamydomonas ift88* insertional mutants have been reported not to have defects in cell division as suggested by a normal growth rate compared to wild-type controls. It is interesting to note that

Ift88 has a dynamic subcellular localisation throughout the cell cycle and colocalises with γ-tubulin at perinuclear foci in G1 and G2-phases (Robert et al, 2007). Furthermore, Ift88 depletion in Hela cells results in an increased mitotic index and delayed mitotic progression (Delaval et al, 2011). More detailed analysis revealed spindle pole disruption, chromosome misalignment and spindle misorientation (Delaval et al, 2011). Mitotic functions for other Ift proteins have been disclosed recently and include Ift57, Ift52 and Ift20 (unpublished data, personal communication).

The phenotype caused by the null *Tg737* mutation closely resembles the phenotype of kinesin-II knockout mice (Nonaka et al. 1998; Marszalek et al. 1999, Takeda et al. 1999). Interestingly, similar to Ift proteins, a mitotic role for Kif3b has also been described (Haraguchi et al, 2005). Subcellular localisation of the Kif3a/3b complex is at the centrosome in interphase and prophase but only weak staining at the centrosome after prometaphase when it is mainly found at the spindle microtubules. From metaphase through telophase, Kif3a is concentrated at the midzone and is mainly at the centrosomes during cytokinesis (Haraguchi et al, 2005). Expression of a truncated Kif3b construct lacking the C-terminus, also results in mitotic defects such as chromosomal aneuploidy and abnormal spindle formation (Haraguchi et al, 2005).

It is interesting to note that conditional deletion of *Ift88* or *Kif3a* in adult mice results in loss of cilia but neither mutant develops kidney cysts or hydrocephalus (Davenport et al, 2007). However, deletion of *Kif3a* during

tubule morphogenesis with a collecting duct-specific knockout of *Kif3a* using a *Ksp-Cre* transgenic mouse which is expressed from embryonic day 15.5 onwards in the mouse, results in renal cystogenesis which begins at postnatal day 5 (Lin et al, 2003). In *KspCre; Kif3a* $^{flox/flox}$ mice, cyst epithelial cells in *Kif3a* mutant mice exhibited evidence of proliferation and apoptosis. Interestingly, apical mislocalisation of the epidermal growth factor receptor (EGFR) receptor was evident in mutant mice as has been also reported in other cystic phenotypes. To elucidate the roles of primary cilia in the kidney after birth, administration of tamoxifen to *Ksp*-CreER^{T2};*Kif3a*$^{flox/-}$;R26R mice (conditional *Kif3a* mutants) at postnatal day 2 and analysis 4 weeks later revealed the presence of multiple cysts in the kidney. Cilia were absent from the *lacZ*-positive cyst epithelial cells in the conditional *Kif3a* mutant mice. Primary cilia were present in adjacent *lacZ*-negative, non-cystic tubules, indicating that the loss of primary cilia and cyst formation was specific to *Kif3a* mutant cells. Interestingly, kidney collecting duct-specific inactivation of *Kif3a* at postnatal day 10 or older ages did not cause cyst formation despite the loss of cilia unless kidneys were subjected to injury by ischaemia (Patel et al, 2008). Cysts did not develop in the uninjured kidney despite the loss of primary cilia, which indicated that ischemic injury associated cell proliferation during epithelial regeneration triggered cyst formation (Patel et al, 2008). Interestingly, *Kif3a* mutant kidneys exhibited mitotic spindle orientation defects compared to their littermate controls (only 46% of mitotic spindles were oriented within 20° of the

axis of the collecting ducts versus in control kidneys, where 91% of mitotic spindles were oriented within 20° of the longitudinal axis of the collecting ducts)(Patel et al, 2008). Therefore it appears that both loss of Ift88 and Kif3a function is associated with defects in mitotic spindle orientation and cystogenesis. Loss of cilia *per se* does not result in cystogenesis in adult kidneys. It is plausible to consider that renal cystogenesis in these models is a consequence of defective planar polarity and mitotic defects, which could ultimately result in defective ciliogenesis. Whether the defective ciliogenesis phenotype described in *Tg737* epithelia is a consequence of mitotic arrest or defective polarity requires further investigation.

6.3 FUTURE WORK

6.3.1 Screening of candidate syndromes for *CENPF* mutations

Following identification of *CENPF* as a new ciliopathy disease gene, it will be of great interest to determine what role *CENPF* loss of function plays, if any, in the context of other ciliopathies. Following screening of BBS and MKS cohorts, my colleagues did not identify any disease-causing mutations in *CENPF* in these ciliopathy phenotypes. However, given the phenotypic overlap with Fryns syndrome, it would be worthwhile screening this cohort of patients for mutations in *CENPF*. Of interest, *CENPF* lies on chromosome 1q41 and recently, Fryns syndrome has been reported to fit the severe end of a syndrome

associated with microdeletions of 1q41q42 (Rosenfeld et al., 2011). While *CENPF* does not lie within this critical microdeletion interval, it is possible that the genes implicated in more severe Fryns-like phenotypes lie outside this interval.

Given the recent elucidation of the Nde1-LC8-IFT88 pathway, and the finding of *NDE1* mutations in primary microcephaly phenotypes, it is possible that *CENPF* mutations may be found in other primary microcephaly cohorts (Alkuraya et al., 2011; Bakircioglu et al., 2011). Interestingly, mutations in several genes encoding centriolar proteins have recently been discovered in primary microcephaly and have been associated with defective ciliogenesis (Sir et al., 2011), (Guernsey et al., 2010; Nicholas et al., 2010; Rauch et al., 2008), (Bond et al., 2005)

6.3.2 Relating CENP-F loss of function to organ-specific phenotypes

Given the ciliogenesis defects and midgestation lethality observed in the affected foetuses features of which is reminiscent of those seen with *Kif3b* and *Ift88*- null mice in addition to the putative interactions suggested by my co-immunoprecipitation assays, it will be necessary to examine the consequences of murine *Cenpf* deletion to investigate whether *Cenpf* mutant mice exhibit left-right patterning defects, hydrocephalus, cleft palate, gastrointestinal manifestations, cerebral or renal differentiation defects.

As defective planar polarity with mitotic spindle misorientation are evident in the kidneys of affected foetuses, future work could be directed at examining the role of CENP-F in kidney development and renal cystogenesis. In order to investigate the role of CENPF in kidney development, it will be necessary to delete CENPF in a spatiotemporal manner. Effects of CENPF depletion in the early stages of kidney development could be faciliated by employing a metanephric mesenchymal specific deletion of CENP-F using the *retinoic acid receptor β isoform 2 (Rarb2)-Cre* transgenic mouse line (Kobayashi et al., 2005). From E9.5 of mouse gestation, Rarb2-Cre, reporter expression is restricted to the nephric mesenchyme in the anterior region of the mesonephros, but not in the nephric duct epithelium. Therefore, crossbreeding with a conditional $Cenpf^{flox/flox}$ (first five exons flanked by loxP sites) (Moynihan et al, 2009), should facilitate analysis of the effects of CENPF depletion on the specification and differentiation of the developing metanephric mesenchyme as nephrogenesis proceeds from differentiation of the condensing metanephric mesenchyme to the renal vesicle, S-shaped body and specification of the proximal and distal fates such as podocyte progenitor, proximal tubule precursors and distal tubular epithelia. Metanephric kidney development begins with the induction of the metanephric mesenchyme by the outgrowing ureteric bud (Saxen et al). Reciprocal signalling between the ureteric bud and the metanephric mesenchyme are involved in the further differentiation of the renal parenchyma. Effects of *Cenpf* depletion in the early stages of kidney

development will be further facilitated by employing a ureteric bud specific deletion of *Cenpf* using the *Hoxb7-Cre* transgenic mouse line (Yu et al., 2002). From E9.5 of mouse gestation, *Hoxb7-Cre*, reporter expression is restricted to the nephric duct epithelium but not the metanephric mesenchyme. Therefore, crossbreeding with a transgenic conditional $Cenpf^{flox/flox}$ (first five exons flanked by lox P sites) (Moynihan et al, 2009) should facilitate analysis of the effects of CENPF depletion on the specification and differentiation of the developing metanephric mesesnchyme.

Following identification of a role for misorientated cell division in renal cystogenesis and the finding that CENP-F interacts with components of the mitotic spindle orientation complex, it would be interesting to determine the consequences of *Cenpf* depletion in the renal collect duct system. Utilising a tamoxifen inducible collecting duct-specific model of *Cenpf* depletion by crossbreeding inducible $Ksp\text{-}CreER^{T2}$ (Patel et al, 2008) and $Cenpf^{flox/flox}$ transgenic mice (Moynihan et al, 2009), subsequent analysis could be undertaken in the early postnatal period and in adult mice to determine whether *Cenpf* is implicated in the pathogenesis of renal cysts. This should provide direct evidence for a role for CENP-F in the regulation of planar cell polarity signalling in the context of renal tubule morphogenesis, a process which has recently been shown to be regulated by Wnt signalling (Karner et al, 2009), of which NuMA, is a downstream target and which has been shown in the present work, to interact with CENP-F.

6.4 FINAL REMARKS

I have shown the utility of whole exome sequencing in the genetic identification of a novel ciliopathy phenotype which is attributed to mutations in *CENPF*, a protein whose function has been well characterised in mitosis. The underlying mechanisms for the phenotypic overlap with other ciliopathies could be explained by my findings which suggests a novel role for CENP-F in vertebrate ciliogenesis. CENP-F localises to the subdistal appendages of the mother centriole and co-immunoprecipitates with proteins implicated in ciliogenesis. Analysis of foetal kidney sections suggests that CENP-F may also regular planar polarization of renal tubular epithelia. These findings are supported by interactions with proteins implicated in mitotic spindle orientation. Future work will now focus on the consequences of mammalian *Cenpf* depletion in the developing kidney and should provide support for emerging evidence which implicates a role for mitotic spindle orientation proteins in the pathogenesis of severe ciliopathy-related phenotypes such as renal dysplasia and renal cystogenesis.

REFERENCES

1994. The polycystic kidney disease 1 gene encodes a 14 kb transcript and lies within a duplicated region on chromosome 16. The European Polycystic Kidney Disease Consortium. Cell 78, 725.

1995. Polycystic kidney disease: the complete structure of the PKD1 gene and its protein. The International Polycystic Kidney Disease Consortium. Cell 81, 289-298.

Adams, M., Simms, R.J., Abdelhamed, Z., Dawe, H.R., Szymanska, K., Logan, C.V., Wheway, G., Pitt, E., Gull, K., Knowles, M.A., Blair, E., Cross, S.H., Sayer, J.A., Johnson, C.A., 2012. A meckelin-filamin A interaction mediates ciliogenesis. Human molecular genetics 21, 1272-1286.

Afzelius, B.A., 1976. A human syndrome caused by immotile cilia. Science 193, 317-319.

Ait-Lounis, A., Baas, D., Barras, E., Benadiba, C., Charollais, A., Nlend Nlend, R., Liegeois, D., Meda, P., Durand, B., Reith, W., 2007. Novel function of the ciliogenic transcription factor RFX3 in development of the endocrine pancreas. Diabetes 56, 950-959.

Ait-Lounis, A., Bonal, C., Seguin-Estevez, Q., Schmid, C.D., Bucher, P., Herrera, P.L., Durand, B., Meda, P., Reith, W., The transcription factor Rfx3 regulates {beta}-cell differentiation, function and glucokinase expression. Diabetes.

Alkuraya, F.S., Cai, X., Emery, C., Mochida, G.H., Al-Dosari, M.S., Felie, J.M., Hill, R.S., Barry, B.J., Partlow, J.N., Gascon, G.G., Kentab, A., Jan, M., Shaheen, R., Feng, Y., Walsh, C.A., 2011. Human mutations in NDE1 cause extreme microcephaly with lissencephaly [corrected]. American journal of human genetics 88, 536-547.

Anderson RG, Brenner RM., 1971. The formation of basal bodies (centrioles) in the Rhesus monkey oviduct. J Cell Biol. 50, 10-34.

Ansley, S.J., Badano, J.L., Blacque, O.E., Hill, J., Hoskins, B.E., Leitch, C.C., Kim, J.C., Ross, A.J., Eichers, E.R., Teslovich, T.M., Mah, A.K., Johnsen, R.C., Cavender, J.C., Lewis, R.A., Leroux, M.R., Beales, P.L., Katsanis, N., 2003. Basal body dysfunction is a likely cause of pleiotropic Bardet-Biedl syndrome. Nature 425, 628-633.

Antonarakis, S.E., Beckmann, J.S., 2006. Mendelian disorders deserve more attention. Nature reviews. Genetics 7, 277-282.

Armour EA, Carson RP, Ess KC, 2012. Cystogenesis and elongated primary cilia in Tsc1-deficient distal convoluted tubules. Am J Physiol Renal Physiol. 303, F584-92.

Arts, H.H., Bongers, E.M., Mans, D.A., van Beersum, S.E., Oud, M.M., Bolat, E., Spruijt, L., Cornelissen, E.A., Schuurs-Hoeijmakers, J.H., de Leeuw, N., Cormier-Daire, V., Brunner, H.G., Knoers, N.V., Roepman, R., 2011. C14ORF179 encoding IFT43 is mutated in Sensenbrenner syndrome. Journal of medical genetics 48, 390-395.

Arts, H.H., Doherty, D., van Beersum, S.E., Parisi, M.A., Letteboer, S.J., Gorden, N.T., Peters, T.A., Marker, T., Voesenek, K., Kartono, A., Ozyurek, H., Farin, F.M., Kroes, H.Y., Wolfrum, U., Brunner, H.G., Cremers, F.P., Glass, I.A., Knoers, N.V., Roepman, R., 2007. Mutations in the gene encoding the basal body protein RPGRIP1L, a nephrocystin-4 interactor, cause Joubert syndrome. Nat Genet 39, 882-888.

Ashique, A.M., Choe, Y., Karlen, M., May, S.R., Phamluong, K., Solloway, M.J., Ericson, J., Peterson, A.S., 2009. The Rfx4 transcription factor modulates Shh signaling by regional control of ciliogenesis. Sci Signal 2, ra70.

Attanasio, M., Uhlenhaut, N.H., Sousa, V.H., O'Toole, J.F., Otto, E., Anlag, K., Klugmann, C., Treier, A.C., Helou, J., Sayer, J.A., Seelow, D., Nurnberg, G., Becker, C., Chudley, A.E., Nurnberg, P., Hildebrandt, F., Treier, M., 2007. Loss of GLIS2 causes nephronophthisis in humans and mice by increased apoptosis and fibrosis. Nat Genet 39, 1018-1024.

Baas, D., Meiniel, A., Benadiba, C., Bonnafe, E., Meiniel, O., Reith, W., Durand, B., 2006. A deficiency in RFX3 causes hydrocephalus associated with abnormal differentiation of ependymal cells. Eur J Neurosci 24, 1020-1030.

Baker, K., Beales, P.L., 2009. Making sense of cilia in disease: the human ciliopathies. American journal of medical genetics. Part C, Seminars in medical genetics 151C, 281-295.

Bakircioglu, M., Carvalho, O.P., Khurshid, M., Cox, J.J., Tuysuz, B., Barak, T., Yilmaz, S., Caglayan, O., Dincer, A., Nicholas, A.K., Quarrell, O., Springell, K., Karbani, G., Malik, S., Gannon, C., Sheridan, E., Crosier, M., Lisgo, S.N., Lindsay, S., Bilguvar, K., Gergely, F., Gunel, M., Woods, C.G., 2011. The essential role of centrosomal NDE1 in human cerebral cortex neurogenesis. American journal of human genetics 88, 523-535.

Bamshad, M.J., Ng, S.B., Bigham, A.W., Tabor, H.K., Emond, M.J., Nickerson, D.A., Shendure, J., 2011. Exome sequencing as a tool for Mendelian disease gene discovery. Nature reviews. Genetics 12, 745-755.

Barr, A.R., Kilmartin, J.V., Gergely, F., 2010. CDK5RAP2 functions in centrosome to spindle pole attachment and DNA damage response. The Journal of cell biology 189, 23-39.

Barrera, J.A., Kao, L.R., Hammer, R.E., Seemann, J., Fuchs, J.L., Megraw, T.L., 2010. CDK5RAP2 regulates centriole engagement and cohesion in mice. Developmental cell 18, 913-926.

Barrett, W.E., 1947. A method of studying ciliary motility by direct observation. Fed Proc 6, 307.

Beales, P.L., Bland, E., Tobin, J.L., Bacchelli, C., Tuysuz, B., Hill, J., Rix, S., Pearson, C.G., Kai, M., Hartley, J., Johnson, C., Irving, M., Elcioglu, N., Winey, M., Tada, M., Scambler, P.J., 2007. IFT80, which encodes a conserved intraflagellar transport protein, is mutated in Jeune asphyxiating thoracic dystrophy. Nature genetics 39, 727-729.

Beckers, A., Alten, L., Viebahn, C., Andre, P., Gossler, A., 2007. The mouse homeobox gene Noto regulates node morphogenesis, notochordal ciliogenesis, and left right patterning. Proc Natl Acad Sci U S A 104, 15765-15770.

Beisson, J., Wright, M., 2003. Basal body/centriole assembly and continuity. Current opinion in cell biology 15, 96-104.

Bell PD, Fitzgibbon W, Sas K, Stenbit AE, Amria M, Houston A, Reichert R, Gilley S, Siegal GP, Bissler J, Bilgen M, Chou PC, Guay-Woodford L, Yoder B, Haycraft CJ, Siroky B, 2011. Loss of primary cilia upregulates renal hypertrophic signaling and promotes cystogenesis.
J Am Soc Nephrol. 22, 839-48.

Bertram JF. Analyzing renal glomeruli with the new stereology. Int Rev Cytol. 1995;161:111-72.

Bettencourt-Dias, M., Glover, D.M., 2007. Centrosome biogenesis and function: centrosomics brings new understanding. Nature reviews. Molecular cell biology 8, 451-463.

Bettencourt-Dias, M., Glover, D.M., 2009. SnapShot: centriole biogenesis. Cell 136, 188-188 e181.

Bettencourt-Dias, M., Hildebrandt, F., Pellman, D., Woods, G., Godinho, S.A., 2011. Centrosomes and cilia in human disease. Trends Genet 27, 307-315.

Bettencourt-Dias, M., Rodrigues-Martins, A., Carpenter, L., Riparbelli, M., Lehmann, L., Gatt, M.K., Carmo, N., Balloux, F., Callaini, G., Glover, D.M., 2005. SAK/PLK4 is required for centriole duplication and flagella development. Current biology : CB 15, 2199-2207.

Biscardi JS, Maa MC, Tice DA, Cox ME, Leu TH, Parsons SJ, 1999. c-Src-mediated phosphorylation of the epidermal growth factor receptor on Tyr845 and Tyr1101 is associated with modulation of receptor function, J. Biol. Chem. 274 8335–8343.

Bisgrove, B.W., Makova, S., Yost, H.J., Brueckner, M., 2012. RFX2 is essential in the ciliated organ of asymmetry and an RFX2 transgene identifies a population of ciliated cells sufficient for fluid flow. Developmental biology 363, 166-178.

Blacque, O.E., Perens, E.A., Boroevich, K.A., Inglis, P.N., Li, C., Warner, A., Khattra, J., Holt, R.A., Ou, G., Mah, A.K., McKay, S.J., Huang, P., Swoboda, P., Jones, S.J., Marra, M.A., Baillie, D.L., Moerman, D.G., Shaham, S., Leroux, M.R., 2005. Functional genomics of the cilium, a sensory organelle. Current biology : CB 15, 935-941.

Blacque, O.E., Reardon, M.J., Li, C., McCarthy, J., Mahjoub, M.R., Ansley, S.J., Badano, J.L., Mah, A.K., Beales, P.L., Davidson, W.S., Johnsen, R.C., Audeh, M., Plasterk, R.H., Baillie, D.L., Katsanis, N., Quarmby, L.M., Wicks, S.R., Leroux, M.R., 2004. Loss of C. elegans BBS-7 and BBS-8 protein function results in cilia defects and compromised intraflagellar transport. Genes & development 18, 1630-1642.

Bomont, P., Maddox, P., Shah, J.V., Desai, A.B., Cleveland, D.W., 2005. Unstable microtubule capture at kinetochores depleted of the centromere-associated protein CENP-F. The EMBO journal 24, 3927-3939.

Bond, J., Roberts, E., Springell, K., Lizarraga, S.B., Scott, S., Higgins, J., Hampshire, D.J., Morrison, E.E., Leal, G.F., Silva, E.O., Costa, S.M., Baralle, D., Raponi, M., Karbani, G., Rashid, Y., Jafri, H., Bennett, C., Corry, P., Walsh, C.A., Woods, C.G., 2005. A centrosomal mechanism involving CDK5RAP2 and CENPJ controls brain size. Nature genetics 37, 353-355.

Bonnafe, E., Touka, M., AitLounis, A., Baas, D., Barras, E., Ucla, C., Moreau, A., Flamant, F., Dubruille, R., Couble, P., Collignon, J., Durand, B., Reith, W., 2004. The transcription factor RFX3 directs nodal cilium development and left-right asymmetry specification. Mol Cell Biol 24, 4417-4427.

Brazelton, W.J., Amundsen, C.D., Silflow, C.D., Lefebvre, P.A., 2001. The bld1 mutation identifies the Chlamydomonas osm-6 homolog as a gene required for flagellar assembly. Curr Biol 11, 1591-1594.

Bredrup, C., Saunier, S., Oud, M.M., Fiskerstrand, T., Hoischen, A., Brackman, D., Leh, S.M., Midtbo, M., Filhol, E., Bole-Feysot, C., Nitschke, P., Gilissen, C., Haugen, O.H., Sanders, J.S., Stolte-Dijkstra, I., Mans, D.A., Steenbergen, E.J., Hamel, B.C., Matignon, M., Pfundt, R., Jeanpierre, C., Boman, H., Rodahl, E., Veltman, J.A., Knappskog, P.M., Knoers, N.V., Roepman, R., Arts, H.H., 2011. Ciliopathies with skeletal anomalies and renal insufficiency due to mutations in the IFT-A gene WDR19. American journal of human genetics 89, 634-643.

Brody, S.L., Yan, X.H., Wuerffel, M.K., Song, S.K., Shapiro, S.D., 2000. Ciliogenesis and left-right axis defects in forkhead factor HFH-4-null mice. Am J Respir Cell Mol Biol 23, 45-51.

Cain, J.E., Di Giovanni, V., Smeeton, J., Rosenblum, N.D., 2010. Genetics of renal hypoplasia: insights into the mechanisms controlling nephron endowment. Pediatric research 68, 91-98.

Cain, J.E., Islam, E., Haxho, F., Chen, L., Bridgewater, D., Nieuwenhuis, E., Hui, C.C., Rosenblum, N.D., 2009. GLI3 repressor controls nephron number via regulation of Wnt11 and Ret in ureteric tip cells. PloS one 4, e7313.

Carvalho-Santos, Z., Machado, P., Branco, P., Tavares-Cadete, F., Rodrigues-Martins, A., Pereira-Leal, J.B., Bettencourt-Dias, M., 2010. Stepwise evolution of the centriole-assembly pathway. Journal of cell science 123, 1414-1426.

Chan, G.K., Schaar, B.T., Yen, T.J., 1998. Characterization of the kinetochore binding domain of CENP-E reveals interactions with the kinetochore proteins CENP-F and hBUBR1. The Journal of cell biology 143, 49-63.

Chen, J., Knowles, H.J., Hebert, J.L., Hackett, B.P., 1998. Mutation of the mouse hepatocyte nuclear factor/forkhead homologue 4 gene results in an absence of cilia and random left-right asymmetry. J Clin Invest 102, 1077-1082.

Chen, J.M., Ferec, C., Cooper, D.N., 2010. Revealing the human mutome. Clinical genetics 78, 310-320.

Cheng HT, Kim M, Valerius MT, Surendran K, Schuster-Gossler K, Gossler A, McMahon AP, Kopan R. 2007. Notch2, but not Notch1, is required for proximal fate acquisition in the mammalian nephron. Development 134(4):801-11.

Choi, M., Scholl, U.I., Ji, W., Liu, T., Tikhonova, I.R., Zumbo, P., Nayir, A., Bakkaloglu, A., Ozen, S., Sanjad, S., Nelson-Williams, C., Farhi, A., Mane, S., Lifton, R.P., 2009. Genetic diagnosis by whole exome capture and massively parallel DNA sequencing. Proceedings of the National Academy of Sciences of the United States of America 106, 19096-19101.

Chung, M.I., Peyrot, S.M., LeBoeuf, S., Park, T.J., McGary, K.L., Marcotte, E.M., Wallingford, J.B., 2012. RFX2 is broadly required for ciliogenesis during vertebrate development. Developmental biology 363, 155-165.

Clark, M.J., Chen, R., Lam, H.Y., Karczewski, K.J., Chen, R., Euskirchen, G., Butte, A.J., Snyder, M., 2011. Performance comparison of exome DNA sequencing technologies. Nature biotechnology 29, 908-914.

Cole, D.G., 2003. The intraflagellar transport machinery of Chlamydomonas reinhardtii. Traffic 4, 435-442.

Cole, D.G., Diener, D.R., Himelblau, A.L., Beech, P.L., Fuster, J.C., Rosenbaum, J.L., 1998. Chlamydomonas kinesin-II-dependent intraflagellar transport (IFT): IFT particles contain proteins required for ciliary assembly in Caenorhabditis elegans sensory neurons. J Cell Biol 141, 993-1008.

Consugar, M.B., Wong, W.C., Lundquist, P.A., Rossetti, S., Kubly, V.J., Walker, D.L., Rangel, L.J., Aspinwall, R., Niaudet, W.P., Ozen, S., David, A., Velinov, M., Bergstralh, E.J., Bae, K.T., Chapman, A.B., Guay-Woodford, L.M., Grantham, J.J., Torres, V.E., Sampson, J.R., Dawson, B.D., Harris, P.C., 2008. Characterization of large rearrangements in autosomal dominant polycystic kidney disease and the PKD1/TSC2 contiguous gene syndrome. Kidney Int 74, 1468-1479.

Corbit, K.C., Aanstad, P., Singla, V., Norman, A.R., Stainier, D.Y., Reiter, J.F., 2005. Vertebrate Smoothened functions at the primary cilium. Nature 437, 1018-1021.

Corbit, K.C., Shyer, A.E., Dowdle, W.E., Gaulden, J., Singla, V., Chen, M.H., Chuang, P.T., Reiter, J.F., 2008. Kif3a constrains beta-catenin-dependent Wnt signalling through dual ciliary and non-ciliary mechanisms. Nature cell biology 10, 70-76.

Craige B, Tsao CC, Diener DR, Hou Y, Lechtreck KF, Rosenbaum JL, Witman GB., 2010. CEP290 tethers flagellar transition zone microtubules to the membrane and regulates flagellar protein content. J Cell Biol 190 927-40.

Dai, D., Zhu, H., Wlodarczyk, B., Zhang, L., Li, L., Li, A.G., Finnell, R.H., Roop, D.R., Chen, J., 2011. Fuz controls the morphogenesis and differentiation of hair follicles through the formation of primary cilia. The Journal of investigative dermatology 131, 302-310.

Das A, Guo W., 2011. Rabs and the exocyst in ciliogenesis, tubulogenesis and beyond. Trends Cell Biol 21, 383-6.

Deane JA, Cole DG, Seeley ES, Diener DR, Rosenbaum JL., 2001. Localization of intraflagellar transport protein IFT52 identifies basal body transitional fibers as the docking site for IFT particles. Curr Biol 11,1586-90.

Deblandre, G.A., Wettstein, D.A., Koyano-Nakagawa, N., Kintner, C., 1999. A two-step mechanism generates the spacing pattern of the ciliated cells in the skin of Xenopus embryos. Development 126, 4715-4728.

Delattre, M., Gonczy, P., 2004. The arithmetic of centrosome biogenesis. Journal of cell science 117, 1619-1630.

Delaval, B., Bright, A., Lawson, N.D., Doxsey, S., 2011. The cilia protein IFT88 is required for spindle orientation in mitosis. Nature cell biology 13, 461-468.

Delous, M., Baala, L., Salomon, R., Laclef, C., Vierkotten, J., Tory, K., Golzio, C., Lacoste, T., Besse, L., Ozilou, C., Moutkine, I., Hellman, N.E., Anselme, I., Silbermann, F., Vesque, C., Gerhardt, C., Rattenberry, E., Wolf, M.T., Gubler, M.C., Martinovic, J., Encha-Razavi, F., Boddaert, N., Gonzales, M., Macher, M.A., Nivet, H., Champion, G., Bertheleme, J.P., Niaudet, P., McDonald, F., Hildebrandt, F., Johnson, C.A., Vekemans, M., Antignac, C., Ruther, U., Schneider-Maunoury, S., Attie-Bitach, T., Saunier, S., 2007. The ciliary gene RPGRIP1L is mutated in cerebello-oculo-renal syndrome (Joubert syndrome type B) and Meckel syndrome. Nat Genet 39, 875-881.

Dixon-Salazar, T., Silhavy, J.L., Marsh, S.E., Louie, C.M., Scott, L.C., Gururaj, A., Al-Gazali, L., Al-Tawari, A.A., Kayserili, H., Sztriha, L., Gleeson, J.G., 2004. Mutations in the AHI1 gene, encoding jouberin, cause Joubert syndrome with cortical polymicrogyria. Am J Hum Genet 75, 979-987.

Dolk, H., Loane, M., Garne, E., 2010. The prevalence of congenital anomalies in Europe. Advances in experimental medicine and biology 686, 349-364.

Doxsey, S., Zimmerman, W., Mikule, K., 2005. Centrosome control of the cell cycle. Trends in cell biology 15, 303-311.

Du J, Wilson PD, 1995. Abnormal polarization of EGF receptors and autocrine stimulation of cyst epithelial growth in human ADPKD, Am. J. Physiol. 269 C487–C495.

Dubruille, R., Laurencon, A., Vandaele, C., Shishido, E., Coulon-Bublex, M., Swoboda, P., Couble, P., Kernan, M., Durand, B., 2002. Drosophila regulatory factor X is necessary for ciliated sensory neuron differentiation. Development 129, 5487-5498.

Dzhindzhev, N.S., Yu, Q.D., Weiskopf, K., Tzolovsky, G., Cunha-Ferreira, I., Riparbelli, M., Rodrigues-Martins, A., Bettencourt-Dias, M., Callaini,

G., Glover, D.M., 2010. Asterless is a scaffold for the onset of centriole assembly. Nature 467, 714-718.

Efimenko, E., Bubb, K., Mak, H.Y., Holzman, T., Leroux, M.R., Ruvkun, G., Thomas, J.H., Swoboda, P., 2005. Analysis of xbx genes in C. elegans. Development 132, 1923-1934.

Emery, P., Durand, B., Mach, B., Reith, W., 1996. RFX proteins, a novel family of DNA binding proteins conserved in the eukaryotic kingdom. Nucleic acids research 24, 803-807.

Evans, H.J., Edwards, L., Goodwin, R.L., 2007. Conserved C-terminal domains of mCenp-F (LEK1) regulate subcellular localization and mitotic checkpoint delay. Experimental cell research 313, 2427-2437.

Ezratty, E.J., Stokes, N., Chai, S., Shah, A.S., Williams, S.E., Fuchs, E., 2011. A role for the primary cilium in Notch signaling and epidermal differentiation during skin development. Cell 145, 1129-1141.

Faragher, A.J., Fry, A.M., 2003. Nek2A kinase stimulates centrosome disjunction and is required for formation of bipolar mitotic spindles. Molecular biology of the cell 14, 2876-2889.

Feng, J., Huang, H., Yen, T.J., 2006. CENP-F is a novel microtubule-binding protein that is essential for kinetochore attachments and affects the duration of the mitotic checkpoint delay. Chromosoma 115, 320-329.

Ferland, R.J., Eyaid, W., Collura, R.V., Tully, L.D., Hill, R.S., Al-Nouri, D., Al-Rumayyan, A., Topcu, M., Gascon, G., Bodell, A., Shugart, Y.Y., Ruvolo, M., Walsh, C.A., 2004. Abnormal cerebellar development and axonal decussation due to mutations in AHI1 in Joubert syndrome. Nat Genet 36, 1008-1013.

Fisch C, Dupuis-Williams P (2011). Ultrastructure of cilia and flagella - back to the future! Biol Cell. 103, 249-70.

Fischer, E., Legue, E., Doyen, A., Nato, F., Nicolas, J.F., Torres, V., Yaniv, M., Pontoglio, M., 2006. Defective planar cell polarity in polycystic kidney disease. Nature genetics 38, 21-23.

Fry, A.M., Mayor, T., Meraldi, P., Stierhof, Y.D., Tanaka, K., Nigg, E.A., 1998. C-Nap1, a novel centrosomal coiled-coil protein and candidate substrate of the cell cycle-regulated protein kinase Nek2. The Journal of cell biology 141, 1563-1574.

Gerdes, J.M., Liu, Y., Zaghloul, N.A., Leitch, C.C., Lawson, S.S., Kato, M., Beachy, P.A., Beales, P.L., DeMartino, G.N., Fisher, S., Badano, J.L., Katsanis, N., 2007. Disruption of the basal body compromises proteasomal function and perturbs intracellular Wnt response. Nature genetics 39, 1350-1360.

Germino, G.G., 2005. Linking cilia to Wnts. Nat Genet 37, 455-457.

Gherman, A., Davis, E.E., Katsanis, N., 2006. The ciliary proteome database: an integrated community resource for the genetic and functional dissection of cilia. Nature genetics 38, 961-962.

Gilissen, C., Arts, H.H., Hoischen, A., Spruijt, L., Mans, D.A., Arts, P., van Lier, B., Steehouwer, M., van Reeuwijk, J., Kant, S.G., Roepman, R., Knoers, N.V., Veltman, J.A., Brunner, H.G., 2010. Exome sequencing identifies WDR35 variants involved in Sensenbrenner syndrome. American journal of human genetics 87, 418-423.

Gilissen, C., Hoischen, A., Brunner, H.G., Veltman, J.A., 2011. Unlocking Mendelian disease using exome sequencing. Genome biology 12, 228.

Ginger, M.L., Portman, N., McKean, P.G., 2008. Swimming with protists: perception, motility and flagellum assembly. Nat Rev Microbiol 6, 838-850.

Glazov, E.A., Zankl, A., Donskoi, M., Kenna, T.J., Thomas, G.P., Clark, G.R., Duncan, E.L., Brown, M.A., 2011. Whole-exome re-sequencing in a family quartet identifies POP1 mutations as the cause of a novel skeletal dysplasia. PLoS genetics 7, e1002027.

Goetz SC, Anderson KV., 2010. The primary cilium: a signalling centre during vertebrate development. Nat Rev Genet. May;11(5):331-44.

Gonzalez, C., Saunders, R.D., Casal, J., Molina, I., Carmena, M., Ripoll, P., Glover, D.M., 1990. Mutations at the asp locus of Drosophila lead to multiple free centrosomes in syncytial embryos, but restrict centrosome duplication in larval neuroblasts. Journal of cell science 96 (Pt 4), 605-616.

Gradilone, S.A., Masyuk, A.I., Splinter, P.L., Banales, J.M., Huang, B.Q., Tietz, P.S., Masyuk, T.V., Larusso, N.F., 2007. Cholangiocyte cilia express TRPV4 and detect changes in luminal tonicity inducing bicarbonate secretion. Proc Natl Acad Sci U S A 104, 19138-19143.

Graser S, Stierhof YD, Lavoie SB, Gassner OS, Lamla S, Le Clech M, Nigg EA., 2007. Cep164, a novel centriole appendage protein required for primary cilium formation. J Cell Biol 179, 321-30.

Gray, R.S., Abitua, P.B., Wlodarczyk, B.J., Szabo-Rogers, H.L., Blanchard, O., Lee, I., Weiss, G.S., Liu, K.J., Marcotte, E.M., Wallingford, J.B., Finnell, R.H., 2009. The planar cell polarity effector Fuz is essential for targeted membrane trafficking, ciliogenesis and mouse embryonic development. Nature cell biology 11, 1225-1232.

Guernsey, D.L., Jiang, H., Hussin, J., Arnold, M., Bouyakdan, K., Perry, S., Babineau-Sturk, T., Beis, J., Dumas, N., Evans, S.C., Ferguson, M., Matsuoka, M., Macgillivray, C., Nightingale, M., Patry, L., Rideout, A.L., Thomas, A., Orr, A., Hoffmann, I., Michaud, J.L., Awadalla, P., Meek, D.C., Ludman, M., Samuels, M.E., 2010. Mutations in centrosomal protein CEP152 in primary microcephaly families linked to MCPH4. American journal of human genetics 87, 40-51.

Habedanck, R., Stierhof, Y.D., Wilkinson, C.J., Nigg, E.A., 2005. The Polo kinase Plk4 functions in centriole duplication. Nature cell biology 7, 1140-1146.

Hanaoka K, Devuyst O, Schwiebert EM, Wilson PD, Guggino WB, 1996. A

role for CFTR in human autosomal dominant polycystic kidney disease, Am. J. Physiol. 270 C389–C399.

Happe, H., de Heer, E., Peters, D.J., 2011. Polycystic kidney disease: the complexity of planar cell polarity and signaling during tissue regeneration and cyst formation. Biochimica et biophysica acta 1812, 1249-1255.

Haraguchi, K., Hayashi, T., Jimbo, T., Yamamoto, T., Akiyama, T., 2006. Role of the kinesin-2 family protein, KIF3, during mitosis. The Journal of biological chemistry 281, 4094-4099.

Harris, P.C., 2009. 2008 Homer W. Smith Award: insights into the pathogenesis of polycystic kidney disease from gene discovery. J Am Soc Nephrol 20, 1188-1198.

Heald, R., Tournebize, R., Blank, T., Sandaltzopoulos, R., Becker, P., Hyman, A., Karsenti, E., 1996. Self-organization of microtubules into bipolar spindles around artificial chromosomes in Xenopus egg extracts. Nature 382, 420-425.

Heydeck, W., Zeng, H., Liu, A., 2009. Planar cell polarity effector gene Fuzzy regulates cilia formation and Hedgehog signal transduction in mouse.

Developmental dynamics : an official publication of the American Association of Anatomists 238, 3035-3042.

Hildebrandt, F., Attanasio, M., Otto, E., 2009. Nephronophthisis: disease mechanisms of a ciliopathy. Journal of the American Society of Nephrology : JASN 20, 23-35.

Hildebrandt, F., Otto, E., 2005. Cilia and centrosomes: a unifying pathogenic concept for cystic kidney disease? Nat Rev Genet 6, 928-940.

Hildebrandt, F., Otto, E., Rensing, C., Nothwang, H.G., Vollmer, M., Adolphs, J., Hanusch, H., Brandis, M., 1997. A novel gene encoding an SH3 domain protein is mutated in nephronophthisis type 1. Nat Genet 17, 149-153.

Hiraki M, Nakazawa Y, Kamiya R, Hirono M., 2007. Bld10p constitutes the cartwheel-spoke tip and stabilizes the 9-fold symmetry of the centriole. Curr Biol. 17, 1778-83.

Hirokawa, N., Tanaka, Y., Okada, Y., Takeda, S., 2006. Nodal flow and the generation of left-right asymmetry. Cell 125, 33-45.

Hoefele, J., Wolf, M.T., O'Toole, J.F., Otto, E.A., Schultheiss, U., Deschenes, G., Attanasio, M., Utsch, B., Antignac, C., Hildebrandt, F., 2007. Evidence of oligogenic inheritance in nephronophthisis. J Am Soc Nephrol 18, 2789-2795.

Holt, S.V., Vergnolle, M.A., Hussein, D., Wozniak, M.J., Allan, V.J., Taylor, S.S., 2005. Silencing Cenp-F weakens centromeric cohesion, prevents chromosome alignment and activates the spindle checkpoint. Journal of cell science 118, 4889-4900.

Hou, X., Mrug, M., Yoder, B.K., Lefkowitz, E.J., Kremmidiotis, G., D'Eustachio, P., Beier, D.R., Guay-Woodford, L.M., 2002. Cystin, a novel cilia-associated protein, is disrupted in the cpk mouse model of polycystic kidney disease. J Clin Invest 109, 533-540.

Hu, D., Helms, J.A., 1999. The role of sonic hedgehog in normal and abnormal craniofacial morphogenesis. Development 126, 4873-4884.

Huangfu, D., Anderson, K.V., 2005. Cilia and Hedgehog responsiveness in the mouse. Proc Natl Acad Sci U S A 102, 11325-11330.

Huangfu, D., Liu, A., Rakeman, A.S., Murcia, N.S., Niswander, L., Anderson, K.V., 2003. Hedgehog signalling in the mouse requires intraflagellar transport proteins. Nature 426, 83-87.

Hughes, J., Ward, C.J., Peral, B., Aspinwall, R., Clark, K., San Millan, J.L., Gamble, V., Harris, P.C., 1995. The polycystic kidney disease 1 (PKD1) gene encodes a novel protein with multiple cell recognition domains. Nat Genet 10, 151-160.

Ishikawa H, Kubo A, Tsukita S, Tsukita S., 2005. Odf2-deficient mother centrioles lack distal/subdistal appendages and the ability to generate primary cilia. Nat Cell Biol. 7, 517-24.

Jekely, G., Arendt, D., 2006. Evolution of intraflagellar transport from coated vesicles and autogenous origin of the eukaryotic cilium. Bioessays 28, 191-198.

Jonassen, J.A., San Agustin, J., Follit, J.A., Pazour, G.J., 2008. Deletion of IFT20 in the mouse kidney causes misorientation of the mitotic spindle and cystic kidney disease. The Journal of cell biology 183, 377-384.

Jurczyk, A., Gromley, A., Redick, S., San Agustin, J., Witman, G., Pazour, G.J., Peters, D.J., Doxsey, S., 2004. Pericentrin forms a complex with

intraflagellar transport proteins and polycystin-2 and is required for primary cilia assembly. The Journal of cell biology 166, 637-643.

Karner, C.M., Chirumamilla, R., Aoki, S., Igarashi, P., Wallingford, J.B., Carroll, T.J., 2009. Wnt9b signaling regulates planar cell polarity and kidney tubule morphogenesis. Nature genetics 41, 793-799.

Kiefer, S.M., Ohlemiller, K.K., Yang, J., McDill, B.W., Kohlhase, J., Rauchman, M., 2003. Expression of a truncated Sall1 transcriptional repressor is responsible for Townes-Brocks syndrome birth defects. Human molecular genetics 12, 2221-2227.

Kiefer, S.M., Robbins, L., Stumpff, K.M., Lin, C., Ma, L., Rauchman, M., 2010. Sall1-dependent signals affect Wnt signaling and ureter tip fate to initiate kidney development. Development 137, 3099-3106.

Kim, J.J., Gill, P.S., Rotin, L., van Eede, M., Henkelman, R.M., Hui, C.C., Rosenblum, N.D., 2011. Suppressor of fused controls mid-hindbrain patterning and cerebellar morphogenesis via GLI3 repressor. The Journal of neuroscience : the official journal of the Society for Neuroscience 31, 1825-1836.

King, S.M., Dillman, J.F., 3rd, Benashski, S.E., Lye, R.J., Patel-King, R.S., Pfister, K.K., 1996. The mouse t-complex-encoded protein Tctex-1 is a light chain of brain cytoplasmic dynein. J Biol Chem 271, 32281-32287.

Kiyomitsu, T., Cheeseman, I.M., 2012. Chromosome- and spindle-pole-derived signals generate an intrinsic code for spindle position and orientation. Nature cell biology 14, 311-317.

Kleylein-Sohn, J., Westendorf, J., Le Clech, M., Habedanck, R., Stierhof, Y.D., Nigg, E.A., 2007. Plk4-induced centriole biogenesis in human cells. Developmental cell 13, 190-202.

Knoblich, J.A., 2008. Mechanisms of asymmetric stem cell division. Cell 132, 583-597.

Knödler A, Feng S, Zhang J, Zhang X, Das A, Peränen J, Guo W, 2010. Coordination of Rab8 and Rab11 in primary ciliogenesis. Proc Natl Acad Sci U S A. 107, 6346-51.

Kobayashi, A., Kwan, K.M., Carroll, T.J., McMahon, A.P., Mendelsohn, C.L., Behringer, R.R., 2005. Distinct and sequential tissue-specific activities

of the LIM-class homeobox gene Lim1 for tubular morphogenesis during kidney development. Development 132, 2809-2823.

Kozminski, K.G., Beech, P.L., Rosenbaum, J.L., 1995. The Chlamydomonas kinesin-like protein FLA10 is involved in motility associated with the flagellar membrane. J Cell Biol 131, 1517-1527.

Kozminski, K.G., Johnson, K.A., Forscher, P., Rosenbaum, J.L., 1993. A motility in the eukaryotic flagellum unrelated to flagellar beating. Proc Natl Acad Sci U S A 90, 5519-5523.

Kramer-Zucker, A.G., Olale, F., Haycraft, C.J., Yoder, B.K., Schier, A.F., Drummond, I.A., 2005. Cilia-driven fluid flow in the zebrafish pronephros, brain and Kupffer's vesicle is required for normal organogenesis. Development 132, 1907-1921.

Kruglyak, L., Daly, M.J., Reeve-Daly, M.P., Lander, E.S., 1996. Parametric and nonparametric linkage analysis: a unified multipoint approach. American journal of human genetics 58, 1347-1363.

Kwiatkowski DJ., 2003. Tuberous sclerosis: from tubers to mTOR. Ann Hum Genet. 67, 87-96.

Lantinga-van Leeuwen, I.S., Leonhard, W.N., van der Wal, A., Breuning, M.H., de Heer, E., Peters, D.J., 2007. Kidney-specific inactivation of the Pkd1 gene induces rapid cyst formation in developing kidneys and a slow onset of disease in adult mice. Hum Mol Genet 16, 3188-3196.

Liao H, Winkfein RJ, Mack G, Rattner JB, Yen TJ, 1995. CENP-F is a protein of the nuclear matrix that assembles onto kinetochores at late G2 and is rapidly degraded after mitosis. J Cell Biol. 1995 Aug;130(3):507-18.

Lee, J., 2010. De novo formation of basal bodies during cellular differentiation of Naegleria gruberi: progress and hypotheses. Seminars in cell & developmental biology 21, 156-162.

Lee, J.H., Silhavy, J.L., Lee, J.E., Al-Gazali, L., Thomas, S., Davis, E.E., Bielas, S.L., Hill, K.J., Iannicelli, M., Brancati, F., Gabriel, S.B., Russ, C., Logan, C.V., Sharif, S.M., Bennett, C.P., Abe, M., Hildebrandt, F., Diplas, B.H., Attie-Bitach, T., Katsanis, N., Rajab, A., Koul, R., Sztriha, L., Waters, E.R., Ferro-Novick, S., Woods, C.G., Johnson, C.A., Valente, E.M., Zaki, M.S., Gleeson, J.G., 2012. Evolutionarily assembled cis-regulatory module at a human ciliopathy locus. Science 335, 966-969.

Lefers MA, Wang QT, Holmgren RA., 2001. Genetic dissection of the Drosophila Cubitus interruptus signaling complex. Dev Biol. 236, 411-20.

Li, J.B., Gerdes, J.M., Haycraft, C.J., Fan, Y., Teslovich, T.M., May-Simera, H., Li, H., Blacque, O.E., Li, L., Leitch, C.C., Lewis, R.A., Green, J.S., Parfrey, P.S., Leroux, M.R., Davidson, W.S., Beales, P.L., Guay-Woodford, L.M., Yoder, B.K., Stormo, G.D., Katsanis, N., Dutcher, S.K., 2004. Comparative genomics identifies a flagellar and basal body proteome that includes the BBS5 human disease gene. Cell 117, 541-552.

Li ZJ, Nieuwenhuis E, Nien W, Zhang X, Zhang J, Puviindran V, Wainwright BJ, Kim PC, Hui CC, 2012. Kif7 regulates Gli2 through Sufu-dependent and -independent functions during skin development and tumorigenesis. Development. 2012 Oct 3.

Lin, F., Hiesberger, T., Cordes, K., Sinclair, A.M., Goldstein, L.S., Somlo, S., Igarashi, P., 2003. Kidney-specific inactivation of the KIF3A subunit of kinesin-II inhibits renal ciliogenesis and produces polycystic kidney disease. Proceedings of the National Academy of Sciences of the United States of America 100, 5286-5291.

Liu, Y., Pathak, N., Kramer-Zucker, A., Drummond, I.A., 2007. Notch signaling controls the differentiation of transporting epithelia and multiciliated cells in the zebrafish pronephros. Development 134, 1111-1122.

Logan, C.V., Abdel-Hamed, Z., Johnson, C.A., 2011. Molecular genetics and pathogenic mechanisms for the severe ciliopathies: insights into neurodevelopment and pathogenesis of neural tube defects. Molecular neurobiology 43, 12-26.

Luders, J., Stearns, T., 2007. Microtubule-organizing centres: a re-evaluation. Nature reviews. Molecular cell biology 8, 161-167.

Ma, L., Zhao, X., Zhu, X., 2006. Mitosin/CENP-F in mitosis, transcriptional control, and differentiation. Journal of biomedical science 13, 205-213.

Ma, M., Jiang, Y.J., 2007. Jagged2a-notch signaling mediates cell fate choice in the zebrafish pronephric duct. PLoS genetics 3, e18.

MacArthur, D.G., Balasubramanian, S., Frankish, A., Huang, N., Morris, J., Walter, K., Jostins, L., Habegger, L., Pickrell, J.K., Montgomery, S.B., Albers, C.A., Zhang, Z.D., Conrad, D.F., Lunter, G., Zheng, H., Ayub, Q., DePristo, M.A., Banks, E., Hu, M., Handsaker, R.E., Rosenfeld, J.A.,

Fromer, M., Jin, M., Mu, X.J., Khurana, E., Ye, K., Kay, M., Saunders, G.I., Suner, M.M., Hunt, T., Barnes, I.H., Amid, C., Carvalho-Silva, D.R., Bignell, A.H., Snow, C., Yngvadottir, B., Bumpstead, S., Cooper, D.N., Xue, Y., Romero, I.G., Wang, J., Li, Y., Gibbs, R.A., McCarroll, S.A., Dermitzakis, E.T., Pritchard, J.K., Barrett, J.C., Harrow, J., Hurles, M.E., Gerstein, M.B., Tyler-Smith, C., 2012. A systematic survey of loss-of-function variants in human protein-coding genes. Science 335, 823-828.

Magenheimer BS, St John PL, Isom KS, Abrahamson DR, De Lisle RC, Wallace DP, Maser RL, Grantham JJ, Calvet JP, 2006. Early embryonic renal tubules of wildtype and polycystic kidney disease kidneys respond to cAMP stimulation with cystic fibrosis transmembrane conductance regulator/Na(+), K(+), 2Cl(-) Cotransporter-dependent cystic dilation, J. Am. Soc. Nephrol. 17 3424–3437.

Mao, J., Kim, B.M., Rajurkar, M., Shivdasani, R.A., McMahon, A.P., 2010. Hedgehog signaling controls mesenchymal growth in the developing mammalian digestive tract. Development 137, 1721-1729.

Matthies, H.J., McDonald, H.B., Goldstein, L.S., Theurkauf, W.E., 1996. Anastral meiotic spindle morphogenesis: role of the non-claret disjunctional kinesin-like protein. The Journal of cell biology 134, 455-464.

May-Simera, H.L., Kai, M., Hernandez, V., Osborn, D.P., Tada, M., Beales, P.L., 2010. Bbs8, together with the planar cell polarity protein Vangl2, is required to establish left-right asymmetry in zebrafish. Developmental biology 345, 215-225.

McNeill, H., 2010. Planar cell polarity: keeping hairs straight is not so simple. Cold Spring Harbor perspectives in biology 2, a003376.

Merrill, A.E., Merriman, B., Farrington-Rock, C., Camacho, N., Sebald, E.T., Funari, V.A., Schibler, M.J., Firestein, M.H., Cohn, Z.A., Priore, M.A., Thompson, A.K., Rimoin, D.L., Nelson, S.F., Cohn, D.H., Krakow, D., 2009. Ciliary abnormalities due to defects in the retrograde transport protein DYNC2H1 in short-rib polydactyly syndrome. American journal of human genetics 84, 542-549.

Metzker, M.L., 2010. Sequencing technologies - the next generation. Nature reviews. Genetics 11, 31-46.

Mikami, A., Tynan, S.H., Hama, T., Luby-Phelps, K., Saito, T., Crandall, J.E., Besharse, J.C., Vallee, R.B., 2002. Molecular structure of cytoplasmic

dynein 2 and its distribution in neuronal and ciliated cells. J Cell Sci 115, 4801-4808.

Miyamoto, T., Porazinski, S., Wang, H., Borovina, A., Ciruna, B., Shimizu, A., Kajii, T., Kikuchi, A., Furutani-Seiki, M., Matsuura, S., 2011. Insufficiency of BUBR1, a mitotic spindle checkpoint regulator, causes impaired ciliogenesis in vertebrates. Human molecular genetics 20, 2058-2070.

Mochizuki, T., Wu, G., Hayashi, T., Xenophontos, S.L., Veldhuisen, B., Saris, J.J., Reynolds, D.M., Cai, Y., Gabow, P.A., Pierides, A., Kimberling, W.J., Breuning, M.H., Deltas, C.C., Peters, D.J., Somlo, S., 1996. PKD2, a gene for polycystic kidney disease that encodes an integral membrane protein. Science 272, 1339-1342.

Mollet, G., Salomon, R., Gribouval, O., Silbermann, F., Bacq, D., Landthaler, G., Milford, D., Nayir, A., Rizzoni, G., Antignac, C., Saunier, S., 2002. The gene mutated in juvenile nephronophthisis type 4 encodes a novel protein that interacts with nephrocystin. Nat Genet 32, 300-305.

Morimoto, M., Liu, Z., Cheng, H.T., Winters, N., Bader, D., Kopan, R., 2010. Canonical Notch signaling in the developing lung is required for determination of arterial smooth muscle cells and selection of Clara versus ciliated cell fate. Journal of cell science 123, 213-224.

Moyer, J.H., Lee-Tischler, M.J., Kwon, H.Y., Schrick, J.J., Avner, E.D., Sweeney, W.E., Godfrey, V.L., Cacheiro, N.L., Wilkinson, J.E., Woychik, R.P., 1994. Candidate gene associated with a mutation causing recessive polycystic kidney disease in mice. Science 264, 1329-1333.

Moynihan, K.L., Pooley, R., Miller, P.M., Kaverina, I., Bader, D.M., 2009. Murine CENP-F regulates centrosomal microtubule nucleation and interacts with Hook2 at the centrosome. Molecular biology of the cell 20, 4790-4803.

Mumm, J.S., Schroeter, E.H., Saxena, M.T., Griesemer, A., Tian, X., Pan, D.J., Ray, W.J., Kopan, R., 2000. A ligand-induced extracellular cleavage regulates gamma-secretase-like proteolytic activation of Notch1. Mol Cell 5, 197-206.

Murcia, N.S., Richards, W.G., Yoder, B.K., Mucenski, M.L., Dunlap, J.R., Woychik, R.P., 2000. The Oak Ridge Polycystic Kidney (orpk) disease gene is required for left-right axis determination. Development 127, 2347-2355.

Nachury, M.V., Loktev, A.V., Zhang, Q., Westlake, C.J., Peranen, J., Merdes, A., Slusarski, D.C., Scheller, R.H., Bazan, J.F., Sheffield, V.C.,

Jackson, P.K., 2007. A core complex of BBS proteins cooperates with the GTPase Rab8 to promote ciliary membrane biogenesis. Cell 129, 1201-1213.

Nadasdy T, Laszik Z, Lajoie G, Blick KE, Wheeler DE, Silva FG., 1995. Proliferative activity of cyst epithelium in human renal cystic diseases. J Am Soc Nephrol. 5:1462-8.

Neugebauer, J.M., Amack, J.D., Peterson, A.G., Bisgrove, B.W., Yost, H.J., 2009. FGF signalling during embryo development regulates cilia length in diverse epithelia. Nature 458, 651-654.

Ng, P.C., Levy, S., Huang, J., Stockwell, T.B., Walenz, B.P., Li, K., Axelrod, N., Busam, D.A., Strausberg, R.L., Venter, J.C., 2008. Genetic variation in an individual human exome. PLoS genetics 4, e1000160.

Ng, S.B., Turner, E.H., Robertson, P.D., Flygare, S.D., Bigham, A.W., Lee, C., Shaffer, T., Wong, M., Bhattacharjee, A., Eichler, E.E., Bamshad, M., Nickerson, D.A., Shendure, J., 2009. Targeted capture and massively parallel sequencing of 12 human exomes. Nature 461, 272-276.

Nicholas, A.K., Khurshid, M., Desir, J., Carvalho, O.P., Cox, J.J., Thornton, G., Kausar, R., Ansar, M., Ahmad, W., Verloes, A., Passemard,

S., Misson, J.P., Lindsay, S., Gergely, F., Dobyns, W.B., Roberts, E., Abramowicz, M., Woods, C.G., 2010. WDR62 is associated with the spindle pole and is mutated in human microcephaly. Nature genetics 42, 1010-1014.

Nigg, E.A., 2007. Centrosome duplication: of rules and licenses. Trends in cell biology 17, 215-221.

Nigg, E.A., Raff, J.W., 2009. Centrioles, centrosomes, and cilia in health and disease. Cell 139, 663-678.

Nishinakamura, R., Matsumoto, Y., Nakao, K., Nakamura, K., Sato, A., Copeland, N.G., Gilbert, D.J., Jenkins, N.A., Scully, S., Lacey, D.L., Katsuki, M., Asashima, M., Yokota, T., 2001. Murine homolog of SALL1 is essential for ureteric bud invasion in kidney development. Development 128, 3105-3115.

Nonaka, S., Tanaka, Y., Okada, Y., Takeda, S., Harada, A., Kanai, Y., Kido, M., Hirokawa, N., 1998. Randomization of left-right asymmetry due to loss of nodal cilia generating leftward flow of extraembryonic fluid in mice lacking KIF3B motor protein. Cell 95, 829-837.

Novalic Z, van der Wal AM, Leonhard WN, Koehl G, Breuning MH,

Geissler EK, de Heer E, Peters DJ, 2012. Dose-dependent effects of sirolimus on mTOR signaling and polycystic kidney disease. J Am Soc Nephrol. 23, 842-53.

O'Connell, C.B., Wang, Y.L., 2000. Mammalian spindle orientation and position respond to changes in cell shape in a dynein-dependent fashion. Molecular biology of the cell 11, 1765-1774.

O'Toole, J.F., Liu, Y., Davis, E.E., Westlake, C.J., Attanasio, M., Otto, E.A., Seelow, D., Nurnberg, G., Becker, C., Nuutinen, M., Karppa, M., Ignatius, J., Uusimaa, J., Pakanen, S., Jaakkola, E., van den Heuvel, L.P., Fehrenbach, H., Wiggins, R., Goyal, M., Zhou, W., Wolf, M.T., Wise, E., Helou, J., Allen, S.J., Murga-Zamalloa, C.A., Ashraf, S., Chaki, M., Heeringa, S., Chernin, G., Hoskins, B.E., Chaib, H., Gleeson, J., Kusakabe, T., Suzuki, T., Isaac, R.E., Quarmby, L.M., Tennant, B., Fujioka, H., Tuominen, H., Hassinen, I., Lohi, H., van Houten, J.L., Rotig, A., Sayer, J.A., Rolinski, B., Freisinger, P., Madhavan, S.M., Herzer, M., Madignier, F., Prokisch, H., Nurnberg, P., Jackson, P.K., Khanna, H., Katsanis, N., Hildebrandt, F., Individuals with mutations in XPNPEP3, which encodes a mitochondrial protein, develop a nephronophthisis-like nephropathy. J Clin Invest 120, 791-802.

Ocbina, P.J., Eggenschwiler, J.T., Moskowitz, I., Anderson, K.V., 2011. Complex interactions between genes controlling trafficking in primary cilia. Nature genetics 43, 547-553.

Olbrich H, Schmidts M, Werner C, Onoufriadis A, Loges NT, Raidt J, Banki NF, Shoemark A, Burgoyne T, Al Turki S, Hurles ME; UK10K Consortium, Köhler G, Schroeder J, Nürnberg G, Nürnberg P, Chung EM, Reinhardt R, Marthin JK, Nielsen KG, Mitchison HM, Omran H, 2012. Recessive HYDIN Mutations Cause Primary Ciliary Dyskinesia without Randomization of Left-Right Body Asymmetry. Am J Hum Genet. 91, 672-84.

Omran H 2010. NPHP proteins: gatekeepers of the ciliary compartment. J Cell Biol. 190, 715-7.

Onuchic, L.F., Furu, L., Nagasawa, Y., Hou, X., Eggermann, T., Ren, Z., Bergmann, C., Senderek, J., Esquivel, E., Zeltner, R., Rudnik-Schoneborn, S., Mrug, M., Sweeney, W., Avner, E.D., Zerres, K., Guay-Woodford, L.M., Somlo, S., Germino, G.G., 2002. PKHD1, the polycystic kidney and hepatic disease 1 gene, encodes a novel large protein containing multiple immunoglobulin-like plexin-transcription-factor domains and parallel beta-helix 1 repeats. Am J Hum Genet 70, 1305-1317.

Ostrowski, L.E., Blackburn, K., Radde, K.M., Moyer, M.B., Schlatzer, D.M., Moseley, A., Boucher, R.C., 2002. A proteomic analysis of human cilia: identification of novel components. Molecular & cellular proteomics : MCP 1, 451-465.

O'Toole ET, 2007. In Methods in Cell Biology. Volume 79. Edited by McIntosh JR: Waltham, MS: Academic Press. 125-143.

Otto, E., Hoefele, J., Ruf, R., Mueller, A.M., Hiller, K.S., Wolf, M.T., Schuermann, M.J., Becker, A., Birkenhager, R., Sudbrak, R., Hennies, H.C., Nurnberg, P., Hildebrandt, F., 2002. A gene mutated in nephronophthisis and retinitis pigmentosa encodes a novel protein, nephroretinin, conserved in evolution. Am J Hum Genet 71, 1161-1167.

Otto, E.A., Schermer, B., Obara, T., O'Toole, J.F., Hiller, K.S., Mueller, A.M., Ruf, R.G., Hoefele, J., Beekmann, F., Landau, D., Foreman, J.W., Goodship, J.A., Strachan, T., Kispert, A., Wolf, M.T., Gagnadoux, M.F., Nivet, H., Antignac, C., Walz, G., Drummond, I.A., Benzing, T., Hildebrandt, F., 2003. Mutations in INVS encoding inversin cause nephronophthisis type 2, linking renal cystic disease to the function of primary cilia and left-right axis determination. Nature genetics 34, 413-420.

Otto, E.A., Tory, K., Attanasio, M., Zhou, W., Chaki, M., Paruchuri, Y., Wise, E.L., Wolf, M.T., Utsch, B., Becker, C., Nurnberg, G., Nurnberg, P., Nayir, A., Saunier, S., Antignac, C., Hildebrandt, F., 2009. Hypomorphic mutations in meckelin (MKS3/TMEM67) cause nephronophthisis with liver fibrosis (NPHP11). J Med Genet 46, 663-670.

Otto, E.A., Trapp, M.L., Schultheiss, U.T., Helou, J., Quarmby, L.M., Hildebrandt, F., 2008. NEK8 mutations affect ciliary and centrosomal localization and may cause nephronophthisis. J Am Soc Nephrol 19, 587-592.

Park, T.J., Haigo, S.L., Wallingford, J.B., 2006. Ciliogenesis defects in embryos lacking inturned or fuzzy function are associated with failure of planar cell polarity and Hedgehog signaling. Nature genetics 38, 303-311.

Park, T.J., Mitchell, B.J., Abitua, P.B., Kintner, C., Wallingford, J.B., 2008. Dishevelled controls apical docking and planar polarization of basal bodies in ciliated epithelial cells. Nature genetics 40, 871-879.

Patel, V., Li, L., Cobo-Stark, P., Shao, X., Somlo, S., Lin, F., Igarashi, P., 2008. Acute kidney injury and aberrant planar cell polarity induce cyst formation in mice lacking renal cilia. Human molecular genetics 17, 1578-1590.

Pazour, G.J., Agrin, N., Leszyk, J., Witman, G.B., 2005. Proteomic analysis of a eukaryotic cilium. The Journal of cell biology 170, 103-113.

Pazour, G.J., Dickert, B.L., Vucica, Y., Seeley, E.S., Rosenbaum, J.L., Witman, G.B., Cole, D.G., 2000. Chlamydomonas IFT88 and its mouse homologue, polycystic kidney disease gene tg737, are required for assembly of cilia and flagella. The Journal of cell biology 151, 709-718.

Pazour, G.J., Dickert, B.L., Witman, G.B., 1999. The DHC1b (DHC2) isoform of cytoplasmic dynein is required for flagellar assembly. The Journal of cell biology 144, 473-481.

Pazour, G.J., San Agustin, J.T., Follit, J.A., Rosenbaum, J.L., Witman, G.B., 2002. Polycystin-2 localizes to kidney cilia and the ciliary level is elevated in orpk mice with polycystic kidney disease. Curr Biol 12, R378-380.

Pazour, G.J., Wilkerson, C.G., Witman, G.B., 1998. A dynein light chain is essential for the retrograde particle movement of intraflagellar transport (IFT). The Journal of cell biology 141, 979-992.

Pedersen, L.B., Rosenbaum, J.L., 2008. Intraflagellar transport (IFT) role in ciliary assembly, resorption and signalling. Curr Top Dev Biol 85, 23-61.

Pooley, R.D., Moynihan, K.L., Soukoulis, V., Reddy, S., Francis, R., Lo, C., Ma, L.J., Bader, D.M., 2008. Murine CENPF interacts with syntaxin 4 in the regulation of vesicular transport. Journal of cell science 121, 3413-3421.

Pigino G, Ishikawa T., 2012. Axonemal radial spokes: 3D structure, function and assembly. Bioarchitecture 2, 50-58.

Porter, M.E., Bower, R., Knott, J.A., Byrd, P., Dentler, W., 1999. Cytoplasmic dynein heavy chain 1b is required for flagellar assembly in Chlamydomonas. Molecular biology of the cell 10, 693-712.

Przewloka, M.R., Glover, D.M., 2009. The kinetochore and the centromere: a working long distance relationship. Annual review of genetics 43, 439-465.

Qin, H., Diener, D.R., Geimer, S., Cole, D.G., Rosenbaum, J.L., 2004. Intraflagellar transport (IFT) cargo: IFT transports flagellar precursors to the tip and turnover products to the cell body. J Cell Biol 164, 255-266.

Rauch, A., Thiel, C.T., Schindler, D., Wick, U., Crow, Y.J., Ekici, A.B., van Essen, A.J., Goecke, T.O., Al-Gazali, L., Chrzanowska, K.H., Zweier, C., Brunner, H.G., Becker, K., Curry, C.J., Dallapiccola, B., Devriendt, K., Dorfler, A., Kinning, E., Megarbane, A., Meinecke, P., Semple, R.K., Spranger, S., Toutain, A., Trembath, R.C., Voss, E., Wilson, L., Hennekam, R., de Zegher, F., Dorr, H.G., Reis, A., 2008. Mutations in the pericentrin (PCNT) gene cause primordial dwarfism. Science 319, 816-819.

Richards WG, Sweeney WE, Yoder BK, Wilkinson JE, Woychik RP, Avner, ED, 1998. Epidermal growth factor receptor activity mediates renal cyst formation in polycystic kidney disease, J. Clin. Invest. 101 935–939.

Rodrigues-Martins, A., Riparbelli, M., Callaini, G., Glover, D.M., Bettencourt-Dias, M., 2007. Revisiting the role of the mother centriole in centriole biogenesis. Science 316, 1046-1050.

Roepman R, Wolfrum U., 2007. Protein networks and complexes in photoreceptor cilia. Subcell Biochem 43 209-35.

Rohatgi, R., Milenkovic, L., Scott, M.P., 2007. Patched1 regulates hedgehog signaling at the primary cilium. Science 317, 372-376.

Rosenbaum JL, Witman GB., 2002. Intraflagellar transport. Nat Rev Mol Cell Biol 3, 813-25.

Rosenfeld, J.A., Lacassie, Y., El-Khechen, D., Escobar, L.F., Reggin, J., Heuer, C., Chen, E., Jenkins, L.S., Collins, A.T., Zinner, S., Babcock, M., Morrow, B., Schultz, R.A., Torchia, B.S., Ballif, B.C., Tsuchiya, K.D., Shaffer, L.G., 2011. New cases and refinement of the critical region in the 1q41q42 microdeletion syndrome. European journal of medical genetics 54, 42-49.

Ross, A.J., May-Simera, H., Eichers, E.R., Kai, M., Hill, J., Jagger, D.J., Leitch, C.C., Chapple, J.P., Munro, P.M., Fisher, S., Tan, P.L., Phillips, H.M., Leroux, M.R., Henderson, D.J., Murdoch, J.N., Copp, A.J., Eliot, M.M., Lupski, J.R., Kemp, D.T., Dollfus, H., Tada, M., Katsanis, N., Forge, A., Beales, P.L., 2005. Disruption of Bardet-Biedl syndrome ciliary proteins perturbs planar cell polarity in vertebrates. Nat Genet 37, 1135-1140.

Saadi-Kheddouci, S., Berrebi, D., Romagnolo, B., Cluzeaud, F., Peuchmaur, M., Kahn, A., Vandewalle, A., Perret, C., 2001. Early development of polycystic kidney disease in transgenic mice expressing an activated mutant of the beta-catenin gene. Oncogene 20, 5972-5981.

Saburi, S., Hester, I., Fischer, E., Pontoglio, M., Eremina, V., Gessler, M., Quaggin, S.E., Harrison, R., Mount, R., McNeill, H., 2008. Loss of Fat4 disrupts PCP signaling and oriented cell division and leads to cystic kidney disease. Nat Genet 40, 1010-1015.

Satir, P., Guerra, C., Bell, A.J., 2007. Evolution and persistence of the cilium. Cell Motil Cytoskeleton 64, 906-913.

Saunier, S., Calado, J., Heilig, R., Silbermann, F., Benessy, F., Morin, G., Konrad, M., Broyer, M., Gubler, M.C., Weissenbach, J., Antignac, C., 1997. A novel gene that encodes a protein with a putative src homology 3 domain is a candidate gene for familial juvenile nephronophthisis. Hum Mol Genet 6, 2317-2323.

Saxen, L., Sariola, H., 1987. Early organogenesis of the kidney. Pediatr Nephrol 1, 385-392.

Sayer, J.A., Otto, E.A., O'Toole, J.F., Nurnberg, G., Kennedy, M.A., Becker, C., Hennies, H.C., Helou, J., Attanasio, M., Fausett, B.V., Utsch, B., Khanna, H., Liu, Y., Drummond, I., Kawakami, I., Kusakabe, T., Tsuda, M., Ma, L., Lee, H., Larson, R.G., Allen, S.J., Wilkinson, C.J., Nigg, E.A., Shou, C., Lillo, C., Williams, D.S., Hoppe, B., Kemper, M.J., Neuhaus, T.,

Parisi, M.A., Glass, I.A., Petry, M., Kispert, A., Gloy, J., Ganner, A., Walz, G., Zhu, X., Goldman, D., Nurnberg, P., Swaroop, A., Leroux, M.R., Hildebrandt, F., 2006. The centrosomal protein nephrocystin-6 is mutated in Joubert syndrome and activates transcription factor ATF4. Nat Genet 38, 674-681.

Serio, G., Margaria, V., Jensen, S., Oldani, A., Bartek, J., Bussolino, F., Lanzetti, L., 2011. Small GTPase Rab5 participates in chromosome congression and regulates localization of the centromere-associated protein CENP-F to kinetochores. Proceedings of the National Academy of Sciences of the United States of America 108, 17337-17342.

Signor, D., Wedaman, K.P., Orozco, J.T., Dwyer, N.D., Bargmann, C.I., Rose, L.S., Scholey, J.M., 1999. Role of a class DHC1b dynein in retrograde transport of IFT motors and IFT raft particles along cilia, but not dendrites, in chemosensory neurons of living Caenorhabditis elegans. J Cell Biol 147, 519-530.

Siller, K.H., Doe, C.Q., 2009. Spindle orientation during asymmetric cell division. Nature cell biology 11, 365-374.

Silverman MA, Leroux MR., 2009. Intraflagellar transport and the generation of dynamic, structurally and functionally diverse cilia. Trends Cell Biol 19 306-16.

Simons, M., Gloy, J., Ganner, A., Bullerkotte, A., Bashkurov, M., Kronig, C., Schermer, B., Benzing, T., Cabello, O.A., Jenny, A., Mlodzik, M., Polok, B., Driever, W., Obara, T., Walz, G., 2005. Inversin, the gene product mutated in nephronophthisis type II, functions as a molecular switch between Wnt signaling pathways. Nature genetics 37, 537-543.

Sir, J.H., Barr, A.R., Nicholas, A.K., Carvalho, O.P., Khurshid, M., Sossick, A., Reichelt, S., D'Santos, C., Woods, C.G., Gergely, F., 2011. A primary microcephaly protein complex forms a ring around parental centrioles. Nature genetics 43, 1147-1153.

Sluder, G., 2005. Two-way traffic: centrosomes and the cell cycle. Nature reviews. Molecular cell biology 6, 743-748.

Smith EF, Yang P., 2004. The radial spokes and central apparatus: mechano-chemical transducers that regulate flagellar motility. Cell Motil Cytoskeleton 57, 8-17.

Snape, K., Hanks, S., Ruark, E., Barros-Nunez, P., Elliott, A., Murray, A., Lane, A.H., Shannon, N., Callier, P., Chitayat, D., Clayton-Smith, J., Fitzpatrick, D.R., Gisselsson, D., Jacquemont, S., Asakura-Hay, K., Micale, M.A., Tolmie, J., Turnpenny, P.D., Wright, M., Douglas, J., Rahman, N., 2011. Mutations in CEP57 cause mosaic variegated aneuploidy syndrome. Nature genetics 43, 527-529.

Sorokin, S.P., 1968. Reconstructions of centriole formation and ciliogenesis in mammalian lungs. Journal of cell science 3, 207-230.

Stannard, W., O'Callaghan, C., 2006. Ciliary function and the role of cilia in clearance. J Aerosol Med 19, 110-115.

Strnad P, Gönczy P. 2008. Mechanisms of procentriole formation. Trends Cell Biol.18, 389-96.

Surendran, K., Selassie, M., Liapis, H., Krigman, H., Kopan, R., Reduced Notch signaling leads to renal cysts and papillary microadenomas. J Am Soc Nephrol 21, 819-832.

Surendran, K., Selassie, M., Liapis, H., Krigman, H., Kopan, R., 2010. Reduced Notch signaling leads to renal cysts and papillary microadenomas. Journal of the American Society of Nephrology : JASN 21, 819-832.

Swoboda, P., Adler, H.T., Thomas, J.H., 2000. The RFX-type transcription factor DAF-19 regulates sensory neuron cilium formation in C. elegans. Molecular cell 5, 411-421.

Szymanska, K., Johnson CA., 2012. The transition zone: an essential functional compartment of cilia. Cilia 2012, **1**:10.

Thomas, J., Morle, L., Soulavie, F., Laurencon, A., Sagnol, S., Durand, B., 2010. Transcriptional control of genes involved in ciliogenesis: a first step in making cilia. Biology of the cell / under the auspices of the European Cell Biology Organization 102, 499-513.

Tissir, F., Goffinet, A.M., 2010. Planar cell polarity signaling in neural development. Current opinion in neurobiology 20, 572-577.

Tissir F, Qu Y, Montcouquiol M, Zhou L, Komatsu K, Shi D, Fujimori T, Labeau J, Tyteca D, Courtoy P, Poumay Y, Uemura T, Goffinet AM. 2010. Lack of cadherins Celsr2 and Celsr3 impairs ependymal ciliogenesis, leading to fatal hydrocephalus. Nat Neurosci. 13, 700-7.

Torres, V.E., Harris, P.C., 2009. Autosomal dominant polycystic kidney disease: the last 3 years. Kidney Int 76, 149-168.

Tsao, P.N., Vasconcelos, M., Izvolsky, K.I., Qian, J., Lu, J., Cardoso, W.V., 2009. Notch signaling controls the balance of ciliated and secretory cell fates in developing airways. Development 136, 2297-2307.

Tuson, M., He, M., Anderson, K.V., 2011. Protein kinase A acts at the basal body of the primary cilium to prevent Gli2 activation and ventralization of the mouse neural tube. Development 138, 4921-4930.

Ullrich O, Reinsch S, Urbé S, Zerial M, Parton RG., 1996. Rab11 regulates recycling through the pericentriolar recycling endosome. J Cell Biol 135, 913-24.

Vaisberg, E.A., Grissom, P.M., McIntosh, J.R., 1996. Mammalian cells express three distinct dynein heavy chains that are localized to different cytoplasmic organelles. J Cell Biol 133, 831-842.

Valente, E.M., Silhavy, J.L., Brancati, F., Barrano, G., Krishnaswami, S.R., Castori, M., Lancaster, M.A., Boltshauser, E., Boccone, L., Al-Gazali, L., Fazzi, E., Signorini, S., Louie, C.M., Bellacchio, E., Bertini, E.,

Dallapiccola, B., Gleeson, J.G., 2006. Mutations in CEP290, which encodes a centrosomal protein, cause pleiotropic forms of Joubert syndrome. Nat Genet 38, 623-625.

van Breugel M, Hirono M, Andreeva A, Yanagisawa HA, Yamaguchi S, Nakazawa Y, Morgner N, Petrovich M, Ebong IO, Robinson CV, Johnson CM, Veprintsev D, Zuber B., 2011. Structures of SAS-6 suggest its organization in centrioles. Science. 331,196-9.

Varis, A., Salmela, A.L., Kallio, M.J., 2006. Cenp-F (mitosin) is more than a mitotic marker. Chromosoma 115, 288-295.

Vaughan, K.T., Vallee, R.B., 1995. Cytoplasmic dynein binds dynactin through a direct interaction between the intermediate chains and p150Glued. The Journal of cell biology 131, 1507-1516.

Vergnolle, M.A., Taylor, S.S., 2007. Cenp-F links kinetochores to Ndel1/Nde1/Lis1/dynein microtubule motor complexes. Current biology : CB 17, 1173-1179.

Voronina, V.A., Takemaru, K., Treuting, P., Love, D., Grubb, B.R., Hajjar, A.M., Adams, A., Li, F.Q., Moon, R.T., 2009. Inactivation of Chibby affects function of motile airway cilia. The Journal of cell biology 185, 225-233.

Walczak-Sztulpa, J., Eggenschwiler, J., Osborn, D., Brown, D.A., Emma, F., Klingenberg, C., Hennekam, R.C., Torre, G., Garshasbi, M., Tzschach, A., Szczepanska, M., Krawczynski, M., Zachwieja, J., Zwolinska, D., Beales, P.L., Ropers, H.H., Latos-Bielenska, A., Kuss, A.W., 2010. Cranioectodermal Dysplasia, Sensenbrenner syndrome, is a ciliopathy caused by mutations in the IFT122 gene. American journal of human genetics 86, 949-956.

Wallingford, J.B., Mitchell, B., 2011. Strange as it may seem: the many links between Wnt signaling, planar cell polarity, and cilia. Genes & development 25, 201-213.

Ward, C.J., Hogan, M.C., Rossetti, S., Walker, D., Sneddon, T., Wang, X., Kubly, V., Cunningham, J.M., Bacallao, R., Ishibashi, M., Milliner, D.S., Torres, V.E., Harris, P.C., 2002. The gene mutated in autosomal recessive polycystic kidney disease encodes a large, receptor-like protein. Nat Genet 30, 259-269.

Watanabe, D., Saijoh, Y., Nonaka, S., Sasaki, G., Ikawa, Y., Yokoyama, T., Hamada, H., 2003. The left-right determinant Inversin is a component of node monocilia and other 9+0 cilia. Development 130, 1725-1734.

Watnick, T., Germino, G., 2003. From cilia to cyst. Nat Genet 34, 355-356.

Westerfield, M., McMurray, J.V., Eisen, J.S., 1986. Identified motoneurons and their innervation of axial muscles in the zebrafish. J Neurosci 6, 2267-2277.

Williams, S.E., Beronja, S., Pasolli, H.A., Fuchs, E., 2011. Asymmetric cell divisions promote Notch-dependent epidermal differentiation. Nature 470, 353-358.

Wolf, M.T., Saunier, S., O'Toole, J.F., Wanner, N., Groshong, T., Attanasio, M., Salomon, R., Stallmach, T., Sayer, J.A., Waldherr, R., Griebel, M., Oh, J., Neuhaus, T.J., Josefiak, U., Antignac, C., Otto, E.A., Hildebrandt, F., 2007. Mutational analysis of the RPGRIP1L gene in patients with Joubert syndrome and nephronophthisis. Kidney Int 72, 1520-1526.

Woolf, A.S., Price, K.L., Scambler, P.J., Winyard, P.J., 2004. Evolving concepts in human renal dysplasia. J Am Soc Nephrol 15, 998-1007.

Woolley, D., 2000. The molecular motors of cilia and eukaryotic flagella. Essays Biochem 35, 103-115.

Yan, X., Li, F., Liang, Y., Shen, Y., Zhao, X., Huang, Q., Zhu, X., 2003. Human Nudel and NudE as regulators of cytoplasmic dynein in poleward protein transport along the mitotic spindle. Molecular and cellular biology 23, 1239-1250.

Yang P, Sale WS., 2000. Casein kinase I is anchored on axonemal doublet microtubules and regulates flagellar dynein phosphorylation and activity. J Biol Chem. 275, 18905-12.

Yang, J., Adamian, M., Li, T., 2006. Rootletin interacts with C-Nap1 and may function as a physical linker between the pair of centrioles/basal bodies in cells. Molecular biology of the cell 17, 1033-1040.

Yang, Z., Guo, J., Chen, Q., Ding, C., Du, J., Zhu, X., 2005. Silencing mitosin induces misaligned chromosomes, premature chromosome decondensation before anaphase onset, and mitotic cell death. Molecular and cellular biology 25, 4062-4074.

Yang, Z.Y., Guo, J., Li, N., Qian, M., Wang, S.N., Zhu, X.L., 2003. Mitosin/CENP-F is a conserved kinetochore protein subjected to cytoplasmic dynein-mediated poleward transport. Cell research 13, 275-283.

Yang B, Sonawane ND, Zhao D, Somlo S, Verkman AS, 2008. Small-molecule CFTR inhibitors slow cyst growth in polycystic kidney disease, J Am Soc Nephrol. 19 1300–1310.

Yoder, B.K., Hou, X., Guay-Woodford, L.M., 2002. The polycystic kidney disease proteins, polycystin-1, polycystin-2, polaris, and cystin, are co-localized in renal cilia. J Am Soc Nephrol 13, 2508-2516.

Yoder, B.K., Richards, W.G., Sweeney, W.E., Wilkinson, J.E., Avener, E.D., Woychik, R.P., 1995. Insertional mutagenesis and molecular analysis of a new gene associated with polycystic kidney disease. Proc Assoc Am Physicians 107, 314-323.

Yu, J., Carroll, T.J., McMahon, A.P., 2002. Sonic hedgehog regulates proliferation and differentiation of mesenchymal cells in the mouse metanephric kidney. Development 129, 5301-5312.

Yu, X., Ng, C.P., Habacher, H., Roy, S., 2008. Foxj1 transcription factors are master regulators of the motile ciliogenic program. Nature genetics 40, 1445-1453.

Zeng, H., Hoover, A.N., Liu, A., 2010. PCP effector gene Inturned is an important regulator of cilia formation and embryonic development in mammals. Developmental biology 339, 418-428.

Zheleznova NN, Wilson PD, Staruschenko A., 2011. Epidermal growth factor-mediated proliferation and sodium transport in normal and PKD epithelial cells. Biochim et Biophys Acta 1812, 1301–1313.

Zhu, X., Mancini, M.A., Chang, K.H., Liu, C.Y., Chen, C.F., Shan, B., Jones, D., Yang-Feng, T.L., Lee, W.H., 1995. Characterization of a novel 350-kilodalton nuclear phosphoprotein that is specifically involved in mitotic-phase progression. Molecular and cellular biology 15, 5017-5029.

Zuo, X., Guo, W., Lipschutz, J.H., 2009. The exocyst protein Sec10 is necessary for primary ciliogenesis and cystogenesis in vitro. Molecular biology of the cell 20, 2522-2529.

Zylkiewicz, E., Kijanska, M., Choi, W.C., Derewenda, U., Derewenda, Z.S., Stukenberg, P.T., 2011. The N-terminal coiled-coil of Ndel1 is a regulated scaffold that recruits LIS1 to dynein. The Journal of cell biology 192, 433-445.

LIST OF SUPPORTING PUBLICATIONS

1. The kinetochore protein, *CENPF* is mutated in a novel human ciliopathy.
Aoife M Waters [1], Francesco Lescai [1], Alison Bright [2], Sonja Christou [1], Anthony Brooks [1], Chiara Bacchelli [1], David M Bader [2], Estelle Chanudet [1], Charu Deshpande [3], Horia Stanescu [4], Helen Stewart [5], Robert Kleta [4], Mike Hubank [1], Stephen Doxsey [2], Elia Stupka [5], Mark Winey [6], & Philip L Beales [1]
In revision for *Human Molecular Genetics.*

2. Comparison of 173 disease exomes to 1,000 Genome data suggests a role for private loss of function insertions and deletions in disease genetics.
Francesco Lescai, Silvia Bonfiglio, Chiara Bacchelli, Estelle Chanudet, **Aoife Waters**, Sanjay M. Sisodiya, Dalia Kasperavičiūtė, Julie Williams, Denise Harold, John Hardy, Robert Kleta, Sebahattin Cirak, Richard Williams, John C. Achermann, John Anderson, David Kelsell, Tom Vulliamy, Henry Houlden, Nicholas Wood, Una Sheerin, Gian Paolo Tonini, Donna Mackay, Khalid Hussain, Jane Sowden, Veronica Kinsler, Justyna Osinska, Tony Brooks, Mike Hubank, Philip Beales and Elia Stupka
In press *PLoS One*.

3. A founder mutation in Vps37A causes autosomal recessive complex hereditary spastic paraparesis. Zivony-Elboum Y, Westbroek W, Kfir N, Savitzki D, Shoval Y, Bloom A, Rod R, Khayat M, Gross B, Samri W, Cohen H, Sonkin V, Freidman T, Geiger D, Fattal-Valevski A, Anikster Y, **Waters AM**, Kleta R, Falik-Zaccai TC. *J Med Genet.* 2012 Jul;49(7):462-72.

4. *Integrin α3* mutations cause kidney, lung and skin disease.
Has C, Sparta G, Kiritsi D, Weibel L, Moeller A, Vega-Warner V, **Waters, A**, He Y, Esser P, Straub B, Hausser I, Bockenhauer D, Dekel B, Hildebrandt F, Bruckner-Tuderman L, Laube G
N Engl J Med 2012 19;366(16):1508-14.

5. Interstitial Lung Disease And Epidermolysis Bullosa In A Proteinuric Infant
Waters AM, Has G, Laube G, Sparta G, Hildebrandt F, Rees L, Sebire N, Bockenhauer D
Manuscript under review at the *Journal of the American Society of Nephrology*

6. An enzyme-linked immunosorbent assay (ELISA) for quantification of human collectin 11 (CL-11, CL-K1).
Selman L, Henriksen ML, Brandt J, Palarasah Y, **Waters A**, Beales PL, Holmskov U, Jørgensen TJ, Nielsen C, Skjodt K, Hansen S.
J Immunol Methods. 2012 Jan 31;375(1-2):182-8.

7. Mutations in lectin complement pathway genes COLEC11 and MASP1 cause 3MC syndrome. Rooryck C, Diaz-Font A, Osborn DP, Chabchoub E, Hernandez-Hernandez V, Shamseldin H, Kenny J, **Waters A**, Jenkins D, Kaissi AA, Leal GF, Dallapiccola B, Carnevale F, Bitner-Glindzicz M, Lees M, Hennekam R, Stanier P, Burns AJ, Peeters H, Alkuraya FS, Beales PL.
Nat Genet. 2011 Mar;43(3):197-203.

8. Ciliopathies: an expanding disease spectrum.
Waters AM, Beales PL.
Pediatr Nephrol. 2011 Jul;26(7):1039-56.